Characterisation of Radiation Fields with Combined Fast-neutron and Gamma-ray Imaging

Jonathan Stuart Beaumont

Department of Engineering
Lancaster University

This thesis is submitted for the degree of
Doctor of Engineering (EngD)

June 2017

Declaration

I hereby declare that except where specific reference is made to the work of others, the contents of this thesis are original and have not been submitted in whole or in part for consideration for any other degree or qualification in this, or any other university. This thesis is my own work and contains nothing which is the outcome of work done in collaboration with others, except as specified in the text.

Jonathan Stuart Beaumont
June 2017

Acknowledgements

I would like to acknowledge many people for their help and guidance, first and foremost my supervisors Prof. Malcolm Joyce, Dr. Matthew Mellor and Dr. Alan Shippen who provided invaluable feedback and support during the EngD programme. I thank Andrew Verden, Peter Jones, Bob Mackin, Dr. Fabrice Andrieux, Dr. Kelum Gamage and Kath Rucastle at Lancaster University; Prof. Jon Billowes, Dr. Paul Campbell and Dr. David Stanley at the University of Manchester; Dr. Graeme Taylor at the National Physical Laboratory and Dr. Mario Villa at the Atominstitut, Vienna University of Technology for brilliant technical and administrative assistance.

To all my fellow researchers at Lancaster University I have worked alongside, in particular: Dr. Matthew Balmer, Helen Parker, Dr. Andrew Parker, Nadya Rauff-Nisthar, Dr. Bethany Colling, Dr. Ashley Jones, Alex Grievson, Rashed Sarwar and Chris Tighe, and to all my fellow Research Engineers on the Nuclear EngD programme (it would be a very long list); I thank you for the interesting discussions, technical or otherwise, and for being great company. It was a pleasure to work with everyone at Createc Ltd. and with engineering undergraduates in laboratory classes and projects at Lancaster University.

I gratefully acknowledge the Nuclear Decommissioning Authority (NDA), Createc Ltd. and the Engineering and Physical Sciences Research Council (EPSRC) for funding this project; and Lancaster University, the National Physical Laboratory, the University of Manchester and the Atominstitut, Vienna University of Technology for use of facilities and resources during this research project.

Abstract

This research explores the use of organic liquid scintillation detectors coupled with digital pulse-processing electronics, mechatronics and shielding materials to non-destructively characterise radiation sources and their emitted radiation fields through passive imaging techniques. The research sought to expand upon existing gamma-ray imaging techniques, but with focus on fast-neutron imaging techniques which are few in number. The study involved conceptual design, Monte Carlo optimisation and characterisation of collimator and detector geometry, followed by the subsequent design and procurement, assembly and modification to produce several probe configurations. The full system was then realised through control system design, electronic interfacing between custom and commercial off-the-shelf components, communication interfacing and software engineering to produce the data acquisition systems. Coordination with universities and nuclear facilities, logistics and experimental planning enabled the successful deployment of imagers at the University of Lancaster, University of Manchester, the National Physical Laboratory and the Atominstitut at Vienna University of Technology. Data were then analysed by custom code, interpreted and benchmarked to conclude the accuracy of the output images.

Three types of imaging devices were investigated. The first was a slot-modulated imaging approach with a tungsten and polythene collimator. This imager was the backbone of the study and underwent significant developments to allow for deployment in different environments. The principle of operation was a heavily shielded single detector which sequentially interrogated space through a small unshielded and sensitive region over the time-scale of a few hours. The objectives were to create a compact, lightweight and portable system which could be used in high-dose or highly-shielded environments to image radiation fields. The second was a slot-modulated imaging approach with a tungsten anti-collimator, effectively using the first imaging system in geometric inversion. As with the first imager, this required sequential interrogation of space over the order of hours, though here the sensitive region was large. This introduced some drawbacks on the image quality but addressed situations where a more compact and lightweight probe was required or where neutron radiation fields were of very high energy (up to deuterium-tritium fusion at 14.1 MeV). The third system was an uncollimated multi-detector system which used readings from four detectors with a real-time algorithm to determine the position of a single source. This configuration was incapable of imaging complex fields, but was effective at tracking the position of a single source every 2 seconds.

The bulk of the research was conducted with the slot-modulated imaging approach which was demonstrated with the following radiation sources: a ^{252}Cf source and ^{241}Am/Be source stored in cans, a ^{252}Cf source stored in a steel-shielded water tank and a TRIGA test reactor core. These sources of neutrons and gamma-rays in combination with variation in shielding provided a range of scenarios which were representative of potential industrial deployments in nuclear medicine, nuclear safeguards, nuclear security and nuclear decommissioning. The anti-collimated imaging technique was demonstrated using a ^{252}Cf source stored in a steel-shielded water tank. The uncollimated real-time approach was demonstrated in tracking a single ^{137}Cs source in 3D space which was representative of nuclear security and nuclear medicine applications. The potential applications were explored in the context of other technologies in previous and active research.

Contributions and achievements

Author contributions

Unique achievements in this study included high-quality imaging of fast-neutron fields with slot modulation techniques, in both collimated and anti-collimated approaches. These imager probes were more compact, lightweight, and portable than other neutron imaging systems. The latter in particular indicated the possibility of creating a highly lightweight imaging probe functional in high-energy neutron fields (including deuterium-tritium fusion at 14.1 MeV). The ability of a collimated imager to locate and image multiple sources including some components of the surrounding objects with scattered neutrons was shown. A heavily shielded fission source with a neutron field reduced to below 1 μSv/h was imaged, demonstrating that this source could be located with an imaging technique. The ability to discern two different neutron source types using neutron pulse-height spectroscopy in combination with neutron imaging was also exhibited.

The TRIGA mk II test reactor at Vienna University of Technology was characterised using neutron and gamma-ray fields emitted from the reactor core during high-power operation. It was demonstrated that the fission reaction in the core could be visualised and the steady-state power level could be measured with this approach. These experiments were accompanied by the additional challenge of high-dose conditions at the probe location due to the limited shielding of the reactor core in its irradiation chamber.

A method for real-time tracking of a radiation source in three dimensions using four fixed detectors was demonstrated.

Journal paper contributions

- Jonathan S. Beaumont, Matthew P. Mellor, Malcolm J. Joyce; The analysis of complex mixed-radiation fields using near real-time imaging. Radiation Protection Dosimetry 2014; 161 (1-4): 331-334. doi: 10.1093/rpd/ncu044

- Jonathan S. Beaumont, Matthew P. Mellor, Mario Villa, Malcolm J. Joyce; High-intensity power-resolved radiation imaging of an operational nuclear reactor. Nature Communications 2015;6:8592. doi:10.1038/ncomms9592

- Malcolm J. Joyce, Stewart Agar, Michael D. Aspinall, Jonathan S. Beaumont, Edmund Colley, Miriam Colling, Joseph Dykes, Phoevos Kardasopoulos, Katie Mitton; Fast neutron tomography with real-time pulse-shape discrimination in organic scintillation detectors, Nuclear Instruments and Methods in Physics Research Section A: Accelerators, Spectrometers, Detectors and Associated Equipment, Volume 834, 2016, Pages 36-45, ISSN 0168-9002, http://dx.doi.org/10.1016/j.nima.2016.07.044

- Jonathan S. Beaumont, B. Alan Shippen, Matthew P. Mellor, Malcolm J. Joyce; Imaging of fast neutrons and gamma rays from 252Cf in a heavily shielded environment, Nuclear Instruments and Methods in Physics Research Section A: Accelerators, Spectrometers, Detectors and Associated Equipment, Volume 847, 1 March 2017, Pages 77-85, ISSN 0168-9002, https://doi.org/10.1016/j.nima.2016.11.043

Conference paper contributions

- Jonathan S. Beaumont, Matthew P. Mellor, Malcolm J. Joyce; Real-time, fast-neutron spectroscopy for source identification in mixed-field imaging applications; 2012 IEEE Nuclear Science Symposium and Medical Imaging Conference Record (NSS/MIC), Anaheim, CA, 2012, pp. 219-221, doi: 10.1109/NSSMIC.2012.6551097

- Jonathan S. Beaumont, Bethany Colling, Matthew P. Mellor, Malcolm J. Joyce; On the design and test of a neutron collimator for real-time neutron imaging in the MeV energy range, 2013 3rd International Conference on Advancements in Nuclear Instrumentation, Measurement Methods and their Applications (ANIMMA), Marseille, 2013, pp. 1-8, doi: 10.1109/ANIMMA.2013.6728019

- Jonathan S. Beaumont, Matthew P. Mellor, Malcolm J. Joyce; On the resolving and source identification limitations of a real-time fast-neutron imaging system, 2013 IEEE Nuclear Science Symposium and Medical Imaging Conference (2013 NSS/MIC), Seoul, 2013, pp. 1-7, doi: 10.1109/NSSMIC.2013.6829503

Conferences and meetings

- Universities Nuclear Technology Forum (UNTF) 2012, Birmingham, UK (Oral presentation)

- Nuclear Decommissioning Authority PhD Seminar 2012, Manchester, UK (Poster presentation)
- Neutron and Ion Dosimetry Symposium (NEUDOS12) 2012, Aix en Provence, France (Oral presentation)
- Energy CDT Network, Manchester, UK (Oral presentation)
- The Frédéric Joliot / Otto Hahn Summer School on Nuclear Reactors: Physics, Fuels and Systems (FJOH) 2012, Aix en Provence, France
- IEEE Nuclear Science Symposium 2012, Anaheim, CA, USA (Poster presentation)
- Nuclear Decommissioning Authority PhD seminar 2013, Manchester, UK (Oral presentation)
- Universities Nuclear Technology Forum (UNTF) 2013, London, UK (Oral presentation)
- International Conference on Advancements in Nuclear Instrumentation Measurement Methods and their Applications (ANIMMA) 2013, Marseille, France (Oral presentation)
- Neutron Users' Club 2013, Teddington, UK
- IEEE Nuclear Science Symposium 2013, Seoul, Republic of Korea (Oral presentation)
- Nuclear Decommissioning Authority PhD seminar 2014, Manchester, UK (Oral presentation)
- Universities Nuclear Technology Forum (UNT) 2014, Oxford, UK (Oral presentation)
- Neutron Users' Club 2014, Teddington, UK
- IEEE Nuclear Science Symposium 2014, Seattle, WA, USA (Poster presentation)
- European Nuclear Young Generation Forum (ENYGF) 2015, Paris, France (Oral presentation)
- Neutron Users' Club 2015, Teddington, UK (Oral presentation)

Visits to research and commercial facilities

- Neutron Metrology Laboratory, National Physical Laboratory, Teddington, UK
- Schuster Laboratory, University of Manchester, Manchester, UK
- Oliver Lodge Laboratory, University of Liverpool, Liverpool, UK
- Westinghouse Springfields Fuels Ltd, Salwick, UK
- Preston Laboratory, National Nuclear Laboratory, Salwick, UK
- Heysham Nuclear Power Plant, Heysham, UK
- Central Laboratory, National Nuclear Laboratory, Sellafield, UK
- Windscale Laboratory, National Nuclear Laboratory, Sellafield, UK
- LECA-STAR Facility, Cadarache, France
- JHR Facility, Cadarache, France
- National Grid Dispatch Center (RTE), Paris, France
- Atominstitut, Vienna University of Technology, Vienna, Austria
- National Nuclear Laboratory, Warrington, UK

Nuclear EngD taught component

- IMechE and IET accredited Professional and Personal Skills Development programme completed
- NTEC technical modules *Radiation Shielding*, *Management of the Decommissioning Process* and *Experimental Reactor Physics* completed with distinction
- Post-graduate diploma in Enterprise Management awarded with merit

Contents

List of Figures

List of Tables

Glossary

List of acronyms and definitions

^{241}Am/B	A neutron source comprising both americium-241 and boron
^{241}Am/Be	A neutron source comprising both americium-241 and beryllium
4π image	An image which contains information from all possible solid angles, i.e. from a full universe
ADC	Analogue-to-digital converter
ALARA	As low as reasonably achievable (risk or radiation dose)
ART	Algebraic reconstruction technique, a method for finding an image solution from collected data
Backscatter	Radiation scattering through a large angle (> 90 °) before detection
BPE	Borated polyethylene
BWR	Boiling water reactor
CCD	Charge-coupled device
CCM	Charge comparison method
CLYC	Cs_2LiYCl_6:Ce scintillation crystal
CT	Computed tomography
FNIT	The fast neutron imaging telescope
FOV	Field of view
FPGA	Field-programmable gate array
FWHM	Full width at half maximum
GARR	Gamma ray rejection, a quantitative metric for gamma-ray misclassification
GPIO	General purpose input/output
HDPE	High-density polyethylene
Hotspot	A region of high radiation flux in comparison to surrounding regions

Image artefact	An apparent structure in an image solution which is introduced in error by the equipment or processing method
Imager	Apparatus used to acquire data and subsequently process it into a human-interpretable output image
INL	Idaho National Laboratory
Ionizing radiation	Radiation which carries enough energy to liberate electrons from atoms or molecules, producing ions
MCA	Multi-channel analyser
MCNP	Monte Carlo N-Particle radiation transport code
MFA	Mixed-field analyser, a signal processing unit coupled with a detector to discriminate neutron and gamma-ray events
MOSFET	Metal–oxide–semiconductor field-effect transistor
NGMA	Neutron-gamma model analysis
NPL	National Physical Laboratory
ORNL	Oak Ridge National Laboratory
PCV	Primary containment vessel
PE	Polyethylene
PET	Positron emission tomography
PGA	Pulse gradient analysis
Pile-up	The detection of two or more radiation events within a short time resulting in multiple peaks in the output pulse due to overlap
PINEX	Pin-hole neutron camera experiment
PMT	Photo-multiplier tube
pps	Pulses per second
PSD	Pulse-shape discrimination, a classification of the radiation type based on the shape of the output pulse from a radiation detector
Raster scanning	Sequential measurement of data from a grid of spatial coordinates obtained one line at a time
RPV	reactor pressure vessel
Sensitivity map	A map of solid angles where the value in each bin characterises the probability to detect radiation emitted from the corresponding solid angle
S/N	Signal-to-noise ratio
SNL	Sandia National Laboratory
SNM	Special nuclear material (plutonium or enriched uranium)

SPECT	Single-photon emission computed tomography
System matrix	Array of sensitivity maps for every collimator position where data are measured
TRIGA	Training, research and isotope production General Atomic (a nuclear test reactor type)
USB	Universal serial bus
Voxel	A three-dimensional pixel

List of symbols

4π	4π steradians, the solid angle subtended by a complete sphere
α	α particle, a ^{4}He nucleus
$\hat{\alpha}$	Rotation angle of a collimator around its cylindrical axis
β	β particle, an electron
$\hat{\beta}$	Rotation angle of a collimator around a vertical axis perpendicular to the cylindrical axis
γ [γ']	Gamma-ray photon [gamma-ray photon after collision]
ε	Intrinsic efficiency of a radiation detector
η	Number of collisions of a neutron
θ	Azimuth angle
κ_k	Relaxation parameter in ART algorithm
λ	Mean free path
Λ	Path length inside radiation detector
μ	Attenuation parameter (subscript indicates reaction type)
ν	Number of neutrons released in a single fission event
$\bar{\nu}$	Mean number of neutrons released in fission
ρ	Material density
σ	Reaction cross-section
$\bar{\sigma}$	Standard deviation
ϕ	Elevation angle
χ^2	Value of chi-squared statistical hypothesis test
ψ	Digitised detector output pulse
ω	Period
A	Atomic mass number
a, b, c, d	Parameters in fitted function
$\hat{c}$	Unit vector normal to detector face and along collimator cylindrical axis
Ch_{peak}	MCA channel containing peak near Compton edge
Cj	Collimator type j
D	Image data matrix
$\hat{d}_i$	Position vector of detector i
d_{ij}	Single element of data matrix D
E	Energy
E_γ [E'_γ]	Energy of gamma ray [after collision]
E_n [E'_n]	Energy (kinetic) of neutron [after collision]

F	Fission product
f	Fission reaction
I	Image solution data
I_0	Initial intensity of radiation beam
I'	Intensity of radiation beam after transmission
i	Index integer
j	Index integer
k	Iteration number of ART algorithm
l	Displacement of detectors from origin
M	Imager system matrix
m_{ij}	Imager sensitivity map for a single collimator position i,j
N	Number density
n [n']	Neutron [neutron after collision]
$\hat{o}$	Position vector of the origin of the uncollimated multi-detector system
p	Proton
$\hat{p}$	Position vector of a single radiation source
$\hat{r}$	Position vector between a radiation source and the imager detector
r_{SI}	Distance between a radiation source and the imager detector
R_i	Fraction of total events detected in detector i
$\hat{R}_\alpha$	Rotational transform in angle $\hat{\alpha}$
t_b	Time for background data collection
t_d	Time for image data collection at a single collimator orientation
v	Neutron velocity
w	Weighting used to sum neutron pulse-height spectra
X [X^*]	Nucleus in ground state [excited state]
$\hat{x}$	Unit vector in positive-x direction
$\hat{y}$	Unit vector in positive-y direction
$\hat{z}$	Unit vector in positive-z direction
Z	Atomic number

Chapter 1

Introduction

Chapter summary

This chapter discusses the general motivations for imaging technology and imaging using ionizing radiation. Information about the industrial partners, Createc Ltd., who supported this research is provided. The chapter concludes with specific goals, metrics for achievement and reasoning.

1.1 Vision

Visible light is an abundant information carrier in our local environment; it will transmit over long distances through atmosphere and is easily blocked or reflected by objects with which we might interact. We have a regular supply by day from the sun and by night from celestial bodies or modern innovations. Light is lensed by the eye and projected on to the retina, our own biological radiation detector, where thousands of electrical signals are produced and transferred to the brain by the optic nerve. The primary visual cortex in human beings is estimated to contain 140 million neurons [1] which decode this information in as little as 100 ms [2], producing in our minds detailed images and models of our surroundings. Throughout evolution, high resolution vision has allowed our predecessors to rapidly interpret and interact in complex, dynamic environments which led to its resultant abundance in the animal kingdom. We have progressed since the eighteenth century to view other radiations not normally detectable by the human eye.

1.2 Imaging

Radio astronomy was first demonstrated eighty years ago by Karl Jansky [3] who built a spatially-biased radio receiver, showing the Milky Way was a significant source of long-wavelength electromagnetic radiation. This result paved the way for modern radio telescopes which convert radio waves on Earth into images of extraterrestrial objects which with some small context, we can instantly interpret and understand. Therefore it might be unsurprising that we invest a huge collective effort into imaging technology, engineering new extensions to our own vision such that we can visualise structures and dynamics which might be otherwise invisible from atomic architectures to the coalescence of distant stars.

Ionizing radiation is used widely as an information carrier in imaging systems. The most well known is the X-ray: a high energy photon generally produced by bombarding metals with electrons. X-ray systems are relatively cheap and are frequently deployed worldwide in security applications to monitor checkpoints for the passage of weapons or other illicit materials. X-rays are highly attenuated by dense substances such as metals and can form high-resolution images, allowing a human (or machine) interpreter to spot shapes and structures which may indicate the presence of contraband. A great advantage of these methods is that they are non-destructive, i.e. the material under scrutiny is not changed by the interrogation. This advantage is huge when dealing with subjects which otherwise could not be examined without damage such as historic artefacts, structural materials and human bodies.

Radiation imaging has rapidly become prevalent in medicine: it (as well as other forms) is now a standard practice worldwide and has had a huge impact on the way in which diagnoses are attained and medical research can be performed. These great leaps in technology have revolutionised patient treatment in the modern age, demonstrating the value of radiation images in these applications.

1.3 Research motivation

Neutron detection is of widespread interest because of the implications of the presence of neutron radiation. The emission of neutrons is very rare in comparison with α, β and γ and is associated with uranium, the fission reaction, and the subsequently produced transuranic elements which do not occur naturally on Earth. Although other channels of neutron production do exist (see section 2.2.1), neutron emission in context has an extremely strong correlation with fissile nuclear materials, e.g. nuclear fuels or weapons which are the focus of interest in nuclear safeguards, nuclear security and nuclear decommissioning. These materials are tightly controlled under the Non-Proliferation Treaty [4] and pose some of the highest risks to global security. Removal of these materials from nuclear reactors is required for decommissioning and is usually performed at the earliest possible stage for these reasons (as well as to reduce radiation dose). Any amounts, even residues, must be accounted for and handled with extreme stringency. Knowledge of the distribution and abundance of these materials is therefore fundamental in these fields.

Nuclear power is now a major global energy source with 440 commercial power reactors currently in operation, accounting for 380 GWe (around 11% of the worlds energy consumption) [5]. Although reactors have high start-up capital costs, they provide a large continuous base-load of cheap energy. France has 58 nuclear reactors which account for 75% of its energy demand. Consequently the country has the cheapest electricity in Europe and gains €3 billion annually from net exports [6]. Nuclear power has become more favourable in recent years as it provides a viable solution to energy security in the light of recent restrictions on carbon emissions imposed by the Kyoto Protocol [7]. The lifetimes of Generation-II commercial power reactors, built between the mid ’60s and mid ’90s, is 30-45 years with 50 -

60 years more typical for recently designed and commissioned plants. To date approximately 110 commercial power reactors and 250 research reactors are no longer in operation and are in the decommissioning phase [8]. The cost of decommissioning in the UK alone has been recently estimated by the UK's Nuclear Decommissioning Authority (NDA), who own 17 nuclear sites in the UK, at £161 billion (discounted) over the next century [9] (nuclear decommissioning is an extremely long-term process). The NDA regard the development of the right technology and the use of the right resources as a cornerstone of the decommissioning effort [10].

There are a handful of systems available which are capable of imaging fast-neutron fields, each with their own strengths and weaknesses appropriate for their target applications (discussed thoroughly in section 2.5). The majority of these systems have been applied to nuclear security to quickly identify and locate a small number (typically 1) of neutron sources. Some of these systems are considered portable and the front-end of the smallest reported neutron imaging systems, a time projection chamber configuration, fills a sphere of approximately 80 cm diameter. Perhaps only one or two of these systems could be considered field-ready and none of these are truly as compact, lightweight and portable as would be required in nuclear decommissioning applications. Most of those which are transportable have unshielded detectors for maximum detection efficiency and are therefore unsuited to high-dose environments which would drastically reduce the signal to noise ratio of any of these devices. There is therefore a significant gap in technology which this research aims to address. In addition, slot-modulated imaging, a technique prevalent in nuclear medicine, has not been applied to neutron fields and therefore presents a gap in scientific knowledge.

1.4 Industrial partnership with Createc Ltd.

This thesis has been conducted in association with Createc Ltd., an engineering consultancy enterprise based in Cumbria, UK [11]. The company was founded in 2010, spinning out from REACT Engineering Ltd., an engineering firm with a large stake in nuclear decommissioning projects in the UK from whom they inherited expertise in the nuclear industry. Createc have pursued their vision of applying innovative approaches to imaging technologies, focussing on applied novel research as the backbone of their business model to create new value-driven capabilities or more financially effective alternatives. Projects are diverse and range from security, petrochemical, renewable energies and infrastructure applications to those in the nuclear sector. The central project of the company is the N-Visage™ [12] gamma-ray imager, shown in Fig. 1.1a, and associated software which has been used at such installations as Sellafield and Fukushima Daiichi and the extreme radiation environments therein [13]. N-Visage provides high resolution gamma-ray imaging, is integrated with optical cameras and a laser range-finder and is compact and lightweight. An image from a survey at Fukushima Daiichi is shown in Fig. 1.1b. 3D models of radiation sources and dose maps can be generated from this information. The managing director, Dr. Matt Mellor, and research associate, Dr. Alan Shippen, have acted as supervisors on this project, providing an invaluable context of industry and focus to applications of the research as an end product. The key features of N-Visage™ as a gamma-ray imaging device are the low weight and size, high radiation tolerance, ease of interpretation, competitive pricing and elegance of the system, fulfilling all necessary criteria for the target market and therefore perfectly demonstrating the ultimate goals of a compact neutron imaging device in these applications.

“See things differently” - Createc Ltd. mission statement

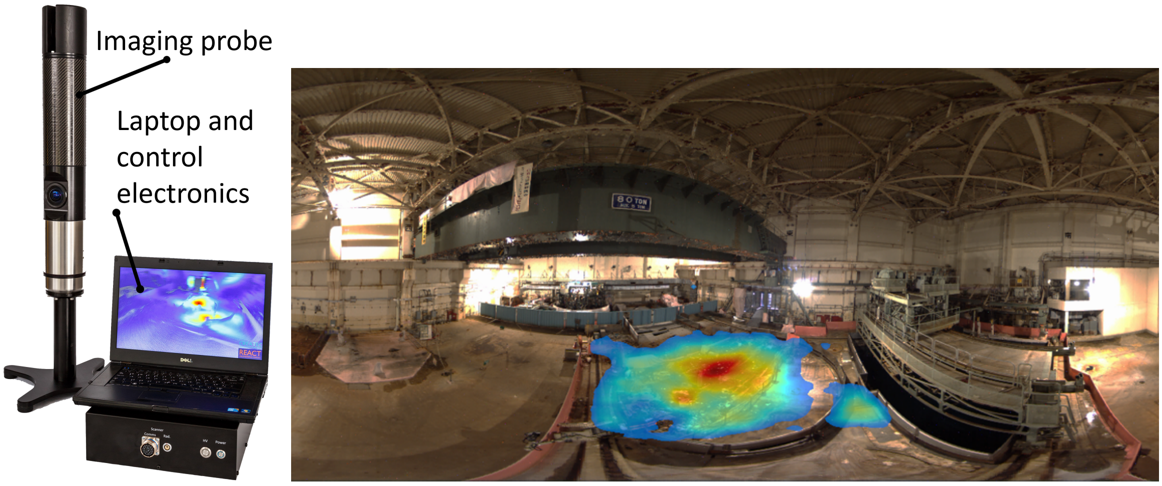

(a) The imaging system hardware: probe, PC and electronics

(b) Gamma-ray images from the N-Visage ™ survey of Fukushima Daiichi showing the distribution of gamma-ray emitting radionuclides (blue-red colour scale: red indicating highest flux contributions) overlaid on an optical image

Figure 1.1 The N-Visage ™ gamma-ray imaging system: hardware and output images.

1.5 Research goals

The goal of this thesis is to develop fast-neutron imaging capabilities in combination with gamma-ray imaging, the target applications are nuclear decommissioning and related fields. The system will collect information from radiation fields which can then be easily visually interpreted by the user to facilitate subsequent strategic decisions relating to radioactive materials. This thesis is intended to develop fast-neutron imaging technology towards a commercial product which could be deployed in the nuclear industry. To be considered for deployment in an active area at a nuclear site, it is important that all end-user criteria are considered. These are discussed here and summarised in Table 1.1.

Table 1.1 Summary of goals in this research.

Goal	Required	Desired
Discretely image combined fast-neutron and gamma-ray fields	Yes	
Image resolution allows individual sources to be resolved	20°	2°
Determine relative detected flux associated with each source or localised source distribution	Yes	
Associate source distributions with locations in real space	Yes	
No interference with plant operations during imaging process	Yes	
Quickly assembled, disassembled and packaged	Yes	
Compact probe outer diameter	50 cm	15 cm
Lightweight probe	10 kg	5 kg
Fast data acquisition time	< 8 hours	2 hours
Discern special nuclear materials from other radioactive materials	No	Yes
System can be transported by a single individual and vehicle	No	Yes
System fully operated remotely	Yes	
Imaging probe is radiation tolerant	50 mSv/h	1 Sv/h

1.5.1 Image quality

The purpose of the imager is to collect unknown information from an environment to inform the user about neutron and gamma-ray emitting materials in the space local to the imaging probe. This can be quantified as the location of emission, the type of emission (neutrons or gamma rays) and relative field strength originating from each location in space. The imager must therefore be capable of imaging combined fast-neutron and gamma-ray fields which have significant complexity, i.e. with multiple sources or distributions. The ability to discern special nuclear materials (fissile uranium and plutonium) amongst other contaminants such as caesium would be desired for maximum strategic impact to the end user. In order to link emission hotspots with physical objects and to discern discrete radiation sources an imaging resolution of 2° is desired; these resolutions are achievable with user-tested systems like N-Visage. A resolution of at least 20° is required to produce any meaningful results; this is based on resolving two 55-gallon drums at a distance of 2 m.

1.5.2 Deployment time

Any type of nuclear facility has high operational costs and interference with plant output would drastically affect the economic viability of an imager. The imaging process therefore must not interfere with plant operations. Data collection time may also be a strongly influencing factor. Although in some situations this is not critical, plant operators would always see faster data collection as beneficial, as less deployment time would create the least possible disruption. Access to nuclear sites is often time-restricted to the order of days. Multiple scans from several locations may be required. Based on 3 scans per day a scan time of 2 hours was set as a target. A scan time of less than 8 hours is required for a data collection time of less than one working day. For the same reasons the system must be quickly assembled with ease of physical and software set-up, then quickly disassembled and packaged for transport.

1.5.3 Size and weight

As access to some areas is often severely restricted in terms of geometry, there is a strong motivation to engineer the probe to be as compact as possible. Access ports for instrumentation can be as little as 15 cm diameter; this is therefore the target restriction on the probe size. Coupled with these difficult deployments are restrictions on weight. Often these hard-to reach areas are only accessible by robots or other methods which have significant restrictions on payload. 10 kg and 5 kg payloads are common limits and are therefore the target weights. A preference for multiple sensors on a single probe is also taken into account; the probe should be as light as possible. For maximum portability the entire system should be compact and ideally transported by one person in one vehicle.

1.5.4 Radiation tolerance

Areas requiring survey may often be high-dose environments with limited or impossible access by a human operator. In these circumstances the system must be operated remotely and have a tolerance to the required dose. A target dose in line with Createc's N-Visage™ of 1 Sv/h is desired. To be economically viable the imager must be able to tolerate limits which exceed those of a radiation worker performing the survey manually. On the assumption of a 1 hour survey requiring the maximum annual whole-body dose of 50 mSv (as recommended by the ICRP [14]), the minimum operational dose range should be at least 50 mSv/h for the imager.

Chapter 2

Background

Chapter summary

This chapter discusses the foundation science and technology underpinning this research including production, interactions and detection methods of gamma-ray and neutron radiation, introduction to imaging methods and fast-neutron imaging devices used in the nuclear industry.

2.1 Gamma-ray radiation

Natural radioactivity was first discovered by Henri Becquerel in 1896 from experimentation with uranium salts and photographic plates [15] (Nobel Prize in Physics 1903 - shared with Pierre and Marie Curie). Subsequent experiments led to the discovery of gamma rays by Paul Villard, a French physicist and chemist, in 1900 who noticed the highly penetrating form of this radiation [16]. α, β and γ radiation were differentiated by Rutherford in 1903 [17] (Nobel Prize in Chemistry 1908). The radiation types are named according to their relative penetrating distance.

2.1.1 Production

Gamma rays are high energy photons of electromagnetic radiation emitted from the nucleus whenever a transition from a high energy X^* to a low energy X state occurs, following a close analogy with X-ray transitions [18]. Gamma rays are produced according to the principle of the conservation of energy and therefore the energy of the photon E_γ is equal to the energy change of the nucleus according to Eq. 2.1. Gamma rays are produced alongside most nuclear reactions, most commonly radioactive decay which is the source of gamma rays for the major applications of this imaging work.

$$E_\gamma = E_{X^*} - E_X \tag{2.1}$$

2.1.2 Interactions

Gamma rays interact mainly through three processes: photoelectric absorption, Compton scattering and pair production. These processes are dependent on the atomic number (Z) of the target material and the energy of the incoming photon E_γ; their regions of dominance are outlined in Fig. 2.1.

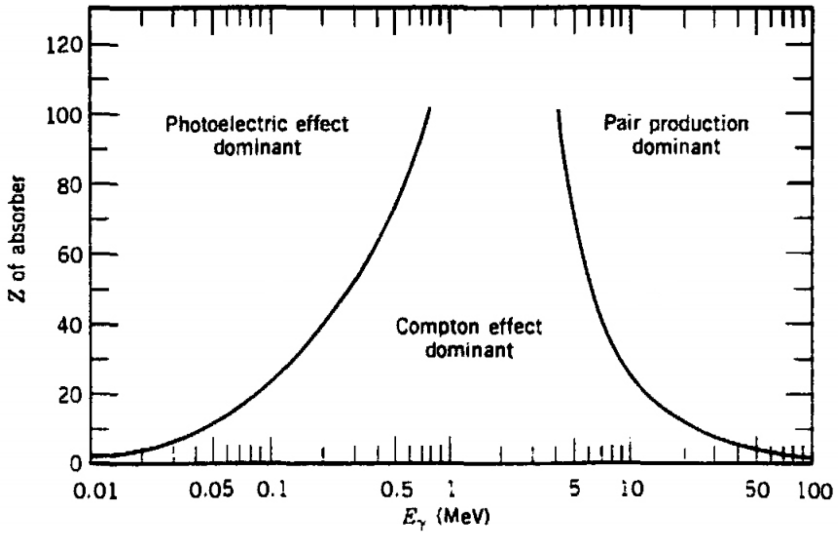

Figure 2.1 Photon interactions and their dominance with respect to atomic number and photon energy as a function of atomic number Z and incoming photon energy E_γ [18].

Photoelectric effect

Interactions via the photoelectric effect involve the absorption of a gamma ray by an electron, transforming the photon energy into kinetic energy of the electron which is ejected from an atom [19]. The probability of this interaction is highest at low energies ($\lesssim$ 100 keV), decreases rapidly with photon energy ($\sim E_\gamma^{-3}$) and increases rapidly with atomic number ($\sim Z^4$) [18].

Compton scattering

Compton scattering involves the interaction of a gamma ray with an electron where the gamma ray is scattered, transferring some (not all) of its energy to the electron which leaves the gamma ray with energy E'_γ [20]. This process is outlined in Fig. 2.2a. The mathematics of this interaction is derived from the conservation of energy and momentum, shown in Eq. 2.2 [18] where m_e is the electron mass, c is the speed of light and θ is the scattering angle as described in Fig. 2.2a. This interaction is most significant in the mid energy range (100 keV - 10 MeV) and therefore is the most important gamma-ray interaction relevant to this thesis. Fig. 2.2b shows the angular distribution of Compton scattered photons over the energy range 1 keV to 10 MeV, it can be seen that photons above 100 keV are forward focussed and therefore retain some of their directionality through Compton scattering.

$$E'_\gamma = \frac{E_\gamma}{1 + (E'_\gamma/m_e c^2)(1 - cos\theta)} \tag{2.2}$$

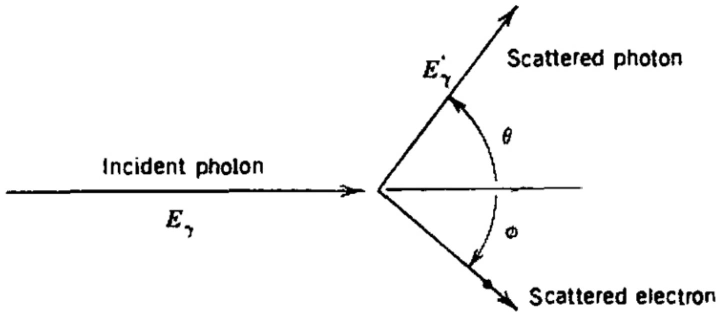

(a) The kinetics of Compton scattering showing photons incident from left-hand side scattering through angle θ and electron scattering through angle ϕ [18]

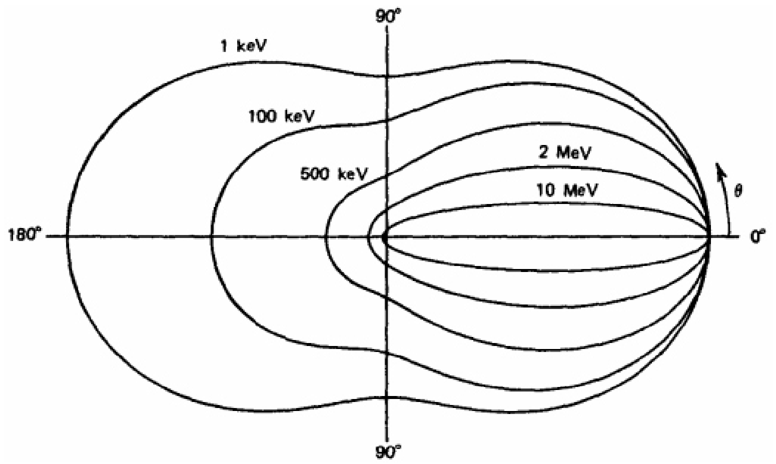

(b) The number of photons of different initial energies (incident from θ = 180 °) Compton scattered into unit solid angles at angle θ [21]

Figure 2.2 The geometry of Compton scattering relating incoming and outgoing photons.

Pair production

Pair production was observed as back-to-back charged particle emission in cloud chambers [22]. The effect is now understood to be the interaction of a gamma ray with $E_\gamma > 2m_ec^2$ = 1022 keV with matter which is converted into an electron-positron pair with total kinetic energy equal to $E_\gamma - 2m_ec^2$. Momentum is conserved by transferring a small amount of energy to a nearby atom. This effect is most significant in the high energy range (>5 MeV).

Gamma-ray shielding

Knowledge of the above effects can be used to design materials which interact with radiation in a desired way, such as to shield radiation in order to reduce its damaging effect on biological tissues. This can be considered in terms of an attenuation model describing the intensity I' of a photon beam of initial intensity I_0 passing through a material of thickness x. At a given depth x the intensity of the beam (in terms of the number of particles which have not undergone an interaction) has been reduced according to Eqs. 2.3 and 2.4 where the attenuation coefficient μ_γ comprises the sum of components μ_{PE}, μ_{CS} and μ_{PP} from photoelectric absorption, Compton scattering and pair production respectively [23].

$$I' = I_0 e^{-\mu_\gamma x} \tag{2.3}$$

$$\mu_\gamma = \mu_{PE} + \mu_{CS} + \mu_{PP} \tag{2.4}$$

Photons interacting through Compton scattering will not have been eliminated and remain with lower energies and different trajectories to the original beam. Absorption can be addressed with the same mathematics by considering interactions which lead to absorption only, i.e. by omitting Compton scattering. This mathematics is useful for first order estimations. Further accuracy involves more rigorous calculation and consideration of secondary and tertiary radiations, and non-trivial geometry which are usually solved by computer software such as Monte Carlo radiation transport codes.

Photon shielding generally increases with electron density. Common shielding materials range from water and concrete to high-Z materials such as lead and tungsten which provide significantly more stopping power.

2.2 Neutron radiation

The neutron was postulated in 1932 by James Chadwick in his paper “Possible existence of a neutron” [24], following observations by Marie and Pierre Curie which showed that light elements bombarded with α particles produced a penetrating form of radiation that interacted with hydrogenous materials to eject protons. Chadwick explained these observations by the existence of a neutral particle with similar mass to the proton (Nobel Prize in Physics 1935). Following this discovery was work by Enrico Fermi, using neutron capture to produce elements otherwise not present on Earth [25] (Nobel Prize in Physics 1938) and unknowingly producing the world’s first artificial nuclear fission reaction. The fission reaction is observed by Hahn and Strassman [26] and interpreted by Meitner and Frisch [27] in 1939 providing the foundations for the nuclear age.

The neutron is a neutral hadron comprising 3 quarks: udd with a mass of 939.57 MeV/c^2. When confined inside an atomic nucleus the neutron is stable, however free neutrons decay through the weak interaction according to Eq. 2.5 [28] with a mean life of 882 seconds (around 15 minutes).

$$n \rightarrow p + e^- + \bar{\nu}_e \tag{2.5}$$

2.2.1 Production

With the exception of cosmogenic neutrons and isolated examples such as the ancient natural nuclear reactors at Oklo in Gabon [29], neutron radiation is not seen naturally on Earth in any significant amount. There are only a few special circumstances where neutron radiation is produced.

Cosmic-ray neutron background

The neutron background on Earth is mainly due to cosmic rays, high-energy radiation originating outside the Solar System which interacts with the atmosphere, ground and any massive objects to produce neutrons. The flux of cosmic rays is found to vary with altitude, the diurnal cycle, latitude, solar activity and weather; the neutron-producing reactions vary with the local composition of massive objects such as the ground or even ships [30]. Fig. 2.3 shows the measured neutron background at five different sites in the USA. The distribution has three peaks: thermal neutrons at around 0.025 eV, a 1-2 MeV peak, and a high energy peak at around 100 MeV. The total flux without altitude normalisation was found to vary by a factor of 15 between the sites [31].

(α, n) reaction

First used by Marie and Pierre Curie, this reaction involves the fusion of an α particle (typically 5-6 MeV) and a light nucleus releasing a neutron from the compound nucleus [18]. A common laboratory source is a composition of an α emitter ^{241}Am and natural beryllium ^{9}Be which produces neutrons up to 11 MeV, according to Eq. 2.6. The neutron flux for emitted neutrons is shown in Fig. 2.4. This reaction is not unique to these nuclides and has been used with light nuclei target sources of ^{10}B, ^{7}Li, ^{19}F, ^{13}C and ^{18}O; and α-emitting sources ^{210}Po, ^{226}Ra, ^{227}Ac, ^{228}Th, ^{238}Pu, ^{239}Pu, ^{242}Cm and ^{244}Cm [32].

$$^{4}\alpha + ^{9}Be \rightarrow ^{12}C^{*} + ^{1}n \tag{2.6}$$

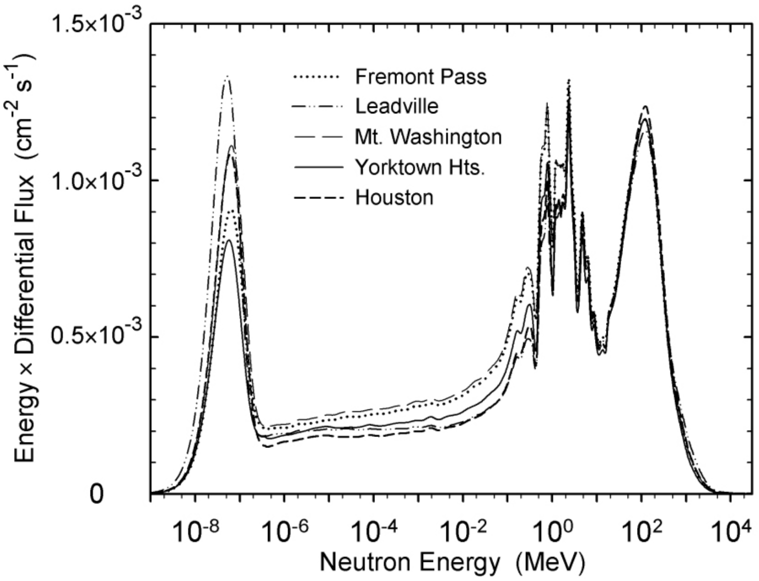

Figure 2.3 The neutron background flux as a function of energy at ground level at five sites in the USA, normalised to sea level [31].

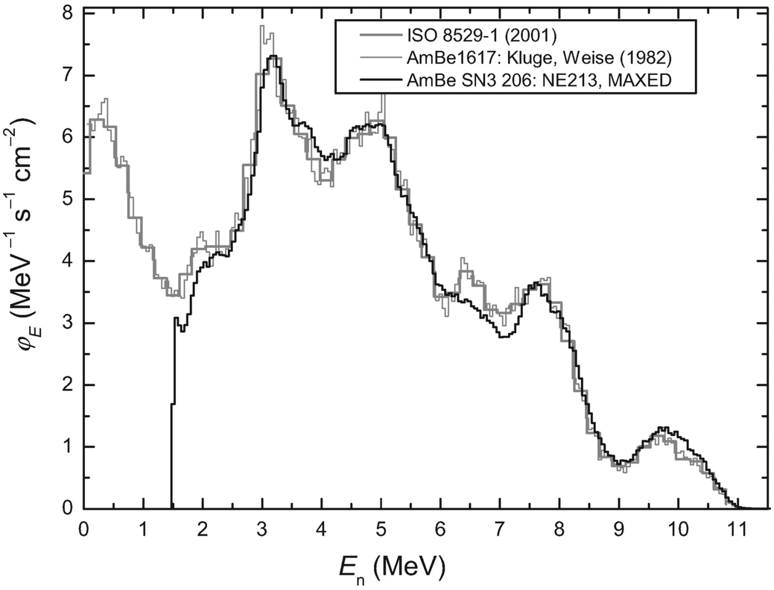

Figure 2.4 Neutron flux from a ^{241}Am/Be neutron source [33].

Photoneutron

Analogous to the (α, n) reaction, neutrons can be produced using the (γ, n) reaction whereby a high-energy gamma ray is absorbed by a nucleus producing a neutron. An advantage of this method is that the neutron energy can be more precisely controlled from the incident photon energy (choice of γ-emitting radionuclide) and the neutron binding energy of the target nucleus [18].

Nuclear fission

Nuclear fission is the process whereby a heavy nucleus divides into two smaller parts, known as fission fragments, releasing energy in the process through emitted radiation and kinetic energy of the fission fragments. It is this energy which provides the heat ultimately used for the end purpose, e.g. industrial processes or electricity generation. Fig. 2.5 shows the binding energy per nucleon as a function of number of nucleons which peaks at ^{56}Fe, the nucleus with the lowest mass per nucleon. Transmuting any nuclide into ^{56}Fe releases energy according to Eq. 2.7 [19] where m is the mass difference between the nuclides, this is equal to the change in binding energy. Transmutation is only possible along certain paths permitted according to the energetically available mechanisms.

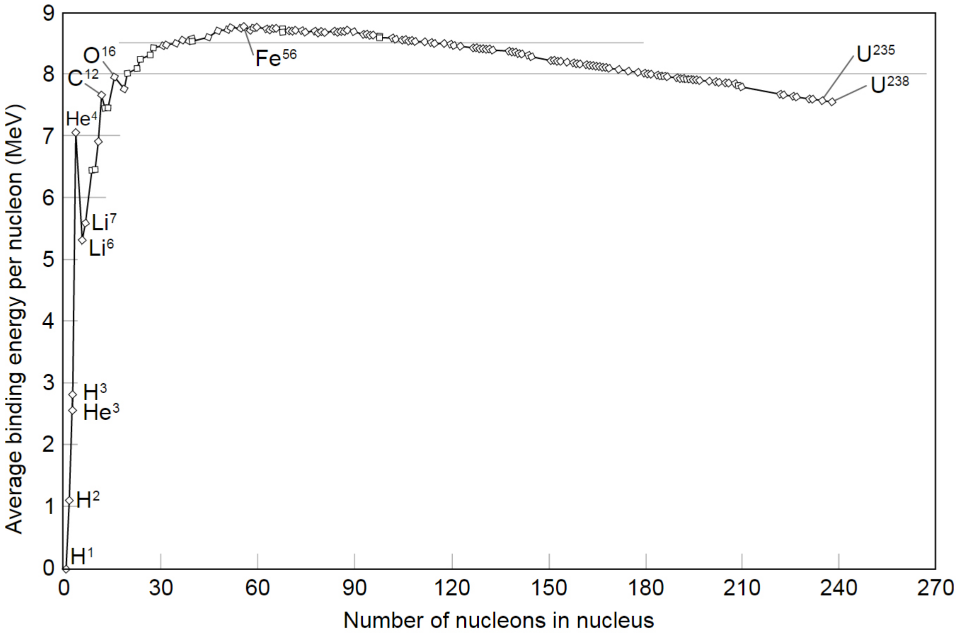

Figure 2.5 Average binding energy per nucleon as a function of number of nucleons for all naturally occurring nuclides.

$$E = mc^2 \tag{2.7}$$

Fission falls under two categories: spontaneous fission and induced fission. Spontaneous fission is where fission occurs through radioactive decay of an unstable heavy nucleus. A common spontaneous fission source is ^{252}Cf in which 3% of decays are fission events, each producing on average around 3.8 neutrons. Fission can be induced by the absorption of a gamma ray known as photofission (γ, f), by the absorption of a neutron (n, f), proton (p, f), or α particle (α, f). A sustainable fission reaction can be created from isotopes which are easily stimulated by neutrons to fission and produce a high number of secondary neutrons which are able to then stimulate further fission reactions. This is the principle upon which nuclear power and nuclear weapons operate. Nuclear reactors can be constructed with variation in the shielding to allow beams of thermal and/or fast neutrons to escape the reactor.

$$^{235}U + n \rightarrow ^{236} U^{*} \rightarrow F_1 + F_2 + \gamma' s + \nu n \tag{2.8}$$

Eq. 2.8 describes the fission of ^{235}U by neutron absorption leading to the production of two fission fragments F_1 and F_2, gamma rays and a number of neutrons ν. The probability of a fission event occurring in a given material is related to the neutron capture cross-section which is dependent on the energy of the incoming neutron. The general trend is for the cross-section to decrease with increasing energy, though neutron absorption resonances between energy level states in the nucleus strongly influence this probability. The (n, f) fission reaction cross-sections for ^{235}U and ^{238}U are shown in Fig. 2.6.

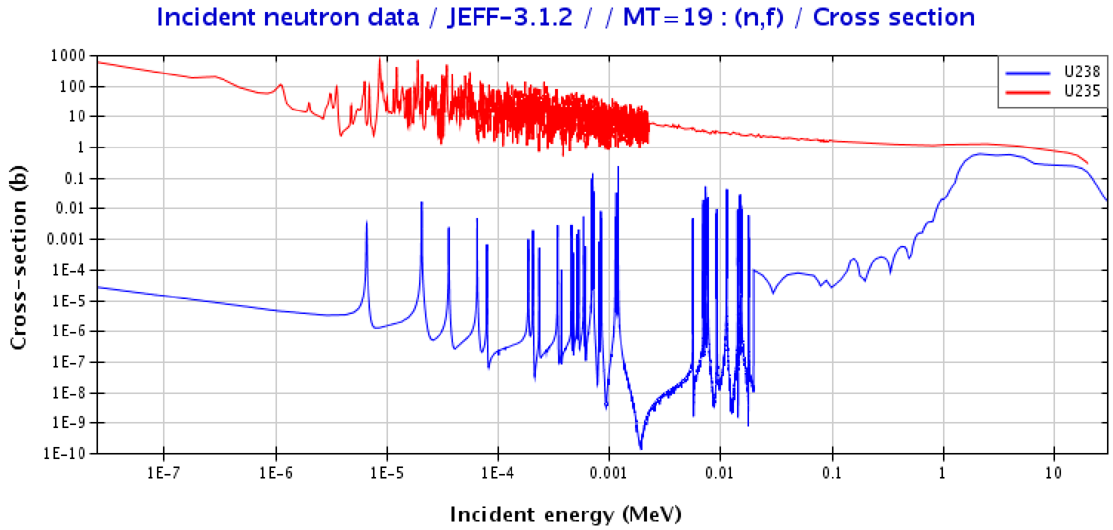

Figure 2.6 Energy-dependent cross-sections for neutron absorption resulting in fission of ^{235}U and ^{238}U [34].

Table 2.1 describes the average number of neutrons produced per fission ($\bar{\nu}$) of various nuclides involved in fission processes in the nuclear industry.

Table 2.1 Average neutron yields per fission from uranium and transuranic nuclides in irradiated nuclear fuel [35].

Nuclide	Reaction	Application	Evaluated $\bar{\nu}$
^{238}U	Spontaneous fission	Uranium fuel constituent	1.97 ± 0.07
^{235}U	Fast fission	Fast fission reactors with uranium fuel	2.42 ± 0.12
^{235}U	Thermal fission	Thermal fission reactors with uranium fuel	2.47 ± 0.12
^{233}U	Thermal fission	Thermal fission reactors with thorium fuel	2.50 ± 0.12
^{239}Pu	Thermal fission	Thermal fission reactors with MOX fuel	2.88 ± 0.14
^{252}Cf	Spontaneous fission	Laboratory/ industrial neutron source	3.82 ± 0.12

The kinetic energy of fission neutrons is a continuum with a typical average energy of 1-2 MeV. The spectra of ^{235}U thermal fission, ^{238}U spontaneous fission and ^{252}Cf spontaneous fission are shown in Fig. 2.7.

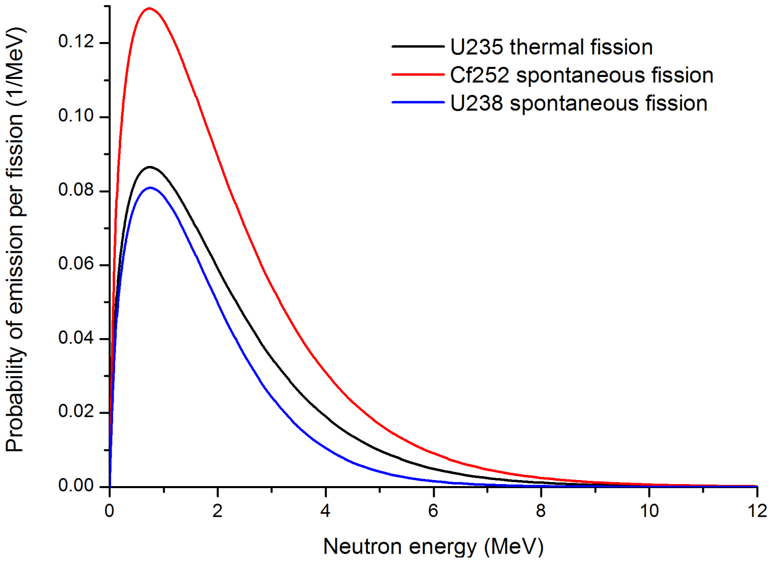

Figure 2.7 Energy dependent neutron emission per fission of ^{235}U thermal fission, ^{238}U spontaneous fission and ^{252}Cf spontaneous fission [36].

Nuclear fusion

Nuclear fusion concerns the fusing of two or more nuclei to produce a compound nucleus. When approaching ^{56}Fe in Fig. 2.5, the point of maximum binding energy, energy is released from the mass deficit according to Eq. 2.7. Nuclear fusion does not always produce neutrons but some of the most favourable reactions, shown in Eqs. 2.9 and 2.10, do. Neutron imaging techniques have been reported on different designs of fusion reactors [37] [38] [39] to image neutrons emitted from the plasma or fuel pellet during fusion events. Many other nuclear reactions also produce neutrons in close analogy with the fusion reaction.

$$d+t=^4He\ (3.5MeV)+n\ (14.1MeV) \tag{2.9}$$

$$t+t=^4He+2n+11.3MeV \tag{2.10}$$

Spallation neutron sources

Neutrons can be created by the neutron spallation reaction which produces many neutrons from a high-Z target. Several facilities around the world have these capabilities. The Spallation Neutron Source at Los Alamos National Laboratory uses a linear accelerator and proton accumulator to produce an intense proton beam. This beam is collided with a neutron rich heavy element (in this case a liquid mercury target) and 20-30 neutrons are ejected from each atom after a successful collision [40].

Neutron yields from nuclear materials

In passive assay the main contributors to neutron fields are spontaneous fission and the (α,n) reaction. Two major neutron production channels are outlined in Eqs. 2.11 and 2.12 [41]. Table 2.2 summarises the neutron yields per gram-second from various materials commonly found in the nuclear industry.

$$\alpha+^{18}O\rightarrow^{21}Ne+n \tag{2.11}$$

$$\alpha+^{19}F\rightarrow^{22}Na+n \tag{2.12}$$

Following the recent reactor damage accident involving Fukushima Daiichi BWR reactors, the Japan Atomic Energy Agency have released a report on the elemental composition of the reactor cores calculated using the burn-up code ORIGEN2 [42]. The data includes estimates of the photon and neutron emission for each reactor core, a useful example of the radiation

Table 2.2 Average neutron yields per gram-second from the main passive contributors to neutron fields in irradiated nuclear fuel [41].

Material	Half-life (yr)	SF (n/g/s)	(α,n) in oxide (n/g/s)	(α,n) in flouride[†] (n/g/s)
^{232}U	71.7	1.3	1.49×10^4	2.6×10^6
^{233}U	1.59×10^5	8.6×10^{-4}	4.8	7.0×10^2
^{234}U	2.45×10^5	5.02×10^{-3}	3.0	5.8×10^2
^{236}U	2.34×10^7	5.49×10^{-3}	2.4×10^{-2}	2.9
^{238}Pu	87.74	2.59×10^3	1.34×10^4	2.2×10^6
^{239}Pu	2.41×10^4	2.18×10^{-2}	3.81×10^1	5.6×10^3
^{240}Pu	6.56×10^3	1.02×10^3	1.41×10^2	2.1×10^4
^{241}Pu	14.35	5×10^{-2}	1.3	1.7×10^2
^{242}Pu	3.76×10^5	1.72×10^3	2.0	2.7×10^2
^{241}Am	433.6	1.18	2.69×10^3	
^{242}Cm	0.447	2.10×10^7	3.76×10^6	
^{244}Cm	18.1	1.08×10^7	7.73×10^4	
^{249}Bk	0.877	1.0×10^5	1.8×10^1	
^{252}Cf	2.646	2.34×10^{12}	6.0×10^5	

† UF_6 or PuF_4 as appropriate

emitted by a commercial power reactor at time of shut down and over the following years. Table 2.3 summarises the major contributors to the neutron emission one year from shut down in reactor Unit 1, it is expected that a minimum of 1 year would be needed to plan the introduction of a probe into the reactor environment. The total neutron emission rate from all materials was 1.42×10^{10} neutrons per second. At the time of shut down this value was 2.94 $\times 10^{10}$ neutrons per second.

Table 2.3 Calculated emission from major contributors to the fast-neutron field in Fukushima Daiichi unit 1 one year after shut down [42].

Material	Half-life (yr)	(α,n) neutrons (n/s)	SF neutrons (n/s)
^{238}Pu	87.74	1.28×10^8	2.08×10^7
^{239}Pu	2.41×10^4	1.39×10^7	
^{240}Pu	6.56×10^3	1.82×10^7	9.58×10^7
^{242}Pu	3.76×10^5		3.40×10^7
^{241}Am	433.6	2.36×10^7	
^{242}Cm	0.447	6.90×10^8	3.35×10^9
^{244}Cm	18.1	8.04×10^7	9.68×10^9

2.2.2 Interactions

In general the probability for neutron interactions (the reaction cross-section) increases with decreasing neutron energy and is usually dominated initially by elastic scattering reactions following absorption after many scattering interactions. At certain energies interaction cross-sections can be huge due to resonances which are important to account for in neutron transport.

Scattering

Neutrons most commonly interact via the short-range strong nuclear force and therefore mainly with the nucleus, all other interactions can be considered negligible in this thesis. Scattering as described in Eq. 2.13 can occur through elastic or inelastic scattering reactions [43]. The elastic scattering reaction is largely responsible for neutron moderation as it is the dominant energy loss process at medium to high energies. After elastic scattering, the nucleus remains in the same state X after the collision, though the energy and directionality of the incoming neutron has been altered. At high neutron energies above several MeV, inelastic scattering events are more likely to occur where the nucleus is left in an excited state X^*.

$$n + X \rightarrow \begin{cases} \mathrm{X + n} & \text{elastic scattering} \\ X^* + \mathrm{n}' & \text{inelastic scattering} \end{cases} \tag{2.13}$$

Moderation

Moderation is the process whereby a population of neutrons lose their average energy through scattering interactions with matter. For an initial population of monoenergetic neutrons of energy E_n the average energy $\bar{E}_n'$ after η collisions in a target of atomic number A is given by Eqs. 2.14 and 2.15 [18]. The best neutron moderators are therefore those with low A such as hydrogenous materials like water and polyethylene.

$$log\bar{E}_n' = logE_n - \eta\xi \tag{2.14}$$

$$\xi = 1 + \frac{(A-1)^2}{2A} log\frac{A-1}{A+1} \tag{2.15}$$

After moderation neutrons eventually reach thermal equilibrium with the surroundings at around 0.025 eV, neutrons in this region are referred to as thermal neutrons. The thermalisation process for hydrogen, carbon and uranium are outlined in Table 2.4. Cold neutrons can be produced by guiding thermal neutrons into a few litres of liquid deuterium or hydrogen (a smaller amount of hydrogen due to increased cold neutron capture) at around 20-30° K. In this thesis fast neutrons are defined as having kinetic energy greater than 100 keV.

Table 2.4 Thermalisation dynamics of neutrons from scattering with different nuclei [18].

Nuclide	ξ	Average η for thermalisation
^{1}H	1.00	18
^{12}C	0.158	110
^{238}U	0.0084	2200

Absorption

Low energy neutrons at near thermal energies are absorbed mainly by radiative capture in (n,γ) reactions, however at higher energies many more reactions are possible such as (n,p), (n,α) and $(n,2n)$ [18]. Neutron capture can increase the atomic mass number of a nuclide according to Eq. 2.16 if the product is stable. Some thermal neutron detectors rely on neutron capture mechanisms such as the reaction outlined in Eq. 2.17.

$$n + {}^{A}X \rightarrow {}^{A+1}X^{*} \rightarrow {}^{A+1}X + \gamma \tag{2.16}$$

$$n + {}^{10}B \rightarrow {}^{11}B^{*} \rightarrow {}^{7}Li + \alpha + \gamma \tag{2.17}$$

Kinetics

The velocity of a neutron v can be calculated at relativistic and non-relativistic energies ($\frac{v}{c} << 1$) respectively from Eqs. 2.19 and 2.18 using the neutron kinetic energy E_n.

$$\frac{v}{c} = \sqrt{\frac{2E_n(MeV)}{939.57\,MeV}} \tag{2.18}$$

$$\frac{v}{c} = \sqrt{1 - \left(\frac{939.57\,MeV}{E_n(MeV) + 939.57\,MeV}\right)^2} \tag{2.19}$$

The mean free path λ of a neutron energy E in a target medium composed of m nuclides can be calculated from the microscopic cross section of the nuclide σ_i and its atomic density N_i as shown in Eq. 2.20.

$$\lambda(E) = \frac{1}{\sum\limits_{i=1}^{m} N_i \sigma(E)_i} \tag{2.20}$$

Neutron shielding

The same mathematics used to describe gamma-ray scattering as described in section 2.1.2 can also be used with neutrons using the attenuation parameter μ_n. The attenuation of a monoenergetic beam is outlined in Eqs. 2.21 and 2.22 and has many components due to all possible reactions channels which can occur to a given beam. Elastic scattering, inelastic scattering and neutron absorption with associated gamma-ray emission (denoted μ_{El}, μ_{InEl}

and $\mu_{n,\gamma}$ respectively) are some of the most common. For non-trivial geometries hand calculations are not recommended and use of a radiation transport code is advised.

$$I' = I_0 e^{-\mu_n x} \tag{2.21}$$

$$\mu_n = \mu_{El} + \mu_{InEl} + \mu_{n,\gamma} + ... \tag{2.22}$$

Neutron shields are commonly made of hydrogenous or other low-A materials which are effective neutron moderators to lower energy and facilitate capture. Commonly cadmium or boron are used to capture thermal neutrons, due to high cross-sections around the thermal region. Borated polyethylene combines these two approaches to form a material with very high moderation and capture properties, making a successful neutron shield.

2.3 Radiation detection

Radiation detectors for photons and neutrons are materials which interact via one or more of the methods outlined in section 2.1.2 and 2.2.2, converting the transmitted energy into a measurable form (usually electric current or voltage). Detectors are manufactured to address various needs such as high energy resolution necessary for spectroscopy; fast signal rise-time required for precision timing measurements; or high efficiency necessary to detect weak radiation fields. Each detector type presents a trade-off between these characteristics and therefore must be chosen carefully for a given application. The major detection methods able to count individual radiation events in pulse mode will be outlined here.

2.3.1 General detector types

Gas-filled detectors

Gas-filled detectors are made up of chambers filled with gas which is ionized by charged particles in the fill volume, producing an output signal. Photons and neutrons are uncharged, therefore the detector requires an initial reaction producing charged particles, e.g. Compton scattering producing electrons. Electron-ion pairs created in the gas volume are accelerated towards electrodes by an applied electric field, generally creating an avalanche effect of further ionization, the resulting charge is collected. This electric signal is monitored and used to determine the presence, and flux, of radiation. Commonly neutron detectors of these types use neutron capture reactions, such as discussed in Eq. 2.17, to produce high energy ions which give large signals due to the high level of energy released (several MeV) and short penetrating distance of these products. The resulting large amplitude signal is therefore easy to discriminate with an energy threshold against smaller gamma-ray interactions, yielding to very high gamma-ray rejection.

Solid state semiconductor detectors

Solid state detectors have much higher densities than gas detectors due to the nature of the material phase and therefore can give much higher intrinsic detection efficiencies. These detectors have an applied electric field across a depletion region which collects charge from electron-hole pairs in the semiconductor structure produced by collision of ionizing radiation. These detectors often have very high energy resolution as an incident radiation produces a much higher number of charge carriers per quanta of energy, thereby reducing the statistical fluctuations associated with the detection of these carriers [44].

Scintillators

Scintillation detectors produce light following excitation by charged particles. This light is then collected by some mechanism such as photomultiplier tubes (PMTs) or photodiodes. Scintillation light comprises fluorescence: prompt emission of visible light from electron transitions in a single molecule; delayed florescence: identical to fluorescence but after some delay time; and phosphorescence: excitations which have converted into lower energy states producing light of lower energy with a longer decay constant when compared with fluorescence [21].

Ideal scintillators should have the following properties [21]:

- Kinetic energy of charged particles is converted into detectable light with high efficiency and linearity of light intensity with deposited energy (for electrons)
- The produced scintillation light comprises a majority of prompt fluorescence and a minimum amount of delayed fluorescence and phosphorescence (when pulse-shape discrimination (PSD) is not required)
- The scintillation material is transparent to its own scintillation light, has good optical qualities and has a refractive index close to that of the coupling material to its detection mechanism
- The scintillation material can be produced in quantities large enough for high intrinsic detector efficiency

Organic scintillators contain carbon molecules and come in the forms of crystals, liquids and plastics. Crystals, such as anthracene and stilbene, have high scintillation efficiency but are expensive to produce in large sizes and have a dependence of efficiency on the relative alignment of the crystal structure and incident radiation trajectory. Crystals are also susceptible to radiation damage, as the arrangement of molecules is altered by the interactions of ionizing radiation. Liquids, such as EJ-301 and EJ-309, contain a solution of scintillator in a solvent and have no crystal structure. These scintillators therefore have high resistance to radiation damage and can be produced in large quantities with no restriction on geometry. There is also the possibility to achieve extremely high efficiencies by dissolving radioactive samples within the solvent itself. Liquid scintillators must be sealed to avoid the dissolving of oxygen into the solvent which strongly quenches the scintillator, this reduces light output and additionally prevents leakage of the potentially corrosive or flammable substance. Plastic scintillators contain a scintillator in a plastic matrix, allowing the scintillator to be easily crafted to the desired shape and size, allowing the availability of many off-the shelf geometries such as thin films, rods and sheets. The downsides of plastic scintillators are that the scintillation light attenuation must be considered for these materials with any significant length and the degradation of the material can also be problematic [21].

Inorganic scintillators such as CsI(Tl), NaI(Na) and BGO consist of crystal lattices comprising valence electrons, those bound to atoms and mobile conduction electrons which are responsible for the conductive properties of the material. Radiation transfers energy to electrons in the valence band, promoting them to the conduction band where they de-excite, emitting optical photons. Often these materials are doped with activators such as thallium or sodium as in CsI(Tl) and NaI(Na) to provide additional energy states where electron transitions result in optical photons; these can be more easily converted into useful output signals. When compared with organic scintillators, inorganic scintillators tend to have a higher yield of scintillation light with better proportionality to deposited energy, although they tend to have slower time constants [21].

2.3.2 Fast neutron detection

Moderated thermal detectors

Thermal neutron detectors commonly rely on materials with high cross-sections for nuclear reactions which promptly emit highly charged particles such as protons, α or fission fragments. The energy released is converted into the kinetic energy of these charged particles which is usually much higher than the incoming neutron energy. Therefore these detectors are usually difficult to use for spectrometry through charge measurement alone. Thermal detectors commonly involve ^{3}He, ^{10}B, ^{6}Li and Gd. ^{3}He has a very large thermal neutron cross-section and can safely be used at high pressure in highly stable gas-filled detectors, giving very high intrinsic detector efficiencies with very good gamma-ray rejection; it has consequently been widely used in research, nuclear security and safeguards applications. ^{3}He has however become scarce and costly since the reduction in global nuclear weapons production: finding an adequate replacement has become a significant driver in scientific research.

Thermal neutron detectors will usually have a low response to a fast neutron field, as the trend of cross-section σ is $\propto \frac{1}{v}$ with neutron velocity. This can be addressed by coupling detectors with a layer of moderating material, reducing a component of the fast neutron flux into epithermal or thermal neutrons which can then be detected with much higher efficiency. Instrumentation of this type for research include the long counter [45] which by geometric design gives a similar efficiency over a wide range of neutron energies, useful for giving absolute neutron flux values as well as an indication of directionality. Another frequently used tool is the Bonner sphere spectrometer [46] and variations thereof which can determine the energy-flux distribution of thermal to fast neutron fields by using many measurements with varying thickness of moderator by adding or subtracting shells around the detector.

Fast-neutron capture

The cross-section of the (n,α) reaction in ^{6}Li, shown in Fig. 2.8, has a large resonance peak at around 0.24 MeV, peaking at around 4 barns and up to around 1 barn between 3.5 - 10 MeV. This gives significant scope for fast neutrons detectors to utilise this reaction and detection of the resulting charged particles. Variations include LiI(Eu) [47] and other Li loaded scintillators [48], Li-glass [49], Li glass fibres [50] and Li-glass polymer composites [51]. These detector types are used with pulse-shape discrimination to isolate neutron detections, although it can be challenging to get suitably high rejection for some scenarios. Lithium is also used within solid state semiconductor detectors [52]. Of course the ^{6}Li (n,α) is not the only reaction channel used by neutron capture detectors; similar approaches can be taken with ^{3}He and Gd.

Neutron scattering

This method of detection utilises the transfer of kinetic energy between an incident neutron and (usually) a light recoil nucleus, such as hydrogen, in an elastic scatter. The energy transfer occurs by kinetic energy to a charged particle producing a large prompt signal, which can be easily discriminated from gamma rays at high incident neutron energy (above 1 MeV).

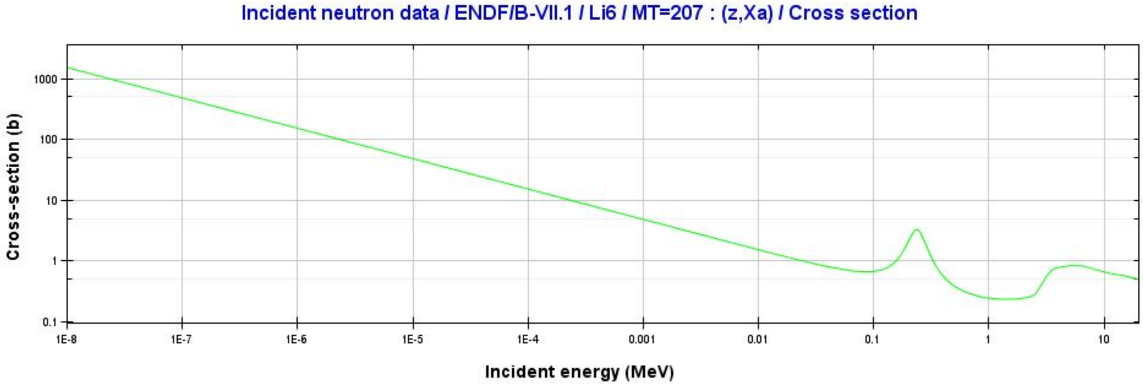

Figure 2.8 The (n,α) cross section of ^{6}Li [34].

The elastic scattering cross-section is generally much higher than other reaction channels at fast-neutron energies and is therefore the preferred choice for high efficiency fast-neutron detectors.

The energy transferred from the incident neutron of energy E_n to the recoil nucleus E_R depends on its atomic mass and outgoing angle of the scattered neutron in the laboratory system θ_n according to Eq. 2.23 and the maximum energy transfer $E_{R_{MAX}}$, given by Eq. 2.24 [21].

$$E_R = \frac{2A}{(1+A)^2}(1 - cos\theta_n)E_n \tag{2.23}$$

$$E_{R_{MAX}} = \frac{4A}{(1+A)^2}E_n \tag{2.24}$$

Hydrogen is most commonly used and gives a maximum energy transfer of 100%. The probability of energy transfer is uniform between 0 and $E_{R_{MAX}}$, such that the pulse-height spectrum cannot be directly related to the incident neutron energy-flux distribution and will contain contributions from all possible recoil nuclei, e.g. from hydrogen and carbon in organic liquid scintillators. This means that spectroscopy is achievable when these responses are known, but not straightforward.

Neutron scattering detectors can be produced as gas-filled [53], solid state semiconductor [54] or scintillation detectors [55], with the positives and negatives as described in section 2.3.1; the choice depends on the application. The intrinsic efficiency ε of a recoil detector is described in Eq. 2.25 [21] which depends on the elastic scattering cross-section σ_{EL} and number density N of the chosen recoil nucleus and the neutron path length in the detector Λ.

$$\varepsilon = 1 - e^{-N\sigma_{EL}\Lambda} \tag{2.25}$$

Liquid scintillation detectors have high intrinsic efficiencies, can be used to discriminate radiation types and few restrictions on geometry beyond the efficacy of light collection. The intrinsic efficiency of these detectors is normally higher than alternatives. In gas-filled detectors because N is much higher, and in solid state semiconductor detectors because Λ is limited (crystal and wafer sizes are always increasing but become very expensive).

For liquid scintillators, a smaller detector has better light collection and therefore better resolution and lower efficiency but less chance of pile-up. A larger detector increases efficiency to both neutrons and gamma rays, which can be problematic in cases of high gamma-gamma pile-up. The scintillator will also be chosen for its light-production qualities and subsequent PSD capabilities.

2.3.3 Digitising electronics

Light pulses produced by scintillators are converted into electrical signals through PMTs or other devices. These pulses can be recorded by fast digitising electronics to sample the pulse at small time intervals, measuring the current or voltage with high frequency. 2-nanosecond sampling is sufficient for the requirements of this thesis as the pulse length produced by the detector is 100-200 nano seconds and differences in pulse shapes between incident gamma rays and fast neutrons can be resolved. Additional resolution does not benefit pulse-shape discrimination due to limited statistics of light collection. These devices contain an analogue-to-digital converter which converts the electrical signals into binary data by continuously sampling the input signal and producing discrete amplitude values at a given sampling rate. These data are then handled and recorded by other electronics. This process is commonly addressed using a field-programmable gate array (FPGA), a relatively cheap, off-the-shelf computer comprising arrays of programmable logic blocks which can be customised by the user using electrically programmable switches. This allows the creation of integrated logic functions up to the complexity of microprocessors [56]. These devices then provide a communication or processing bridge between the ADC and a PC, allowing information on the pulses or analysis to be transferred and stored at sufficiently high rates.

2.3.4 Pulse-shape discrimination in liquid scintillators

As discussed, scintillators are usually preferred to give a majority of scintillation light in the fast component of the decay through prompt fluorescence to allow minimum dead-times in radiation measurement. The delayed fluorescence component can be dependent on the incident particle type such that the falling edge of the pulse is characteristic of the radiation type [21].

This thesis concerns the detection of neutrons and gamma rays, two uncharged particles which are not detected directly. The mechanism for detection is as follows:

1. In each event the uncharged particle transfers energy to a charged particle within the detector volume.
2. The charged particle collides with molecules of the scintillation fluid causing electrons to be promoted to excited states.
3. Electrons in the scintillation fluid de-excite producing scintillation photons of lower energy (between 400 nm and 520 nm wavelength in EJ-301).
4. These scintillation photons are reflected by the walls of the scintillation volume and are collected at an optical window where they interact with a photo cathode, the first component of the photomultiplier tube.
5. Scintillation photons at the photo cathode are converted into electrons via the photoelectric effect.
6. An electric field accelerates photo cathode electrons through a series of dynodes where further electrons are created creating an electron cascade.
7. The charge due to the electron cascade is collected at the anode of the detector. This is sampled as a function of time and can be used to deduce the particle type and energy for each detection event.

The charged particle produced by gamma-ray interaction is the electron, mainly by Compton scattering. In this case scintillation light output is linear with the energy of the electron. The charged particle associated with neutron detection is generally the proton (though other charged ions will be produced). In the case of a proton, light output is generally non-linear due to quenching effects occurring within the scintillator. A comparison of light-output as a function of charged particle energy is given in Fig. 2.9, and in numerical form in Eq. 2.26 [57] which increases with increasing amplitude of pulses produced by the detector. The detection energy of neutrons and gamma rays must therefore be determined by these data, or are commonly quoted in terms of electron equivalent energy by normalising to electron detection.

$$Light\ output\ (MeVee) = 0.0350\ E_n^2 + 0.1410\ E_n \tag{2.26}$$

Pulse-shape discrimination can be performed with analogue electronics and has been used for many decades to differentiate neutron and gamma-ray radiation [58], although it is

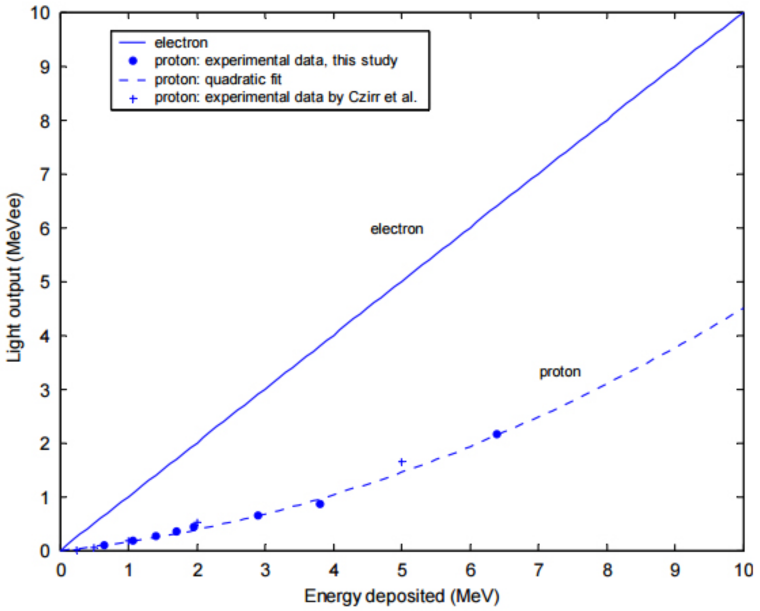

Figure 2.9 A plot of light-output as a function of deposited energy for neutrons (via protons) and gamma rays (via electrons) in EJ-301 scintillator [57].

more commonly performed with digitising electronics in contemporary science. After pulses have been digitised, an algorithm acts on each pulse to determine whether the pulse is likely to be due to neutron or gamma-ray detection. The typical shape of a neutron and gamma-ray pulse is shown in Fig. 2.10 including key time samples. Algorithms determine the incident particle type by analysis of this pulse shape. Many algorithms have been tested with varying levels of success at this discrimination, some of the methods are discussed here.

$$\begin{gathered} GARR = \frac{measured\ neutron\ events}{all\ detected\ events} \\ (Performed\ with\ pure\ \gamma - ray\ source) \end{gathered} \tag{2.27}$$

It is worth noting that none of these methods are foolproof for discriminating neutrons from gamma rays and it can only be hoped to achieve the correct classification most of the time. The merit of each technique is usually quantified by the number of gamma rays misclassified as neutrons from a sample of events recorded from a pure gamma-ray source called gamma-ray rejection, otherwise known as GARR, which is described in Eq. 2.27 [59]. GARR values of below 0.1% are easily achievable and can be much lower if required by the application, e.g. in an intense gamma-ray field. High frequency gamma-ray detection has an additional complication due to pulse pile-up, where multiple gamma-ray detections in the same detector at the same time can be misclassified as neutron events by discrimination algorithms. The solution to this problem is to use pile-up rejection filters which search the digitised pulses for those which contain two peaks; these events are then rejected.

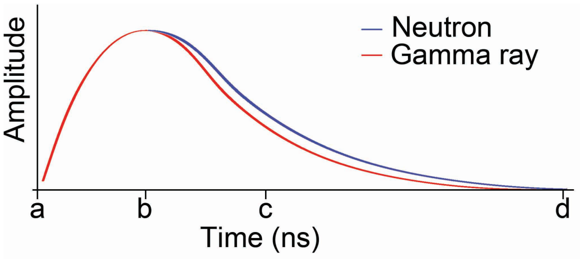

Figure 2.10 Sketch of peak normalised pulses produced from the detection of neutrons and gamma rays in a liquid scintillation detector, illustrating the different pulse shapes. The labels on the time axis correspond to the start of the pulse (a), the pulse peak (b), some time after the pulse peak where the amplitude difference is at a maximum (c) and the point at which the pulse amplitude is below noise level (d).

Charge comparison method (CCM)

The charge comparison method [60] is performed by taking integrals under each recorded pulse ψ in two different time gates usually referred to as the "fast" and "slow" gates or "short" and "long" gates. These respectively refer to the fast rise region of the pulse ($\lesssim 40$ ns) and slow decay ($\gtrsim 100$ ns). The fast gate acts as a normalisation constant for the pulse amplitude and the slow gate contains the usual decay of prompt fluorescence and the delayed fluorescence component, if present. By taking the ratio of these components as shown in Eq. 2.28, it is possible to determine if the PSD value is above a threshold and contains delayed fluorescence, indicating the particle type as a neutron.

$$PSD_{CCD} = \frac{\int_b^d \psi \, dt}{\int_a^b \psi \, dt} \tag{2.28}$$

Pulse gradient analysis (PGA)

Pulse gradient analysis discrimination is analogous to CCM, however instead of comparing two integrals, two samples are compared: the first at the peak of the pulse and the second after some time typically between 15 and 25 ns after the peak [61]. This method can be used in conjunction with a moving-average filter on the pulse to reduce the effect of ADC noise.

The pulse can be determined to be from a neutron detection if the PSD value shown in Eq. 2.29 is above a threshold.

$$PSD_{PGA} = \frac{\psi(c)}{\psi(b)} \tag{2.29}$$

Neutron-gamma model analysis (NGMA)

Discrimination is achieved in this method by comparing the digitised waveform ψ with modelled pulses m_n and m_γ, for neutrons and gamma rays respectively, and determining a χ^2 value for each pulse. The PSD value is then calculated by subtraction of the chi squared values, a positive value indicating a neutron. The algorithm is summarised with Eqs. 2.30, 2.31 and 2.32 [62].

$$\chi_\gamma^2 = \sum_{i=a}^{d} \frac{\psi(i) - m_\gamma(i)}{m_\gamma(i)} \tag{2.30}$$

$$\chi_n^2 = \sum_{i=a}^{d} \frac{\psi(i) - m_n(i)}{m_n(i)} \tag{2.31}$$

$$PSD_{NGMA} = \chi_\gamma^2 - \chi_n^2 \tag{2.32}$$

2.4 Imaging with ionizing radiation

2.4.1 General imaging approaches

In a general sense, all images have: a **subject**, the object being interrogated; information about the subject is ultimately transferred through the imaging process; a **capture device**, the device which is responsible for interacting with the observable information (this device converts the observable information into another format which can be recorded); a **processor**, the device which converts the stored output from the capture device into a human readable format via an optical **display**. The image then undergoes further processing by the **interpreter**, the human who ultimately views the image and is thus the recipient of the image information. This information is then applied to the given task and usually brings about preferred results of the subsequent actions.

Active imaging

Wilhelm Roentgen first used X-rays to image a human hand in 1895 which sparked the birth of radiation imaging, a field which has only continued to grow into many different applications from medical examinations to cosmology. The medical X-ray is an example of radiography or active imaging and is outlined in Fig. 2.11. Here a radiation source is used to interrogate the subject and an image is formed from the spatial response in a detection medium, such as a photographic plate, which is related to the intensity of incident radiation. The presence of material is indicated by the drop in intensity, a result of attenuation, e.g. X-rays attenuated by bone. The response of the detector is continuous and depends on the density and thickness of the subject along each radiation path. The detector response must undergo a transformation and other processing to image the subject at each point.

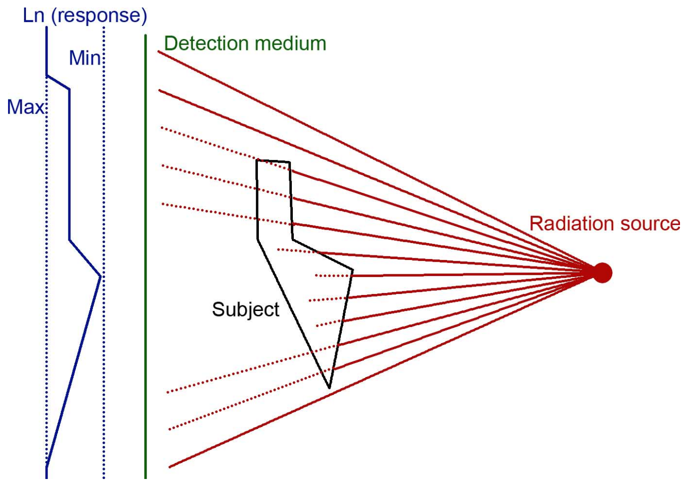

Figure 2.11 Schematic of radiography, a form of active imaging, in two dimensions where the subject is interrogated with radiation.

X-ray computed tomography (CT) uses many X-ray images from different angles coupled with computer processing to build a three-dimensional model of a patient, allowing physicians to view the internal structures of the body. CT relies on the varying attenuation lengths of X-rays in different tissues in the body, allowing the tissues of one organ and another to be distinguished. Other forms of imaging can be targeted to specific areas such as positron emission tomography (PET), which locates positron emission within a body. The body does not naturally provide much β^+ decay and a radioisotope source must be introduced to facilitate this imaging method. Radioisotope tracers such as ^{18}F, chosen for their short half-lives which limit an unnecessary radiation dose, are introduced into the area of interest, e.g. by injecting into the bloodstream. The tissues of interest can be targeted through chemical and biological processes. The tissues up-taking the tracers become a source of back-to-back photon emission produced by the annihilation of the positrons emitted from the tracer. These events can then be isolated using detectors with geometry and timing constraints to hugely reduce noise in the capture process. The position of each originating photon pair is calculated during the processing and the sum of this dataset forms the human interpretable images. Single-photon emission computed tomography (SPECT) also uses radioactive tracers within the body; the information carriers in this case are single uncorrelated photons which are usually captured using a collimated detection system. When compared with SPECT, PET scanning gives better resolution and is less prone to image artefacts, a result of the coincidence constraint of correlated photon emission. However, due to the higher price of the equipment and tracers in PET, SPECT is more widely used, illustrating the importance of imaging technology to be fit-for-pupose and economically viable.

Passive imaging

In passive radiation imaging, no interrogation radiation is produced and the information carrier is radiation produced by the subject itself, as outlined in Fig. 2.12. The radiation must also interact with a response modulator, commonly a radiation shield, to increase the spatial dependence of the detector to surrounding space. Without this the detector response would be virtually identical at each point, usually making imaging impossible (unless the distance between the subject and detection medium was very small). The most simplistic type of imager is a pin-hole camera where the response modulator is a planar radiation shield with a single hole, allowing radiation to pass through unattenuated. An inverse projection of the subject's radiation emission is then detected by the detection medium (Fig. 2.12 assumes homogeneous emission from the sample and negligible self-shielding). An image of the radiation field can then be produced by transformation and processing of the detector response.

A passive stand-off imager is analogous to a photographic camera which detects ionizing radiation in place of visible light photons. The benefits of this type of imager is that distance between radiation emitters and the imager can remain large ($\gg$1m), allowing lower radiation exposure to the user and large fields of view, and therefore regions of physical space, to be investigated simultaneously. This is particularly useful when the radiation distribution is not known and could be spread over a large area such as within a room or building. Imagers used without stand-off distances have more in common with scanners where the radiation distribution is known to be contained within a small sample. This involves significant prior knowledge of the subject and close handling.

2.5 Fast neutron imaging techniques

The goal of this research was to develop a device capable of passive, stand-off imaging of fast-neutron fields. Other systems have been reported to have this capability and are discussed here to set the context of this work against other research.

2.5.1 Pin-hole cameras

Fig. 2.12 shows a schematic of a pin-hole camera where rays of incident radiation are focussed through a small hole in a shield, resulting in a transformed image projection of their origin onto the detection medium. The distribution of detections is then related back to the original angles of incidence of the emitted radiation.

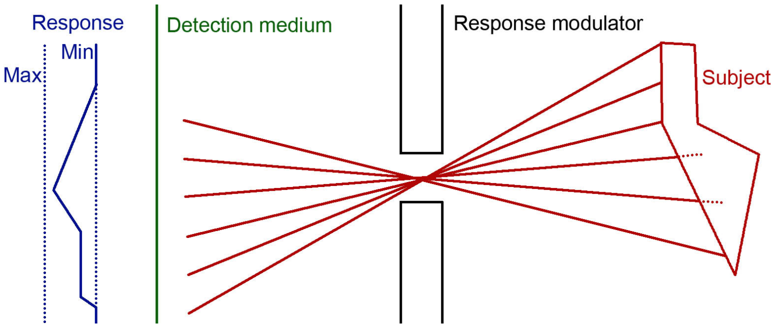

Figure 2.12 Schematic of passive radiation imaging in two dimensions using a pin-hole camera where the subject is a radiation emitter.

These imagers are used in cases of extremely high neutron fields, thereby allowing a narrow pin-hole to block the passage of the majority of radiation; the efficiency is resultantly very low. A large area detection medium is used, coupled with bulky shielding and other apparatus such as intensified cameras as part of the system's front-end. These systems are designed for specific tasks, such as investigating laser fusion, with much prior knowledge about the environment. Imaging can be achieved in very short timescales with extremely high resolution. They do not lend themselves well to stand-off detection due to the lack of portability.

Pin-hole neutron camera experiment (PINEX)

The pin-hole neutron camera experiment or PINEX is a pin-hole camera which has been used in underground nuclear tests to measure 14 MeV neutron radiation produced from nuclear fusion reactions [63]. Neutrons from the plasma are focussed by a pin-hole in a thick shield, those passing through hit a detection medium. This can be a neutron activation target, which is subsequently cut up into small chunks, i.e. pixels, and analysed to find the amount of neutron capture (hence neutron flux per pixel). The detector can also be a fluorescent screen which is filmed using optical cameras to relate the fluorescence back to neutron flux, known as PINEX-2. Fig. 2.13 shows the set-up and image produced from a 5 mm diameter, prototype liquid metal fast breeder reactor fuel pin undergoing fission at the Transient Reactor Test Facility. 10^{17} neutrons per $\mathrm{cm}^2\mathrm{s}$ were emitted from the pin when irradiated at a pulsed reactor power of 100 MW [64]. This configuration has a spatial resolution of the orders of mm.

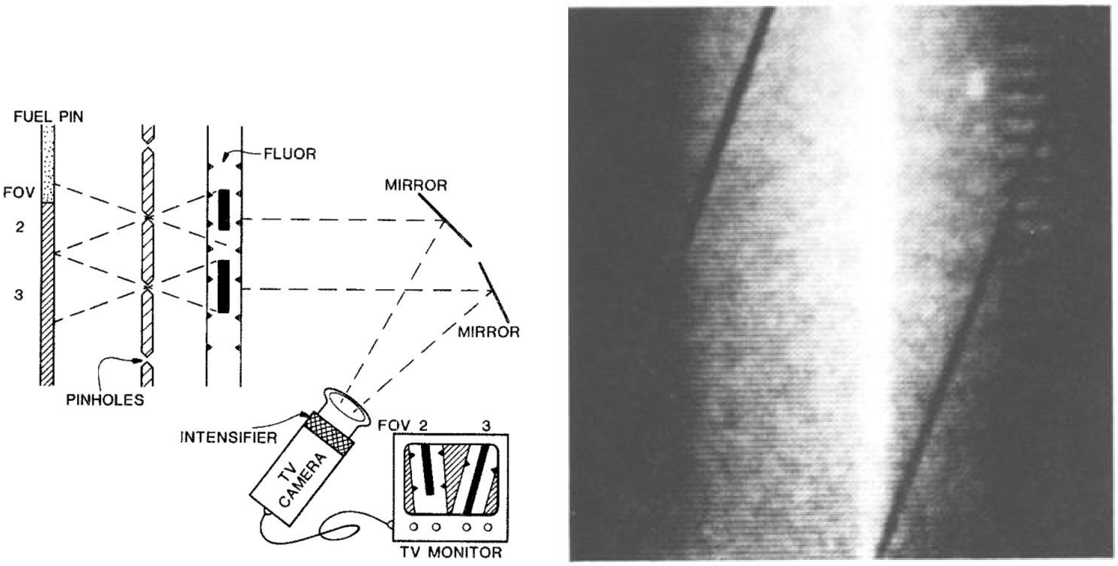

(a) Schematic of imaging set-up

(b) Output image of the fissioning fuel pin

Figure 2.13 The PINEX-2 imaging system imaging a 5 mm diameter, prototype liquid metal fast breeder reactor fuel pin undergoing fission at the Transient Reactor Test Facility [64]. In (b) the pin is the central narrow white band; other artefacts are due to background.

This method has also been applied to fusion research by Los Alamos National Laboratory [64] using the PINEX-2 approach for real-time imaging with highly intensified television cameras. High-intensity neutron fields were required from fusion within a Tokamak. It was estimated that 3-6 cm spatial resolution and 10-100 ms time resolution would be achievable for 5×10^{15} neutrons s^{-1} emission rates. The PINEX cameras can produce rapid images of extremely high-intensity neutron fields with very high resolution as low as in the mm range. These large systems are not portable or compact and have a limited field of view, requiring very high neutron fields to operate.

Lawrence Livermore National Laboratory penumbral imaging technique

Lawrence Livermore National Laboratory in the USA have developed a method for imaging inertial confinement targets under laser-driven fusion at the Nova laser facility [65] [66]. This method is very closely related to the pin-hole camera approach, the difference being that the pin-hole is larger than the source of the neutrons. The aperture must prevent 14 MeV neutrons released from the fusion target reaching the detectors. This is achieved through the use of a 0.63 cm diameter, 6 cm thick gold cylinder. The aperture has a taper from 580 μm down to a minimum diameter of 407 μm.

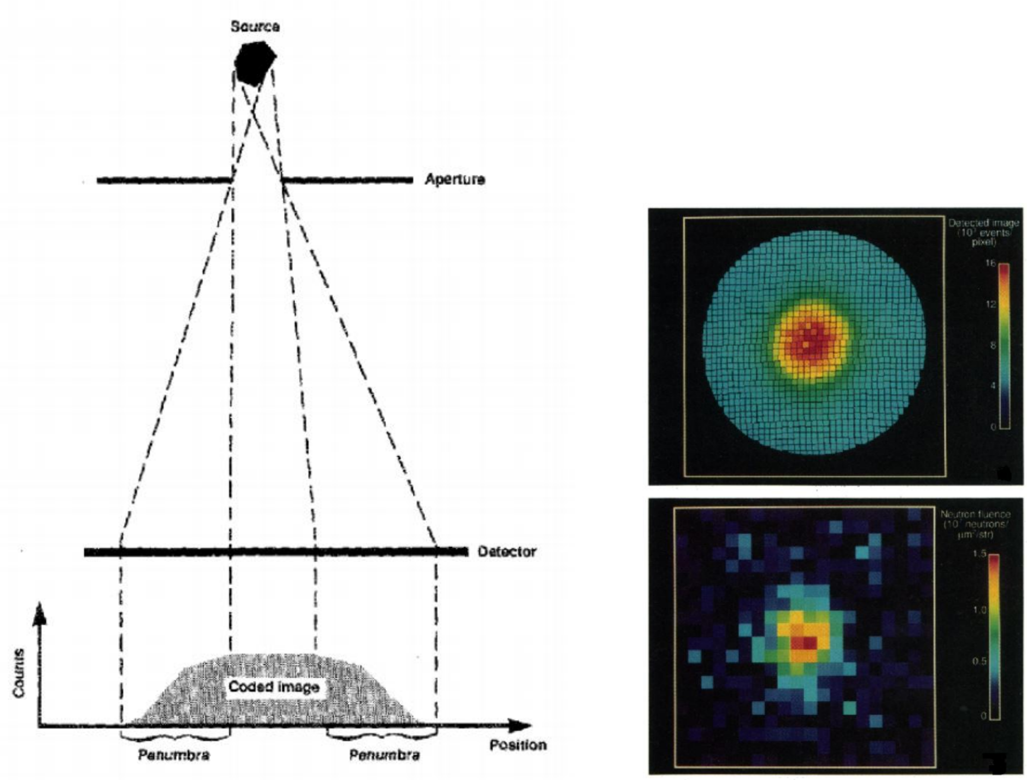

(a) Sketch of imaging process

(b) CCD image (top) and reconstructed flux image (bottom) with pixel size 25 μm

Figure 2.14 The penumbral coded-aperture imager developed at Lawrence Livermore National Laboratory [65] [66].

The laser produces implosions on the fuel which only include a hot-spot region (target does not ignite) of around 25 μm in diameter, producing neutrons. The neutron field is too low to be detected by conventional pin-hole neutron imaging such as PINEX, therefore the penumbral technique is used where the pin-hole is much larger and allows more radiation to reach the detectors. Other radiations do not escape the target, only neutrons. The gold does not shield the neutrons, rather it causes the neutrons to undergo large angle scattering which prevents them from reaching the detector. A schematic of the imager set-up is shown in Fig. 2.14a. The neutron field passing through the aperture is detected by an array of 1240 2 mm × 2 mm NE102 plastic scintillators coupled with an image intensifier and CCD camera to capture a digital image of the radiation field. The CCD image and reconstructed neutron image is shown in Fig. 2.14b; here the pixel size is 25 μm and the two-point resolution is calculated to be 60 μm.

These imagers are capable of producing images with resolution on the order of μm and have higher sensitivity than the PINEX imagers. The image data is captured in a very short time. These systems are neither compact nor portable by a single individual. Though there is much research involving such systems, this is not further discussed given the requirement for an extremely high neutron flux which is specific to fusion research.

2.5.2 Scatter cameras

The most frequently reported neutron imagers are neutron scatter cameras. These imagers use several detectors in conjunction with digitising electronics and nanosecond-level timing electronics to image neutron fields. These systems generally have a large detection volume and therefore high efficiency and sensitivity where good discrimination is employed, though this is partially offset by a reduction in efficiency due to the fact that double scatters are required for operation. These systems have been shown to detect fission and special nuclear material (SNM) sources at large stand-off distances. The drawbacks of scatter cameras is that they are very large, complex and expensive and often produce image artefacts in the image solution. The design goal of these systems overall is to have some level of portability and to rapidly accumulate data to demonstrate presence of a single source and its approximate location. They are therefore ideal for measurements where time is critical such as in nuclear security applications.

Brookhaven National Laboratory large-area fast neutron directional detector

The large-area fast neutron directional detector at Brookhaven National Laboratory uses 1m-long plastic scintillator paddles, each coupled with 2 photomultiplier tubes to detect fast neutrons over a large area giving good efficiency [67] [68] [69]. Fast neutrons interact via proton recoil reactions and gamma rays deposit energy via Compton scattering. All pulses are digitised to 1 ns timing resolution, which are processed to determine information about detected events. The location of the interaction in the paddle is estimated by the relative amplitudes of the pulses in each detector. Discrimination of neutrons against muons or gamma rays is performed by time-of-flight between the paddles. The angle of scatter is estimated from the energy deposited in the first paddle and the time-of-flight to the second paddle. The image is then formed from back-projections of these angle cones as demonstrated in Fig. 2.15a. This system has been demonstrated to image a ^{252}Cf source of emission rate 2 $\times 10^8$ neutrons s^{-1} at distances of up to 255 m demonstrating good sensitivity. The field of view of this system is 90°× 90 °.

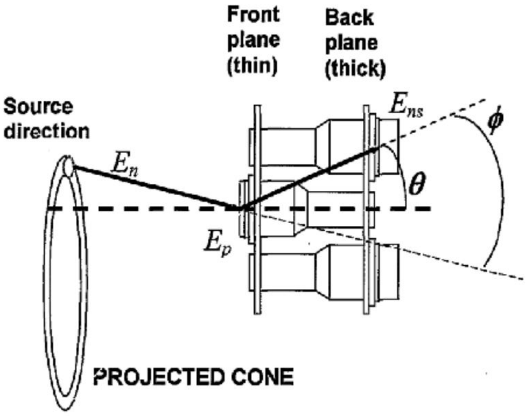

(a) Schematic of the imager operation [67]

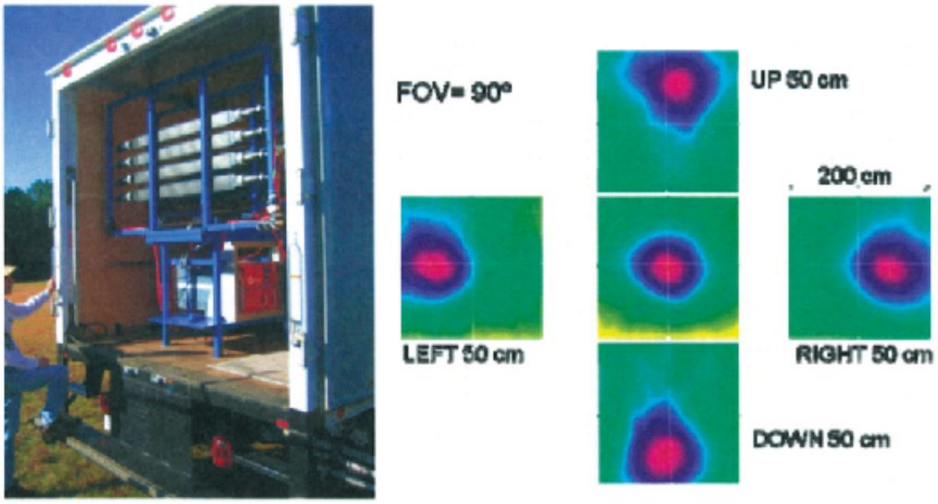

(b) Photograph of imager mounted in a truck [68]

(c) Output neutron images of a ^{252}Cf source at 1m central or displaced in X or Y by 50 cm as indicated [68]

Figure 2.15 The large-area fast neutron directional detector at Brookhaven National Laboratory

Fast Neutron Imaging Telescope

The fast neutron imaging telescope has been reported in the literature for use in measuring solar neutrons and for SNM detection [70] [71] [72]. This imager has been developed through collaboration between the University of Bern, the University of New Hampshire, Texas A and M University and the University of Glasgow. This imager uses 12 bars of NE-213A liquid scintillator, giving good efficiency, to detect neutrons (0.5 MeV neutron minimum), and uses time-of-flight as well as PSD to discriminate neutrons. In very close similarity with the Brookhaven National Laboratory large-area fast neutron directional detector, the location of each detection is calculated from relative signal from each bars 2 PMTs and the image is formed from cone projections. The resolution in the z axis for event detection was demonstrated to be 0.85 cm at single sigma level. This system is modular and was used with 3 detector elements to image a weapons grade plutonium source placed 1m from the detector at Pacific Northwest National Laboratory. The image was accumulated over several days and is shown in Fig. 2.16c; artefacts appearing in this image are expected to be a a result of using only three tubes in the modular system. The estimated angular resolution of the system is 5° and energy spectra can be reconstructed offline at an energy resolution estimated at 20%. The probe is reasonably compact and the system could be adapted for portability. The system has a 360° field of view in azimuth and a good range in elevation.

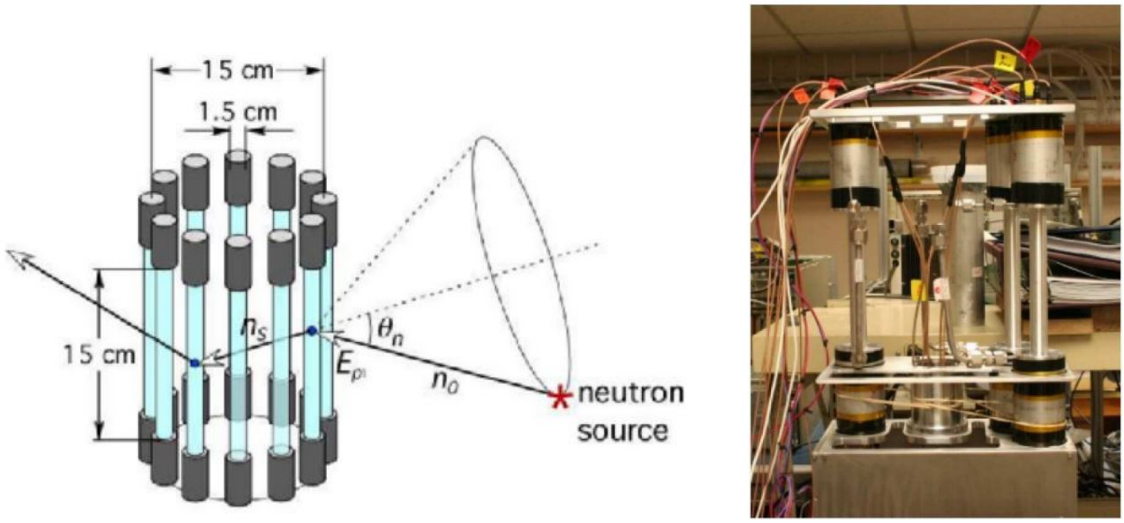

(a) Schematic of the system with 12 elements and cone projections

(b) Photograph of the system with 3 detector elements

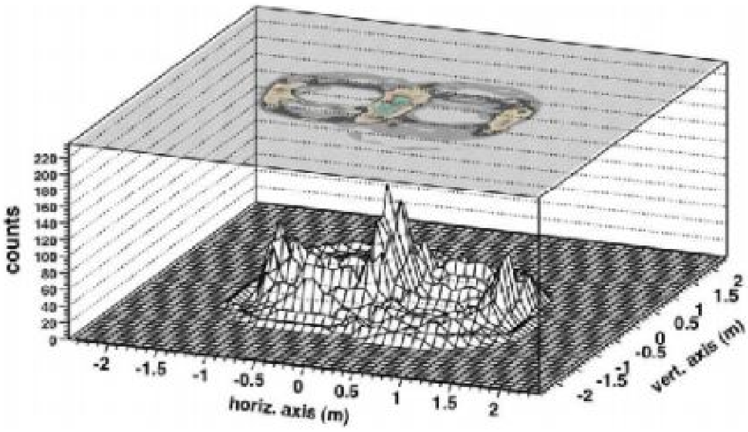

(c) Image of weapons grade plutonium source placed 1m from the detector. The image was accumulated over several days with the 3 element system

Figure 2.16 The fast neutron imaging telescope (FNIT) developed through collaboration between the University of Bern, the University of New Hampshire, Texas A and M University and the University of Glasgow [73].

Sandia National Laboratory neutron scatter camera

The neutron scatter camera at Sandia National laboratory is reported in several documents [74] [75] [76] [77] [78] [79] including two patents [80] [81].

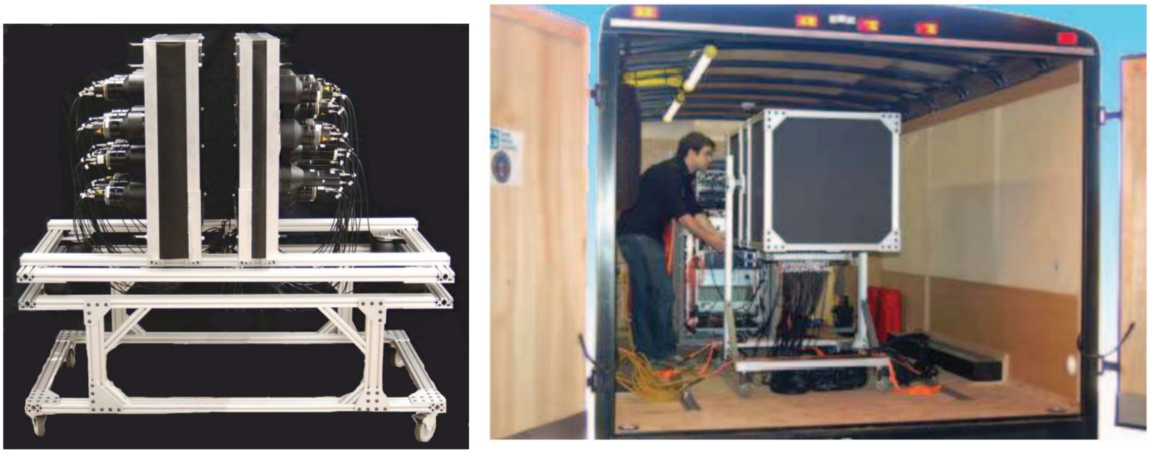

(a) Photograph of the scatter camera without housing[76]

(b) Photograph of the scatter camera mounted in a truck[78]

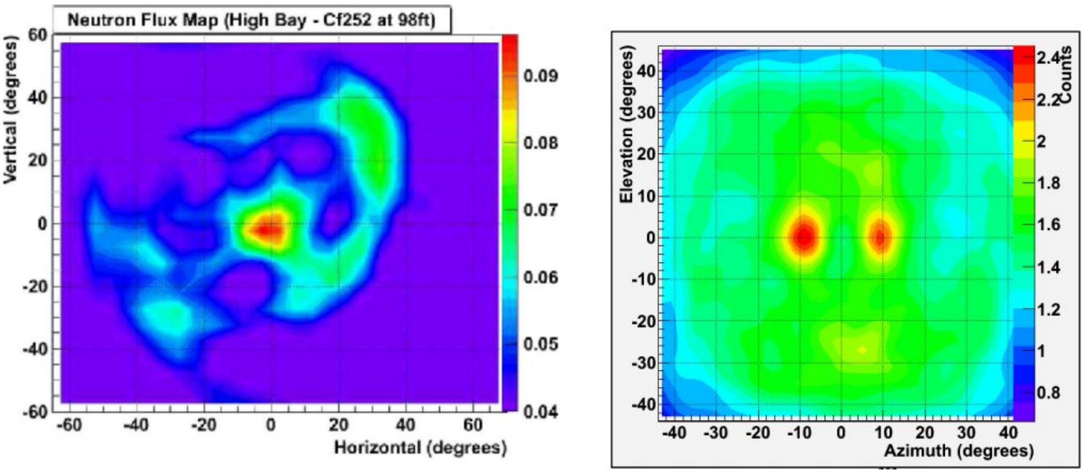

(c) Image of ^{252}Cf source at a distance of 30m from the imager [75]

(d) Image of two ^{252}Cf sources [76]

Figure 2.17 The neutron scatter camera developed at Sandia National laboratory.

This system is estimated at a technology readiness level of 6 and is offered for licensing opportunities. This camera has been investigated for applications including warhead counting and SNM detection for homeland security applications. The imager comprises a modular array of EJ-309 liquid scintillation detectors, giving good efficiency, coupled with digitisers to perform pulse-shape discrimination. A photograph of the system is given in Fig. 2.17a without housing and is shown mounted in a vehicle in Fig. 2.17b. Measurements of the deposited energy are used with the cell positions to generate back-projections of radiation paths. These are accumulated to form the image with an achievable resolution of 5°. Energy spectra can be collected sufficiently to distinguish ^{241}Am/Be from ^{252}Cf in separate images. An image solution of a ^{252}Cf source (designed to emulate 8 kg plutonium) at a distance of 30 m is shown in Fig. 2.17c, demonstrating good sensitivity. There, the data collection time was 2 hours. The source position is visible but some image artefacts are visible. The field of view of this detector is approximately 60 °. An image of two ^{252}Cf sources is also shown in Fig. 2.17d.

University of Michigan neutron scatter camera

There have been many reports on the neutron scatter camera at the University of Michigan [82] [83] [84] [85] [86] [87] [88]. The system is outlined in Fig. 2.18.

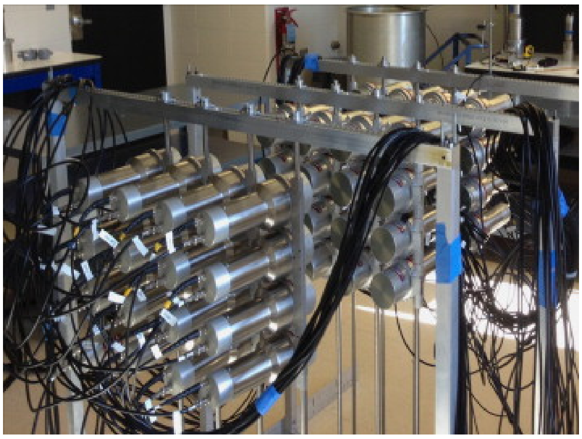

(a) Photograph of the neutron scatter camera [89]

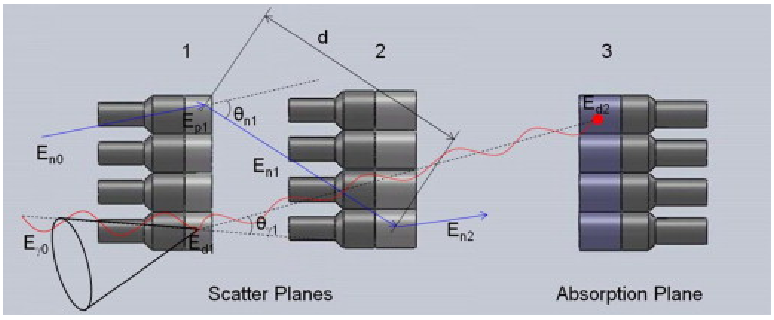

(b) Schematic of gamma-ray and neutron scattering in image contributions [89]

Figure 2.18 The neutron scatter camera developed at the University of Michigan.

This imager uses three planes of detectors to image combined gamma-ray and neutron fields, giving good efficiency. A photograph of the system and its 48 detectors is shown in Fig. 2.18a. A schematic of possible interactions is shown in Fig. 2.18b; note that planes 1 and 2 comprise EJ-309 liquid scintillation detectors and are used for imaging the neutron field. The third plane comprises NaI(Tl) and is used for gamma-ray-related imaging and measurements only.

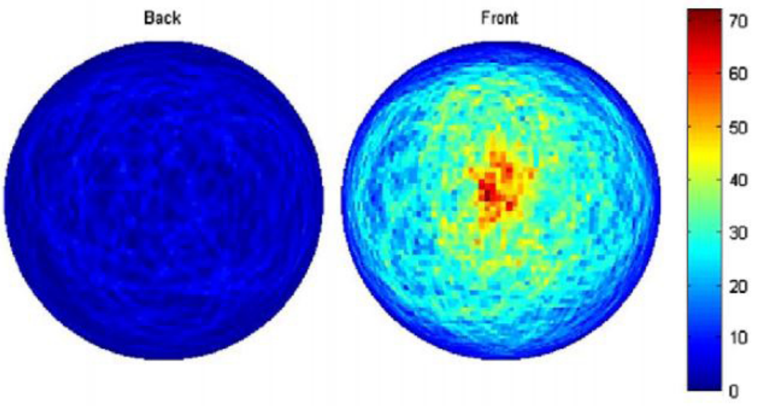

(a) Output neutron image of a single localised ^{252}Cf source emission rate 2 $\times 10^5$ neutrons s^{-1} imaged for 1 hour at a distance of 2.5 m[89]

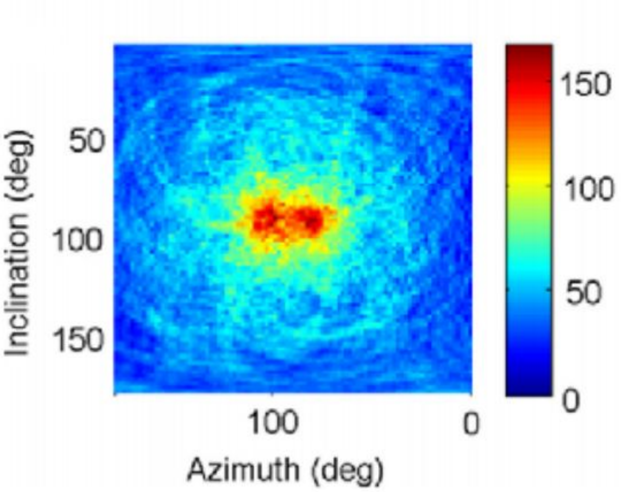

(b) Output neutron image of two MOX canisters (approx. 1 kg each) seperated by 30° imaged for 2 hours at a distance of 2.5 m [83]

Figure 2.19 Output images from the University of Michigan neutron scatter camera.

An incoming neutron must scatter in plane 1 and plane 2 in order to contribute to the image data. The pulses from the detectors are digitised and pass through two filters: pulse-shape discrimination and time correlation. The former selects neutron events through the pulse shape, the latter selects neutron events based on the travel time between the detector planes (gamma rays travel at light speed, neutrons much slower). Events passing through these filters are included in the data set and the solid angle of origin is determined from the geometry of the detectors in each double scatter event. The location of the sources is found by comparison of the many solid angle regions with various methods. This system processes scatters from both directions and therefore gives a near 4π field of view. An image of a ^{252}Cf source, emission rate 2×10^5 neutrons s^{-1}, imaged for 1 hour at a distance of 2.5 m is shown in Fig. 2.19a. The neutron energy spectrum can also be calculated with this approach, using the measured deposited energy and scattering angle. This system has been demonstrated to image plutonium and mixed-oxide (MOX) fuel materials; an image of two MOX canisters separated by 30° are shown in Fig. 2.19b.

University of New Hampshire scatter camera, NSPECT

The University of New Hampshire have developed a scatter camera [90] [91], shown in Fig. 2.20 which is a scaled down more portable version of the University of Michigan neutron scatter camera. Due to the smaller detectors the efficiency is reduced in comparison. The angular resolution of the system is 12 °. This camera has also been demonstrated to measure SNM including plutonium and depleted uranium. Images of a ^{252}Cf source moderated by a 15 cm radius sphere were also produced, as well as images from large stand-off distances.

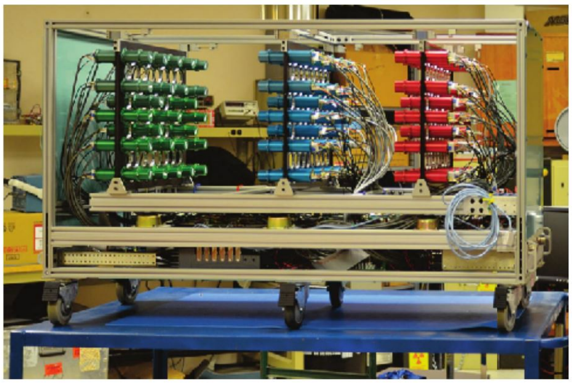

(a) The system, comprising 3 detection layers

(b) The system mounted in an SUV

(c) Neutron hotspot (left) and gamma ray hotspot (right) overlaid on an optical image

Figure 2.20 Summary photographs of the University of New Hampshire scatter camera [90]

2.5.3 Coded aperture imagers

Coded aperture imagers operate in a similar way to pin-hole cameras, using a shielding material as a response modulator to block out a large proportion of the incident radiation, allowing only some trajectories to pass through. Rather than having a single transmission region, as with pin-hole cameras, there are many which greatly improves the signal-to-noise ratio though the image reconstruction is more complex. A sample of a binary coded-aperture mask is shown in Fig. 2.21. The result is that a pattern emerges on the detection medium, a superposition of many pin-hole transmissions which can be related back to the radiation field.

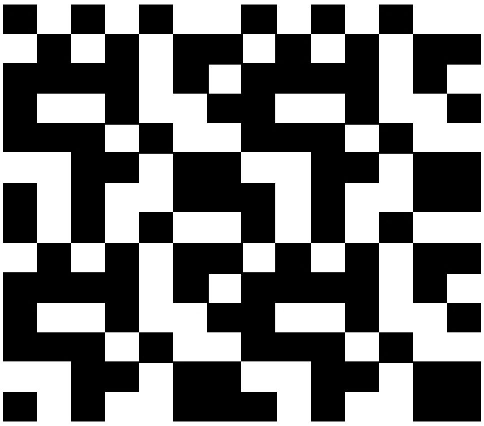

Figure 2.21 Example of a binary coded-aperture mask for coded-aperture imaging. Black and white pixels represent opaque and transmission regions respectively.

Coded aperture imagers discussed in the literature have a range of capabilities depending on the design goals which have been extremely varied, from stand-off source location to counting warheads in nuclear weapons.

Oak Ridge National Laboratory, Sandia National Laboratories and Idaho National Laboratory coded aperture neutron imager

Coded aperture imaging with fast-neutron detection has been investigated in the United States with a joint effort between Oak Ridge National Laboratory, Sandia National Laboratories and Idaho National Laboratory [92] [93]. This system is shown in Fig. 2.22a. A plane of custom-built pixelated EJ-309 liquid scintillator cells (coupled with digitisers for PSD) are located behind a coded mask made of polyethylene 2.22b. The material under scrutiny is placed in front of the mask which blocks out neutrons along some paths, and not through others where holes in the mask are present. The pattern of neutron flux at the cells consisting of transmission or shadow is dependent on the distribution of the neutron sources in front of the mask. PMTs coupled to groups of cells read the distribution of scintillations due to neutron interactions which is used along with the known mask geometry to calculate the source distribution in front of the imager. Gamma rays are filtered out by digitisation of the pulses and applying a pulse-shape discrimination algorithm. This system has been used to demonstrate effective imaging of complex neutron fields produced by five sources, see Figs. 2.22c and 2.22d with resolution of at least 10 cm (the closest spacing of the sources).

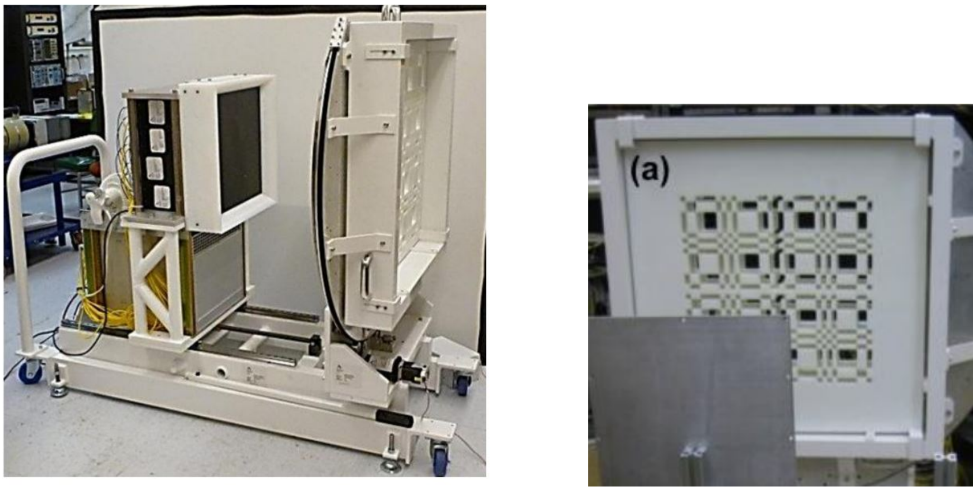

(a) Photograph of system

(b) Photograph of mask

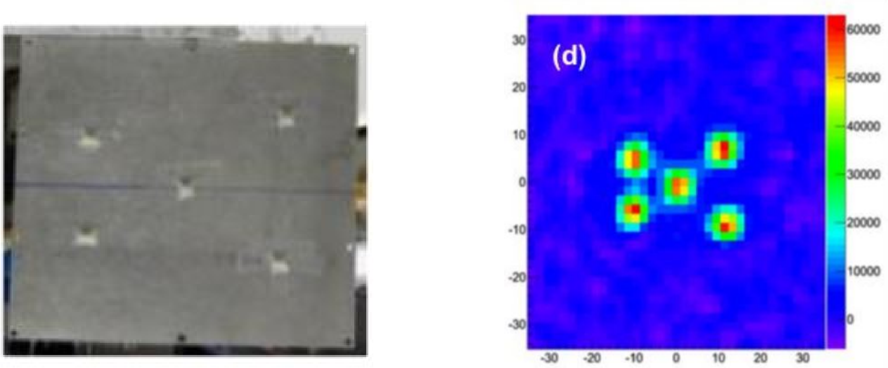

(c) Layout of five ^{252}Cf sources each with emission rate of 4 $\times 10^4$ neutrons s^{-1} imaged at a distance of 1.11 m

(d) Output neutron image of five ^{252}Cf sources after 1 hour exposure

Figure 2.22 The fast-neutron coded aperture imager developed by national laboratories in the United States [92].

This system has high efficiency due to the large detection volume and clearly has a good image resolution. This system requires digitising electronics to apply neutron-gamma discrimination but does not require coincidence filters, making this approach simpler than for the neutrons scatter camera. The drawbacks of this system is that it is large and non-portable and has a limited field of view. The system also has a focus length and therefore requires the source to be placed in a known region of space. This imager was designed to have a high resolution suitable for identifying nuclear warheads for treaty verification purposes.

CLYC RadCam™

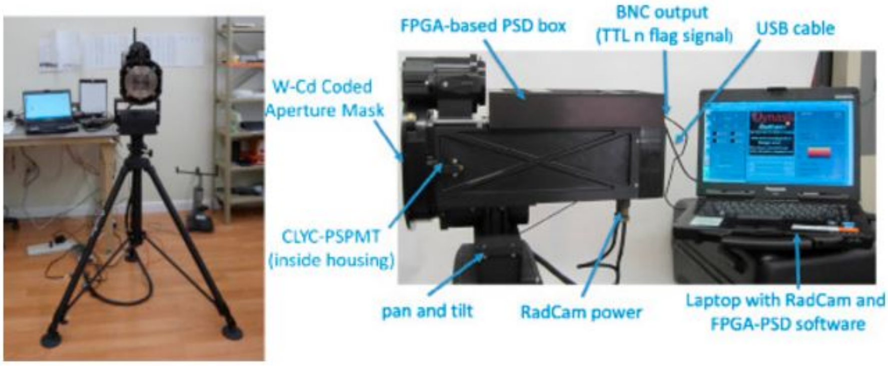

Figure 2.23 Photographs and annotations of the RadCam-2 combined neutron and gamma-ray imaging system [94].

RMD have recently developed a coded-aperture imager, shown in Fig. 2.23, based on the RadCam™design, using a small amount of the scintillator Cs_2LiYCl_6:Ce [95] [94]. This detector interacts via recoil scattering to detect fast neutrons and also allows the detection of thermal neutrons via the ^{6}Li(n,α)t channel; these events are separated using pulse-shape discrimination. The coded aperture mask is composed of tungsten and cadmium, the latter used to shield thermal neutrons. The system has a limited field of view but has been motorised to permit rotation of the probe. The system has an outer probe radius of approximately 65 cm and can be considered lightweight and portable. Output images are shown in Fig. 2.24. Research has shown that this system performs best when imaging fast neutrons below 2 MeV, as many image artefacts are otherwise produced, e.g. when imaging ^{241}Am/Be. Although the addition of thermal-neutron imaging can be considered an advantage in a general sense of capability, this may not always be the case in practice. Neutrons have undergone many scatters through the thermalisation process; these fields therefore will have lost much of their directionality, reducing the efficacy of thermal neutron imaging at determining the precise source location. Secondly, there are many situations which involve both very high thermal-neutron backgrounds and nuclear fuel materials. Where the fast-neutron imaging of fuel materials is the goal, the addition of a thermal neutron background to the gamma-ray background would add additional complications when discriminating fast-neutron fields. Contributions from ^{35}Cl(n,p) reactions also add thermal neutron points in the PSD plot which extend into further regions of the PSD distribution than the ^{6}Li(n,α)t, making fast-neutron discrimination increasingly difficult.

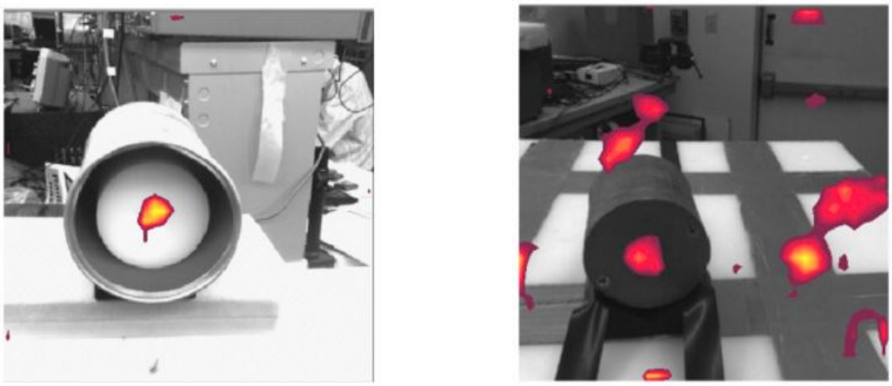

(a) Image of a 39 μCi ^{252}Cf source at 30 cm imaged for 2 days

(b) Image of a 340 mCi ^{241}Am/Be source at 30 cm imaged for 2 days

Figure 2.24 Output images of fast-neutron fields produced by RadCam-2 overlaid on optical images [94].

Sandia National Laboratory time-encoded imager

More recently a system has been described which uses time encoding to image fast-neutron fields [96]. This system, developed by Sandia National Laboratory, works analogously to a coded aperture system, including using a coded mask. Most systems require an array of detectors to read the flux distribution in space, this system requires only two EJ-309 scintillation cells. The mask is moved with time; the known orientation of the mask at a given time in conjunction with the number of neutron detection events at the detectors is compiled into the data set following neutron-gamma discrimination. The data set is used with the known mask parameters (pattern and shape) to determine the distribution of fast-neutron emitters in the local environment. This system requires digitisation and pulse-shape discrimination, though the remaining mechanical requirements are reasonably simplistic. A photograph of this system is shown in Fig.2.25a.

This system overcomes the issues of low efficiency of multi-scatter systems and the high cost and complexity of conventional coded aperture imaging systems. This system has a reasonable field of view, although cannot image directly above or below the cylindrical axis. The system is reasonably compact and portable, however the resolution will be traded off against the size of the mask. This means that smaller masks of this type will be more compact but with a lower resolution. This property is related to the fact that the collimator must be a few cm thick to effectively shield fast neutrons, and the mask cells must therefore be of an

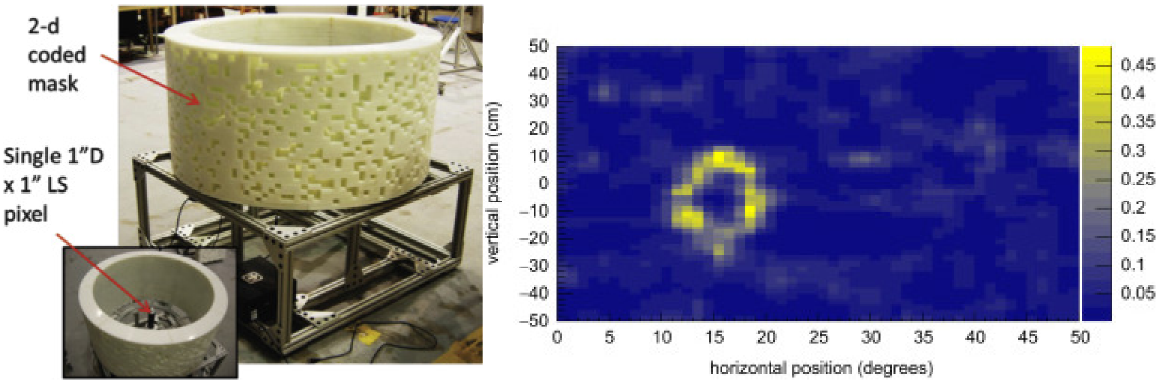

(a) Annotated photograph of the system [96] (b) Image of a ring of californium sources each 35 μCi imaged for 3 days at 2m distance [96]

Figure 2.25 The time encoded fast-neutron imager developed at Sandia National Laboratory.

approximately similar size. The system has been used to image complex fields such as those produced by a ring of ^{252}Cf sources shown in Fig.2.25b. This image shows that resolution is better than 12°. There are some artefacts in the images and imaging time is over one day.

2.5.4 Single-detector imagers

These imagers use a single position-sensitive detector to determine the directionality of the fast neutron field. This is achieved either through collimation or by measuring tracks of recoil particles. Back-projection is then applied to the tracks to determine the origin of the radiation. The use of a single detector leads to poor efficiency due to the implementation of either mechanism for position sensitivity.

Lancaster University single-detector collimated imager

A single-detector system has been developed at Lancaster University to image fast neutrons [97] [98] [99] [100]. This system, depicted in 2.26a uses a tungsten cylinder ID = 37 mm, OD = 57 mm, length = 250 mm to collimate a small EJ-301 liquid scintillation detector to neutrons and gamma rays. Raster scanning performed by an equatorial mount allows data for each 'pixel' of space to be accumulated using a fast digitiser and laptop PC. The data are then discriminated in post-processing to separate neutrons from gamma rays. Each pixel is then attributed with the number of discriminated neutrons or gamma rays to form the neutron and gamma-ray images respectively.

This system benefits from simplicity and is able to determine the neutron field along a line of sight of the cylindrical collimator. A precise response function of the collimator is not considered and is assumed to be binary, depending if the source is within a cone of sight or

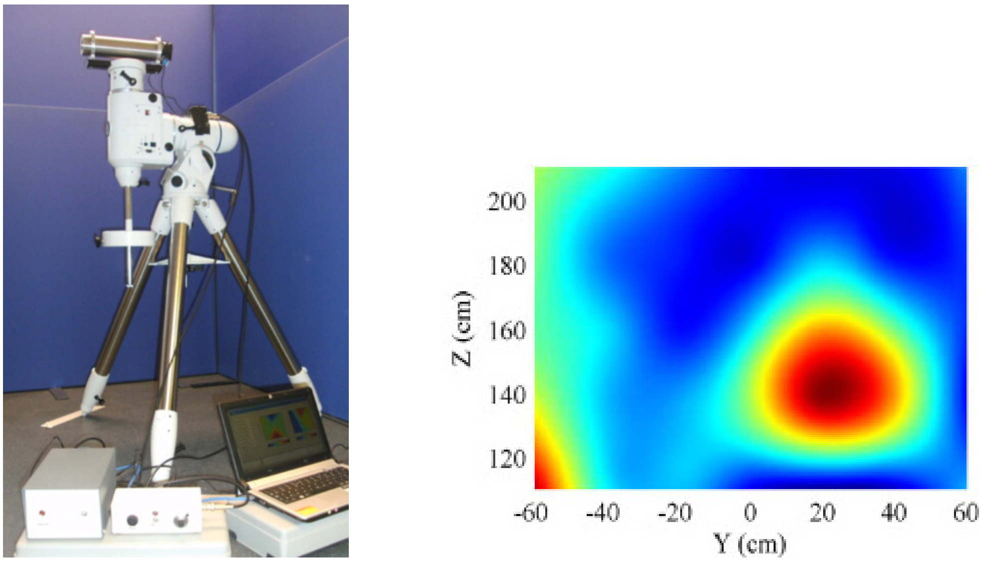

(a) Photograph of the collimated single-detector system

(b) Image of a ^{241}Am/Be source (2.0×10^7 ns^{-1}) at a distance of 1.72 m

Figure 2.26 The tungsten-collimated single-detector neutron imaging system at Lancaster University, UK [98].

not. In reality the response is continuous and related to the path length through the collimator for each position in space. The assumption leads to the production of image artefacts due to a reduction of the shielding thickness when the collimator is not in close alignment with the neutron radiation source. These artefacts can be seen in the $\lesssim$ -40 cm region in Y in Fig. 2.26b, where the angle between the source and collimator axis is 25°. This effect would greatly increase noise when imaging multiple sources or non-point source distributions. The system is transportable, though too large and heavy to be carried by a single individual. The field of view of this system is restricted and requires human intervention to manually adjust the elevation angle.

Lawrence Livermore National Laboratory time-projection chambers

The time-projection chamber measures the path of charged particles through a gaseous medium and allows reconstruction of the particle tracks. These detectors have been used since the 70s in astronomy and particle physics applications [101] and have recently been applied to neutron imaging [102] [103]. These detectors use a volume of several litres of gas as a detection volume and measure particle trajectories using μs level timing electronics. Other electronic processing filters are also applied to remove noise.

A schematic of the time-projection chamber at Lawrence Livermore National Laboratory is shown in Fig. 2.27(a). Incident neutrons interact through elastic scattering with H_2 gas

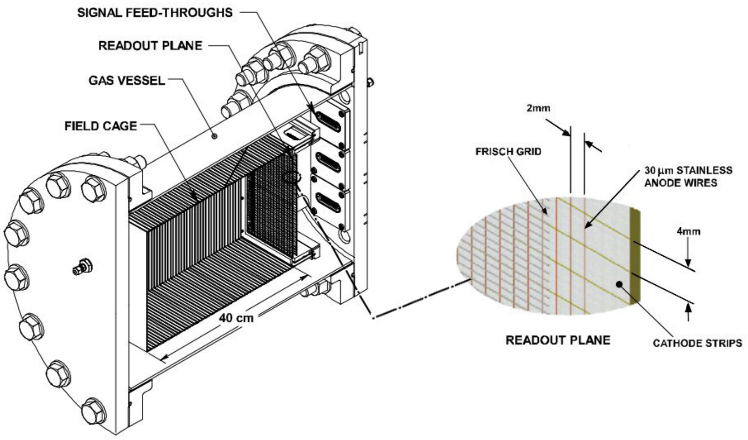

(a) Schematic of a time-projection chamber

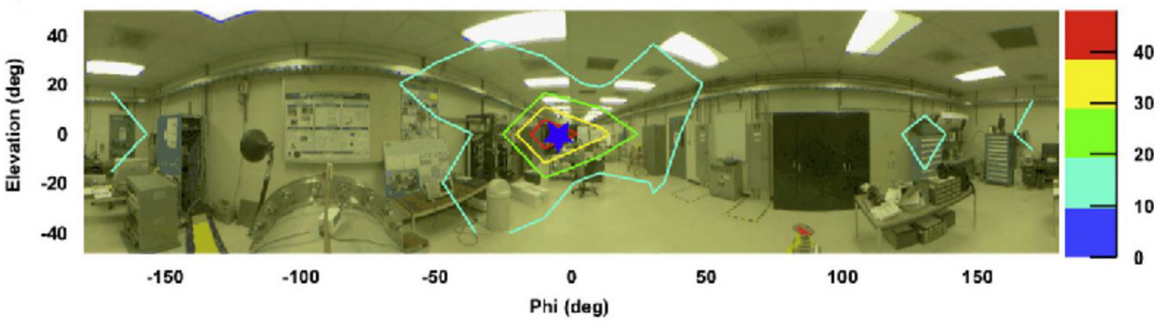

(b) Output image solution of a 60 μCi ^{252}Cf source at 17.7 m overlaid on optical photograph

Figure 2.27 The time-projection chamber neutron imaging system at Lawrence Livermore National Laboratory [102].

in the pressure chamber producing recoil protons. The gas is ionized along the proton trajectory and an electric field placed across the chamber causes electron drift towards the readout planes. The time and position of the electrons reaching the plane is recorded in the signal, therefore allowing the trajectory of the recoil proton and subsequently the incident neutron to be evaluated. The location of neutron-emitting materials is then determined from a compilation of these incident neutron tracks. This system has been demonstrated to locate a ^{252}Cf source from 17.7 m, see Fig. 2.27b. This system was designed for only non-mobile use and therefore no efforts were made to reduce the size and weight; the current size of the chamber is 50 cm × 46 cm diameter. The efficiency of the system with regard to neutron detection is very low at 0.5%.

Several gaseous mediums have been trialled to date. The drawback of H_2 gas is that it is potentially explosive. ^{3}He has been used successfully [103], but due to short supply this is no longer economically viable as a detection medium. BF_3 has also been proposed but is toxic. Other gasses have been suggested but any component of alpha decay in the forming nuclides may lead to a heavy background. ^{4}He would be ideal as it is non-flammable however imaging capabilities are significantly reduced due to limiting the recoil distances and the alignment with the neutron direction following interaction [102].

The advantages of these system is that they are compact, could be adapted to be portable and have a very large field of view (almost 4π), making it plausible for nuclear security applications.

2.5.5 Summary table of alternative fast neutron imagers

A summary of alternative fast neutron imagers is given in Table 2.5. Additional information on the table follows:

*Criteria in Table 2.5 are port. (portability of whole system), compac. (compactness of front end only, i.e. detector and physically attached components, motors, collimators etc), weight (of front end only), eff. (efficiency of detectors), sens. (demonstrated sensitivity of system: good indicates ability to measure weak neutron fields such as those from large stand-off distances or in conjunction with heavy shielding), res. (position resolution of a single source), art. (good indicates that artefacts are not present in image solutions), speed (of data collection: good indicates fast), FOV (field of view), and mult. (good indicates good image quality when imaging multiple sources of the same radiation type).

Table 2.5 Summary table of alternative fast-neutron imagers*.

Imager	Port.	Compac.	Weight	Eff.	Sens.	Res.	Art.	Speed	FOV	Mult.
PINEX-2 pin-hole	poor	poor	poor	v. poor	v. v. poor	v. good	poor	v. good	poor	good
Penumbral imaging technique	poor	poor	poor	v. poor	v. poor	v. good	med	v. good	poor	no info
Brookhaven NL scatter camera	med	poor	poor	good	v. good	good	med	good	poor	no info
FNIT	med	good	poor	med	no info	med	med	med	good	no info
Sandia NL scatter camera	med	med	poor	good	good	good	med	good	poor	no info
U. Michigan scatter camera	med	med	poor	good	med	med	med	good	v. good	good
U. New Hampshire scatter	good	med	poor	med	good	med	med	med	poor	no info
ORNL, SNL, INL coded aperture	poor	poor	poor	good	med	good	good	good	poor	good
CLYC Radcam	good	good	med	poor	no info	good	poor	v. poor	v. good	no info
Sandia NL time-encoded	good	good	med	poor	no info	good	good	poor	med	good
U. Lancaster single-detector †	good	med	med	poor	no info	med	med	good	poor	no info
Time projection chamber	med	good	poor	poor	good	good	med	good	v. good	no info

† This imager is not fully-automated

Chapter 3

Materials and methods

Chapter summary

This chapter includes information on all materials and methods used in this research to obtain the key results which are discussed in the later chapters. This includes information on the imaging system hardware: radiation detectors, data acquisition, signal processing and radiation collimators; and image reconstruction methods used to process image data. Details on complex radiation sources imaged in the research are provided as are details of the modelling methods for these sources, the probe and radiation environments.

3.1 Imaging system overview

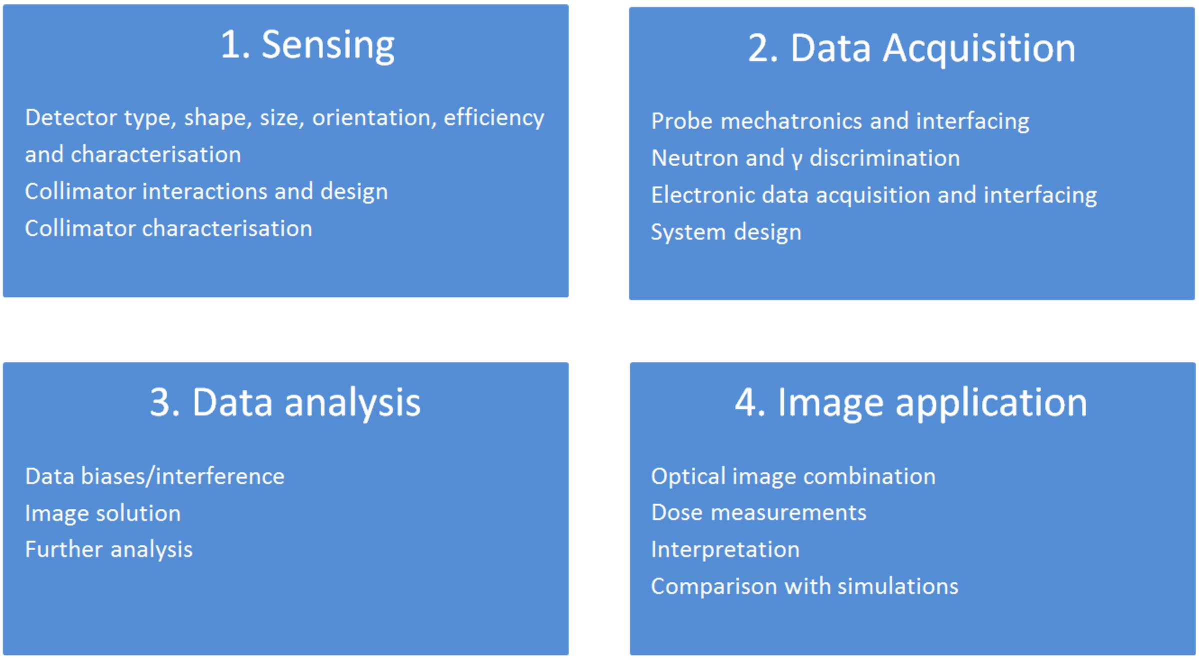

Figure 3.1 System and processing overview of radiation imaging systems used in this research.

Each imaging system can be simplified into four main constituents: sensing, data acquisition, data analysis and image application, which are summarised in Fig. 3.1.

Sensing includes the detection of fast neutrons and gamma rays. This section includes collimation which modified the detector to bias spatial sensitivity; this was critical in determining the origin of radiation. Four different collimators were designed, built and tested over the course of the research. Characterisation of these collimators was also a key component in image reconstruction and is discussed in section 4.4. The second component was **data**

acquisition; how the sensing equipment was best used to obtain useful data, i.e. how data were collected which can be used to produce accurate images of radiation fields. This was achieved by development of a mechatronic system designed to rotate the collimator into a series of positions. At each position, an interfaced acquisition system discriminated neutrons and gamma rays and sent these data, along with the coordinates, to a PC where the dataset was stored.

The acquired data were then processed in the **data analysis** stage; image reconstruction techniques were used to covert the acquired data into meaningful results. These include the location of radiation sources, whether they were emitting gamma rays or neutrons, the relative activity and distribution as well as other specific analysis techniques. The final stage was **image application**; the interpretation of radiation images and their application to the real world and industry. A common theme was overlaying the radiation images on optical images such that a radiation source could be associated with an object in addition to a location in space. It was useful to compare radiation images with simulated images for validation and discussion particularly in the case of complex fields.

3.2 Imaging system hardware

3.2.1 Detectors

The radiation detectors used in this research contain organic liquid scintillators EJ-301 and EJ-309. These scintillation materials have very similar properties regarding the detection of radiation; sensitive to fast neutrons in the MeV range and gamma rays in the early keV range and beyond [104] [105]. These scintillators have both been found to have very good properties for pulse-shape discrimination [106]. The main distinctions between these liquid scintillators are their flashpoint, toxicity and biodegradability which are improved for EJ-309 [107] [108].

Miniature EJ-301, model VS-0653-2

This detector was used as the primary imaging detector due to its compact size. This scintillator has fire safety issues due to a low flashpoint and was therefore used in small 4 ml volume which was suitable for research purposes. If designing a commercial imager, it is recommended that a straight swap is performed of the scintillation liquid to EJ-309. This would remove any issues associated with low flashpoint and toxicity with minimal impact on imaging capabilities given the small performance differences. The data sheet for the scintillator can be found in Appendix B.4 - B.5. The data sheet for the miniature EJ-301 detector can be found in Appendix B.7 and is summarised in Fig. 3.2. The scintillation cell is used with a Hamamatsu R5611 photomultiplier tube. The detector was used with a bias of -840 V, optimised previously to give good pulse shape discrimination [109].

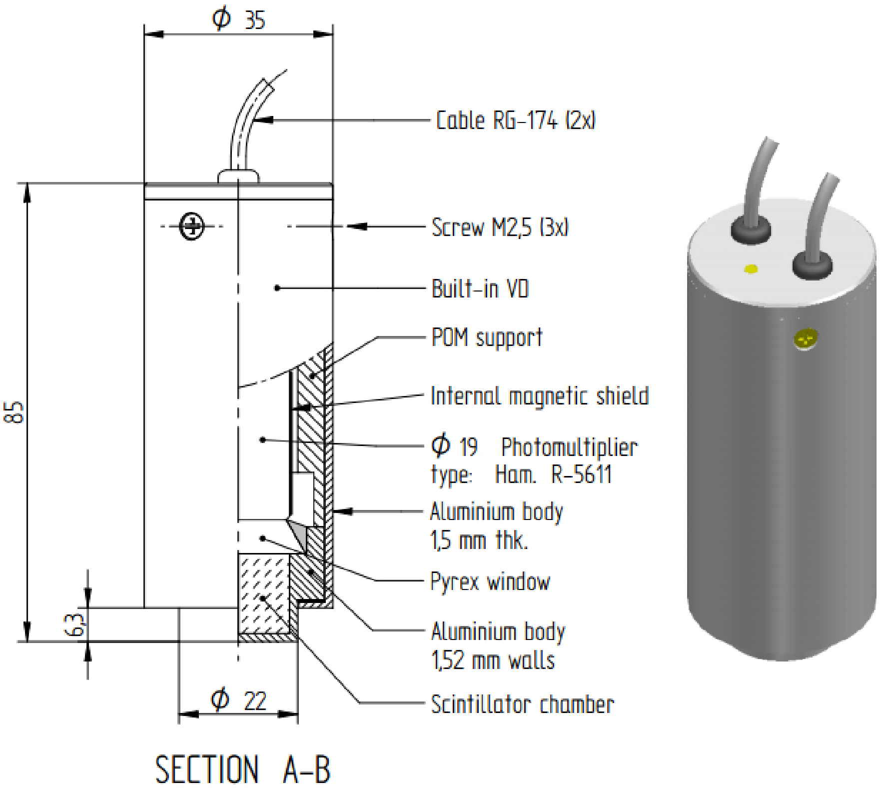

Figure 3.2 Assembly diagram of miniature EJ-301 detector model VS-0653-2 [110].

Cubic EJ-309, model VS-1105-21

These detectors are low hazard and have a low flashpoint, hence they can be produced in large sizes. The data sheet for the scintillator can be found in Appendix B.6. The data sheet for the cubic EJ-309 detector can be found in Appendix B.8 and is summarised in Fig. 3.3. The scintillation cell is used with an ETL type 9821 FLB photomultiplier tube.

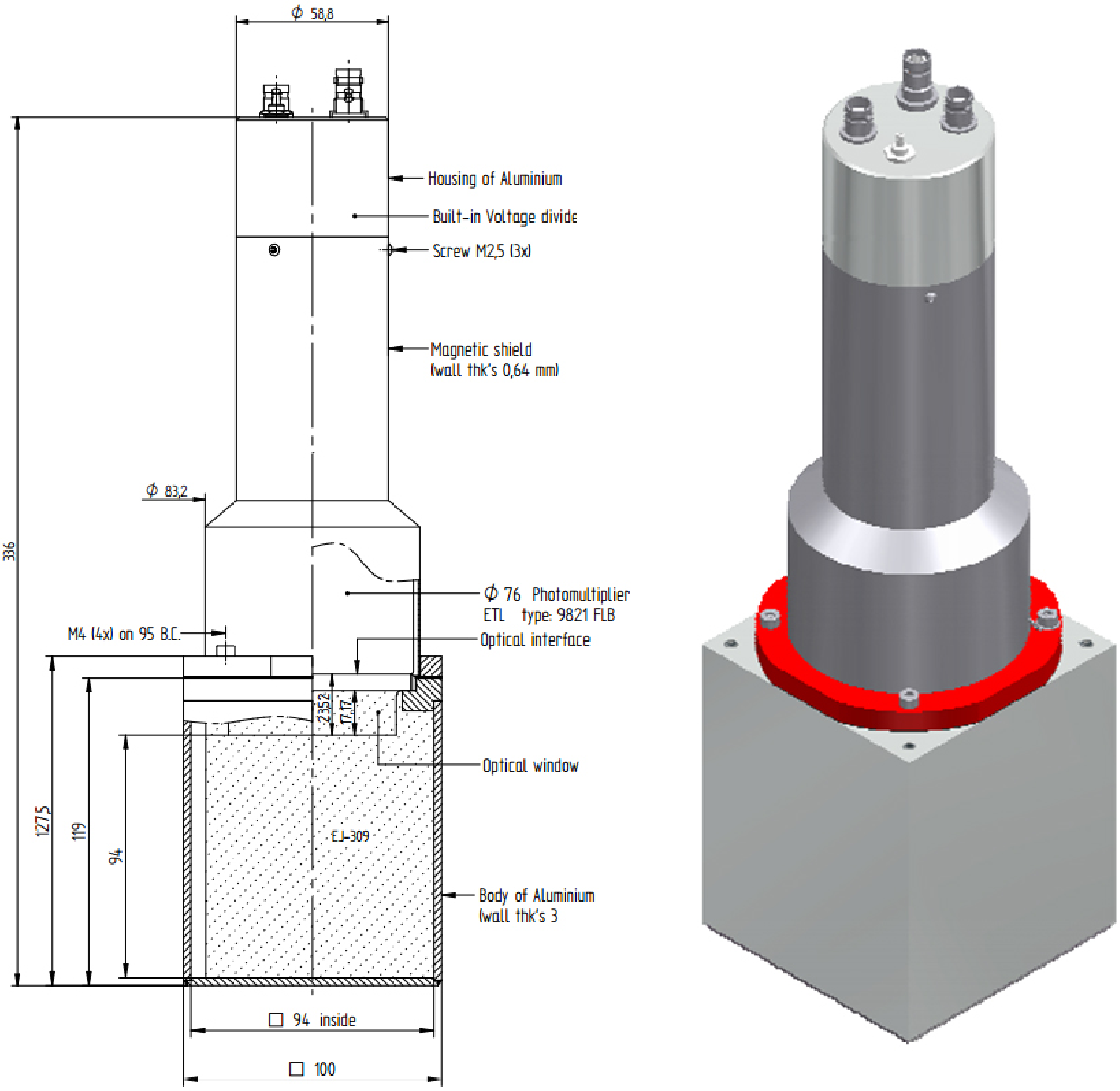

Figure 3.3 Assembly diagram of 10 cm cubic EJ-309 detector model VS-1105-21 [111]

3.2.2 Mixed-field analysers (MFAs)

Radiation pulses from the detectors were discriminated in real-time using off-the-shelf mixed-field analyser (MFA) units [112] [113]. Single and 4 channel versions were used seen respectively in Figs. 3.4 and 3.5.

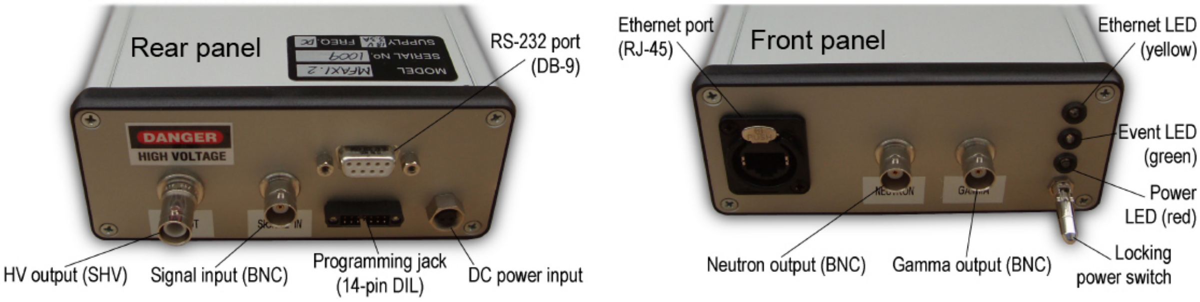

Figure 3.4 Photographs of the single channel MFA (front and back) with illustration of connections.

Technical specification

The MFAs have built-in power supplies to power the associated detectors (one per channel) and were used to discriminate radiation events from the detector into discrete neutron and gamma-ray events. Events are digitised using 500 MSa/s ADCs (2 ns resolution), the waveforms are then discriminated by an algorithm installed on a Xilinx Virtex 5 LXT Field-Programmable Gate array. Discriminated events could be passed over an Ethernet connection to a PC with a limit of 35 pulses per second (pps). The units were equipped with two transistor-transistor logic (TTL) outputs per channel which give out real-time 50 ns logic pulses from the appropriate channel (neutron or gamma ray), following detection and discrimination producing output in real-time. These channels could be interfaced with other electronics to acquire data which allowed the Ethernet limitation to be surpassed. Sample TTL pulses are shown in Fig. 3.6. The units have an upper limit throughput of 9 Mpps, which far exceeded any count rates observed during this research.

For the purpose of this work, the single channel and the 4 channel MFAs could be considered identical other than the number of channels and therefore could be used interchangeably. The 4 channel MFA is shown in Fig. 3.5. The data sheet for these analysers can be found in Appendix B.9.

Figure 3.5 Photograph of the 4 channel MFA.

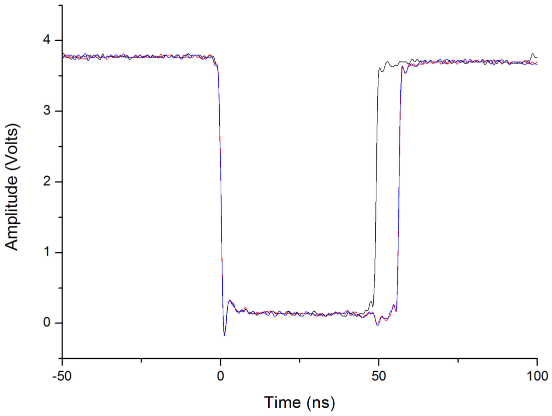

Figure 3.6 3 captured pulses from the MFA TTL outputs captured with a 500 MSa/s TDS520A Tektronix Digital Oscilloscope.

Discrimination set-up

Calibrating the discrimination parameters was a critical initial step in experimental work to correctly isolate the neutron and gamma-ray fields. Output pulses from the detector were transmitted to the MFA where they were digitised. These were then smoothed with a moving average filter, used as part of a pulse-gradient analysis algorithm [114]. The pulses were sampled at the peak amplitude and the discrimination amplitude - the amplitude after time Δt measured from the peak (typically 10-20 ns at which point the neutron and gamma-ray waveforms are most different) as illustrated in Fig. 3.7. Data on these events were passed to the PC over the Ethernet to form a discrimination plot of peak amplitude vs. discrimination amplitude. Once sufficient counts were collected, a segmented line was positioned to divide the two plumes of data into neutrons and gamma rays as shown in Fig. 3.8. Once this line was set the discrimination was performed in real-time for all pulses transmitted to the MFA.

It should be noted that the PGA algorithm is more robust to pile-up events than integral approaches. The discrimination and peak amplitude values rely on a small number of points in the captured waveform, therefore reducing the probability of small pile-up events affecting results which would be included in full integral calculations.

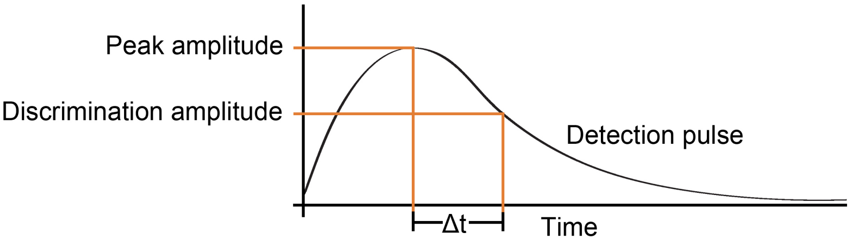

Figure 3.7 A diagrammatic illustration of the operation of the PGA algorithm.

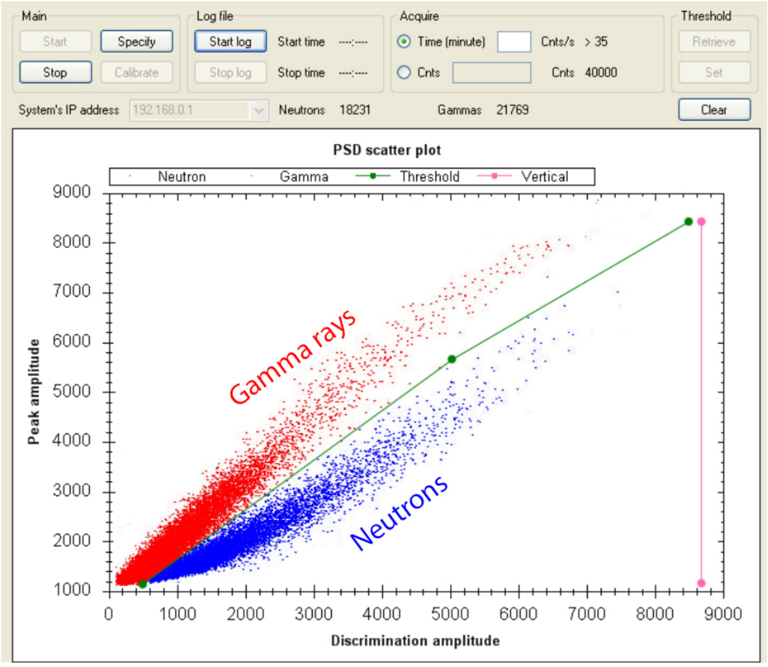

Start time ----:----
Stop time ----:----
● Time (minute)
○ Cnts
Cnts/s > 35
Cnts 40000
System's IP address 192.168.0.1
Neutrons 18231
Gammas 21769

Figure 3.8 Image of the software graphic user interface during PSD-line set-up. Discriminated gamma rays are shown in red, discriminated neutrons in blue, the discrimination line in green and the discrimination cut-off in pink.

3.2.3 Collimators

This section discusses the physical form of the collimators; the collimators are characterised in section 4.4.

Tungsten C0

The C0 collimator was originally designed for use in gamma-ray imaging by Createc Ltd. and was retrofitted with a neutron and gamma-ray detector for use in this work. The collimator was made of tungsten alloy HE-395 (also including nickel and iron), 95% tungsten by weight and has a density of 18.1 g cm^{-3}. The geometry of this collimator was cylindrical, with an outside diameter of 68 mm. A 6 mm-wide, 25 mm-deep void slot allowed unattenuated passage of radiation from the outside environment to inside the collimator which contained the detector. Radiation not incident on the slot was attenuated by the tungsten. A 36 mm diameter hole was milled into the rear to accommodate for the larger neutron and gamma-ray detector which fitted flush behind the slot. Sketches of this collimator are shown in Fig. 3.9; the C0 collimator is shown in blue, the detector in green, and the steel housing in grey in Fig. 3.9b.

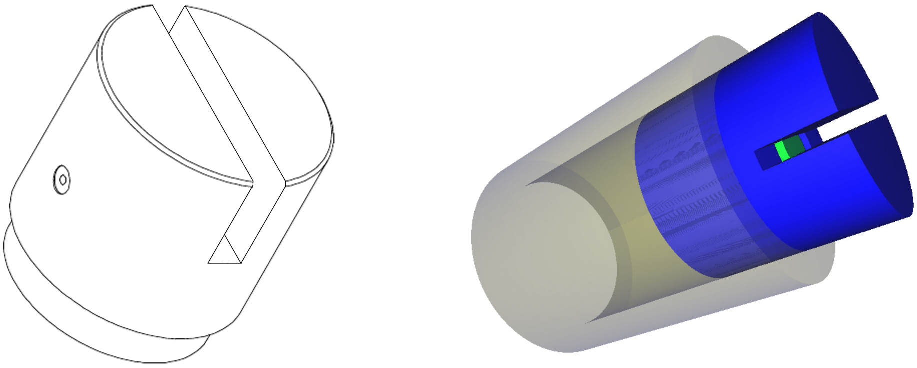

(a) Manufacturing drawing (b) Model of collimator in steel housing

Figure 3.9 Diagrams of the tungsten C0 collimator.

Tungsten PVC C1

The C1 collimator was designed as a modification to collimator C0 to aid in neutron shielding. The shield was a 20 cm diameter hemisphere cut from a solid block of rigid PVC of density 1.4 g cm^{-3}. A 6 mm-wide slot void was cut centrally perpendicular to the flat face. The two pieces were held together with two bolts on each side. Sketches of the collimator are shown in Fig. 3.10, the collimator is shown in red in Fig. 3.10b.

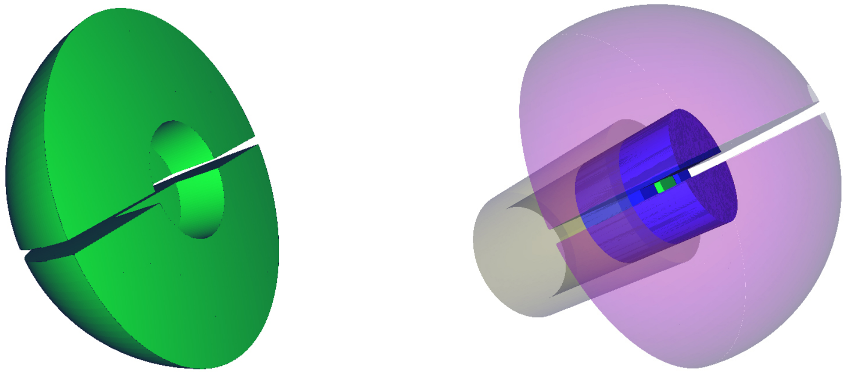

(a) C1 collimator reverse

(b) Model of collimator and steel housing

Figure 3.10 Diagrams of the PVC C1 collimator

Tungsten PE C2

The C2 collimator was also designed as a modification to collimator C0 as a further attempt to aid neutron shielding. Here input from Monte Carlo modelling was used in the design process. This collimator was designed to be more compact than collimator C1, as well as having superior features in the sensitivity matrix to give an improvement in capability. The shield was cut from high-density polyethylene of density 0.97 g cm^{-3} and fitted directly over the probe adding 2.5 cm of HDPE shielding on all sides along the cylindrical axis. The shield extended 1 cm beyond the face of C0 and had a tapered slit extending the void slot widening from 10 mm to 20 mm at the outermost radius. Sketches of the collimator are shown in Fig. 3.11, the collimator is shown in red in Fig. 3.11b.

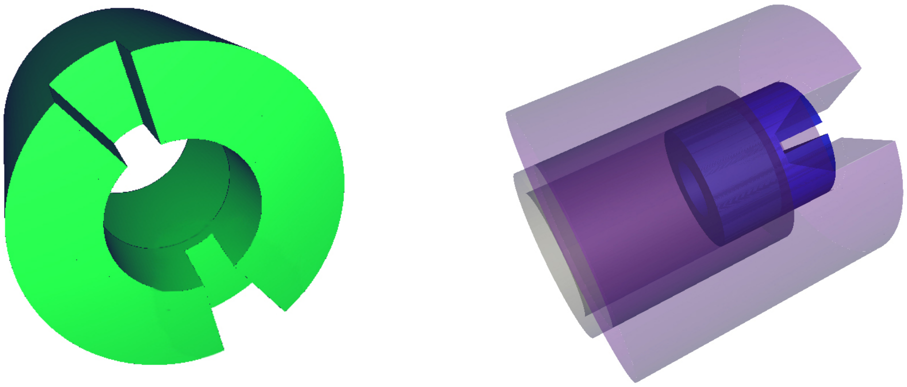

(a) C2 collimator front

(b) Model of collimator and steel housing

Figure 3.11 Diagrams of the polyethylene C2 collimator

Tungsten anti-collimator C3

The C3 collimator was developed after a further study (section 4.4) into neutron shielding and collimation which suggested that a tungsten anti-collimator configuration would be a superior approach in imaging applications, where the dose did not easily overwhelm the detector (up to a detection rate of 1 Mpps). This collimator was designed with input from Monte Carlo modelling; an arc of inner radius 50 mm, outer radius 100 mm and thickness 18 mm, made of tungsten alloy HE-395. The density of 18.1 g cm^{-3} provided 50 mm of tungsten shielding for 180° × 18 mm width. This design left the detector exposed to the majority of surrounding space which increased the count rate at the detector; a drop in signal results when a radiation source is oriented along the radial vector of the collimator. Using this drop, rather than a peak, resulted in a sharper, narrower sensitivity function (desirable for high-resolution imaging) and a higher sensitivity contrast (a general improvement to imaging capabilities). Sketches of the anti-collimator are shown in Fig. 3.12. The C3 collimator appears in green, the detector scintillation cell in yellow in Fig. 3.12a.

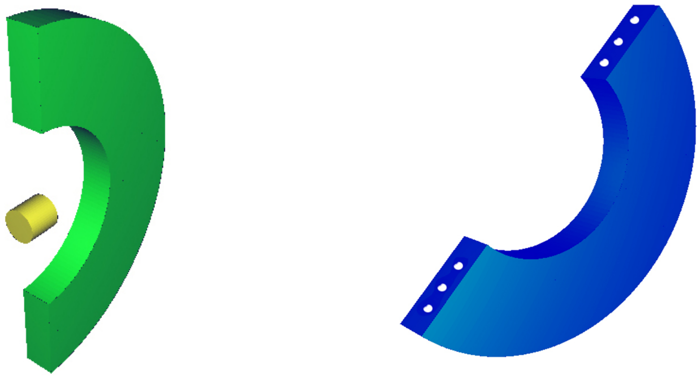

(a) Model of C3 collimator and scintillation cell

(b) C3 collimator with detail

Figure 3.12 Diagrams of the tungsten C3 anti-collimator

3.2.4 Probe configurations

Motor control was necessary to position the collimated detector and was provided in two different ways. The most commonly used apparatus was the NVisage mk I gamma-ray imaging prototype [115] shown in Fig. 3.13a, originally belonging to Createc Ltd. The chassis contained 2 stepper motors (Portescap 42M048C2U) responsible for rotating the collimator through the slot and pan angles. Motor control was via a custom-built motor control board which was interfaced with the PC using an Arduino microcontroller and RS-232 serial communications over a USB connection.

Motor control for the anti-collimator configuration used a compact telescope mount (Merlin TableTop GOTO mount) shown in Fig. 3.13b. Here, motor control was performed by the hand control provided with this apparatus (SynScan hand controller) and the associated electronics within the mount. This was interfaced directly with the PC using RS-232 serial communications over a USB connection. The laptop and analyser were also needed in this configuration but are not shown.

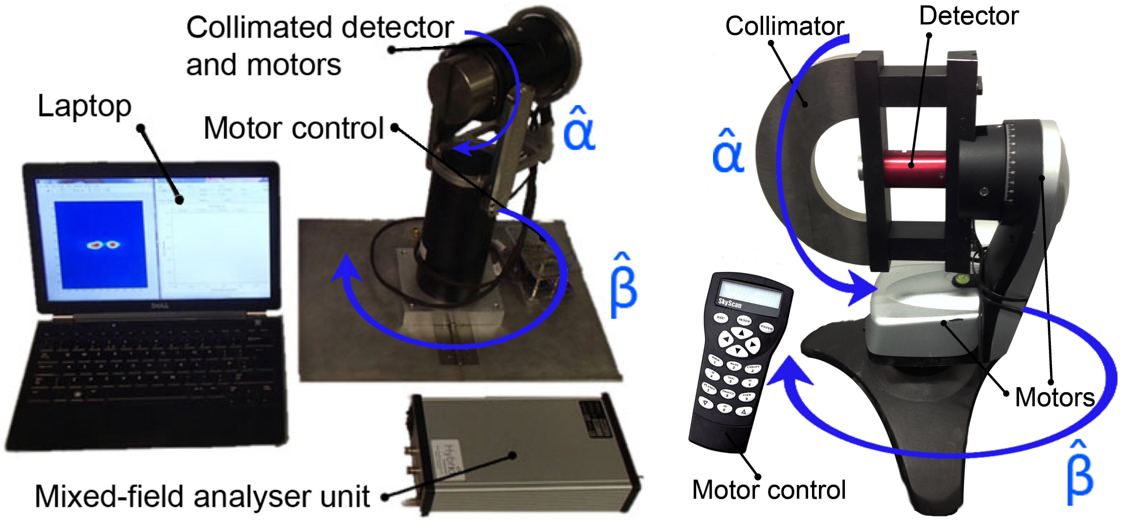

(a) Imaging system including laptop, MFA and probe with collimator C0. Collimators C1 and C2 were also used with this configuration by affixing to collimator C0.

(b) Anti-collimated imaging probe with collimator C3

Figure 3.13 Photographs of imaging system configurations. The blue arrows indicate the range of collimator rotation during the data acquisition routine.

3.2.5 Data acquisition configurations

The imaging systems were made up of interchangeable data acquisition components which led to several different configurations. The major constituents of the systems are summarised in Fig. 3.14 for the early systems using the Ethernet connection, and in Fig. 3.15 for the systems using the custom pulse counter board. The arrows show the flow of information in the system, ultimately resulting in data collection at the PC. In some early experiments the MFA passed discriminated data via Ethernet to the PC whereas in later approaches the TTL signals were routed to a counter instead.

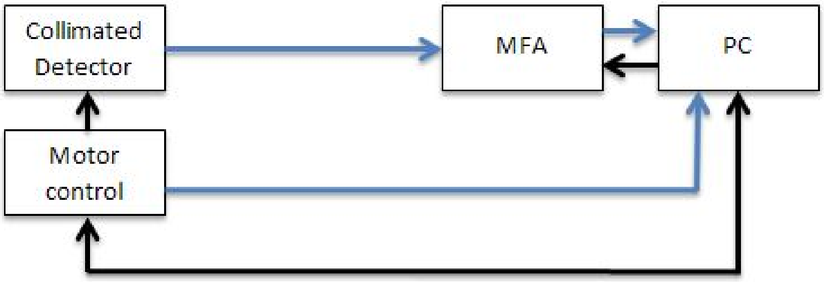

Figure 3.14 Control signals (black) and data flow (blue) in stand-off imaging system configurations using Ethernet connection with MFA.

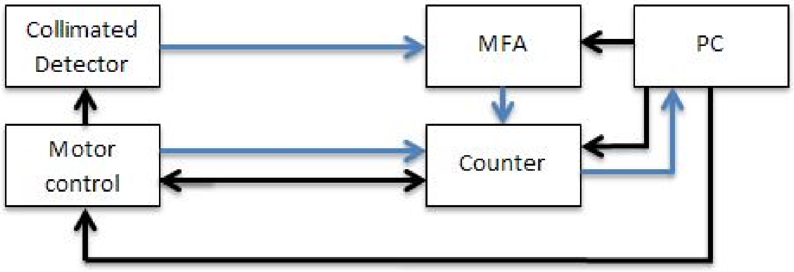

Figure 3.15 Control signals (black) and data flow (blue) in stand-off imaging system configurations using custom pulse counter.

Later experiments used a custom pulse counter to collect discriminated data at a faster rate before passing this to the PC. Here the collimator was also an important interchangeable component. A configuration for source tracking provided another alternative and is summarised in Fig. 3.16.

Motor control board

Experiments conducted with collimators C0, C1 and C2 used the modified NVisage mk I chassis for motor control. A custom board was built to interface the two stepper motors (Portescap 42M048C2U) with the data acquisition system using an Arduino microcontroller.

This item used 8 general purpose input/output (GPIO) channels of an Arduino Leonardo microcontroller linked with power MOSFET transistors (IRFD220PbF) to turn the motor (and hence the collimated detector) in single-step increments for precision measurement. Schottky diodes were used to prevent back-electromagnetic feedback. The motor was driven

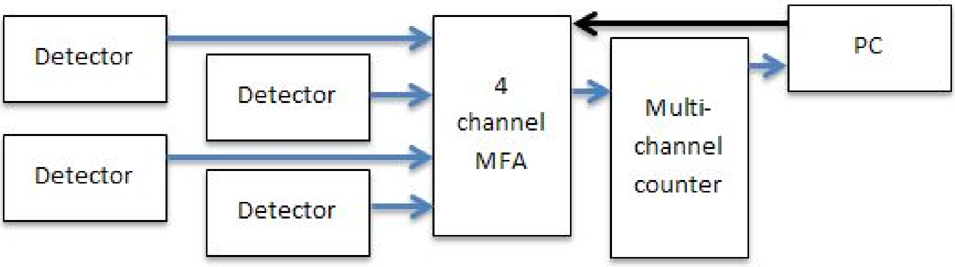

Figure 3.16 Control signals (black) and data flow (blue) in the source tracking system configuration.

to a stop after each 180° rotation to ensure no errors were introduced into the data acquisition routine as this method involved no feedback on the position. A differential line transceiver (ADM3491) was used to connect this board with the pulse counter board, via a 20 m Ethernet cable (necessary for one deployment), to ensure error-free data transmission using serial communications. The motor control board printed circuit board (PCB) layout is shown in appendix Fig. A.1.

Custom pulse counter

Early in the research, data were transferred from the MFA to the PC using the built in Ethernet communications. This method had the advantage of providing information on the pulses. The discrimination and peak amplitudes were retained and could be re-discriminated and used for spectroscopy for both neutrons and gamma rays. This data transfer rate was limited by the hardware and only approximately 35 counts per second could be transferred. Whilst this was adequate for some of the early work due to the low fields involved, other applications required far higher throughput when imaging higher-dose radiation fields. A custom pulse counter was designed to count output TTL pulses from the MFAs. This was used to directly count the number of discriminated neutron and gamma-ray detections from the detectors of the imaging system. This was interfaced with the motor control electronics and the PC, allowing measurement many orders of magnitude faster than previously possible and thus increasing the imaging range of the sensor in terms of dose.

Discriminated radiation events were outputted by the MFA via 50 ns logic pulses on the relevant neutron or gamma-ray outputs on each detector channel. These pulses were accumulated on 32-bit counters (SV74LV8154), one per channel. Each counter was controlled via GPIO ports and data were transferred to the Arduino micro-controller via a GPIO expander chip (MCP23017) using I2C communication. Communications between the Arduino and the laptop were performed with RS-232 serial communication over USB. Communications between the pulse-counter and motor control board were also performed with RS-232 serial communication between the respective microcontrollers on each board with the addition of a differential line transceiver. This interfacing allowed discriminated neutron and gamma-ray data to be collected digitally on the pulse counter board in synchronisation with probe movement controlled by the motor control board. The custom pulse counter PCB layout is shown in appendix Fig. A.2.

3.3 Imaging methods and associated analysis

All collimated imaging methods discussed in this section are demonstrated with the tungsten C0 collimator (with or without additional shielding). When performed with additional shields attached, e.g. C2, the two pieces were in static contact and rotate together. The orientation of the collimator is described by the “slot angle” and “pan angle”. The slot angle or angle $\hat{\alpha}$ is measured from the vertical, and describes the rotation of the collimator around its cylindrical axis. The pan angle or angle $\hat{\beta}$ is orthogonal to this as illustrated in Fig. 3.17 and is normally measured in the horizontal plane.

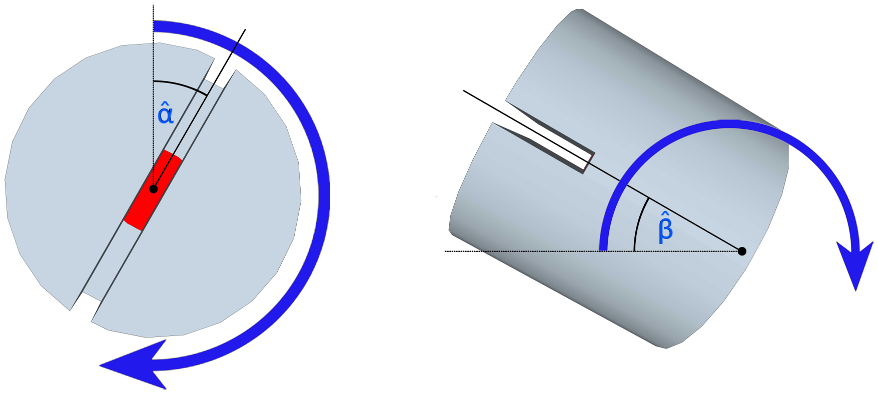

Figure 3.17 Definition of the slot and pan angles with respect to the collimator orientation. In this research angle $\hat{\alpha}$ was measured from the vertical (viewed in the vertical plane), angle $\hat{\beta}$ was measured in the horizontal plane (viewed in plan view). The blue arrows indicate the range of collimator rotation during the data acquisition routine.

3.3.1 Collimator quality

The collimators were assessed by two parameters: the signal-to-noise ratio and the FWHM of the signal. The former determines the sensitivity and performance of the system, whereas the latter is related to the resolution, e.g. the minimum resolvable distance between two point-like sources. These quantities are defined in Fig. 3.18 using a hypothetical scan of a collimated detector over a point-like source in azimuth angle.

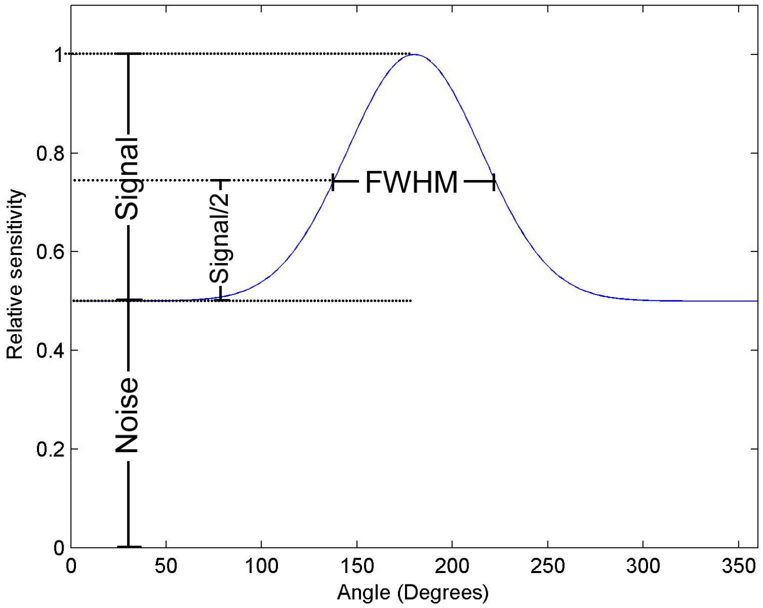

Figure 3.18 Hypothetical function produced by scanning a collimated detector over a point-like source and measuring detected events as a function of azimuth angle. The function is annotated with signal-to-noise ratio and FWHM as defined in this research.

3.3.2 Orthogonal-slot node imaging

This simplistic imaging method was used early on to demonstrate feasibility of imaging fast-neutron fields with a slot-shaped collimator. Used in an appropriate configuration, this gleaned enough information to determine if a more advanced method could be successfully applied with the system.

Once the apparatus was set up and the MFA calibrated for discrimination, the sources were placed in the environment, the approximate location of which was designated as the area of interest (shown within the black border in Fig. 3.19). Two scans of the probe through the pan ($\hat{\beta}$) angle for 2 orthogonal slot angles ($\hat{\alpha}$) were performed. For the first scan the slot angle was rotated to $\hat{\alpha} = 45°$ to the vertical and the collimated detector was scanned over the sources through the required pan angle range in $\hat{\beta}$ (typically 90° in 6° increments). Data were collected for time t_d (typically seconds) at each position, forming the data set S. The process was then repeated with the slot in an orthogonal position, i.e. at $\hat{\alpha} = 135°$ to form the data set S'.

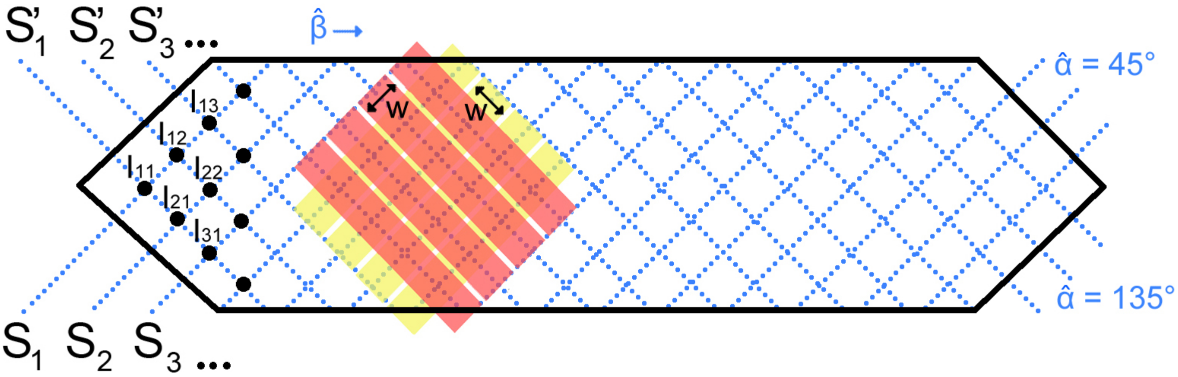

Figure 3.19 Illustration of the orthogonal-slot node imaging technique. Each line S demonstrates a projection of the slot sensitivity region in image space, with demonstrated width w, each point I illustrates a node at which the flux contribution is evaluated. The direction of increasing angle $\hat{\beta}$, and the orientation of the two measured $\hat{\alpha}$ angles are illustrated on the diagram in blue.

The data collection sequence is illustrated in Fig. 3.19. The blue dotted lines show the projections of the slot, at positions where data were acquired projected into angular space. For the given values of $\hat{\alpha}$ and $\hat{\beta}$ the dots represent the sensitivity region, i.e. the locations which, if containing radioactive material, will contribute most to the count rate at the detector. The angles were chosen to optimise the correspondence of the width (roughly rectangular width w) to the increments in angle $\hat{\beta}$; this ensured all the space was interrogated systematically during data collection. Sensitivity regions for some S_i values are shown in yellow, for S'_i values in orange. A value was then calculated at each image node I_{ij}, where S_i and S'_j overlap according to Eq. 3.1.

$$I_{ij} = \sqrt{S_i S'_j} \tag{3.1}$$

This calculation was performed separately for neutrons and gamma rays to produce discrete images for each radiation type. These image data were then plotted on to contour maps, where a lower limit threshold was set to differentiate real signals from fluctuations in background. Sources in the image area were identifiable as peaks in the image I values. Precise locations could be calculated from peak fitting S and S' for each discrete radiation data set using multiple peak fits to find the maxima S_{MAX} and S'_{MAX} and calculating the mean of the associated hotspot pairs. The angle $\hat{\beta}$, equivalent to θ in the spherical coordinate system, was measured from the same position for both S and S', therefore the source location for each source θ_{SOURCE} could be calculated from the initial measurement position where $\hat{\beta} = \theta = 0$, by taking the mean of the maxima in the two data sets according to Eq. 3.2.

$$\theta_{SOURCE} = \frac{S_{MAX} + S'_{MAX}}{2} \tag{3.2}$$

3.3.3 Imaging using algebraic reconstruction technique (ART)

This imaging method was used most commonly and was an advancement on the orthogonal-slot node imaging method, theoretically allowing more complex source distributions to be imaged with fewer pre-requisites on possible source layout relative to the imager and higher accuracy and precision.

Following set-up and calibration, the source distribution was arranged for the experiment. The imaging routine was automated and collected data from many slot and pan angles, typically thousands. The probe was oriented in the initial position at $\hat{\alpha} = 0°$ and $\hat{\beta} = 0°$. The collimator was then rotated systematically through the slot angle, typically in increments of 2°, pausing at each location for time t_d at each position (typically seconds) whilst the number of neutron and gamma-ray detections were counted. The number of recorded events for one radiation type at a given collimator orientation was $d_{\alpha\beta}$. This was then repeated for all the required values of $\hat{\beta}$ in similar increments. The range of $\hat{\alpha}$ was always 0° to 180° and the range of $\hat{\beta}$ was 0° to typically 140-180°. The data matrix D was a compilation of all $d_{\alpha\beta}$ values over the desired range of $\hat{\alpha}$ and $\hat{\beta}$ for each radiation type. D was produced for neutrons and gamma rays. The data collection process is illustrated in Fig. 3.20.

The experimentally acquired data matrix D was related to the sensitivity matrix M and the image I by Eq. 3.3. M was calculated from detailed models of the imaging probe using the Monte Carlo radiation transport code MCNP5 and subsequent geometric transformation (see section 3.4.1).

$$D = MI \tag{3.3}$$

The image I was calculated from M and D using an algebraic reconstruction technique (ART) [116], a single iteration of which is outlined in Eq. 3.4. Here d_j is the j^{th} row of D, m_j is the j^{th} row of M and κ_k is a relaxation parameter. Images were solved to convergence with 1° × 1° pixel resolution in all cases over a 180° × $\hat{\beta}$ (typically 180°) range in θ and ϕ, i.e. a half universe.

$$I^{k+1} = I^k + \kappa_k \frac{d_j - \langle m_j, I^k \rangle}{||m_j^2||} m_j \tag{3.4}$$

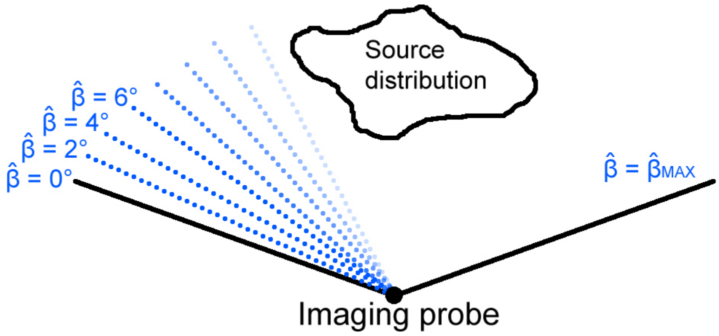

(a) Data collection

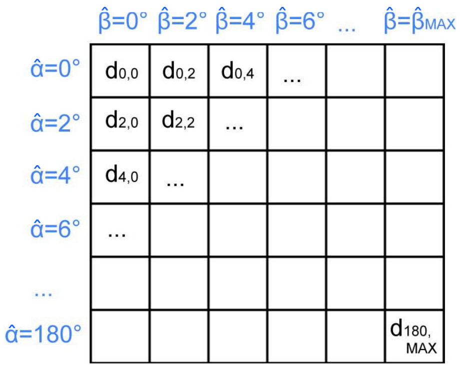

	$\hat{\beta}=0°$	$\hat{\beta}=2°$	$\hat{\beta}=4°$	$\hat{\beta}=6°$	...	$\hat{\beta}=\hat{\beta}_{MAX}$
$\hat{\alpha}=0°$	$d_{0,0}$	$d_{0,2}$	$d_{0,4}$	...		
$\hat{\alpha}=2°$	$d_{2,0}$	$d_{2,2}$	...			
$\hat{\alpha}=4°$	$d_{4,0}$	...				
$\hat{\alpha}=6°$	...					
...						
$\hat{\alpha}=180°$						$d_{180,MAX}$

(b) The data matrix D

Figure 3.20 Illustration of data collection for ART imaging. Figure a) demonstrates the rotation of the collimator through angle $\hat{\beta}$ in the horizontal plane (shown in plan view), for each angle $\hat{\beta}$, data were collected for multiple $\hat{\alpha}$ values. Figure b) illustrates the data matrix obtained in the imaging process where the rows correspond to the detected (neutron or gamma-ray) events at the $\hat{\alpha}$ angle and the columns correspond to the detected events at each $\hat{\beta}$ angle.

Images were reconstructed with best judgement with respect to the κ_k parameter. Those acquired with identical set-up parameters, which were reconstructed with identical sensitivity matrices, were solved with the same reconstruction parameters. Radiation source locations were found from identifying peaks in the image data which corresponded directly to angular locations in θ and ϕ.

ART imaging overview

1. **Imaging system configured with collimator and scan parameters**
2. **System matrix M calculated**
    2.1. Probe is characterised in MCNP to find sensitivity map of collimated detector m_{00} ($\hat{\alpha} = 0°$ and $\hat{\beta} = 0°$) [see section 3.4.1]

2.2. Sensitivity map m_{00} is put through geometric transforms for all $\hat{\alpha}$ and $\hat{\beta}$ angles in the imaging routine to form the system matrix M [see section 3.4.2]

3. **Probe assembled and deployed in radiation environment**

4. **Image data *D* collected with scanning routine**

    4.1. Collimator rotates to start position, $\hat{\alpha} = 0°$ (void slot in vertical) and $\hat{\beta} = 0°$ (first pan angle)

    4.2. Slot rotates sequentially through all $\hat{\alpha}$ angles between 0°and 180°with $\hat{\beta}$ unchanged, data is collected for time t_d at each position

    4.3. Collimator rotates to next $\hat{\beta}$ angle

    4.4. Steps 4.2 and 4.3 are repeated for all $\hat{\beta}$ angles, recorded data form data matrix D (for both neutrons and gamma rays)

5. **Image data solved to find image *I***

    5.1. ART algorithm in Eq. 3.4 used iteratively to solve for I until convergence

The ART imaging process is shown in graphical representation in Fig. 3.21.

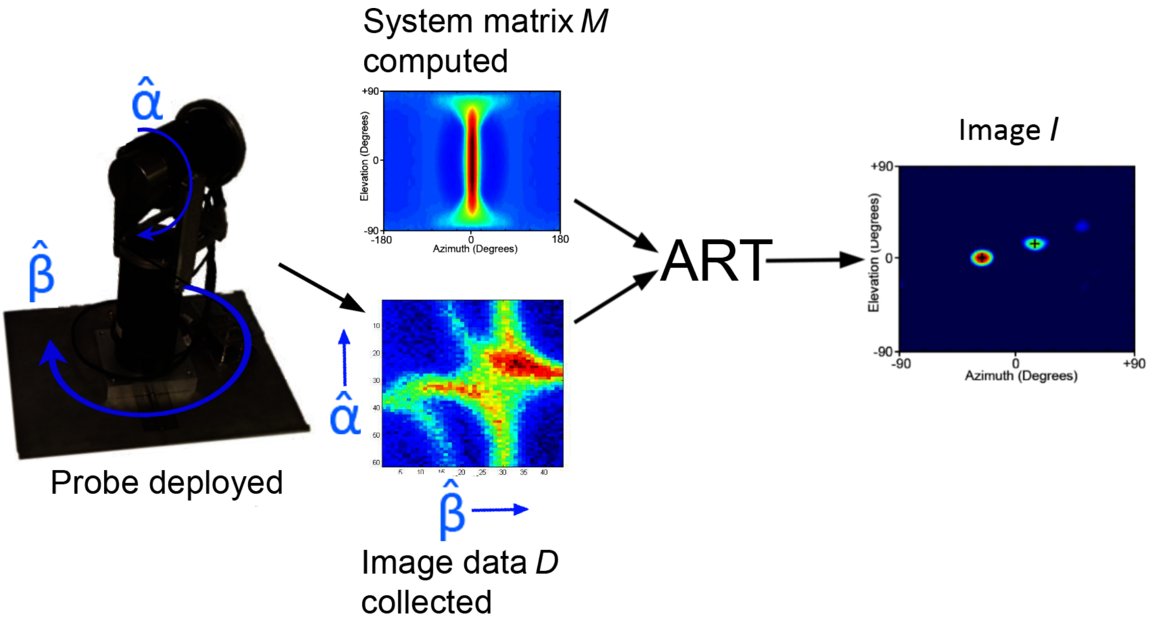

Figure 3.21 Graphical representation of ART imaging process.

3.3.4 Optical image overlay

Where the situation permitted, panoramic images were produced by stitching multiple images from a digital camera. These were performed from the same image origin and in the same coordinate system as the output radiation image. These images could therefore be used for direct comparison with the obtained radiation images. This comparison was best performed by overlaying the radiation image onto the optical images using reference objects in the optical image to aid the alignment, e.g. angular width of object or the corner of a room located at 0° slot angle. The overlaid image allows radiation sources to be attributed to objects in the images, rather than just spherical coordinates, to aid in data interpretation.

3.3.5 Real-time radiation source tracking with uncollimated multi-detector system

This method was used to determine the location of a single radiation point source in three-dimensional space in a frame local to the system origin. Four detectors were used to continuously record count rates and an algorithm calculated the most likely position of the source, based upon the ratio of the counts at each detector per unit time. This was done in real-time.

The detectors (1, 2, 3 and 4) were arranged to maximise the dynamic range in count rates at each detector when a radiation source was placed at position vector $\hat{p}$ within the vicinity of the system. Detector 1 was positioned at some origin $\hat{o}$. The remaining detectors (2, 3 and 4) were placed at some displacement l, at $\hat{o} + l\,\hat{\mathbf{x}}$, $\hat{o} + l\,\hat{\mathbf{y}}$ and $\hat{o} + l\,\hat{\mathbf{z}}$ as shown in Fig. 3.22. The scintillation cell is shown in black, and the PMT is shown in grey. The radiation source $\hat{p}$ is shown in red.

In this geometric configuration, the detector response ratios across all detectors were characteristic of the location of the radiation source at $\hat{p}$ as illustrated in Table 3.1 where the detector response ratios R were calculated using Eq. 3.5 as a function of distance. This was performed for all detectors (1, 2, 3 and 4) with detector i at location $\hat{d_i}$ where $d^2(\hat{d_i}, \hat{p})$ is the squared standard Euclidean distance between position vectors $\hat{d_i}$ and $\hat{p}$, i.e. the distance squared between the source and detector i. This calculation is an approximation used only for illustrative purposes.

$$R_i = \frac{1}{d^2(\hat{d_i},\ \hat{p})} \tag{3.5}$$

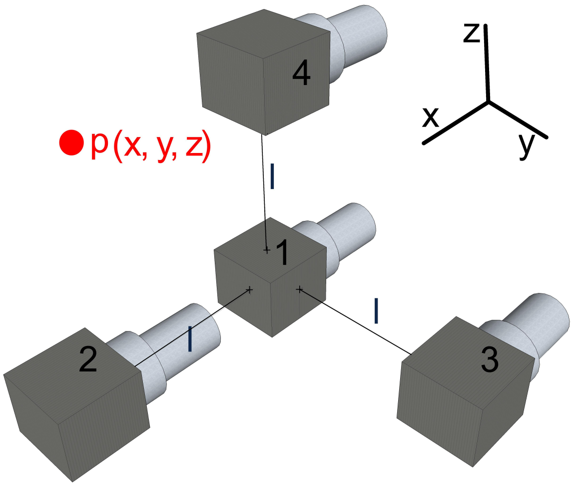

Figure 3.22 Geometric layout of detectors (liquid scintillation cells in dark grey, PMTs in light grey) in real-time radiation tracking system with z axis vertical and x-y plane in horizontal. Point $\hat{p}$ represents a point source location.

The detection rates at each detector were ascribed to a four-element matrix R defined as $R = [R_1,\ R_2,\ R_3,\ R_4]$ which were normalised such that $R_1 + R_2 + R_3 + R_4 = 1$. As illustrated the detector response ratios are a function of source position, i.e. $R = f(\hat{p})$.

Table 3.1 Illustration of unique detector response ratios for various sample coordinates for real-time radiation source tracking system.

	Detector response ratios R			
Source position $\hat{p}$	R_1	R_2	R_3	R_4
$\hat{o} + \frac{1}{2}\,l\,(-2\hat{\mathbf{x}} - 2\hat{\mathbf{y}} - 2\hat{\mathbf{z}})$	0.3983	0.2058	0.1947	0.2012
$\hat{o} + \frac{1}{2}\,l\,(-2\hat{\mathbf{x}} - 2\hat{\mathbf{y}} + \hat{\mathbf{z}})$	0.3489	0.1515	0.1507	0.3489
$\hat{o} + \frac{1}{2}\,l\,(-2\hat{\mathbf{x}} + \hat{\mathbf{y}} - 2\hat{\mathbf{z}})$	0.3480	0.1561	0.3480	0.1479
$\hat{o} + \frac{1}{2}\,l\,(\hat{\mathbf{x}} - 2\hat{\mathbf{y}} - 2\hat{\mathbf{z}})$	0.3458	0.3458	0.1532	0.1552
$\hat{o} + \frac{1}{2}\,l\,(\hat{\mathbf{x}} + \hat{\mathbf{y}} + \hat{\mathbf{z}})$	0.2500	0.2500	0.2500	0.2500

A method was developed to calculate the current position of the source $\hat{p}$ based on R, i.e. to solve for $\hat{p}$ in $R = f(\hat{p})$ from measurement of the detection ratios. First $R(x,\ y,\ z)$, the detector response ratios as a function of source location, were calculated using MCNP (see section 3.4.3) over the desired range of x, y, z (typically 61 × 61 × 61 positions spanning 120 cm × 120 cm × 120 cm in x, y and z). These values were calculated and stored prior to the tracking process.

To calibrate the system a gamma-ray radiation source was placed at location $\hat{p} = \hat{o} + \frac{1}{2}\,l$ $(\hat{\mathbf{x}} + \hat{\mathbf{y}} + \hat{\mathbf{z}})$ and the detector gains were adjusted such that the energy spectra appeared identical in terms of distribution and cut-off. The source was then removed and the background events at each detector were accumulated for an interval t_b. These values were used to calculate the background rate for each detector defining the background rate, $B = [B_1, B_2, B_3, B_4]$.

The number of detections at each detector were recorded consistently over 1-second intervals providing $R^r = [R^r_1, R^r_2, R^r_3, R^r_4]$. These were adjusted by subtracting the background according to Eq. 3.6 with a non-negativity constraint.

$$R^*_i = R^r_i - B_i \tag{3.6}$$

These values were normalised such that $R^*_a + R^*_b + R^*_c + R^*_d = 1$ and were assembled in the recorded count ratios four-element matrix R^* defined as $R^* = [R^*_a, R^*_b, R^*_c, R^*_d]$. With the background correction the corrected recorded count ratios R^* and the detector response ratios R could be compared. A χ^2_p value for each hypothetical source position $\hat{p}$ was calculated comparing the corrected recorded count ratios R^* and the MCNP-calculated detector response ratios R(x, y, z) over the required range of x, y, z using Eq. 3.7.

$$\chi^2_p(x,\ y,\ z) = \sum_{i=1}^{i=4} \frac{(R^*_i - R_i(x,\ y,\ z))^2}{R_i(x,\ y,\ z)} \tag{3.7}$$

The lowest χ^2_p(x, y, z) value was then identified which indicated the x, y, z coordinates corresponding to most likely position of the source $\hat{p}$.

3.3.6 Source identification with neutron spectroscopy

Following an imaging experiment which located radiation sources, this technique allowed the identification of neutron-emitting materials using spectroscopy. This method uses χ^2 analysis to compare pre-recorded neutron pulse-height spectra P with neutron pulse-height spectra obtained using the imaging probe P^*.

The imaging routine was performed, solving the image; the radiation sources were then identified in the image. An example is illustrated in Fig. 3.23, showing two target sources T_a and T_b identified in a 4π (360° × 180°) image. The probe slot angle was set to $\hat{\alpha} = 0°$ and the pan angle was set to each target location in sequence, $\hat{\beta} = \theta_a, \theta_b$ such that the sensitivity region was centred upon the source location. In each position the pulse-height spectrum was recorded for time t_s.

The image pulse-height spectra P^*_a and P^*_b (belonging to T_a and T_b respectively) were then compared against pre-recorded pulse-height spectra from source-types 1 and 2, P_1 and P_2, and any other source-type which may be a candidate P_3 ... P_n (all these pulse-height spectra were recorded in isolation from other contributions, i.e. were “pure”). A collimator provided a non-uniform spatial sensitivity, however even when the sensitivity region was not aligned

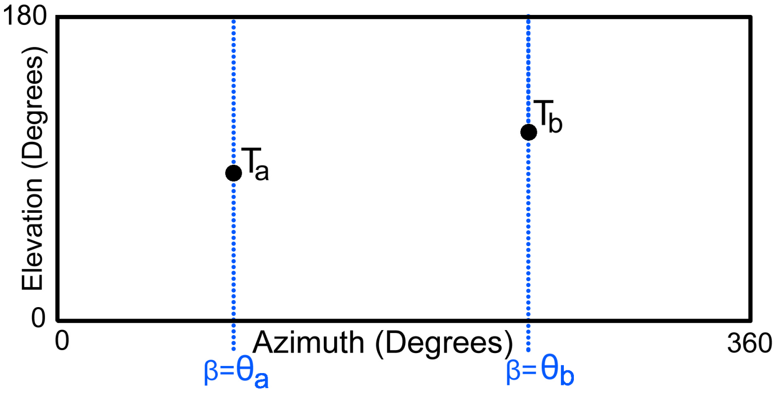

Figure 3.23 Illustration of source identification method used in combination with imaging techniques. T_a and T_b represent two “target” sources to which the imager sensitivity region (blue dotted line) is aligned with angle $\hat{\alpha} = 0$ and $\hat{\beta} = \theta_a$, θ_b; the azimuth angles of each target source respectively.

with a source many neutrons still passed through the collimator and were detected. For this reason the image pulse-height spectra were a weighted sum of the pre-recorded pulse-height spectra present. Test spectra $P'_a(w_a)$ and $P'_b(w_b)$ comprising source-types 1 and 2 (these test spectra could be expanded to test for additional source types) were created with different weightings as illustrated in Eq. 3.8 and Eq. 3.9.

$$P'_a = w_a P_1 + (1 - w_a) P_2 \tag{3.8}$$

$$P'_b = w_b P_1 + (1 - w_b) P_2 \tag{3.9}$$

These test spectra, for many different weightings, were then compared with the image pulse-height spectra to find the weightings w_a and w_b for each target using Eq. 3.10.

$$\chi^2(w) = \frac{(P^* - P'(w))^2}{P'(w)} \tag{3.10}$$

The lowest value of χ^2 for each target indicated the best match and therefore the most likely source-types present in the image. The weighting in each case was indicative of which target source comprised which source-type, e.g. if P^*_a contains P_1 and P_2 with the weighting $w_a = 0.7$, the pulse-height spectra from target a contains the pre-recorded pulse-height spectra from neutron source-types 1 and 2, with a majority weighting of spectrum 1 (70%). If the sources (T_a and T_b) were the same activity it was likely that this source was source-type 1.

An example of a closest match P^* and P' is shown in Fig. 3.24 illustrating how this method provides a reasonable solution.

$$P_a = w_a P_a^* + (1 - w_a) P_b^* \tag{3.11}$$

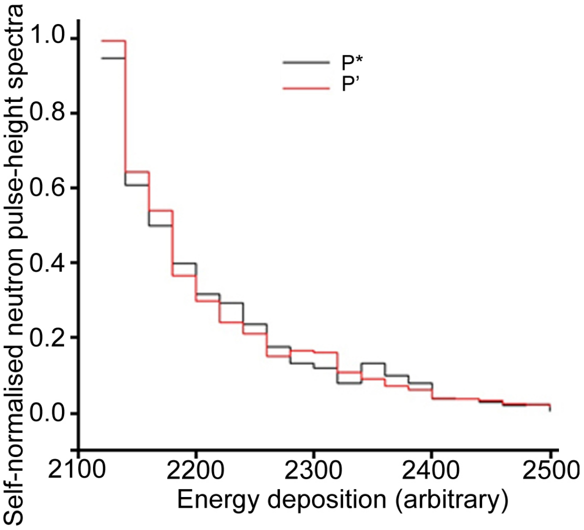

Figure 3.24 Plot of lowest χ^2 solution test spectrum P' with spectrum P^* measured from the imaging device illustrating that a reasonable match is obtained.

3.4 Monte Carlo modelling methods

In the context of any significant radiation shielding, any complexity in geometry means that hand calculations are out of the question for good accuracy. The Monte Carlo code MCNP (versions MCNP5 and MCNPX) [117] was used extensively in this research to provide supporting data. Monte Carlo codes use random number generators to simulate emission, scattering and other interactions of radiation particles according to experimentally derived distributions for each particular effect. The path of a single particle is calculated based upon these probabilities, which simulate the real-world interactions which could be experienced. These family of codes estimate local solutions to radiation fields using pseudo-random statistics and their subsequent effects with intrinsic statistical error.

3.4.1 Collimator characterisation

The Monte Carlo code MCNP5 was used to assess each collimator by the provision of a 2D sensitivity map, mapping the sensitivity of the collimated detector to radiation in the surrounding 4π space. Each collimator was characterised in orientation $\hat{\alpha} = 0$, $\hat{\beta} = 0$. This sensitivity map forms the initial element m_{00} of the system matrix M, composed of elements $m_{\alpha\beta}$. The remainder of M for all angles of $\hat{\alpha}$ and $\hat{\beta}$ used in data collection was obtained through matrix transformations of m_{00} and was required to calculate the image solution I (see section 3.4.2).

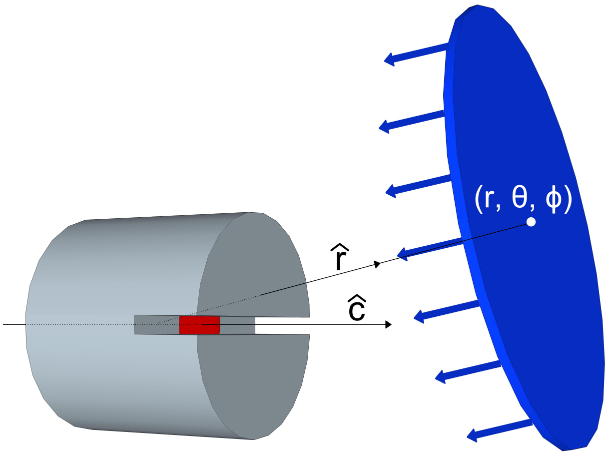

Figure 3.25 Illustration of C0 collimator characterisation (tungsten in grey, detector in red) using a plane source of mono-directional incident radiation (blue) at spherical polar coordinates (r, θ, ϕ) at vector $\hat{r}$ measured from the geometric detector centre in relation to the cylindrical axis of the collimator $\hat{c}$.

A visualisation of the collimator sensitivity assessment is shown in Fig. 3.25, showing the C0 collimator. The collimator C, under investigation, was modelled in MCNP5 in the orientation $\hat{\alpha} = 0$, $\hat{\beta} = 0$, including the liquid scintillation cell in the detector. A plane source was modelled at a constant distance r from the pivot point of the collimator which created a uniform beam of source particles emitted parallel to the vector $-\hat{\mathbf{r}}$ within the sampling radius, connecting the centre of the plane source and the pivot point of the collimator. The radius of the plane source was large enough such that all parts of the collimator were irradiated in each simulation. This arrangement mimics a radiation point source at infinity with greater computational efficiency. The angles θ (azimuth) and ϕ (elevation) from $\hat{\mathbf{r}}$ were measured from the cylindrical axis of the collimator $\hat{\mathbf{c}}$, with the plane $\theta = 0$ passing through the void slot.

The radiations at the plane source were given the appropriate energy spectrum E and a modified F4 tally, measuring the average flux in a cell, was used to determine the detected flux at the detector in each simulation file. The simulation was repeated for all integer degree values of θ and ϕ over a full universe; the recorded flux at each position of the source for a given collimator and interrogative energy spectrum formed the sensitivity map for that collimator and energy spectrum $m_{00}(C,E)$. The gamma-ray sensitivity map for $m_{00}(C2,^{252}Cf)$, i.e. the sensitivity of collimator $C2$ to ^{252}Cf gamma rays is shown in Fig. 3.26.

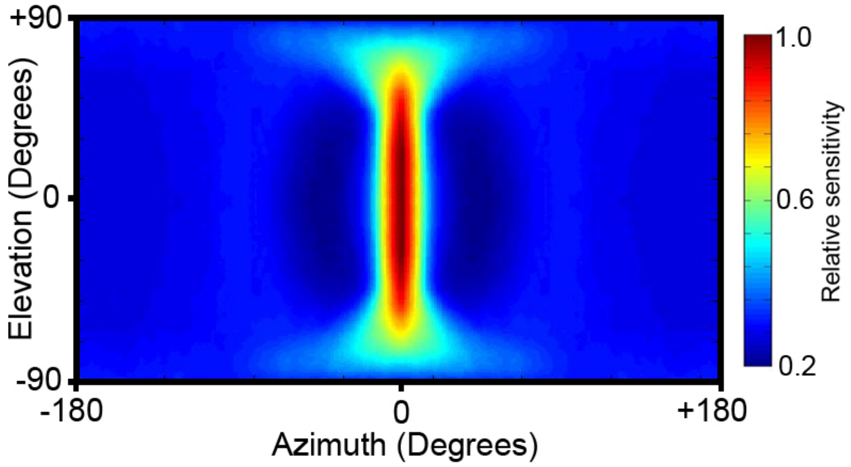

Figure 3.26 The gamma-ray sensitivity map m_{00} in 4π resulting from MCNP characterisation of collimator C2.

3.4.2 Geometric transformation

The system matrix M comprised the sensitivity maps of all positions of the collimator used in the data collection routine where the collimator was rotated through angles $\hat{\alpha}$ and $\hat{\beta}$. These were calculated from transformations of the initial element m_{00}, which was mapped to a sphere in Cartesian coordinates and was then rotated using the rotation matrix shown in Eq. 3.12 through the rotation angles $\hat{\alpha}$ before conversion back to spherical polar coordinates to produce the set of $m_{\alpha 0}$ rotations. Transformations in $\hat{\beta}$ were performed by rotation of this matrix through the angle θ, which is the same as angle $\hat{\beta}$, by simple translation of the matrix elements. These steps were performed for the full set of rotations to produce the full set of system matrix elements. The full system matrix *M(C,E)* was then compiled for all positions of the collimator used in data collection for the given collimator C and appropriate energy spectrum E.

$$m_{\alpha 0} = \hat{R}_{\alpha} m_{00} \tag{3.12}$$

$$\hat{R}_\alpha = \begin{bmatrix} 1 & 0 & 0 \\ 0 & cos(\hat{\alpha}) & -sin(\hat{\alpha}) \\ 0 & sin(\hat{\alpha}) & cos(\hat{\alpha}) \end{bmatrix} \tag{3.13}$$

This process is illustrated with an example using the gamma-ray response of the C2 collimator to a ^{252}Cf source. The sensitivity map m_{00} is shown in Fig. 3.27a, equivalent to the sensitivity map obtained from simulations. The map was then transformed as described through slot angle in the remainder of Fig. 3.27, and through pan angle in Fig. 3.28. These results form some of the components of the system matrix M, the full system matrix which contained all combined rotations of $\hat{\alpha}$ and $\hat{\beta}$ over each appropriate range (all the rotations used in data acquisition). This typically contained thousands of elements. The system matrix was used with the ART algorithm to solve image data.

A video of the system matrix transformations is given in Supplementary Video 1: see appendix A.1 which demonstrates the sensitivity of the detector to 2D space during a data collection routine.

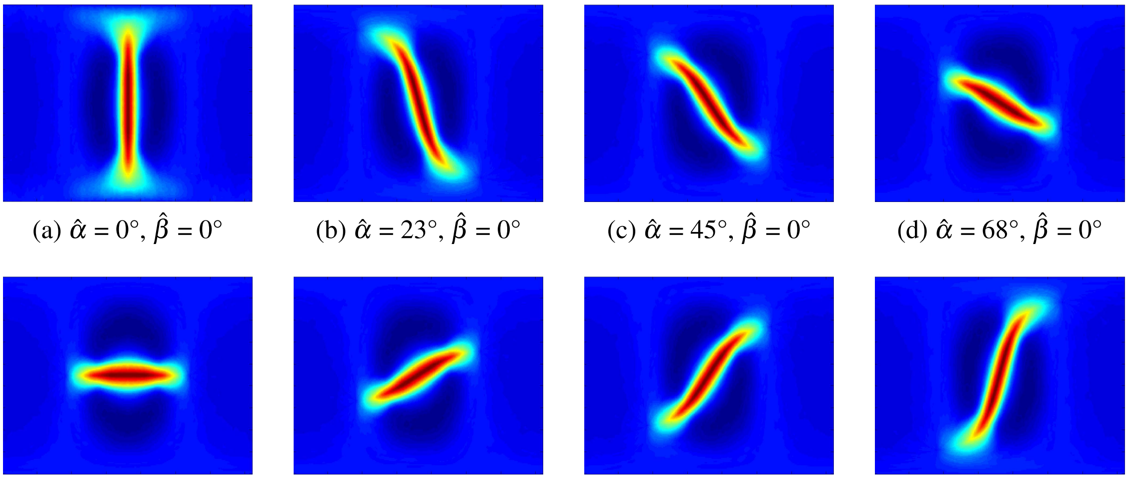

(a) $\hat{\alpha}$ = 0°, $\hat{\beta}$ = 0°
(b) $\hat{\alpha}$ = 23°, $\hat{\beta}$ = 0°
(c) $\hat{\alpha}$ = 45°, $\hat{\beta}$ = 0°
(d) $\hat{\alpha}$ = 68°, $\hat{\beta}$ = 0°
(e) $\hat{\alpha}$ = 90°, $\hat{\beta}$ = 0°
(f) $\hat{\alpha}$ = 113°, $\hat{\beta}$ = 0°
(g) $\hat{\alpha}$ = 135°, $\hat{\beta}$ = 0°
(h) $\hat{\alpha}$ = 168°, $\hat{\beta}$ = 0°

Figure 3.27 Plots of the gamma-ray system matrix for C2 after translation through slot angle $\hat{\alpha}$.

3.4.3 Three-dimensional detector characterisation

The detectors used in this system were characterised using MCNP to create a response matrix to a point source at each position in surrounding 3D space, i.e. to find the detector response ratios $R(x,\ y,\ z)$. The count rate ratio of all the detectors is defined as $R = [R_1, R_2, R_3, R_4]$

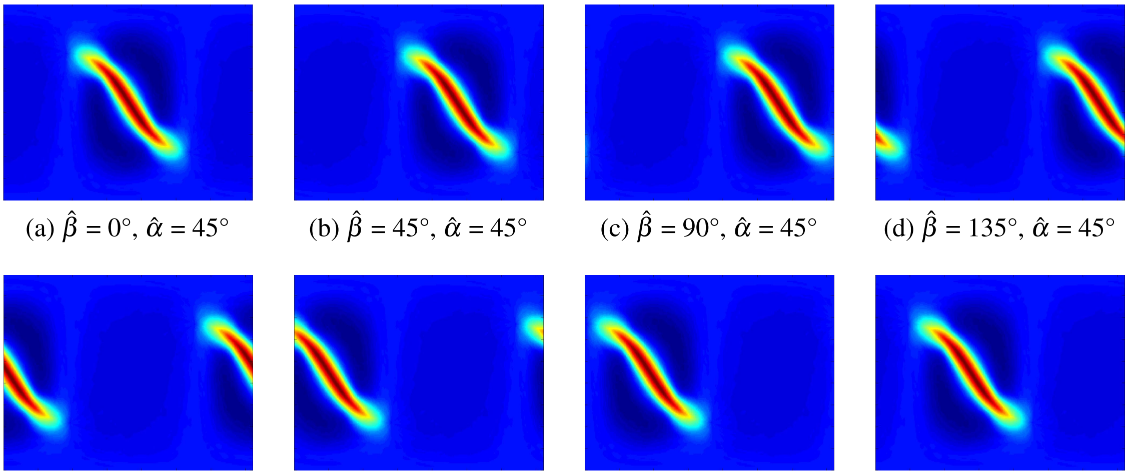

(a) $\hat{\beta} = 0°$, $\hat{\alpha} = 45°$
(b) $\hat{\beta} = 45°$, $\hat{\alpha} = 45°$
(c) $\hat{\beta} = 90°$, $\hat{\alpha} = 45°$
(d) $\hat{\beta} = 135°$, $\hat{\alpha} = 45°$
(e) $\hat{\beta} = 180°$, $\hat{\alpha} = 45°$
(f) $\hat{\beta} = 225°$, $\hat{\alpha} = 45°$
(g) $\hat{\beta} = 270°$, $\hat{\alpha} = 45°$
(h) $\hat{\beta} = 315°$, $\hat{\alpha} = 45°$

Figure 3.28 Plots of the gamma-ray system matrix for C2 after translation through pan angle $\hat{\beta}$.

where $R_1 + R_2 + R_3 + R_4 = 1$. The detector was modelled and a radiation point source was positioned at coordinates x, y, z. The number of detections were tallied at each detector and normalised to find R(x, y, z) for that position. This process was then repeated for all required values of x, y, z.

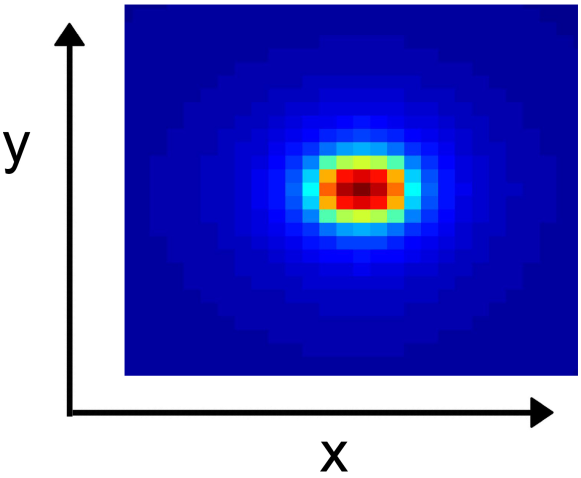

Figure 3.29 Detector characterisation in x-y plane through geometric centre in z of 10 cm cubic EJ-309 detector. The colour scale from blue to red represents increasing counts at the detector as a function of source position in x and y.

Fig. 3.29 shows the values of R_1(x, y), the detections at detector 1 as a fraction of the total detections, through the z-plane containing detector 1. The detector is located centrally within the blue area. When the source is close to detector 1 ($\mathbf{p} \approx \mathbf{o}$), the highest value of R_1

is observed. When the distance between the source and detector 1 is large (and smaller for other detectors), R_1 has a smaller value.

3.4.4 Pin-hole images

Simulated images produced with the MCNP5 pin-hole flux camera function were provided alongside experiments as a comparison to real solved images. For an image simulation the laboratory environment would be modelled, including the radiation source and the simulated camera. The pin-hole images were produced using a perfect pin-hole, comparable with some real apparatus, though the level of collimation exceeds any real physical system. The pin-hole tally principle is illustrated in Fig. 3.30. Any particles reaching the grid which have passed directly through the pin-hole were tallied. Detections in each bin were then totalled to produce the simulated image where each bin corresponds to one pixel. The geometry was set with bins in elevation and azimuth to achieve angular 101 × 101 unit square degree bins, large enough to show all relevant image objects.

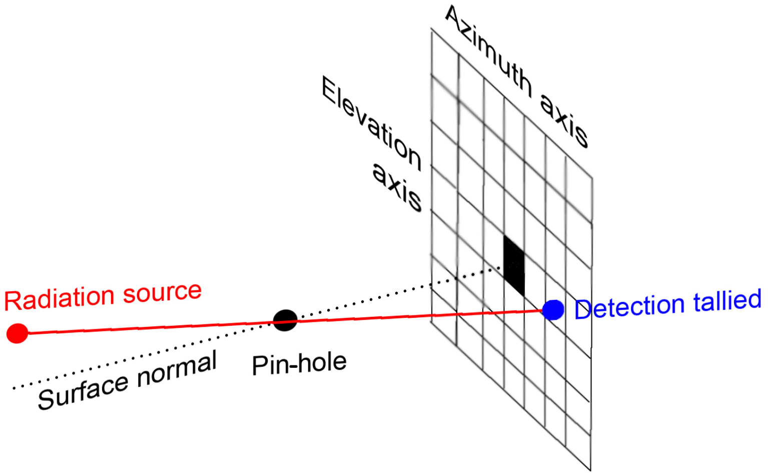

Figure 3.30 Illustration of the simulated pin-hole camera function. Radiation from a source passing through the pinhole is projected onto an image grid and if tallied (detected) binned in elevation and azimuth.

These calculations often had a huge flux reading, relative to other values, at the location of the source. These images corresponded to those produced by an imager with perfect resolution. When viewed in a colour plot, the high-value pixel obscured all other values as they were too small to appear on the same plot. To account for this a low pass filter with Gaussian function was applied to these images to allow representation of smaller flux contributions which would appear in a real image. The built-in MATLAB filter was used with the following code:

```
fspecial('gaussian', hsize, sigma)
```

with *hsize* = [20 20] (acting over a 20×20 pixel area) and *sigma* = 2.3 (pixel spread). These values were chosen based on the maximum resolution of the relevant radiation images.

The application of this filter is illustrated in Fig. 3.31 using a simulated image for the ^{252}Cf survey experiment (see section 5.3.4). With regard to the simulated image, the total contributions are shown in Fig. 3.31a and the remaining contributions following deletion of the peak value are shown in Fig. 3.31b. Fig. 3.31c shows the full data set with the Gaussian filter applied as a combination of contributions from Fig. 3.31a and Fig. 3.31b which would more closely represent a true image and allows smaller contributions to be represented with consistency through different image simulations. Fig. 3.31d shows the result of the Gaussian filter applied to a point source of value 1 at (51, 51).

3.4.5 Particle tracking

MCNP Visual Editor was used to track the interactions of radiation particles within complex geometries, such as collimators and in civil structures. Fig. 3.32 illustrates the interactions of a beam of neutrons with a 10 cm diameter spherical tungsten collimator with 6 mm slot void. The beam is incident from the right-hand side; circles show the first interaction of a single neutron history which occur in the air or in the tungsten. Neutrons then scatter internally in the collimator (not visible). Some are seen to escape before interacting finally with atmosphere (visible).

3.5 Radiation sources and environments

3.5.1 75 MBq ^{252}Cf source and water tank

A 75 MBq ^{252}Cf source at Lancaster University was used extensively during the research. This source is a neutron and gamma-ray emitter, contained within a 93 × 93 × 90 cm light-water tank used to shield the radiation when not in use. The water tank was surrounded by 33 mm of steel on all sides to provide further features for safety and anti-theft.

The source was located by default centrally in the horizontal plane in the water tank, 35 cm above the concrete floor. In this position the source was referred to as "stored" where it was heavily shielded (neutron dose $<1\mu$Sv/h at tank edge on all sides). A pneumatic system moved the source horizontally to the tank edge, allowing a large number of neutrons (of the

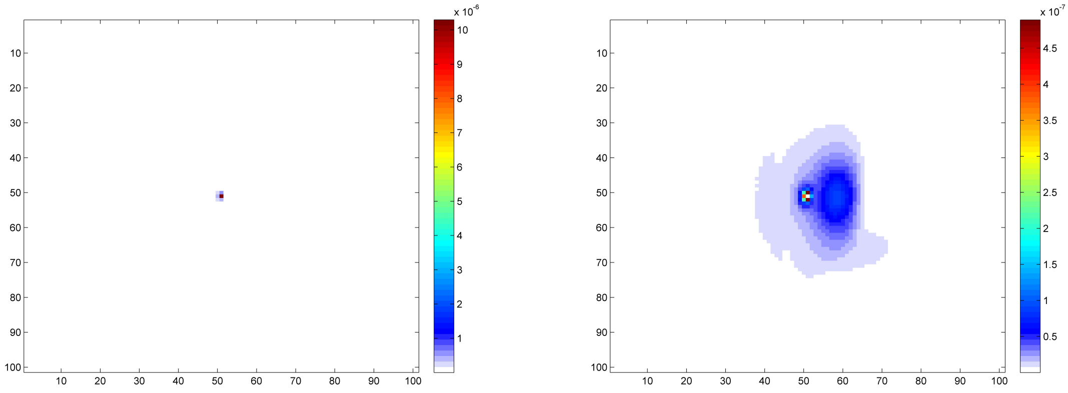

(a) All contributions

(b) Peak contribution deleted

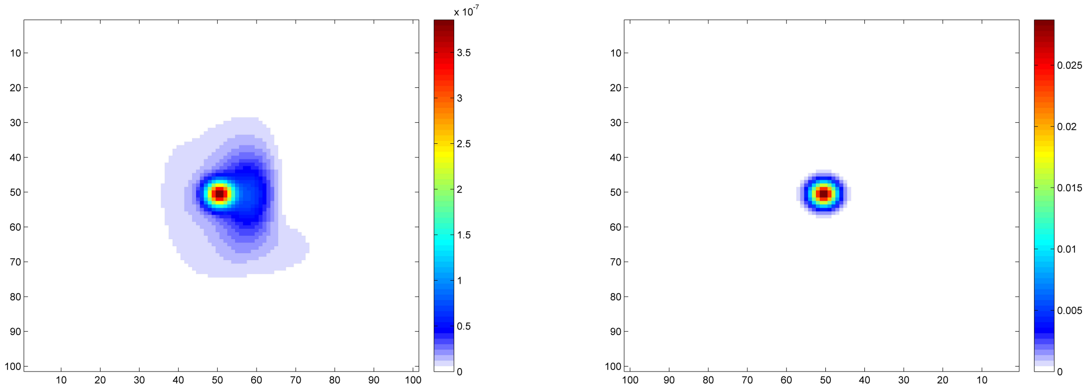

(c) All contributions with Gaussian lowpass filter

(d) Point source value 1 at (51,51) with Gaussian lowpass filter

Figure 3.31 Illustration of Gaussian filter on MCNP simulated images. a) - c) depict the same data: a pin-hole camera neutron image of a ^{252}Cf source stored in water tank. a) illustrates that little information is gleaned from the plot without Gaussian modification other than a small number of high-value pixels, i.e. the peak of radiation origin. It can be seen in b) that the radiation field has more complexity which was not visible in a) due to the colour axis being set over the range including the peaks values. Image c) shows the data with an applied Gaussian filter demonstrating that the complexity of the field, including the peak can be illustrated simultaneously in a way which emulates the non-zero point spread function of a real imaging device. d) shows a plot of a ^{252}Cf point source with no surrounding environment to illustrate visually the effect of the Gaussian point spread function.

order 10^7 neutrons s^{-1}) to escape the tank; this configuration was referred to as “exposed”. A photograph of the source and pneumatic system within the water tank is shown in Fig. 3.33a, and the remaining lab environment in Fig. 3.33b. The surrounding civil structure of concrete

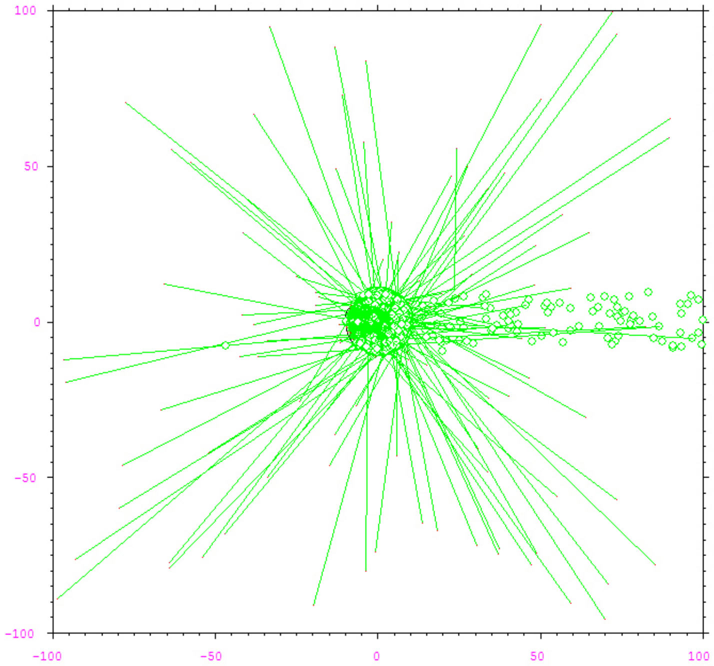

Figure 3.32 Neutron trajectories (green) resulting from scattering of a neutron beam incident from right-hand side on a spherical tungsten slot collimator in air atmosphere.

and concrete block shields radiation to the outside world. Modelling of the environment is described in section 4.3.3. Further information on the source can be found in Appendix B.3.

(a) Inside the storage tank. Pneumatic system visible which moves radiation source to outer edge of tank

(b) Laboratory environment surrounding radiation source and storage tank

Figure 3.33 Photographs of the ^{252}Cf source, steel and water storage tank and laboratory environment.

3.5.2 TRIGA mk II test reactor

The TRIGA mk II training reactor at the Atominstitut, Vienna University of Technology, Austria is a small-scale, pool-type reactor used for **TR**aining, **R**esearch and **I**sotope production. The reactor was manufactured by **G**eneral **A**tomic and is one of 70 worldwide. The core has an active fuel volume of 70 litres and contains 76 fuel elements of uranium-zirconium-hydride (UZrH) fuel (plus reflectors). It is loaded with 3 kg of uranium-235 and has a maximum steady thermal power output of 250 kW corresponding to a peak fast-neutron flux of 4×10^{12} $\mathrm{cm}^{-2}\mathrm{s}^{-1}$. The core is surrounded by a graphite moderator (which slows neutrons to facilitate the fission process) and a light water coolant. The TRIGA reactor is heavily shielded by water and heavy concrete on all sides with exception of an irradiation facility which provides a high flux of neutrons for activation of samples. The energy spectrum of the neutrons can be adjusted by the selective use of a water collimator and a cadmium shield. A schematic of the reactor is shown in Fig. 3.34. Modelling of the TRIGA environment is described in section 4.3. More information relating to TRIGA reactors can be found in [118].

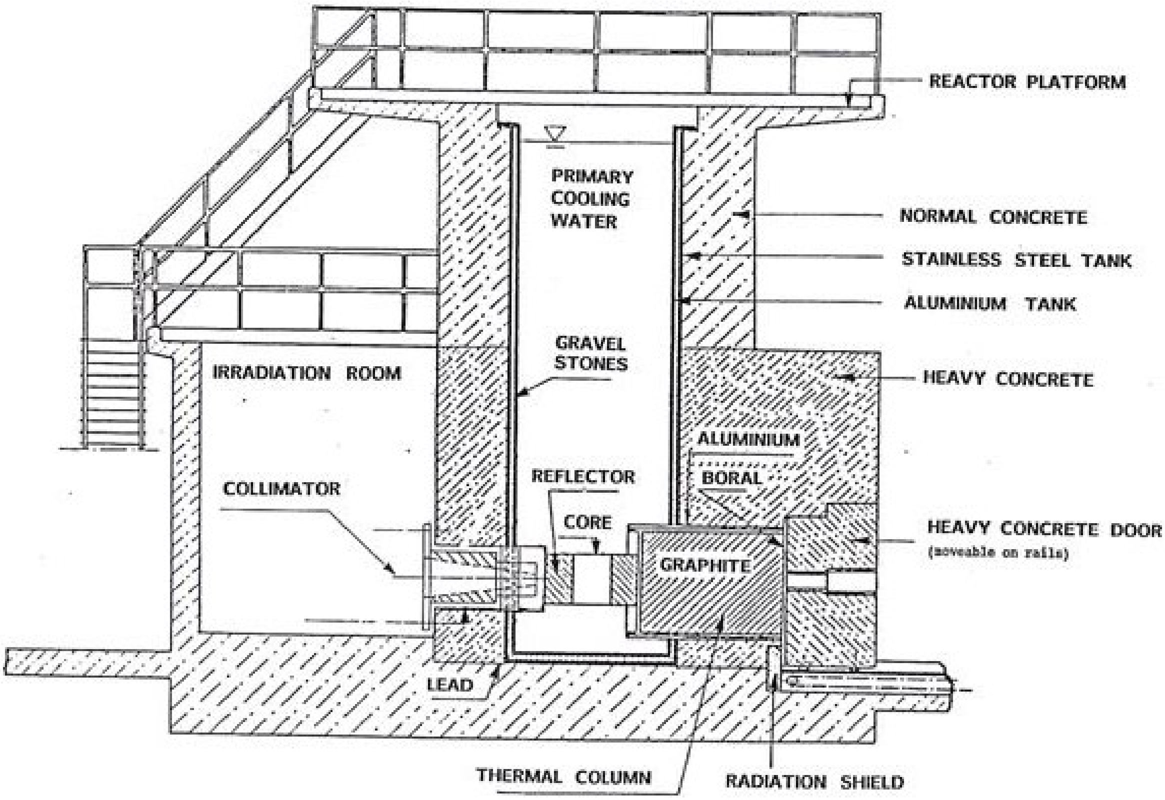

Figure 3.34 Schematic of the TRIGA mk II test reactor in vertical plane showing high-level structure [119].

Chapter 4

Supporting work

Chapter summary

This chapter includes all the work which supports the experimental results in the later chapters. This includes feasibility study, theory, design and development of the imaging systems, accompanying experimentation, prototype testing and modelling of complex (i.e. non-point-source) radiation sources and environments.

4.1 Neutron imaging feasibility study

Neutron imaging based upon back-projection requires neutrons to travel in straight lines in the local atmosphere, containing the imaging device and radiation sources. Maximum transmission T is required for optimised imaging, i.e. minimum scattering in the atmosphere. If transmission is low, many of these back-projection vectors are modified by neutron scattering within the atmosphere and these vectors do not represent the origin of the radiation prior to transport through the atmosphere. If transmission is high (close to 100%), the vectors of neutron trajectories correlate closely with their point of origin and can be used to accurately predict the sources of neutrons detected with this method.

$$T(x) = e^{-\frac{x}{\lambda}} \tag{4.1}$$

The transmission of a particles over a distance x, i.e. the population of particles which travel unattenuated, in a medium of mean free path λ is described by the Beer-Lambert law shown in Eq. 4.1. A typical dimension for practical application of neutron imaging was taken as 10 m, an order of magnitude estimation of room size within a nuclear facility. Fig. 4.1 describes the transmission of neutrons as a function of energy through 10 m of dry air and air with 5% water vapour by weight. Other atmospheres such as nitrogen or argon have very large neutron mean free paths and therefore high transmission. In such situations much lower energy neutrons may be used for imaging. These situations have been treated as a special case and are not investigated in this thesis.

Optimal imaging can be achieved in air in the energy region above 100 keV where transmission averages above 95%. This leads to better imaging capabilities than with lower energy neutrons (the atmosphere appears less foggy for higher energy neutrons in close analogy to optical vision). Neutrons in this energy range can be effectively detected and discriminated from gamma rays using liquid scintillation detectors (see section 3.2.2). Importantly, neutron fields of these energies are commonplace in the nuclear industry (these are summarised in Table 4.1). These higher energy neutrons have the additional advantage of being more penetrating and more forward focussed in collisions, therefore they can be used

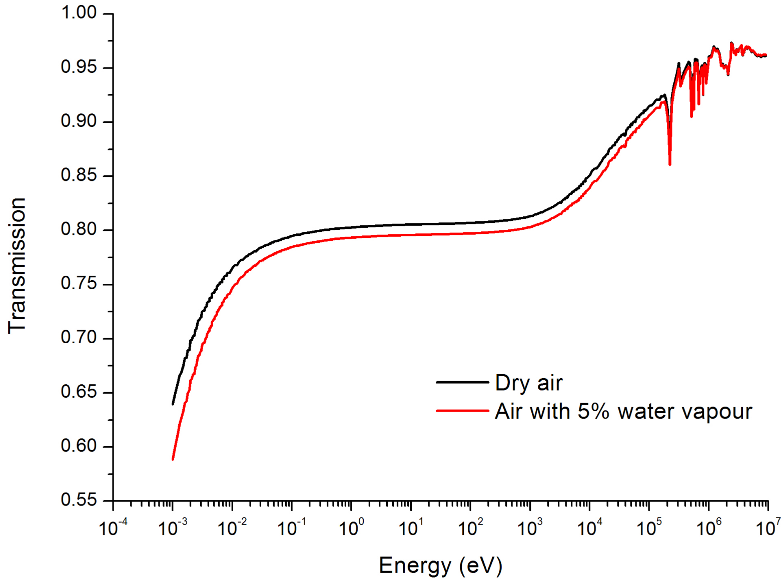

Figure 4.1 Plot of transmission as a function of incoming energy in 10 m of air calculated in MCNP.

to image through significantly more shielding. Fewer scatters also means less perturbation of the field from unwanted background contributions.

Table 4.1 Energy ranges of neutron sources is the nuclear industry.

Situation	Energy range
Laboratory neutron sources (^{252}Cf, ^{241}Am/Be etc.)	$\lesssim$ 9 MeV
Fission reactors	$\lesssim$ 9 MeV
Spontaneous fission in spent fuel (^{244}Cm etc.)	$\lesssim$ 9 MeV
DT Fusion 10 keV	$\lesssim$ 14.1 MeV

Imaging these neutron fields can be affected or manipulated by many factors including: energy spectrum and flux, collimator geometry and materials, neutron background (important for low activity imaging), detector response and energy gating (low energy threshold possible only with recoil proton detection). However if the following criteria are met, neutron sources can be imaged with a back-projection approach:

1. Sufficient neutron flux at the probe.
2. High transmission in the local atmosphere.

3. The neutron field can be detected efficiently.
4. Radiation fields can be accurately discriminated into components, i.e. neutron or gamma rays with good isolation.
5. The detector can be shielded to give an adequate non-uniform spatial sensitivity (or the directionality can be otherwise determined).
6. The radiation field can be considered time-independent over the exposure time of a single complete image.

4.2 Imaging system development

This section discusses the development of the imaging system in terms of its constituent parts: collimators, detectors, MFAs, data acquisition and motor control; relating to the needs and motivations for iterations in the design process. New challenges appeared with each new experiment and the imaging system had to be modified accordingly.

Collimator

The collimator was a critical component in the imaging system and was continually developed during this research with the aim of improving imaging capabilities. Each iteration was designed to improve the sensitivity matrix of the collimator, moving it towards an ideal function such that more accurate and precise radiation images could be obtained. One goal in this thesis was to develop a compact and portable imaging system which introduced constraints on the collimator size. Experiments with the TRIGA research reactor required the probe to be <30 cm diameter in the x-y plane and with significantly improved neutron shielding, prompting the design of the collimator C2. Investigation into an alternative imaging approach using anti-collimation also prompted a new collimator design resulting in the collimator C3. A detailed account of the collimator development is included in section 4.4.

Detectors

The principle imaging detector used in the research was the miniature EJ-301 detector. This detector was used in every example of single-detector imaging and was chosen for its compact size (outer diameter 34 mm). The larger 10 cm cubic EJ-309 detectors were introduced when required by alternative configurations. The first example was during long-exposure experiments over one month which could be affected by the cosmic neutron background. A single cubic EJ-309 detector was included in the system to monitor these background rates. In the real-time source tracking configuration, this set-up required four of the cubic EJ-309 detectors. These detectors were chosen due to their higher intrinsic efficiencies compared with the smaller EJ-301 detectors.

MFAs

The mixed-field analysers were used interchangeably during the research described in the thesis as they could be considered identical other than the number of channels. The 4 channel versions were required when monitoring the background, such as in the long-exposure experiments or when using the real-time source tracking configuration. The single channel units were preferred for portability such as in overseas experiments.

Data acquisition

Initially during this research, transmitting discriminated event data over the Ethernet link (from the MFA to the PC) was beneficial. This method allowed for transmission of more detailed data such that they provided spectroscopic information and an opportunity for re-interrogation of the discrimination parameters. Early experiments with low activity laboratory sources did not exceed count rates of 35 counts per second and therefore did not saturate this connection. Later experiments using the complex radiation sources, the ^{252}Cf tank and the TRIGA research reactor produced much higher radiation fluxes which required an alternative data collection method. The MFAs included TTL outputs which changed state in time correlation with neutron and gamma-ray detections; a custom pulse counter unit was designed and built to acquire these data, collecting event rates (no discrimination data were retained) with an upper limit set by the saturation point of the detector. This unit was interfaced with a custom motor control unit and a PC, constituting the data acquisition system.

The system was equipped with a differential line transceiver to boost serial communications signal between the motor control unit and the pulse counter. The connection was provided by a 20 m Ethernet cable, necessary to span the distance between the support electronics and the deployment position of the probe (down a lift shaft) during the TRIGA research reactor imaging experiments.

Motor control

The N-Visage gamma-ray imaging prototype with its modifications was fitted with two stepper motors which controlled the motion of the probe and the collimator C0. This system formed the basis of the majority of imaging experiments described in this thesis. A motor control unit was designed and built to provide motor control to the probe via a microcontroller interfaced with a PC. The motor control unit was also interfaced with the data acquisition system as described.

The development of a new imaging approach with the tungsten anti-collimator provided the need for a new motor control set-up. A compact telescope mount was procured and a jig was created to fix the mount to the detector and collimator for use in experimentation. Motors and subsequent control were integrated within this unit.

4.3 Monte Carlo modelling

4.3.1 Materials

The materials summarised in table 4.2 were investigated for use in neutron imaging in the MeV range. These materials were chosen for their ability to shield neutrons, their low cost and good machinability/constructibility.

Table 4.2 Summary of materials used in collimator design investigation.

Material	Density (g/cm^3)	Composition	Neutron production
Light water	1.00	1001.60c 2 8016.60c 1	none
Heavy water*	1.11	1002.60c 2 8016.60c 1	(n,2n)
Polyethylene (PE)	0.95	6000.60c 1 1001.60c 2	none
Borated PE (10% wt)	1.12	6000.60c -81.43 1001.60c -13.57 5010.60c -5	none
Graphite	2.16	6000.60c 1	none
Iron*	7.847	26000.50c 1	(n,2n)
Tungsten alloy*	18.1	74000.55c -0.97 28000.50c -0.021 26000.50c -0.009	(n,2n), (n,3n)
Tungsten pure*	19.25	74000.55c 1	(n,2n), (n,3n)

*These materials can have $> 100\%$ transmission due to production of neutrons in (n,xn) reactions.

The materials summarised in Table 4.3 were used to describe the detector and the local environments in the cases of the complex radiation sources: the ^{252}Cf tank and TRIGA research reactor.

Table 4.3 Summary of additional materials used in imaging investigation.

Material	Density (g/cm^3)	Composition
EJ-301 scintillator	0.874	6000.60C 1 1001.60C 1.2121
Aluminium	2.70	13027.50m 1
Concrete (block)	2.00	1001.60c 8.47636E-02 8016.60c 6.040868-01 11023.60c 9.47250E-03 12000.60c 2.99826E-03 13027.60c 2.48344E-02 14000.60c 2.41860E-01 19000.60c 6.85513E-03 20000.60c 2.04808E-02 26054.60c 2.74322E-04 26056.60c 4.26455E-03 26057.60c 9.76401E-05 26058.60c 1.30187E-05
Concrete (standard)	2.25	
Concrete (heavy)	3.50	
Lead	11.34	82000.50c 1
UZrH/Graphite*	2.69	92235.50c 1.242 92238.50c 4.97 40090.66c 37.38 40091.66c 8.13 40092.66c 12.48 40094.66c 12.63 8016.50c 16.07 6000.50c 16.07 1001.50c 2.78

* This material was used as the homogeneous core material - a mixture of uranium-zirconium-hydride fuel at 20% enrichment and graphite moderator.

4.3.2 Detector

The liquid scintillator EJ-301 was described by the material shown in Table 4.3.

4.3.3 ^{252}Cf tank and lab environment

The model of the ^{252}Cf neutron tank included a ^{252}Cf point source, the surrounding water shield (93 × 93 × 90 cm), the 33 mm steel shield, the concrete floor and concrete block walls. The geometry of this model is shown in Fig. 4.2.

4.3.4 TRIGA test reactor

This section is modified from a publication in a peer review journal [120].

A simplified reactor geometry was modelled in MCNP5 comprising a homogeneous core, graphite shielding, light water moderator, lead shield, and heavy concrete exterior. The geometry of this model is shown in Fig. 4.3. To increase computing efficiency, the reactor

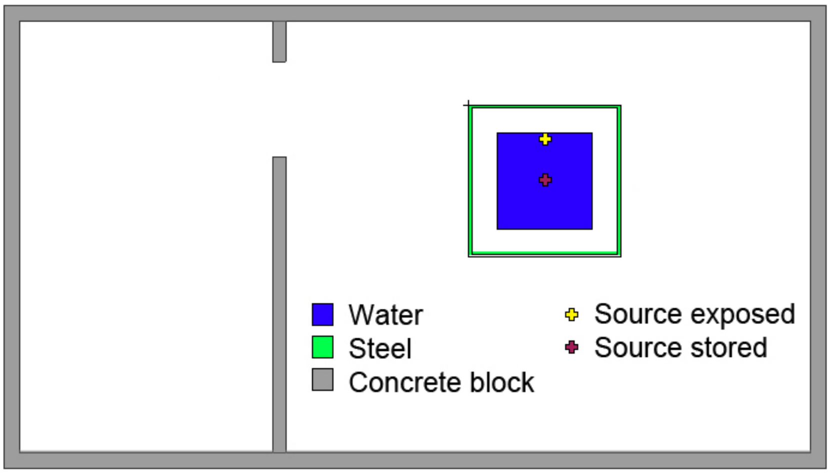

(a) 2D geometry through z-plane

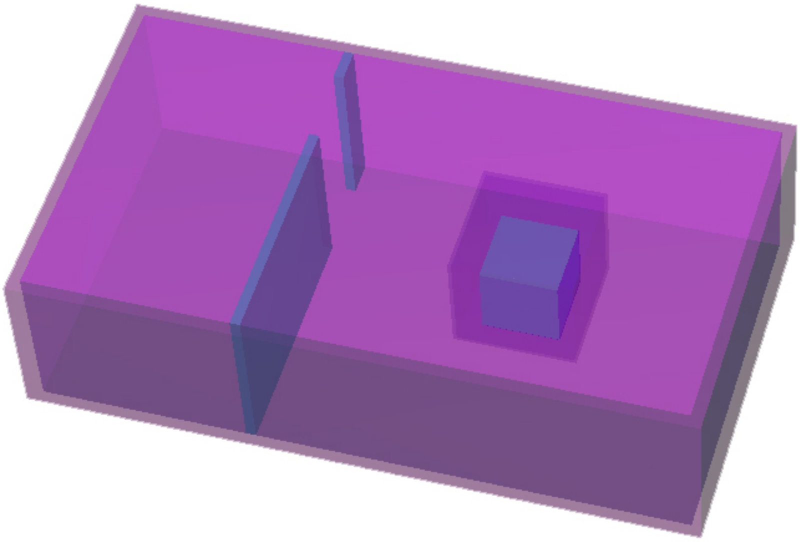

(b) 3D geometry

Figure 4.2 MCNP models of the ^{252}Cf source and lab environment.

core was modelled as one homogeneous cylinder containing the appropriate ratios of fuel element and moderating material. The homogeneous core was treated as a volume source producing the appropriate radiation spectrum and distribution. A Watt fission spectrum was used to seed neutrons and the gamma-ray spectrum measured by Verbinksy et al. [121] was used to seed gamma rays. The gamma-ray component due to neutron capture was also included. Each simulation was set up to mimic the data acquisition as and the data were presented in the same way using the method outlined in section 3.4.4.

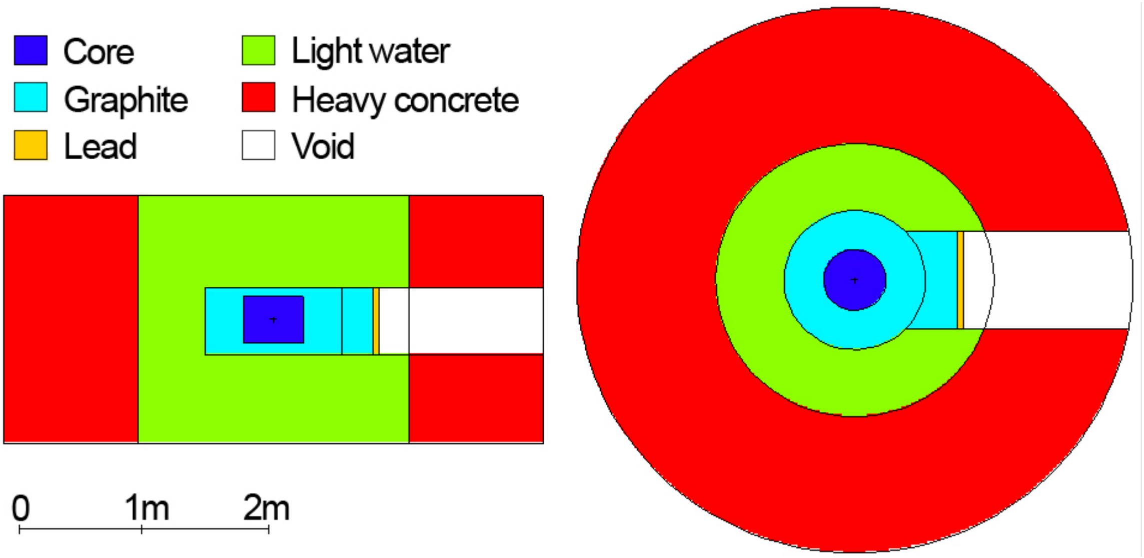

(a) 2D geometry through y-plane

(b) 2D geometry through z-plane

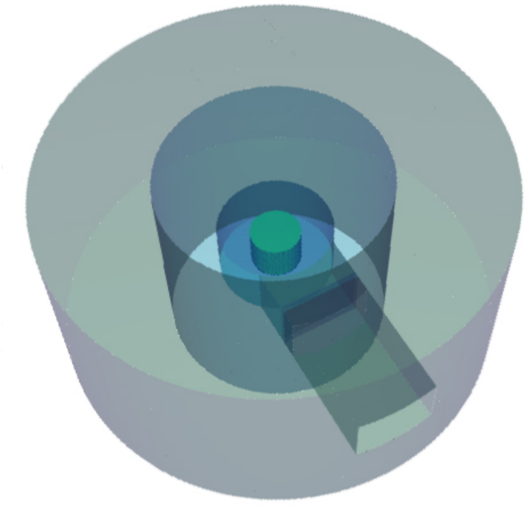

(c) 3D geometry

Figure 4.3 MCNP models of the TRIGA test reactor.

4.4 Collimator development and Monte Carlo characterisation

The method of imaging radiation fields used in this thesis requires a detector which has a non-uniform directional sensitivity. This could be created by surrounding a detector with a collimator preventing radiation reaching the detector from all but a small solid angle, the sensitivity region. This region could be rotated through space to scan the environment, collecting image data from each part of the environment. The collection of these scans form the image data which can be processed into an image solution. In the $\hat{\alpha} = 0°$ $\hat{\beta} = 0°$ position, as defined in section 3.3, an ideal sensitivity map contains a sensitivity band extending from -90° to +90° in elevation; this ensures that data could be collected from all the surrounding space. The band was ideally narrow in azimuth and high in contrast to allow high resolution imaging. An example of an ideal sensitivity map for a collimator detector is shown in Fig. 4.4.

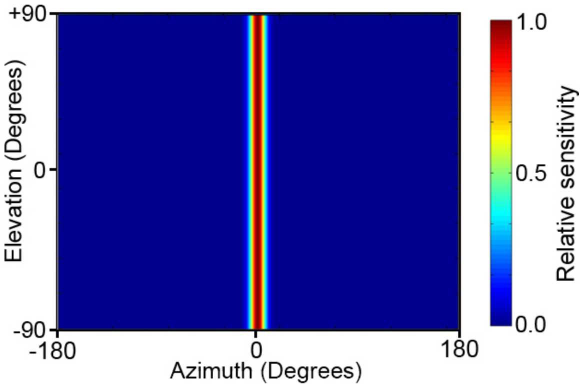

Figure 4.4 An ideal hypothetical sensitivity map for a collimated detector in position $\hat{\alpha} = \hat{\beta} = 0°$.

This section describes the development of the collimators through the research. MCNP5 and MCNPX were used to investigate the subtleties of this collimated approach by characterising geometries and materials for optimal effect. The sensitivity characterisation of each detector was performed using the method outlined in section 3.4.1. A full validation of these sensitivity maps for every square degree bin required 64,800 measurements; this measurement campaign would have taken an enormous amount of time and was therefore infeasible. It was however possible to validate the sensitivity map in one dimension where appropriate. The collimator quality was assessed using the signal-to-noise ratio and FWHM as defined in Fig. 3.18.

4.4.1 Bare detector

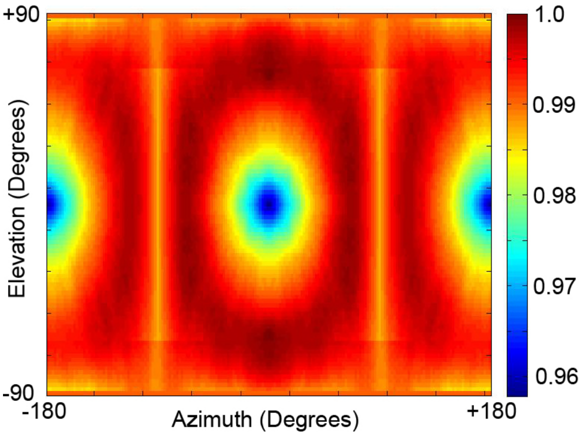

Figure 4.5 Full universe response matrix, calculated with MCNP, of the EJ-301 liquid scintillation detector with no collimator to a ^{252}Cf neutron spectrum.

A key component of each imaging system was the miniature EJ-301 liquid scintillation detector as described in section 3.2.1. This detector was not spherical and therefore has a non-uniform spatial sensitivity. This component was investigated in isolation by interrogating a model comprising only the cylindrical scintillation cell in MCNP5. The spatial sensitivity of the detector to ^{252}Cf is shown in Fig. 4.5. The sensitivity of the bare detector was found to vary by only about 4%. The subsequent collimator sensitivity characterisations accounted for this component by including the detector scintillation cell in the collimator models.

4.4.2 Collimator C0: tungsten

Design

The C0 collimator, as described in section 3.2.3, was designed as a collimator for a gamma-ray imager in an early N-Visage prototype [13]. The only change was a modification with a milling machine in order to retrofit the miniature EJ-301 detector as described.

Characterisation

The collimator and the surrounding probe structure were characterised in MCNP5. The MCNP model of the collimator is illustrated in Fig. 4.6a and the neutron and gamma-ray sensitivity maps can be seen in Figs. 4.6b and 4.6c respectively.

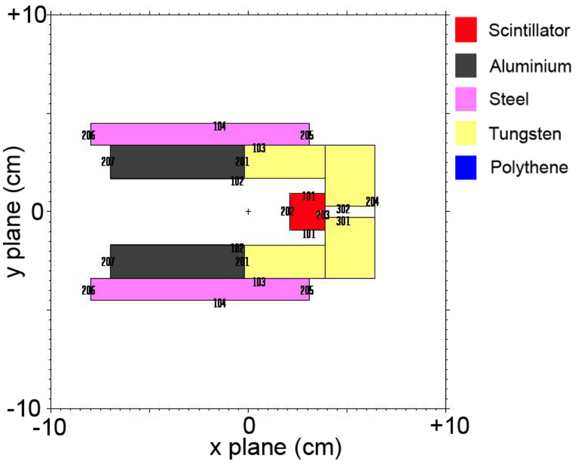

(a) Model of C0 collimator and surrounding housing in z-plane

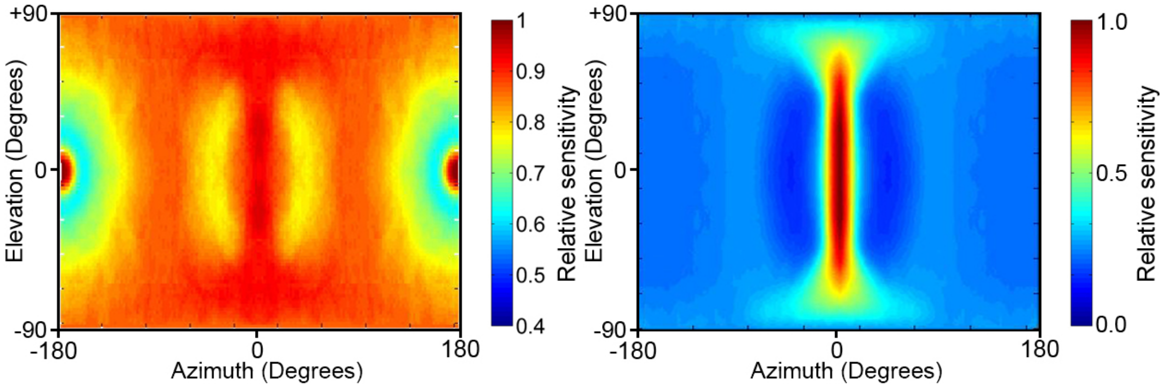

(b) Sensitivity map of collimator C0 and surrounding housing to ^{252}Cf neutrons

(c) Sensitivity map of collimator C0 and surrounding housing to ^{252}Cf gamma rays

Figure 4.6 MCNP5 characterisation of the collimator C0.

Validation

The sensitivity maps were validated against experimental results obtained at the University of Manchester, UK. A single ^{252}Cf source (1.5×10^5 neutrons s^{-1}) was placed in the horizontal plane containing the detector at a distance of 1 m from the centre of the scintillation cell. Using the method outlined in section 3.3.3, data were collected for $\hat{\alpha} = 0°$, $\hat{\beta} = -112° : 127°$ in 3° increments for t_d = 600 seconds per point. The MCNP-calculated functions were produced in 1° increments and were plotted with experimentally-obtained values. The results are shown in Fig. 4.7 and show close agreement between MCNP-calculated values and experimental results. Discrepancies are due to physical parts which were not included in the model as they did not rotate with the collimator, thereby greatly increasing the computer resource required for a solution (factor of 90).

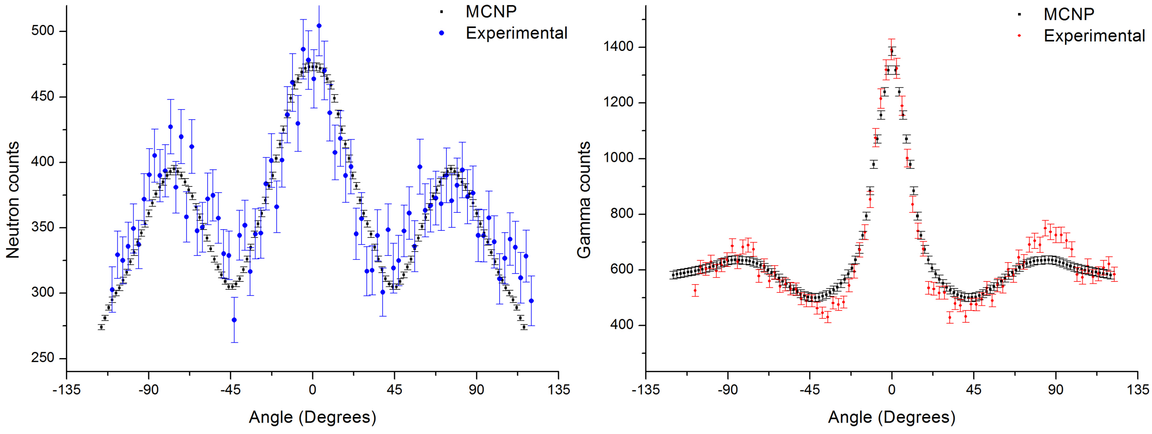

(a) Neutron (b) Gamma ray

Figure 4.7 Plot of experimentally-obtained radiation events as a function of $\hat{\beta}$ when scanning a ^{252}Cf source with collimator C0. Corresponding MCNP calculations from sensitivity matrix also shown.

Comments

These functions were suitable for imaging as the sensitivity was known and validated. However an ideal function for use in image construction would be a single sensitivity band rather than the complex sensitivity structure observed. In profile this function is a triple peak structure, attributed to neutrons passing through the thinner tungsten wall adjacent to the detector scintillation cell. A more ideal sensitivity map would not have this function, i.e. the triple peak sensitivity function to neutrons in Fig. 4.7a would be reduced to a single peak similar to the gamma-ray function shown in Fig. 4.7b.

4.4.3 Collimator C1: PVC

Design

Collimator C1 comprised a PVC addition to collimator C0. This collimator was designed early in the research without MCNP input (details of the geometry are given in section 3.2.3). The design process was simple - to shield the detector in 2π as uniformly as possible (to neutrons) but with the inclusion of the C0 collimator (to shield gamma rays). PVC was chosen for its availability and high hydrogen content. A 10 cm radius PVC hemisphere was created to fulfil these criteria and was machined to fit directly over the C0 collimator without any void space. A 6 mm void region created to allow unattenuated passage of radiation was also cut into the PVC, extending the slot void region.

Characterisation

The MCNP model is shown in Fig. 4.8a, the neutron sensitivity map is shown in Fig. 4.8b.

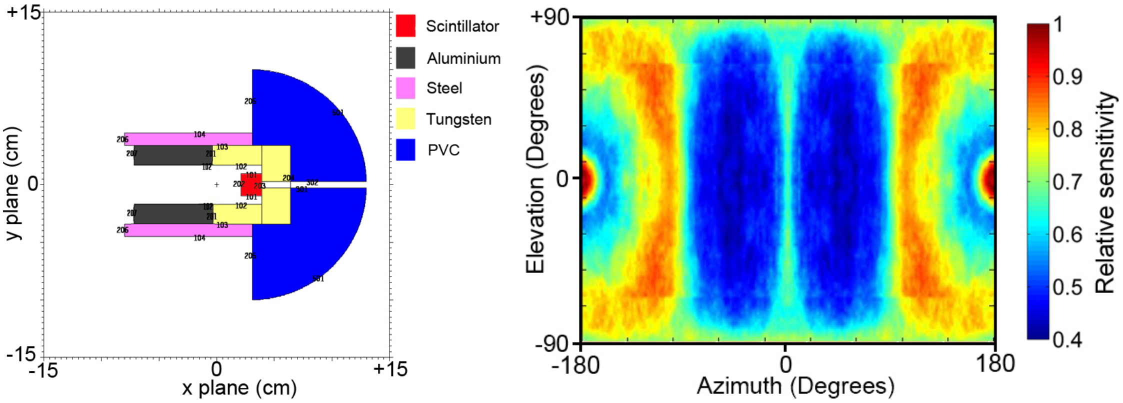

(a) Model of collimator C1 and surrounding housing in z-plane

(b) Sensitivity map of collimator C1 and surrounding housing to ^{252}Cf neutrons

Figure 4.8 MCNP5 characterisation of the collimator C1.

Comments

This collimator was used for one early experiment using the orthogonal slot-node imaging method and therefore did not require the sensitivity maps for image reconstruction, hence validation was also not necessary. The neutron sensitivity map is included for completeness and to illustrate the need for the next iterative step in neutron collimator design.

In the azimuth region from -90° to +90°, this collimator provides a single, narrow sensitivity band which would be suitable for imaging (though without a desirable high contrast) using the ART reconstruction imaging method. Outside this azimuth range, large response values are seen which correspond to the unshielded regions which would interfere with the image reconstruction process, and as a result can be used only in a restricted azimuth range.

This collimator also added significant length to the outer radius of the probe (from 8 cm to 14 cm). Experiments with the TRIGA research reactor required operation within a narrow (∼30 cm wide) lift shaft. Including the motor fitted to the rear of the cylinder, this collimator was too large to operate within this confined space. For this practical reason, and the focus of probe compactness during the thesis, this collimator was not further used.

4.4.4 Collimation theory I: Energy dependence of shield materials

MCNPX was used to investigate the potential shield materials used for collimators discussed in Table 4.2. The transmission of neutrons through 10 cm of shield material was calculated; an overview of the geometry used for this investigation is given in Fig. 4.9. 10 cm was chosen as a typical thickness which might be used in a collimator design, being small enough to be portable.

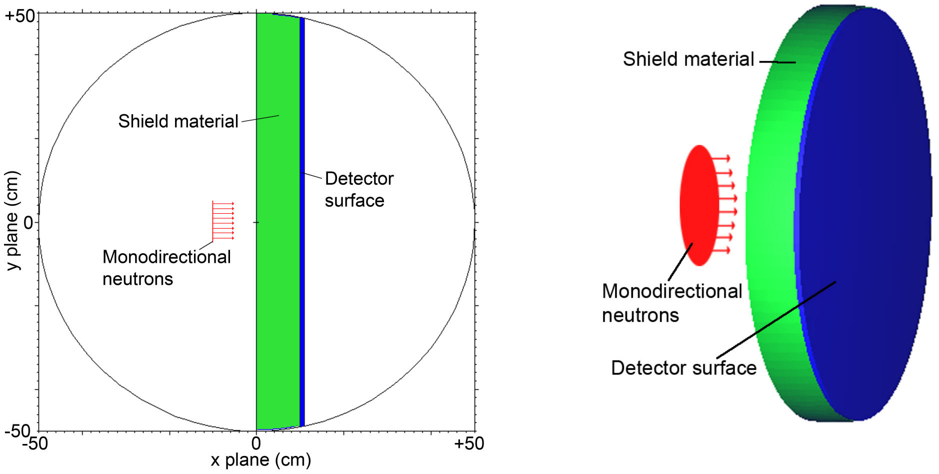

(a) Annotated MCNP model in the z-plane (b) Annotated model in 3D

Figure 4.9 Geometry of the MCNPX simulation to measure transmission of a monodirectional neutron beam through a surface.

Monodirectional neutrons were emitted perpendicular to a circular plane source with vector [x y z] = [1 0 0], directed into the centre of a 10 cm shield. The flux of neutrons was measured by a thin detector on the opposite side spanning the entire area of the shield. Neutrons at a given energy (in 100 keV bands with uniform emission probability) from 100 keV to 20 MeV were emitted in each simulation. The flux was recorded using an F4 tally (average flux in a cell) and was normalised to the flux recorded with no shield present.

Fig. 4.10 shows the neutron transmission as a function of energy. Some of the tallies have a transmission $> 100\%$ due to neutron production reactions such as (n,xn). These results show that borated polyethylene (closely followed by high-density polyethylene) was the best neutron shield material for incident neutrons of virtually all energies. In addition, polyethylene (PE) and borated polyethylene (BPE) are also the most hydrogenous materials which improves shielding due to moderation (followed by neutron capture though these detectors are not thermal-neutron sensitive) in addition to scattering. For these reasons borated polyethylene is the best neutron shield of the materials tested.

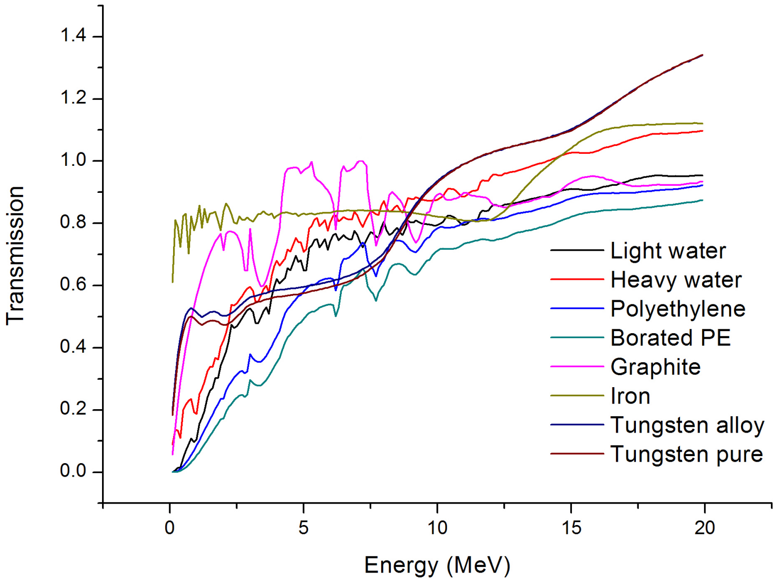

Figure 4.10 Plot of neutron transmission as a function of incident neutron beam energy through 10 cm of shield material calculated in MCNPX.

4.4.5 Collimator C2: high-density polyethylene

Design

This collimator was again designed as an attachment to the C0 collimator. The C0 collimator was maintained as part of the design to shield gamma rays and polyethylene was chosen to address the short comings of the neutron sensitivity map, as discussed in the previous sections. This collimator was designed to be more compact than the C1 collimator and hence suitable for use with the geometric constraints associated with imaging the TRIGA reactor. Although borated polyethylene was found to be a marginally better neutron shield, high-density polyethylene was chosen for its cheapness and availability.

The design of this collimator occurred in many stages. The MCNP model of collimator C0 was altered with several variations of an additional shield, the collimator was characterised and the most ideal variant was chosen. The next iteration was then performed. This method was repeated until a suitable (close to ideal) collimator sensitivity map was obtained.

The first stage was to remove the triple peak structure seen in the characterisation of the C0 collimator. This was achieved by surrounding the probe in a polyethylene tube. The thickness was varied and 2.5 cm was found to be thick enough to significantly reduce the sensitivity of neutrons passing through the thin tungsten wall of the collimator. Clearly a thicker polyethylene tube would further reduce this contribution but the trade-off between the sensitivity function and probe compactness would not be optimal.

The second stage was to design the front face of the collimator. The goal here was to ensure the sensitivity map was a narrow band, as uniform as possible in sensitivity. Here the parameters were the overhang of the polyethylene beyond the face of the collimator and the shape of the slot void. An overhang of 1 cm was determined to be optimal and a tapered slit (increasing with radius) was found to provide the most uniform sensitivity region.

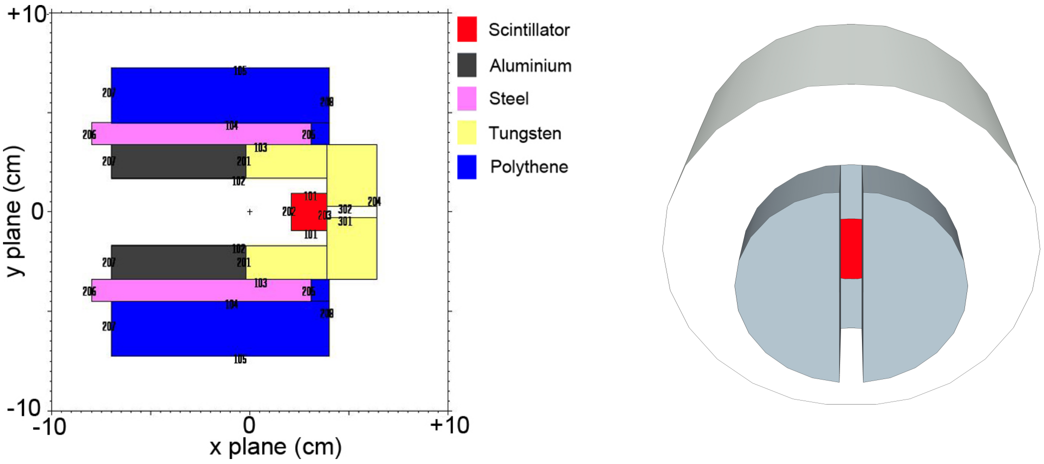

(a) Model of collimator C2 first stage model in the z-plane

(b) 3D visualisation of model

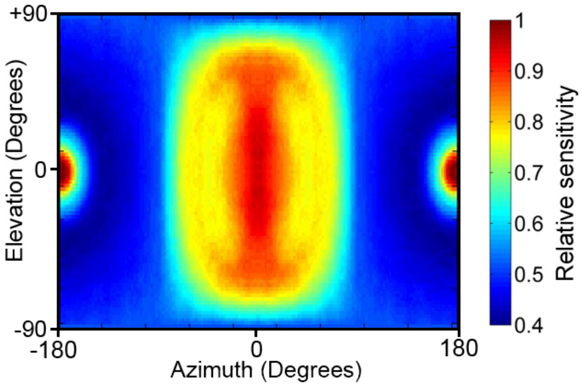

(c) Sensitivity map of collimator C2 first stage design to ^{252}Cf neutrons calculated with MCNP

Figure 4.11 Geometry and characterisation of the first stage C2 design.

Characterisation

The many stages of the design process are not included for brevity, however the models, 3D visualisations and sensitivity maps from the first and second stage of collimator C2 design are shown in Figs. 4.11 and 4.12 respectively.

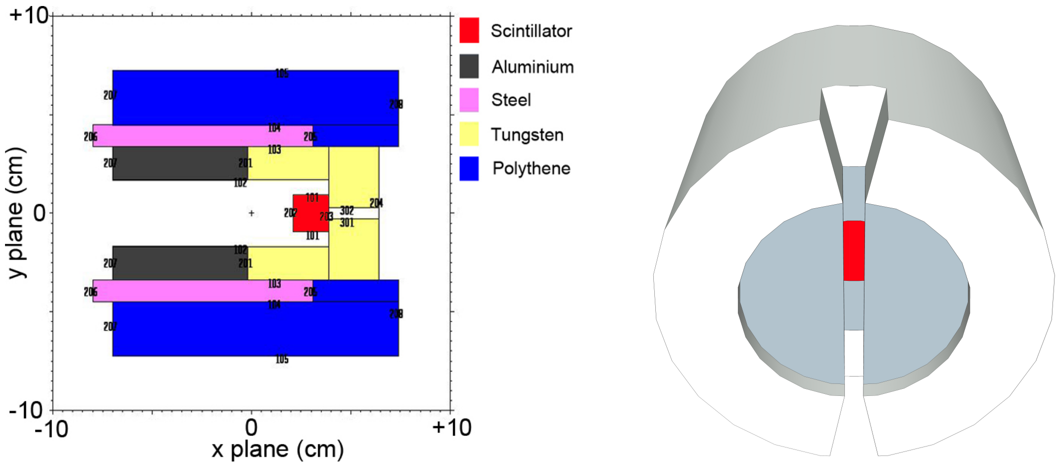

(a) Collimator C2 final stage model in the z-plane

(b) 3D visualisation of model

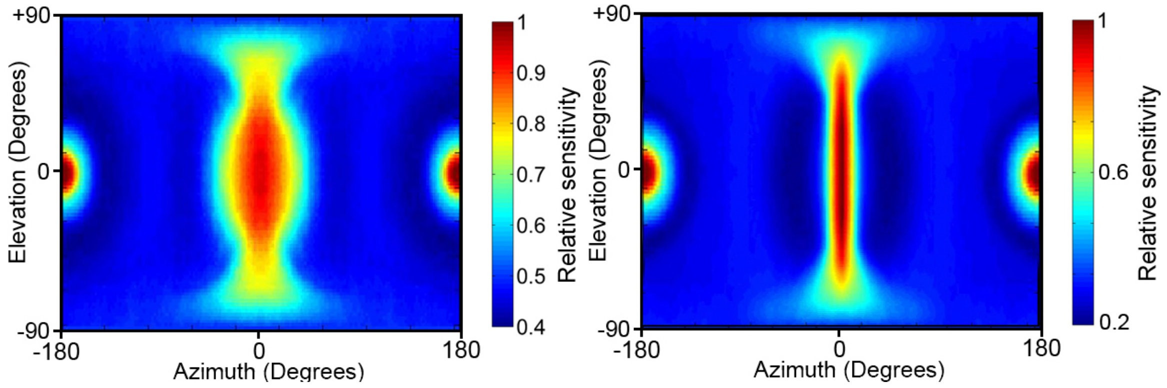

(c) Sensitivity map of collimator C2 final stage design to ^{252}Cf neutrons

(d) Sensitivity map of collimator C2 final stage design to ^{252}Cf gamma rays

Figure 4.12 Geometry and MCNP characterisation of the final stage C2 design.

A video of the system matrix transformations is given in Supplementary Video 1, see appendix A.1, demonstrating the sensitivity of the detector to 2D space during a data collection routine. Additionally the system matrix as a function of the imaged field is also illustrated in Supplementary Video 2, see appendix A.1. This video also demonstrates that the neutron system matrix is slowly varying between 1 and 3 MeV.

For further illustration of the design process, MCNP5-calculated values through elevation $\phi = 0°$ are shown in Fig. 4.13 for C0, first stage C2 and final stage C2 collimators. The final stage collimator C2 design has a narrower width and a high contrast when compared with the other two collimators.

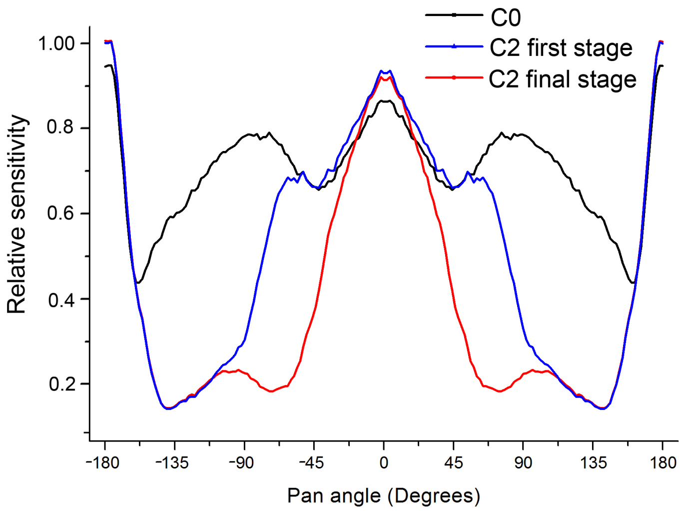

Figure 4.13 Plot of normalised MCNP5-calculated neutron counts with $\hat{\alpha}$ = 0° as a function of angle $\hat{\beta}$ when scanning ^{252}Cf source for collimators C0, first stage C2 and final stage C2.

Validation

The neutron sensitivity map was validated against experimental results obtained at Lancaster University, UK using the ^{252}Cf source discussed in section 3.5.1. The imager was located such that the detector was in the same plane as the ^{252}Cf source and was 1 m from the source when placed in the exposed position. The source was moved to the exposed position, data were accumulated and the discrimination parameters were set (identical to Fig. 5.11). Using the method outlined in section 3.3.3, data were collected for $\hat{\alpha} = 0°$, $\hat{\beta} = -135° : 135°$ in 2° increments for $t_d = 100$ seconds per point. The MCNP-calculated functions were produced in 1° increments and were plotted with the experimentally-obtained values. The results are shown in Fig. 4.14.

Comments

The experimentally-obtained values show close agreement with the MCNP-calculated values between -90° and 90°. Outside this region MCNP underestimates the sensitivity; this mismatch was due to inconsistencies between the real PE shield and the model. Due to the aluminium structural elements on the side of the probe, the PE could not be kept at a consistent thickness of 2.5 cm all the way around and was approximately 1 cm thick in these regions. This allowed a higher flux of neutrons to pass through to the detector from $\hat{\beta}$ angles

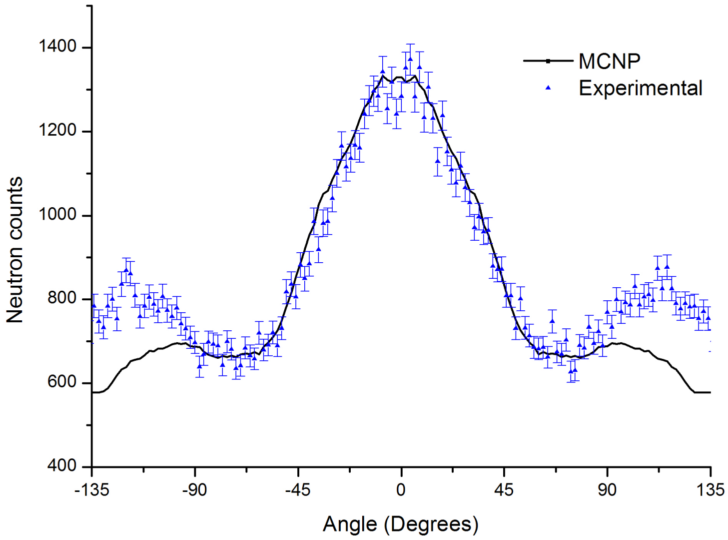

Figure 4.14 Plot of MCNP-calculated neutron counts with $\hat{\alpha} = 0°$ as a function of angle $\hat{\beta}$ when scanning ^{252}Cf source for collimator C2 and corresponding experimental results.

greater than 90° for some elevation angles (estimated to be from $\phi = +30° : -40°$). This feature was non-rotational (not a function of $\hat{\alpha}$) and therefore was not easily accounted for in the sensitivity matrix, due to the reliance on rotational symmetry to produce all the elements from a single MCNP characterisation. The computer time would also be extended by a factor of 90. However, as long as data were collected inside the validated range (and the source distribution not extending more than 90° in azimuth), the sensitivity map and therefore the image solutions would be accurate. 1 cm thick cuboidal PE pieces were placed over the low-shielded region to help reduce the disparity in these regions.

4.4.6 Collimation theory II: neutron interactions in shield materials

This section seeks to explain the motion and interactions of neutrons within the collimator with the goal to design a next generation collimator. MCNPX and MCNPX Visual Editor were used to gain insights into the neutron transport within a collimator model.

Ideal collimator model

An ideal neutron collimator would contain a spherical detector completely shielded on all sides with a uniform thickness of neutron shielding material, with the exception of a narrow slot void allowing the unattenuated passage of neutrons to the detector from a small azimuth

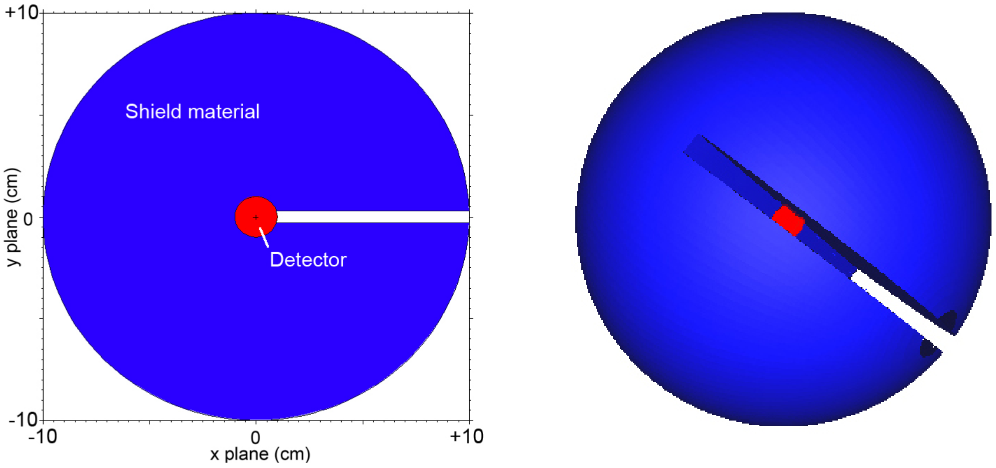

(a) MCNP model in z-plane

(b) 3D visualisiation of model

Figure 4.15 Geometry of a hypothetical ideal neutron collimator used for theory investigation: a 10 cm shield with central 1 cm radius EJ-301 detector.

range and elevation range from -90° to 90°. A model of an ideal neutron collimator is shown in Fig. 4.15. This collimator has an outer radius of 10 cm and a 6 mm wide slot void. The detector, located centrally, is a sphere of radius 1 cm filled with EJ-301 scintillator. This model, used with various shield materials, was used to better understand neutron transport within the collimator structure.

Material assessment

The ideal collimator model was interrogated using the materials discussed in Table 4.2. The shield was modelled using one of the materials and was interrogated using the method outlined in section 3.4.1 to characterise it as a function of θ between 0° and 360° with ϕ = 0°. Three different neutron energy spectra were used: ^{235}U fission, a uniform (flat) energy distribution between 0.1 and 20 MeV, and deuterium-tritium fusion at 10 keV producing an average neutron energy of 14.1 MeV. The resulting sensitivity functions were analysed to find the signal-to-noise ratio and the full width at half maximum (FWHM) in each case.

The results in table 4.4 clearly indicate that borated PE is the most successful shield material for a collimator of this geometry, giving consistently the highest signal-to-noise ratio and low FWHM values. This material is also lightweight, making it ideal for collimator material. The only drawback of borated PE is its poor gamma-ray shielding which may be desirable in some situations (the liquid scintillation detector EJ-301 is also sensitive to gamma rays). All the materials in this list have parameters good enough to image fission spectrum neutrons to some level of success, tungsten in particular has the advantage of

Table 4.4 Signal-to-noise and FWHM values of collimators comprising various shield materials with different energy spectra.

	^{235}U fission		Uniform energy		DT fusion	
Material	S/N	FWHM(°)	S/N	FWHM(°)	S/N	FWHM(°)
Light water	1.061	8.75	0.317	10.63	0.147	12.88
Heavy water	0.719	9.75	0.244	11.58	0.112	14.08
Polyethylene	1.427	8.37	0.360	10.53	0.141	12.17
Borated PE	1.806	7.87	0.407	10.38	0.165	12.82
Graphite	0.446	10.12	0.250	11.22	0.155	13.79
Iron	0.389	10.26	0.196	12.42	0.111	16.04
Tungsten alloy	0.430	9.29	0.144	18.68	0.086	30.89
Tungsten pure	0.438	9.19	0.143	18.06	0.086	32.72

strongly shielding gamma rays. However at higher energies, such as the case of a DT fusion spectrum, the signal-to-noise ratio drops to a low level.

MCNP methods

Several methods were used to characterise neutron transport within the ideal collimator using the model shown in Fig. 4.15. These methods are numbered for ease of reference within the following results section. As discussed, the most effective neutron shield was found to be BPE, hence the investigation of this material. The EJ-301 scintillator was also sensitive to gamma rays and therefore these radiations also needed to be shielded; pure tungsten was investigated for this reason due to its excellent gamma-ray shielding properties.

1. Neutron particle tracking. The neutron trajectories in borated PE and tungsten were investigated for 30 particle histories using the method outlined in section 3.4.5. A circular plane source of radius 10 cm was modelled parallel to the y-plane at x = 20 cm. Monodirectional neutrons of uniform energy distribution between 0 and 20 MeV were emitted parallel to the -x direction towards the collimated detector. A low energy cut-off of 100 keV was applied. This method was intended to illustrate typical neutron paths within the collimators. The number had to be kept low to allow for visibility of the neutron tracks.

2. Neutron interaction distribution. The neutron interactions in tungsten and borated PE were investigated for ten thousand particle histories. A circular plane source of radius 10 cm was modelled parallel to the y-plane at x = 20 cm. Monodirectional neutrons of uniform energy distribution between 0 and 20 MeV were emitted parallel to the -x direction towards the collimated detector. A low energy cut-off of 100 keV neutron was applied to bring the simulation in line with the limits of detection of discriminated neutrons. The interaction points (wherever a neutron interaction occurred, e.g. scattering) were plotted within the collimator structure. Secondly the interaction points were plotted for 200,000 particle histories for neutrons which were ultimately detected.

3. Azimuth dependent neutron detection with interaction segregation. Borated PE and tungsten were investigated further using the method outlined in section 3.4.1 to characterise the collimators as a function of θ between 0° and 360° with ϕ = 0°. This method was used in conjunction with particle tagging, allowing the uncollided, elastically scattered, inelastically scattered and (n,xn) neutrons to be segregated in the tallies. A low energy cut-off of 100 keV was applied. The MCNPX code used in this analysis is summarised below.

```
f24:n 44        $Tally neutrons in cell 44
e24 0 219I 22
FT24 TAG X
FU24 CCCCCZZAAA.RRRRR 1e10
```

The options used to control the particle tagging are summarised in Table 4.5. This allowed the detected events to be attributed to neutrons which had undergone the listen reactions.

Table 4.5 Summary of particle tagging code options in MCNPX.

Value	Meaning
X = 1	Particles lose their tags after collision
X = 3	Particles retain their production tag
CCCCC	Cell number
ZZAAA	Isotope
RRRRR	Reaction identifier, MT number
CCCCC omitted	Cell tagging not required
RRRRR = 00000	Tags all products from ZZAAA
0000000000.00000	Elastically scattered particles
-0000000001	Source (uncollided) particles
1e10	Tallies all other particles not segregated

Results and comments

1. Neutron particle tracking.

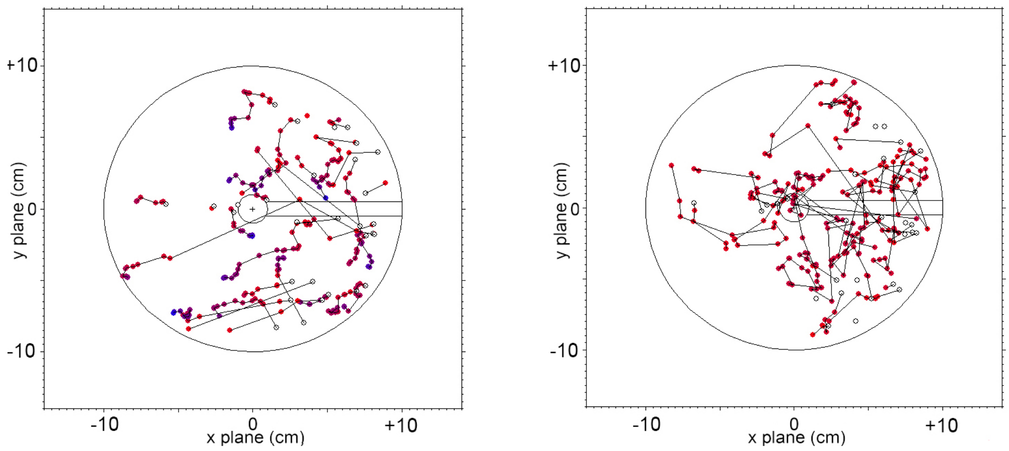

(a) borated PE collimator (b) Pure tungsten collimator

Figure 4.16 Interaction tracks of neutrons in an ideal collimator as the result of an incident monodirectional neutron beam of thirty neutrons from the positive-*X* direction. Interaction points marked blue show that the neutron has an energy below 100 keV.

Fig. 4.16 shows the interactions and paths of neutrons within an ideal collimator. Interaction points marked red show where neutrons have energy in excess of 100 keV and points marked blue show neutrons with energy less than 100 keV. Neutrons incident on the tungsten collimator scatter frequently but were not seen to drop in energy below 100 keV. Borated PE has fewer scatters but those interactions produce significant moderation and many of the neutrons are reduced in energy to below 100 keV.

2. Neutron interaction distribution.

Fig. 4.17 shows the resulting neutron interaction points (marked red where an interaction has occurred) for ten thousand source neutrons incident on the collimator. The distribution of neutron interaction points in both tungsten and borated PE are largely similar with more scatters occurring in the more positive *X* locations. One exception to this in both cases was the region behind the slot void where neutrons passed through to the centre of the collimator without attenuation and were reflected into the detector. This indicates that backscatter may be an important contributor to the signal at the detector. A major difference between these two collimator materials was that neutrons were seen to penetrate more deeply into the tungsten compared with the BPE. The tungsten collimator has many more interactions occurring within the shield volume compared with BPE.

Fig. 4.18 shows the interaction points of neutrons (marked red where an interaction has occurred) for 800 k and 200 k particle histories for borated PE and tungsten respectively. The interaction points were plotted only if the neutron was ultimately detected and contributed

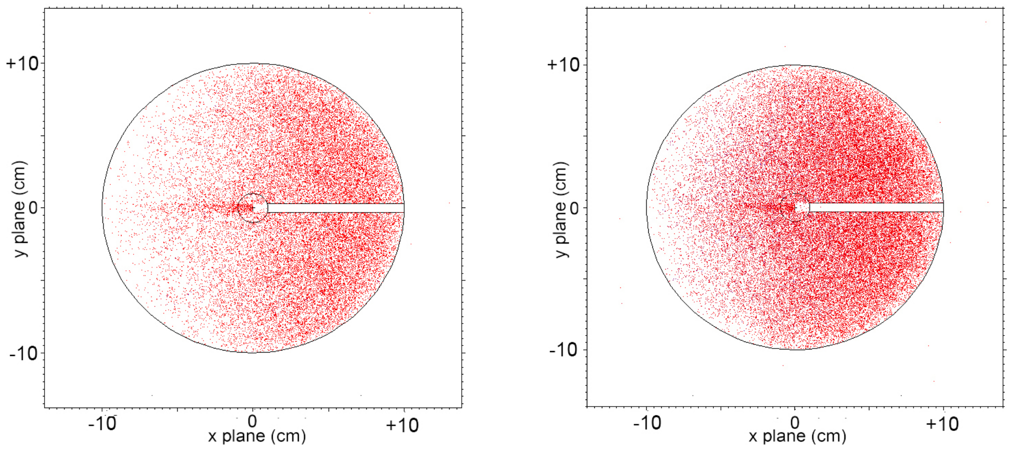

(a) borated PE collimator

(b) Pure tungsten collimator

Figure 4.17 Interaction points of neutrons in an ideal collimator as the result of an incident monodirectional neutron beam of 10k neutrons from the positive-x direction.

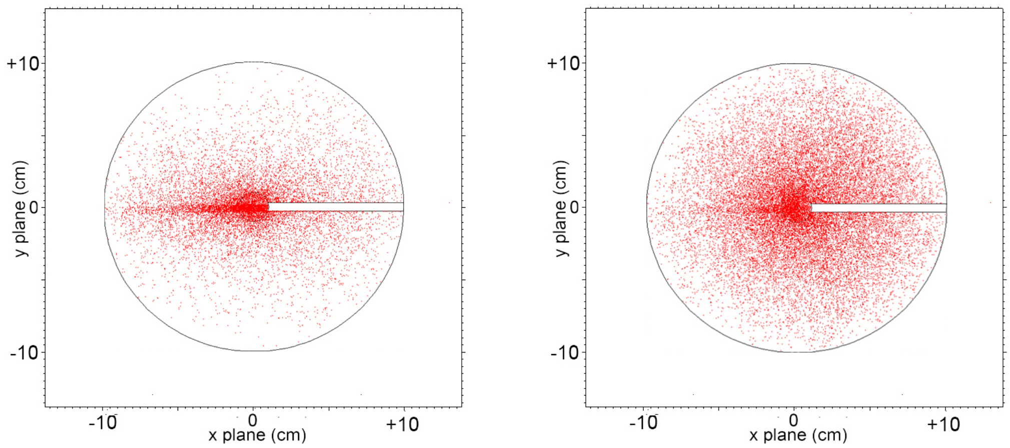

(a) borated PE collimator 800k particle histories

(b) Pure tungsten collimator 200k particle histories

Figure 4.18 MCNP-calculated interaction points of neutrons in an ideal collimator as the result of an incident monodirectional neutron beam of neutrons from the positive-x direction which contributed to the detection tally.

to the tally at the scintillation cell. This constraint causes the distribution to appear quite different to the results in Fig. 4.17. The presence of a large number of interactions to the left of the void slot indicates that backscatter is an important component in the detection of neutrons. These occur when neutrons travel down the slot void unattenuated, pass through the detector and into region of the collimator directly behind the detector, some of these neutrons are scattered through large angles back into the detector where they are detected. A major difference between these two materials was that many more interactions were seen in the tungsten collimator (note that the number of particle histories is four times smaller in the case of BPE compared with tungsten). The interaction points in the borated PE are more clustered around the void slot and backscatter region; in the case of tungsten this distribution is far more spread out, indicating that neutrons from even the outermost radius of the collimator were frequently deflected towards the detector and tallied.

3. Azimuth dependent neutron detection with interaction segregation.

The results of this investigation can be seen in Fig. 4.19. It is apparent that for both materials, the main contributor to the signal (the peak in detected flux close to 0°) was due to the uncollided neutrons, i.e. neutrons which travelled through the slot void without attenuation. The second largest component in the signal was due to elastic neutron scatters; this is likely to comprise neutrons which scatter close to the void region and travelled in part through the slot, or those which passed through the void and are reflected by the region of the collimator behind the detector into the detector. The inelastic component in borated PE was very small and therefore does not require further study. The inelastic component in tungsten comprises virtually 100% of the (n,xn) reaction and has an angular component, suggesting that neutron production occurs as a result of neutrons which have travelled down the slot void. This component was very small and would only need to be considered when imaging high energy neutrons (10 - 20 MeV).

Study of the total detector flux as a function of angle shows that despite borated PE being the best neutron shield, only approximately 50% of the incident neutrons can be shielded outside the slot void region. Note that the flux has been normalised to that detected by a bare detector (with no collimator) to show the effect of the collimator more effectively. The tungsten collimator actually increases the number of neutrons detected in excess of the neutrons produced by (n,xn) reactions. This indicates that neutrons not incident on the detector were scattered elastically through the collimator to the scintillation cell where they were detected, showing that the neutron shield actually has the reverse effect to its intention. Although a signal is produced near 0° due to the void slot, the background was actually increased by the presence of the shield material, diverting some of the neutrons towards the detector.

Conclusions

Borated PE was found to be the most effective material out of those studied, transmitting the lowest flux of neutrons and having the highest signal-to-noise ratio when tested with the

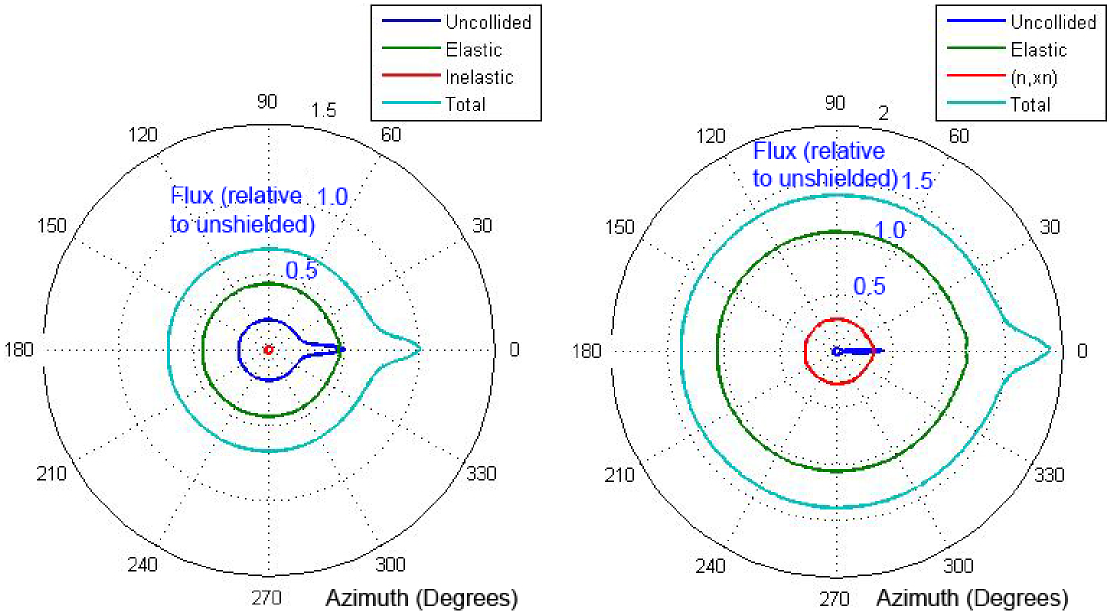

(a) Borated PE collimator (b) Pure tungsten collimator

Figure 4.19 MCNP-calculated angular dependence of neutron flux components: uncollided, elastically and inelastically scattered neutrons; in ideal collimators comprising polyethylene and pure tungsten to a uniform neutron energy distribution between 0.1 and 20 MeV. The detected flux is normalised to the response of a bare detector. The inelastic component in tungsten was negligible.

ideal collimator model. This was attributed to the high hydrogen density within the material, providing maximum energy loss in neutron collisions, and the high interaction probabilities of neutron scattering and moderation to below the detection threshold. Tungsten was found to interact frequently with incident neutrons but did not provide good collimation as interactions led to increased detection at the scintillation cell, greatly decreasing the signal-to-noise ratio.

When creating a compact imaging probe with a diameter of 20 cm, collimation was found to be a significant challenge for neutrons at 10 MeV and beyond when using the best available shield material. The main source of signal in the ideal collimator model was due to the uncollided neutrons which passed directly down the slot void to the detector. The second highest contribution was due to elastically-scattered neutrons which had travelled partially or fully through the slot void and were then scattered into the detector. A neutron-reflective surface behind the detector (opposite the slot void) was predicted to significantly improve signal by the reflection of neutrons travelling parallel to the slot back into the detector.

Tungsten did not perform well using the ideal collimator model, however the prolific scattering characteristics illustrated in this section may provide good collimation in an alternative configuration which takes advantage of this very short mean free path. This was further investigated in section 4.4.7.

4.4.7 Collimation theory III: anti-collimation

The collimator design up to this point has relied on using shield materials to block out all but a narrow sensitivity region. In low-mid dose applications (where the detector would not be easily saturated), an anti-collimation method has also been investigated to improve the contrast in the sensitivity function. This method acts in the reverse sense, to leave the detector completely unshielded and highly sensitive with the exception of a narrow band which is shielded; it relies on a decrease in radiation events rather than a peak to indicate the presence of sources.

Energy dependence of scatter materials

The materials discussed in Table 4.2 were re-interrogated this time for the transmission of neutrons which did not undergo a reaction and passed straight through the 10 cm shield. Neutrons incident on the detector which did interact were likely to be scattered and therefore not detected.

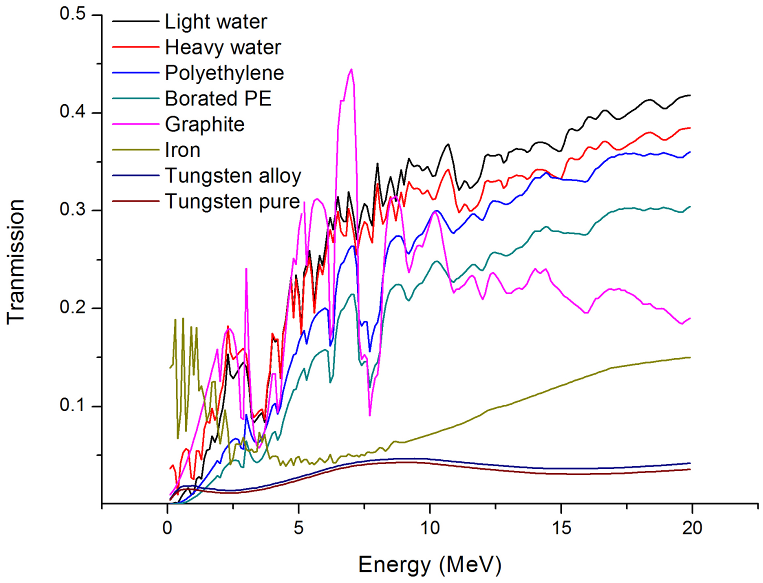

Figure 4.20 Energy dependent transmission of uncollided neutrons through 10 cm of shield material as a function of energy. Calculated using MCNP.

The results from these tallies can be seen in Fig. 4.20. Here the -0000000001 tag in MCNP was used to segregate uncollided neutrons in the tally, i.e. to only tally neutrons which had not undergone reactions before detection. We see here that the heavy metals have the advantage over the lighter isotopes, and very few uncollided neutrons are tallied at all energies. It is apparent that the probability of scattering is highest in the heavier elements than in the light elements and therefore these more easily lose their directionality. The lack of moderation may not be an issue in this geometry as the approach relies solely on altering the directionality of incident neutrons rather than the energy.

Anti-collimator model

The first concept design for the anti-collimator system was a spherical detector of radius 3 mm and a shield fin; a 6 mm thick semicircular piece extending from the surface of the detector sphere to the outer radius of 10 cm. This piece is an inverse of the ideal collimator model described in section 4.4.6, used with a smaller detector to remove unshielded overlap. This was designed to leave the detector unshielded from all angles with the exception of a single shielded region from a small azimuth range and elevation range from -90° to 90°. This geometry used a radiation decrease to indicate the presence of sources. The first concept anti-collimator shown in Fig. 4.21 was used to assess shield materials in this geometry.

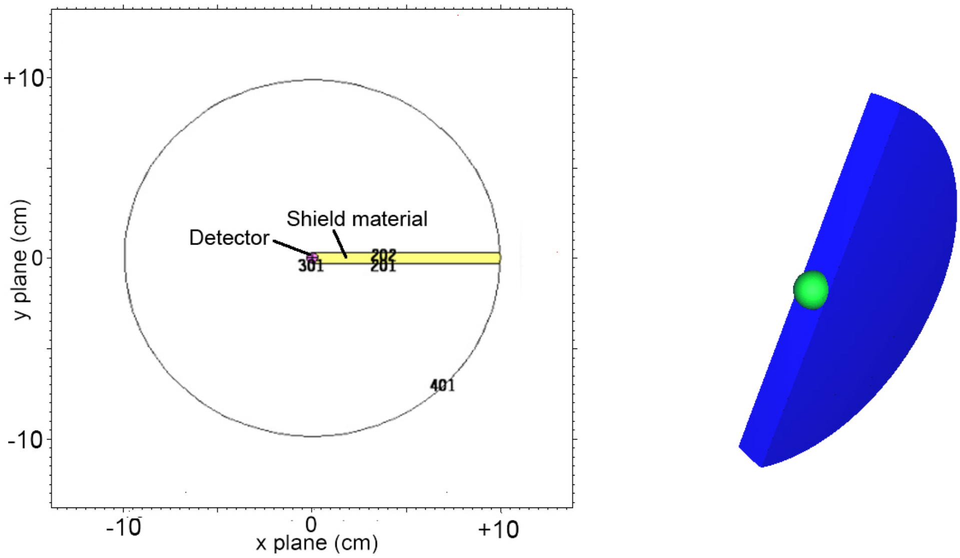

(a) Annotated model in z-plane

(b) 3D visualisation of model

Figure 4.21 The first concept anti-collimator MCNP model comprising scintillation detector cell and fan-shaped shield.

Material assessment

Borated PE, iron and pure tungsten were investigated further using the method outlined in section 3.4.1 to characterise the collimators as a function of θ between 0° and 360° with $\phi = 0°$. Three different neutron energy spectra were used: ^{235}U fission, a uniform energy distribution between 0.1 and 20 MeV and deuterium-tritium fusion at 10 keV producing an average neutron energy of 14.1 MeV. The functions were then analysed to find the FWHM and signal-to-noise ratios in each case. The results are shown in Table 4.6.

Table 4.6 Signal-to-noise ratio and FWHM of first concept anti-collimator derived from MCNP with BPE, iron and tungsten shield materials with three incident neutron energy spectra.

	U-235 fission		Uniform energy		DT fusion	
Material	S/N	FWHM(°)	S/N	FWHM(°)	S/N	FWHM(°)
Borated PE	0.970	14.54	0.834	9.94	0.647	7.11
Iron	0.872	11.07	0.868	10.33	0.838	8.42
Pure tungsten	0.978	13.89	0.942	11.57	0.916	9.35

The results in Table 4.6 indicate that tungsten is the best material for this geometry, having the highest signal-to-noise ratio in every case (with a theoretical limit of 1) which was calculated to be 92% at neutron energies of 14.1 MeV. This means that this method may be used to image high energy neutron fields, such as those emitted during thermal deuterium-tritium fusion, showing a clear advantage in imaging capabilities over the original shielded collimator design. This collimator design was also much lighter as the required volume is considerably smaller. A borated PE collimator could be made extremely light using this geometry ($\approx$ 100 g using this model) and could be useful in some situations where weight is highly restricted. One drawback of this geometry is that the detector remains unshielded to the majority of solid angles and could easily become saturated in high-flux radiation fields.

Conclusions

The sensitivities of both designs (borated PE and tungsten) would be suitable for neutron imaging at all energies tested. Tungsten has an excellent sensitivity matrix with close to 100% contrast at all tested energies including 14.1 MeV neutrons. This was attributed to the high interaction cross section of tungsten with neutrons across the tested energy range compared with other materials. This demonstrated that this method of anti-collimation, reliant on altering only the directionality of the neutron field, might work successfully. The use of an anti-collimator, essentially a small shield for a small number of solid angles rather than shielding all solid angles as with a traditional collimator, allows extremely lightweight and compact probes to be developed. Imaging capabilities up to 20 MeV neutrons and beyond may be achieved. This approach may be used in any circumstance where the detector does not become saturated, though saturation will occur more commonly due to the low amount of shielding, particularly due to gamma rays.

4.4.8 Collimator C3: tungsten anti-collimator

Design

It has been shown in the previous section that a higher signal-to-noise ratio in the neutron sensitivity matrix can be achieved by using an anti-collimation approach (compared with traditional collimation methods). The best material for this method has been identified as tungsten for all energies due to its larger macroscopic scattering cross section. An MCNP model was developed and investigated to optimise the sensitivity matrix for use in neutron imaging. The anti-collimator was bounded by the following parameters: a thickness of 18 mm to prevent unshielded overlap of the detector scintillation cell and a maximum radius of 10 cm to keep the probe compact.

The collimator was modelled in MCNP with an 18 mm thickness. The outer radius was 10 cm and the inner radius was varied between 1.5 and 5.5 cm. The distribution was analysed to find the signal-to-noise ratio and the FWHM in each case. The results from this experiment are summarised in Fig. 4.22. Fig. 4.23b shows the MCNP model used for this investigation with the inner radius set to 5 cm. The lowest tested inner radius, 1.5 cm, had the highest signal-to-noise ratio but a large FWHM above 30. With increasing inner radius the value of FWHM falls off rapidly, whilst the S/N falls off more slowly.

At least 5 cm of shielding was needed to achieve a signal-to-noise ratio of greater than 80%. Two designs were then proposed, anti-collimator A which sought to minimise volume and weight, and anti-collimator B which sought to produce an optimal function for high resolution imaging. These geometries were investigated further using the method outlined in section 3.4.1 to characterise the collimator sensitivity. The function of θ between 0° and 360° with $\phi = 0°$ was analysed to find the signal-to-noise ratio and FWHM in each case.

Characterisation

The MCNP models used for interrogation of designs A and B are summarised in Fig. 4.23. The resulting sensitivity matrices are shown in Fig. 4.24. The signal-to-noise ratios and FWHM are summarised along with other parameters of each design in Table 4.7. Design B, though heavier and larger in radius, gave a much sharper response function (smaller

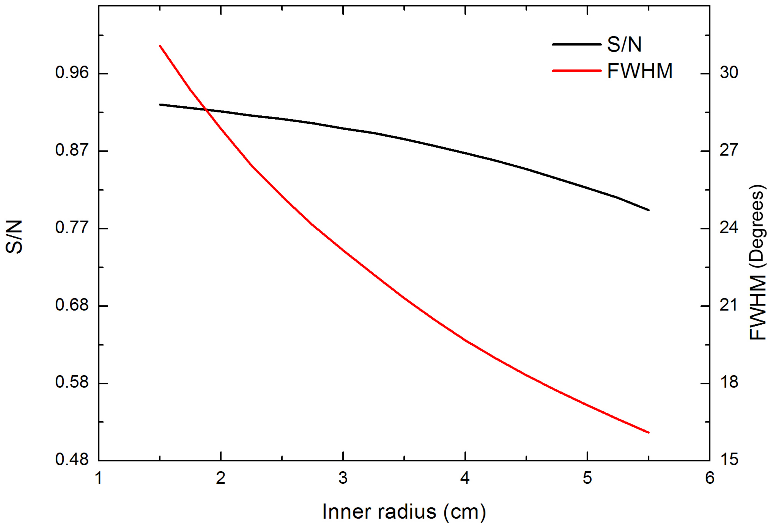

Figure 4.22 MCNP-calculated signal-to-noise ratios and FWHM values derived from MCNP simulations of a tungsten alloy anti-collimator with thickness 18 mm, outer radius 10 cm and a variable inner radius.

FWHM) which is required for high resolution imaging. The properties of these designs are summarised in table 4.7. Design B was chosen due to the smaller FWHM (factor of 2.2), given that the weight and radius were already within the specification of the research goals. Collimator B was procured and manufactured, alongside a portable mount to allow an anti-collimated imaging system to be built.

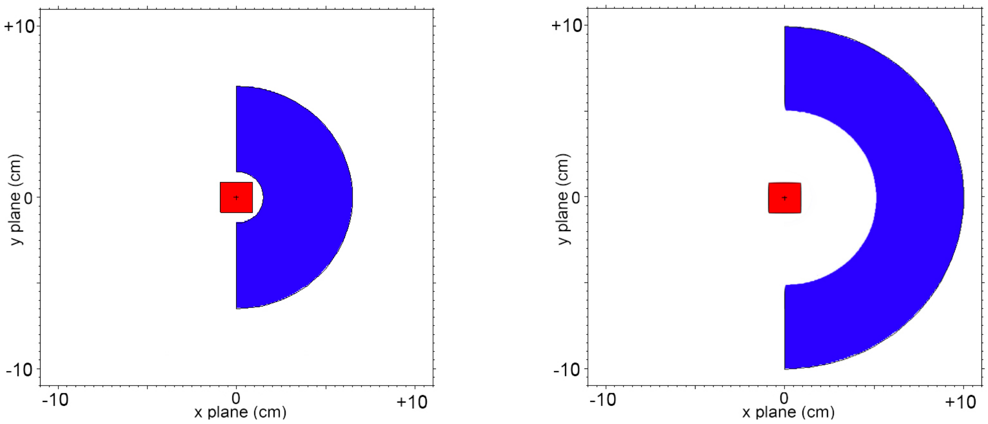

(a) Anti-collimator geometry A (b) Anti-collimator geometry B

Figure 4.23 MCNP models in the z-plane of two investigated anti-collimator geometries A and B.

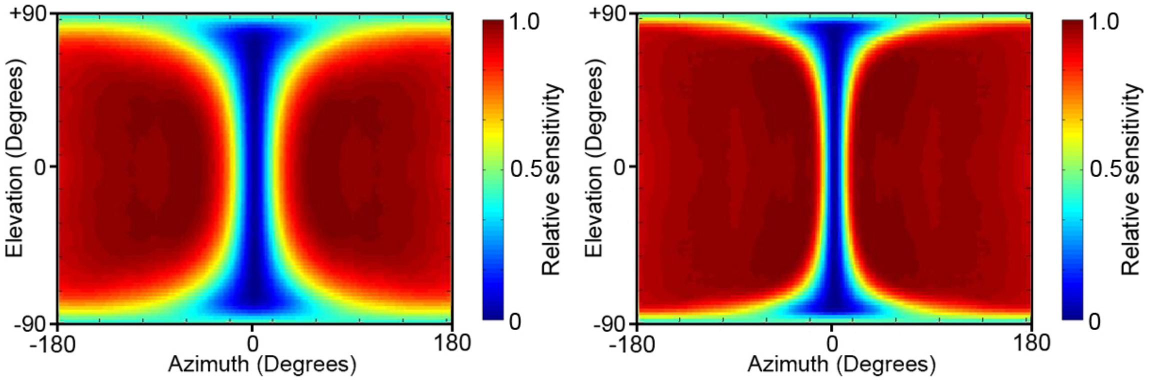

(a) Anti-collimator A geometry (b) Anti-collimator B geometry

Figure 4.24 MCNP-derived sensitivity maps for tungsten anti-collimator designs A and B.

Table 4.7 Signal-to-noise ratios and FWHM values derived from MCNP for two anti-collimator geometries.

Geometry	S/N	FWHM(°)	Weight	Outer radius
Geometry A	0.762	27.8	2.05 kg	6.5 cm
Geometry B	0.766	12.6	3.84 kg	10 cm

Analysis and validation

This experiment was performed to test the functionality of the tungsten anti-collimator C3 and measure a part of the sensitivity matrix *S* for validation with Monte Carlo calculations.

The anti-collimator imaging system was set up in the radiation laboratory at Lancaster University containing the ^{252}Cf source. The detector was located at 35 cm height, level with the source, and 20 cm horizontally along the normal of the face of the steel shield. The source was exposed and discrimination parameters were set. The source was a distance of 45 cm from the rotational centre of the imager. The discrimination parameters were set identical to the subsequent imaging experiments and can be seen in Fig. 6.2.

Data were collected as the collimator was rotated 360° through the pan angle in increments of 2°. The slot angle was kept constant at 0°. The number of neutrons and gamma rays at each angle were totalled for 400 seconds. The results are presented in Fig. 4.26. Both functions show a clear dip in signal at close to 90°, corresponding to the anti-collimator obscuring the source from the detector. A second dip is observed in both functions at 270°; this corresponds to the rear of the mount obscuring the source from the detector. The mount had a complex geometry which was not fully known internally and therefore was not easily modelled in MCNP. The initial dip at 90° can however be used to validate the MCNP model of the collimator.

When assembled, this imaging system did not have the detector in the exact rotational centre when rotated through the pan angle; the detector is offset by 5 cm, i.e. the rotational centre to detector distance r_{ID} = 5 cm (this has no dependence on rotation through the slot angle). As the pan angle was changed during data collection, the source-detector distance r_{SD} varies and resultantly the number of radiation events was influenced by this motion. The detector response with angle $S(\hat{\beta})$ would be expected to vary as the inverse of square distance as shown in Eq. 4.2. This geometry is illustrated in Fig. 4.25. This effect is prominent when r_{SI} is comparable to r_{ID}, as in this case, and is negligible when $r_{SI} \gg r_{ID}$.

$$S(\hat{\beta}) = \frac{a}{r_{SD}^2(\hat{\beta})} \tag{4.2}$$

This effect must be better understood in order to validate the MCNP model of the collimator. The function must be derived such that it can be accounted for in the data. The source-detector distance r_{SD} can be described by the vector triangle illustrated in Fig. 4.25b leading to Eq. 4.3. Resolving these vectors into x and y components yields Eq. 4.4 and Eq. 4.5.

$$\mathbf{r}_{SD} = \mathbf{r}_{SI} + \mathbf{r}_{ID} \tag{4.3}$$

$$r_{SD}^x = r_{SI} - r_{ID}\ \cos(\hat{\beta}) \tag{4.4}$$

$$r_{SD}^y = r_{ID}\ \sin(\hat{\beta}) \tag{4.5}$$

The value for r_{SI}^2 can therefore be expanded to Eq. 4.6 by adding the squares of the x and y components, simplified to Eq. 4.7.

$$r_{SD}^2 = r_{SI}^2 - 2r_{SI}\ r_{ID}\ \cos(\hat{\beta}) + r_{ID}^2\ \cos^2(\hat{\hat{\beta}}) + r_{ID}^2\ \sin^2(\hat{\beta}) \tag{4.6}$$

$$r_{SD}^2 = r_{SI}^2 + r_{ID}^2 - 2r_{SI}\ r_{ID}\ \cos(\hat{\beta}) \tag{4.7}$$

This is further simplified and generalised to be of the form shown in Eq. 4.8 where quantities have been absorbed into constants b and c. d has been included to add a degree of freedom on the angular fit. ω is the period of the response which was 180 pan angles between 0° and 360° (every 2°) for all work conducted with this system configuration.

$$r_{SD}^2 = b - c\ \sin\left(\frac{\hat{\beta} - d}{\omega}\right) \tag{4.8}$$

Assuming the count rate can be approximated by an inverse-square law with source-detector distance, as described in Eq. 4.2, it would be of the form shown in Eq. 4.9. Note that this function ignores any interaction of the collimator and provides a baseline due only to detector motion as a result of the rotational offset.

$$S(\hat{\beta}) = \frac{a}{b - c\ \sin\left(\frac{\hat{\beta} - d}{\omega}\right)} \tag{4.9}$$

The response data were fitted with the function described in Eq. 4.9, and are seen in Fig. 4.26. The data used in the fit excluded points where either the collimator or part of the mount obscured the path of radiations from the source to the detector. The remaining regions contain major dependence on the source-detector distance.

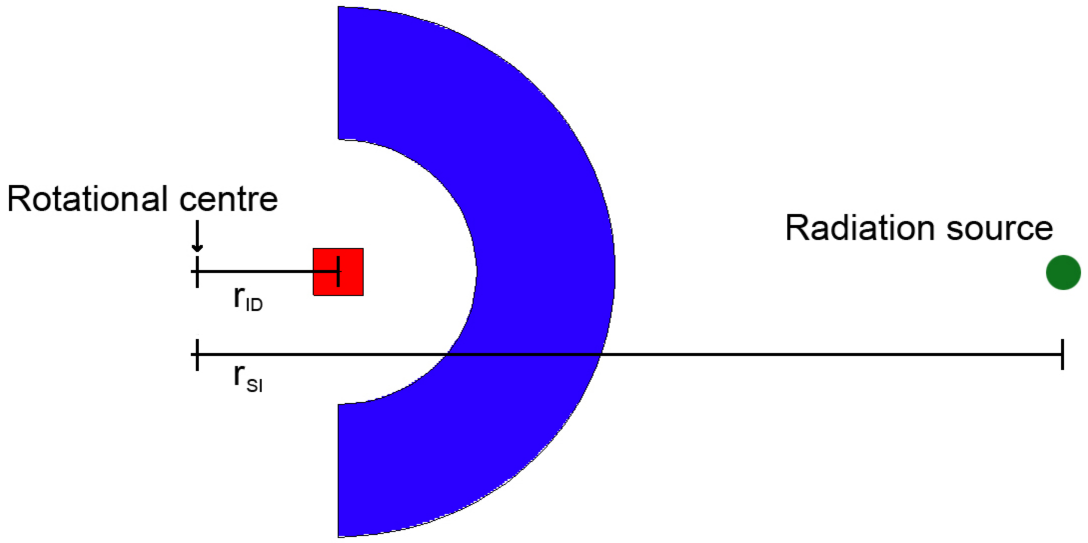

(a) Side view with pan angle $\hat{\beta}$ = 0° $\hat{\alpha}$ = 0°

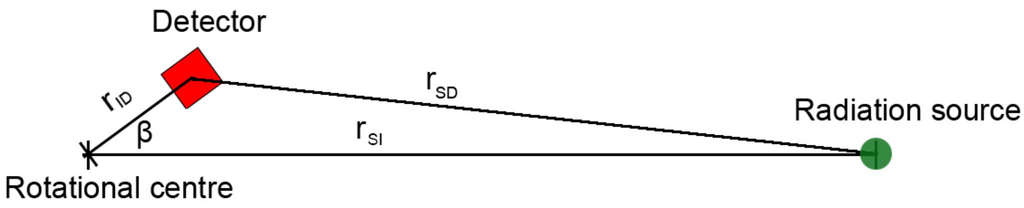

(b) Top view without collimator, rotated through pan angle $\hat{\beta}$

Figure 4.25 Geometry of the anti-collimator mounting illustrating the vectors between the detector, the rotational centre and a source.

The corrected data and the corresponding MCNP calculations are shown in Figs. 4.27 and 4.28, illustrating that the MCNP-calculated values provide a reasonable response. A major difference is that the second drop (at around 135 °) was not present in the simulated data. This was due to a component of the mount which had a complex geometry and the material composition was unknown. This was not problematic for imaging as long as data were not collected where the mount blocked the detector. The cosmic neutron background also contributed to the experimental results, increasing the counts for all pan positions.

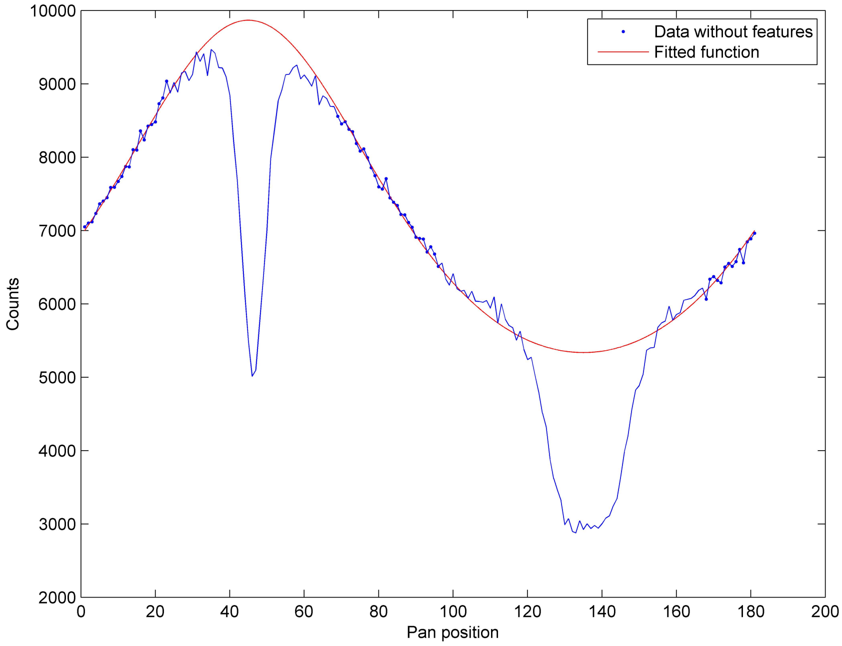

(a) Neutron events

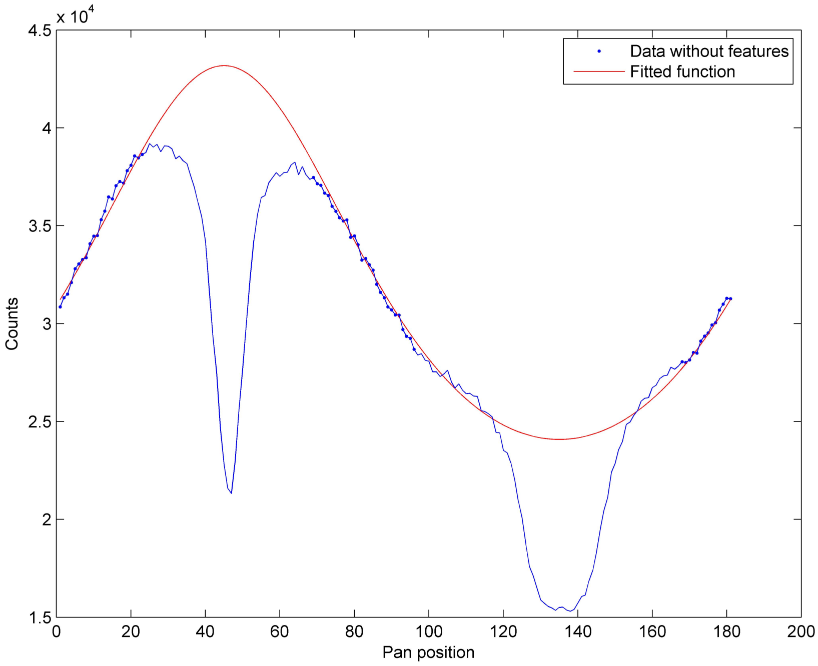

(b) Gamma-ray events

Figure 4.26 Plots of experimentally determined radiation counts as a function of angle $\hat{\beta}$ with $\hat{\alpha} = 0°$ for the anti-collimator imaging system. Data have been fitted with Eq. 4.9. Data points from the two regions where the events drop due to shielding have been excluded from the fit: the first is due to the shielding of the anti-collimator, the second due to a piece of the mount which obscures the detector. Excluding these regions allows the data to be fitted with a function which is dependent only on the detector displacement relative to the source.

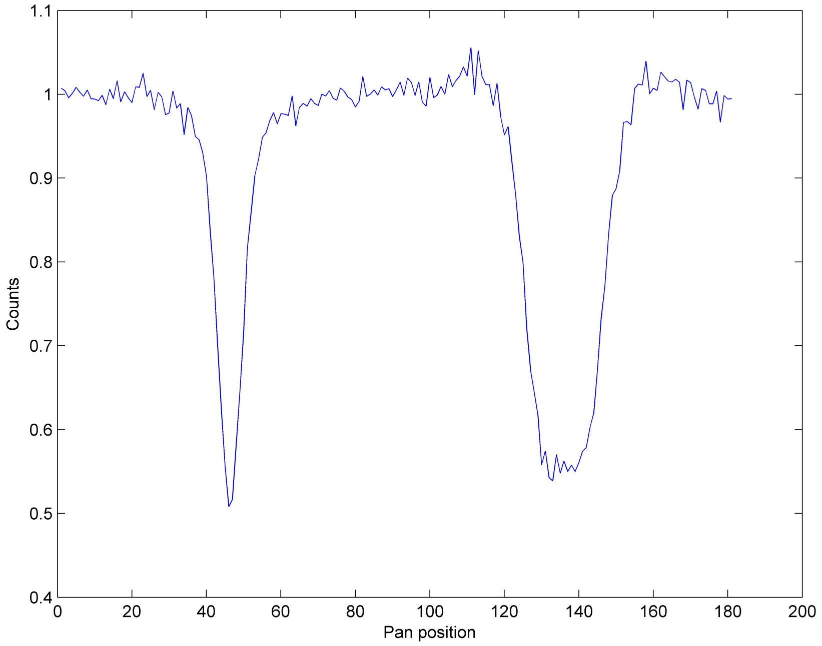

(a) Discriminated neutron events

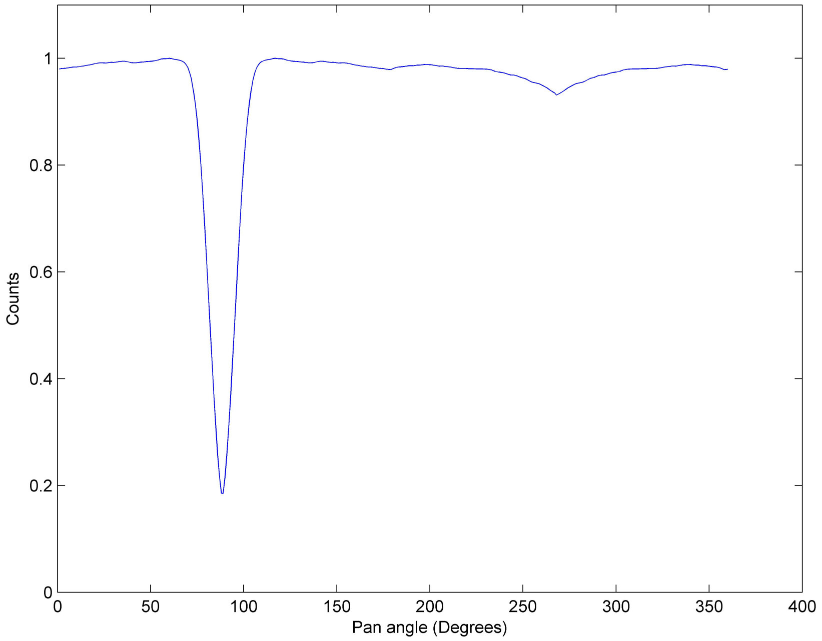

(b) MCNP-calculated neutron events

Figure 4.27 Plot of events as a function of angle $\hat{\beta}$ with $\hat{\alpha} = 0°$ for the anti-collimator imaging system. The data have been corrected for the detector displacement and normalised.

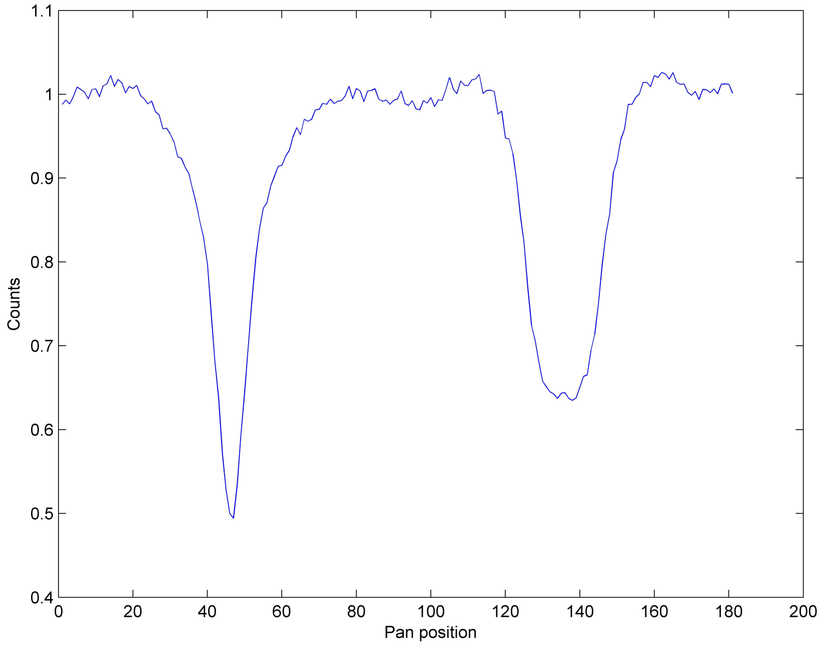

(a) Discriminated gamma-ray events

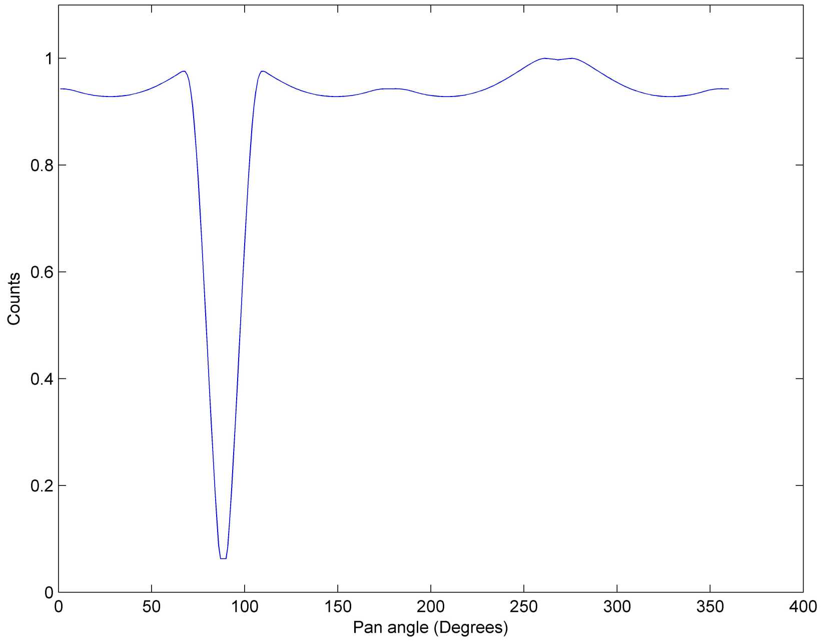

(b) MCNP-calculated gamma-ray events

Figure 4.28 Plot of events as a function of angle $\hat{\beta}$ with $\hat{\alpha} = 0°$ for the anti-collimator imaging system. The data have been corrected for the detector displacement and normalised.

4.5 Custom pulse counter testing

The event counter was tested using both a signal generator and a comparison of the recorded counts with those counted in the MFA software. For the first test the signal generator produced square waves with amplitude 3.8 V, matching the MFA TTL outputs, and the number of pulses was counted over the range 1 - 20 MHz. At the high end frequency this matches the TTL output width of 50 ns. Very good agreement within 0.1% was seen between the generated frequency and the frequency measurement recorded by the counters over various time windows. Secondly, experiments were performed to compare the events recorded by the event counter and the MFA software counter produced by detections of gamma rays emitted from a ^{137}Cs source. Identical agreement was seen over the Ethernet-limited range of 0 to 35 counts per second.

4.6 Uncollimated multi-detector source tracking development

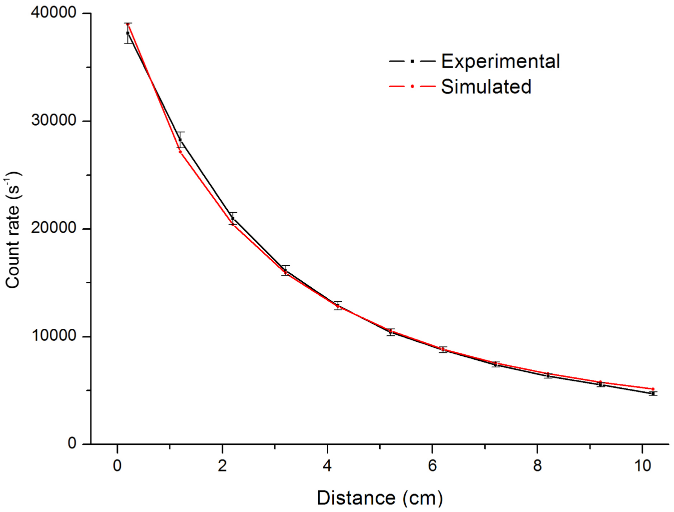

Figure 4.29 Characterisation of square EJ-309 detector via a plot of count rate versus distance drop off for experimentally-obtained results and MCNP results.

MCNP was used to characterise the cubic EJ-309 detector, to a point-source in variable positions as outlined in section 3.3.5. This characterisation was validated using a series of measurements of the detector count rate drop with increasing distance between the source and the face of the detector. The experimental set-up was as outlined in section 7.1. A single 320 kBq ^{137}Cs source was placed at a variable distance from the centre of the detector front face and the time interval was adjusted such that the statistical error on the count rates were below 5% in each case. The count rate was calculated at each position and the corresponding MCNP values were fitted to the experimental results using a least-squares fit to validate the model, seen in Fig. 4.29. Here the shape of the drop off was important, rather than the absolute values due to the method calculating the ratios only.

4.7 Spectroscopy

4.7.1 Gamma-ray spectroscopy and estimation of the low-energy cut-off for photons and neutrons

The detector and MFA system were characterised with respect to the gamma-ray response. Due to the signal processing performed by the MFA, it was necessary to consider the response involving both pieces of apparatus. The lower energy cut-off to photons was determined by the trigger amplitude of the MFA and not by the detector itself (to avoid processing noise signals). This cut-off was also associated with some uncertainty, due to the fact that the MFA triggers on a single amplitude bin which has a larger statistical error than the smoothed function used to obtain the amplitude.

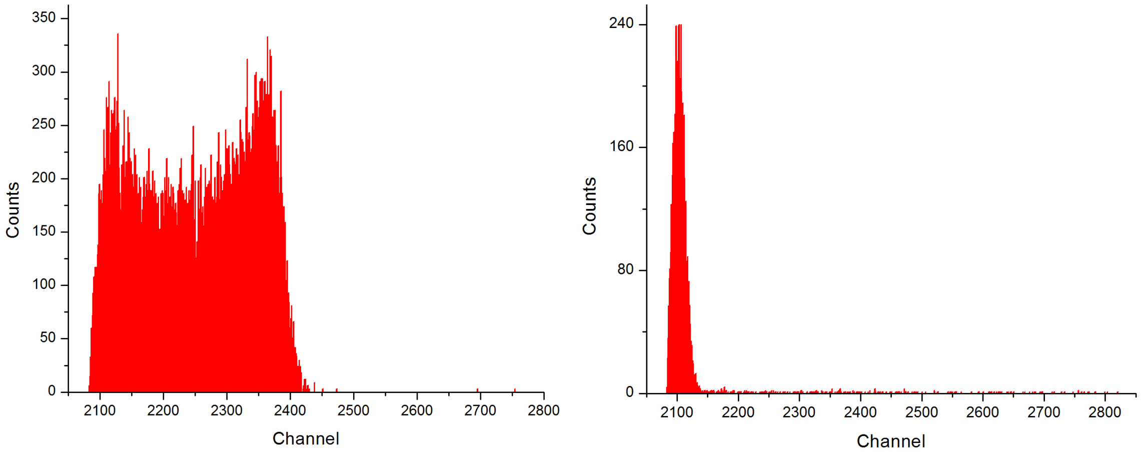

(a) Pulse-height spectrum for ^{137}Cs (b) Pulse-height spectrum for ^{241}Am

Figure 4.30 Pulse-height spectra from gamma-ray sources obtained from measurements with the miniature EJ-301 detector.

Pulse-height spectra were collected from two gamma-ray sources, ^{137}Cs and ^{241}Am, using the single channel MFA. These spectra are seen in Figs. 4.30a and 4.30b respectively. The sources were placed against the detector face and the peak pulse amplitudes from the detector were accumulated by the MFA until the shape of the distribution had reasonably converged. The detector interactions were also modelled using MCNP and can be seen in Figs. 4.31a and 4.31b.

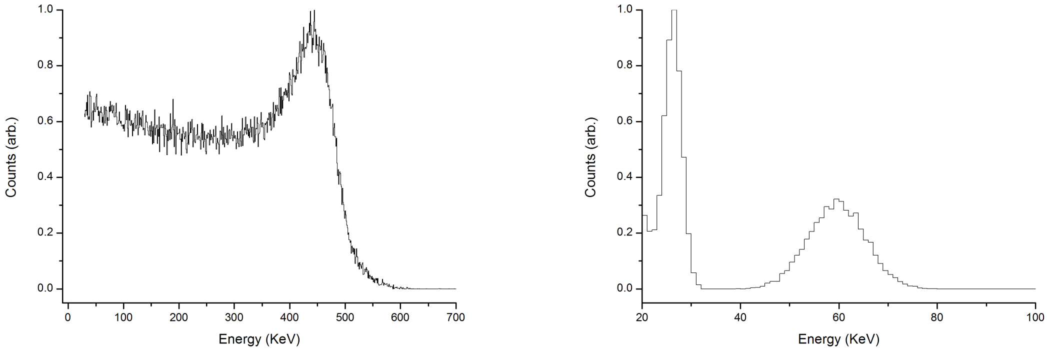

(a) Simulated pulse-height spectrum for ^{137}Cs (b) Simulated pulse-height spectrum for ^{241}Am

Figure 4.31 MCNP-calculated pulse-height spectra from gamma-ray sources obtained from miniature EJ-301 detector.

The spectrum from ^{137}Cs shows no full-energy peak, though the Compton background distribution is clearly visible. Due to the small size of the miniature EJ-301 and the absence of high-Z materials in the detection volume, nearly all 662 keV photons escape before depositing their full energy in the scintillator. The 59 keV photons produced by ^{241}Am give a single peak in the spectrum just above the energy cut-off of the detector. From comparison with the simulated result, this could be seen to be the full energy peak at 59 keV. The photon energy cut-off of the equipment was taken as 59 keV. Fig. 2.9 gives the light output function of protons and electrons for the EJ-301 scintillator can be used to estimate the neutron energy cut-off of equal light output at around 400 keV. Higher thresholds could be applied as required by the MFA trigger or with the PSD line. These thresholds were applied where relevant using this method.

4.7.2 Neutron spectroscopy

Pulse-height spectra were collected using a miniature EJ-301 detector and a single channel MFA at the Neutron Metrology Group, NPL, Teddington UK. The unshielded detector was placed 5 cm from the source, the discrimination parameters were set and data were collected over the Ethernet link to the PC until 60k neutron counts had been collected (typically 15 - 30 minutes). The sources used were unshielded and unmoderated. These spectra can be seen in Fig. 4.32 and were used as the basis for source identification with neutron spectroscopy.

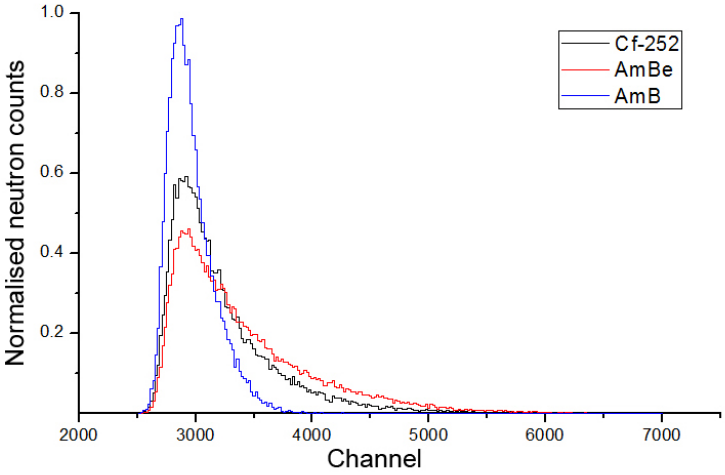

Figure 4.32 Discriminated neutron pulse-height spectra recorded from the miniature EJ-301 detector for ^{252}Cf, ^{241}Am/Be and ^{241}Am/B. Note that channel position is arbitrary.

Chapter 5

Collimated single-detector imaging

Chapter summary

This chapter includes information on all key imaging experiments performed with the collimated single-detector imager configuration during the research including the set-up, calibrations, unprocessed image data and the image solutions. Simulation results are also provided where applicable to provide comparison with recorded images or to illustrate additional information.

5.1 Experiment 1: ^{252}Cf, ^{241}Am/Be and ^{22}Na Orthogonal-slot node imaging

All results in this section have been published in a peer-reviewed journal [122].

5.1.1 Introduction and rationale

Imaging combined neutron and gamma-ray fields using a collimated back-projection method has been performed in previous research with a cylindrical collimator [97] [98] [100]. Raster scanning such a collimator over angular space allows image data to be accumulated one "pixel" at a time, where the "pixel" represents the solid angle of the sensitivity region, i.e. the unshielded area or "view" through the cylinder. The introduction of a slot-shaped collimator allows data from a large solid angle to be accumulated, the equivalent of a line including several "pixels" at once. This addresses the bottleneck of single detector imaging systems: low efficiency due to high shielding. By collecting data over multiple regions simultaneously, more data can be collected per position of the collimator. Image resolution is not affected as this is maintained by the width of this slot. The experiment performed here was designed to test the efficacy of a slot collimator at imaging a multi-source combined neutron and gamma-ray field using a fully-automated compact probe.

5.1.2 Experimental set-up and apparatus

The apparatus used in this experiment is summarised in Table 5.1. This experiment was performed at the Schuster Laboratory, University of Manchester, UK.

The imaging system was assembled on a trolley approximately 50 cm above the ground. This allowed the height and position of the imager to be easily adjusted. The ^{241}Am/Be source was placed in the horizontal plane containing the detector, 10 cm from the detector face (with the collimator present). Radiation events were collected for 1 hour and were used

Table 5.1 Summary of materials and methods used in experiment 1.

MFA	Single channel MFAX1 [section 3.2.2]
Data collection	Ethernet
Discrimination	Real-time
Detector(s)	Miniature EJ-301 4 ml [section 3.2.1]
Collimator	Tungsten and PVC C1 [section 3.2.3]
Imaging method	Orthogonal-slot node imaging [section 3.3.2]
Imaging parameters	2 slot × 15 pan , t_d = 2 min
Radiation sources	^{241}Am/Be with 1 cm lead shield (2.2×10^5 neutrons s^{-1}), ^{252}Cf (1.5×10^5 neutrons s^{-1}), ^{22}Na (560 kBq)

to set the discrimination parameters in this experiment which were performed in real-time following this calibration.

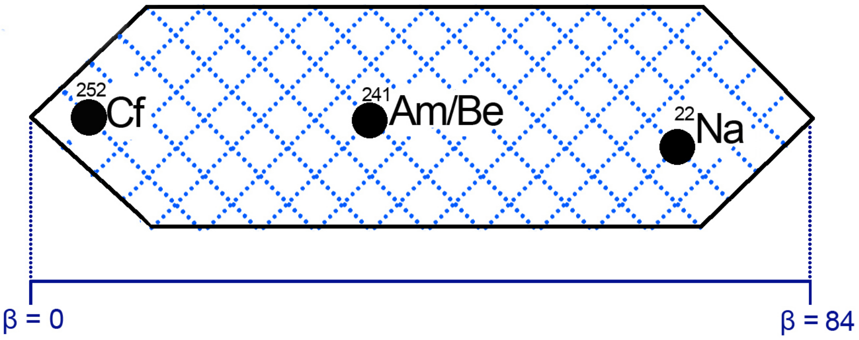

Figure 5.1 Radiation source and measurement geometry in experiment 1 showing the location of radiation sources in the vertical plane from point-of-view of the probe. The black line represents the region where radiation sources must be (in prior knowledge), the blue dotted line represents projections of the sensitivity region, i.e. the detector field of view for a measurement position [122].

The three radiation sources were placed in the plane containing the geometric centre of the detector. The sources were positioned 1 m from the detector face and 50 cm apart from each other. The sources are ^{252}Cf (left), ^{241}Am/Be (centre) and ^{22}Na (right). The sources were in the geometric centres of their containers. Source details are in Table 5.1. A corresponding diagram of the source layout and imaged area is shown in Fig. 5.1. The total imaged area is depicted by the black outside border. This method has a prerequisite that radiation sources were only present inside this imaged area. The source locations are depicted within the imaged region. The blue dashed lines represent projections of the slot where data were collected, i.e. the centroid of the sensitivity region and are spaced by 6°. The imaging routine was initiated and the data set was collected; the total collection time for this image was approximately 1 hour. The image solution was produced using the orthogonal-slot node imaging method outlined in section 3.3.2 and overlaid on an optical image taken from the detector position, i.e. the image origin.

5.1.3 Results

The discrimination set-up used in this experiment is illustrated in Fig. 5.2 and the measured GARR using a ^{22}Na source was 3.44%. The unprocessed image data recorded in this experiment are illustrated in Table 5.2. This table shows the number of events detected at each angle for two orthogonal collimator rotations. The radiation image solutions for this experiment are shown in Figs. 5.3a and 5.3b, the neutron and gamma-ray images respectively. The colour scale is related to the observed count rate as outlined in section 3.3.2.

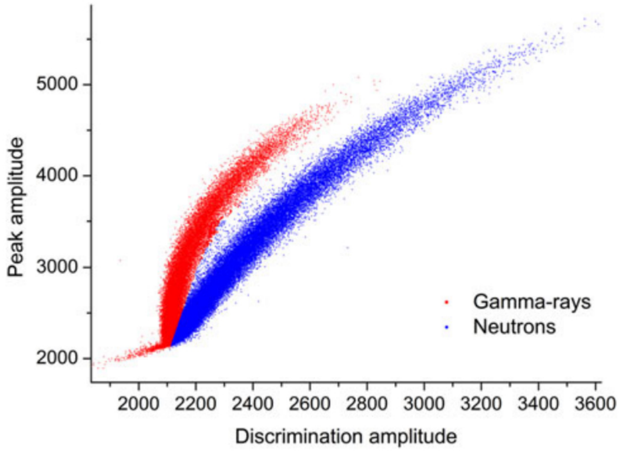

Figure 5.2 Plot of events as a function of the discrimination parameters in experiment 1 showing discriminated gamma rays in red and neutrons in blue [122].

Table 5.2 Raw image data collected in experiment 1 for discriminated neutron and gamma-ray events as a function of $\hat{\beta}$ angle at two orthogonal $\hat{\alpha}$ angles, denoted here $\hat{\alpha}_1$ and $\hat{\alpha}_2$. n and γ indicate neutron and gamma-ray data respectively.

Angle	0°	6°	12°	18°	24°	30°	36°	42°	48°	54°	60°	66°	72°	78°	84°
n$\hat{\alpha}_1$	269	254	280	333	274	240	263	302	260	268	251	255	243	259	254
n$\hat{\alpha}_2$	274	308	269	260	261	270	284	276	251	224	238	252	237	226	226
$\gamma\hat{\alpha}_1$	803	698	828	947	825	837	831	797	771	737	734	808	837	1023	975
$\gamma\hat{\alpha}_2$	802	931	840	809	779	802	811	788	847	865	995	994	866	787	788

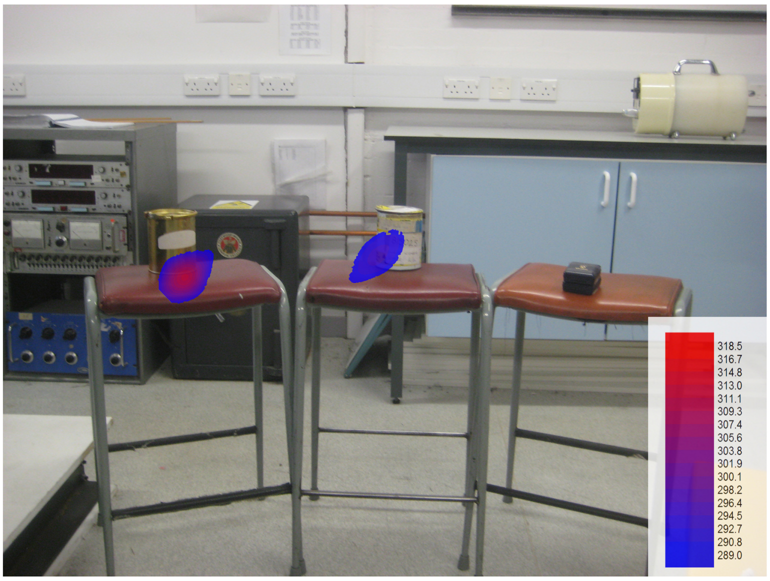

(a) Neutron image solution [122]

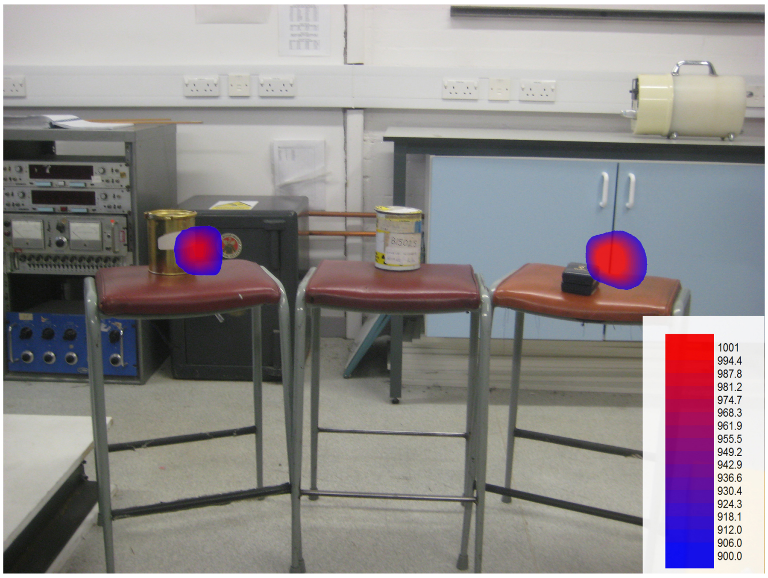

(b) Gamma-ray image solution [122]

Figure 5.3 Radiation images produced in experiment 1 of neutron and gamma-ray fields overlaid on optical images. The three sources are (left to right) ^{252}Cf, ^{241}Am/Be, ^{22}Na placed on stools level with imager.

5.1.4 Discussion

The discrimination plot shown in Fig. 5.2 demonstrates a clear separation of neutrons and gamma rays in the plot with some overlapping at lower energies. The discrimination line divides these distributions and the contribution of misclassified events are virtually all from the lower energy region, below 2800 peak amplitude. The GARR value is large compared with other experiments in this research, however due to the detection rates of neutrons and gamma rays being similar (the same order of magnitude), contributions from misclassification are relatively small. The effect is small enough for the neutron and gamma-ray fields to therefore be considered as independent, which is demonstrated in the resulting image solutions.

The unprocessed image data in Table 5.2 demonstrate that a significant number of neutrons are detected at each angle even when the slot is not directly aligned with a neutron source, giving a poor signal to noise ratio. The collimator is therefore unable to perfectly shield incoming fast-neutrons, a result which agreed with the collimator characterisation in section 4.4.2. This prompted a redesign of the collimator for later experiments.

The neutron image in Fig. 5.3a shows two hotspots of neutron radiation corresponding to the locations of the ^{252}Cf and ^{241}Am/Be sources. The cans containing the sources can be identified as such using the corresponding optical image and overlay. The gamma-ray image in Fig. 5.3b shows a single hotspot indicating that the small box contains a gamma-ray source which is ^{22}Na. The ^{252}Cf and ^{241}Am/Be sources also emitted gamma rays and were not visible in the gamma-ray images due to the higher gamma emission from the ^{22}Na source. This demonstrated the usefulness of combined neutron and gamma-ray imaging to ensure fewer sources escape identification.

This experiment was an early feasibility test of neutron imaging using a slot-collimated approach and the given equipment and methods. This method is limited in terms of the complexity of source distributions which can be successfully imaged and requires initial prior knowledge of the source distribution (in this specific case it must reside inside the black bounding line in Fig. 5.1: a $17^\circ \times 84^\circ$ window). The radiation image and optical overlay did not perfectly agree, possibly due to the shortcomings of the imaging technique and was a focus for improvement in later experiments. This experiment showed that this technique could be applied with these materials to successfully image combined neutron and gamma-ray fields and served as a foundation for the further development of the prototype using a slot collimator. The need for an improved signal to noise ratio from the collimator and image reconstruction technique was highlighted.

5.2 Experiment 2: ^{252}Cf and ^{241}Am/Be imaging with ART and source-type recognition with neutron spectroscopy

5.2.1 Introduction and rationale

Image reconstruction using algebraic reconstruction technique provides a method of analysis to solve a large matrix equation of image data for the most likely solution. It allows the specific response of a collimated detector to be taken into account and can rapidly find a solution of source distribution(s), given many thousands of data points. This allows the solution of data from many slot angles (in contrast to two slot angles in experiment 1) and many pan angles, to solve for up to full 4π images. Using this method, high resolution images can be produced with a lower data acquisition time than "pixel by pixel" imagers. Spectroscopy is commonly used with gamma-ray imaging to identify the distribution of specific radioisotopes. When collecting spectroscopic data, specific photopeaks can be selected and analysed allowing the corresponding radioisotope distributions to be imaged. For example, isolating the 662 keV peak would allow imaging of the ^{137}Cs distribution with minimal interference from other radioisotopes (in most cases). The general distribution of gamma-ray emitters can therefore be further interrogated.

This capability may also be advantageous when imaging neutron fields; for example in nuclear decommissioning applications, the ability to discern neutron-emitting materials (e.g. a shielded californium source from plutonium residues) might greatly impact the cost and strategy of a decommissioning operation. Knowledge of the distribution of radionuclides and/or their emitted neutron energies may lead to improved accuracy beyond imaging, for example dose maps of a given region which are dependent on the isotopic distribution.

This experiment sought to test the feasibility of source recognition using neutron pulse-height spectroscopy. First the sources were imaged to identify their locations, as would be the case without prior knowledge. The collimator slot was then oriented to each hotspot (corresponding to each source) in turn, and neutron pulse-height spectra were collected. These spectra were then compared with a library of spectra, previously recorded, used to identify the source type.

The C0 collimator was used for these experiments due to the minimal impact of the tungsten on the measured neutron pulse-height spectrum, due to the low energy loss per collision in high-A nuclides. In contrast, a hydrogenous collimator such as C1 would moderate the neutron energy spectrum, in turn shifting the pulse-height spectrum and making the spectra obtained from the imager more difficult to compare with those previously recorded.

5.2.2 Experimental set-up and apparatus

The apparatus used in this experiment are summarised in Table 5.3. This experiment was performed at the Schuster Laboratory, University of Manchester, UK.

The imaging system was deployed on a trolley raised approximately 50 cm from the ground. The ^{252}Cf source was placed in the horizontal plane containing the detector at 10 cm from the front of the face of the collimated detector. Data were recorded for one hour to allow set-up of the neutron-gamma discrimination parameters in post-processing.

The radiation sources were placed in the horizontal plane containing the detector, 50 cm from the detector front face. The sources were located in the geometric centres of the cannisters which were separated by 20° in azimuth. A photograph of this set-up is provided in Fig. 5.4 showing the probe, ^{241}Am/Be source (left) and ^{252}Cf source (right). The imaging routine was initiated and the data set was collected, the total data collection time for this image being 15 hours. Following these measurements, the probe was oriented to $\hat{\alpha} = 0°$, i.e. with the slot in the vertical position. The probe was then rotated through angle $\hat{\beta}$ such that the detector was directly facing the first radiation source, aligning the sensitivity region (the minimally shielded slot void). Spectroscopic data were collected for 30 minutes. This process was then performed for the second radiation source.

The image data were analysed using the ART algorithm outlined in section 3.3.3. The collected neutron spectra were analysed using the method outlined in section 3.3.6 using pre-recorded spectroscopic data shown in Fig. 4.32.

Table 5.3 Summary of materials and methods used in experiment 2.

MFA	Single channel MFAX1 [section 3.2.2]
Data collection	Ethernet
Discrimination	Post-processed
Detector(s)	Miniature EJ-301 [section 3.2.1]
Collimator	Tungsten C0 [section 3.2.3]
Imaging method	ART reconstruction [section 3.3.3]
Imaging parameters	35 slot × 49 pan, t_d = 30s
Radiation sources	^{241}Am/Be (target T_a) with 1 cm lead shield (2.2×10^5 neutrons s^{-1}), ^{252}Cf (target T_b) (1.5×10^5 neutrons s^{-1})

5.2.3 Results

The discrimination set-up used in this experiment is illustrated in Fig. 5.5. GARR was measured with a ^{137}Cs source at 1.21%. The unprocessed image data recorded in this

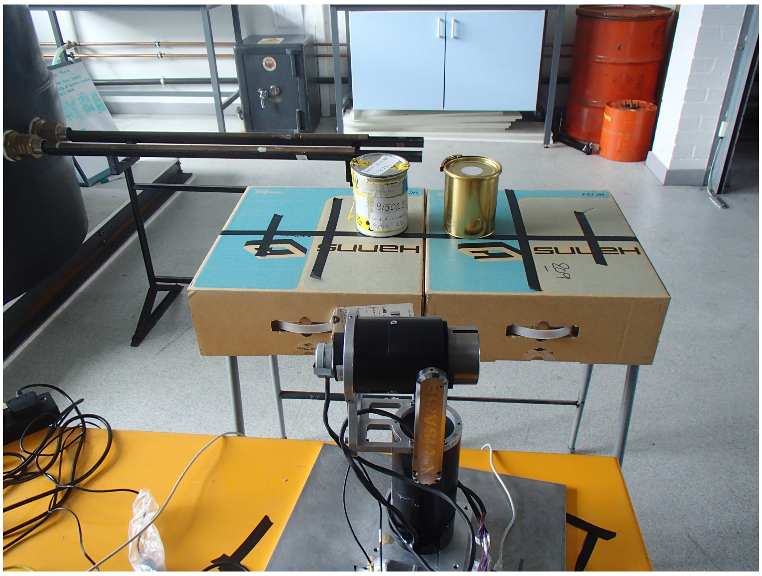

Figure 5.4 Photograph of the probe and radiation sources in experiment 2 during data acquisition. The two sources are (left to right) ^{241}Am/Be and ^{252}Cf placed on hollow cardboard and stools level with imager with a separation of 20° in azimuth.

experiment are shown in Fig. 5.6. The reconstructed neutron images are shown in Fig. 5.7. Fig. 5.7a shows the full neutron image solution; the same data have been replotted with a raised lower threshold on the colour scale shown in Fig. 5.7b. The associated gamma-ray image is also shown in Fig. 5.7c.

The results from the spectral analysis are shown in Fig. 5.8. At this stage it was assumed that two clusters of neutron-emitting materials had been identified from the image, their constituents were known to be of two types and the collected spectroscopy in each case was compared with that of ^{252}Cf and ^{241}Am/Be sources using the method outlined in section 3.3.6. Each experimentally recorded "target" spectrum from targets T_a (^{241}Am/Be) and T_b (^{252}Cf) was compared against a hypothetical spectrum comprising contributions from ^{241}Am/Be and ^{252}Cf. The contributions of each hypothetical spectrum were investigated over the weighting range 0% to 100% to find the lowest χ^2 value, and therefore closest match to the recorded "target" spectrum, e.g. the most likely ratios of ^{241}Am/Be to ^{252}Cf making up a "target" spectrum. Weighting w corresponds to the weighting of ^{241}Am/Be in the spectrum. The lowest χ^2 value for each "target" of spectroscopy indicates the scenario of closest match, and the relative weightings of the ^{241}Am/Be (w) and ^{252}Cf (1-w) neutron pulse-height spectrum in each target T_a (^{241}Am/Be) and T_b (^{252}Cf).

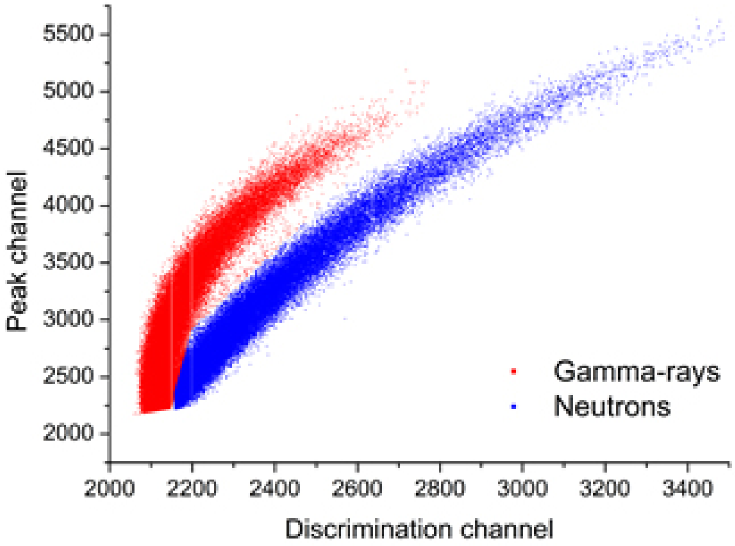

Figure 5.5 Plot of events as a function of the discrimination parameters in experiment 2 showing discriminated gamma rays in red and neutrons in blue.

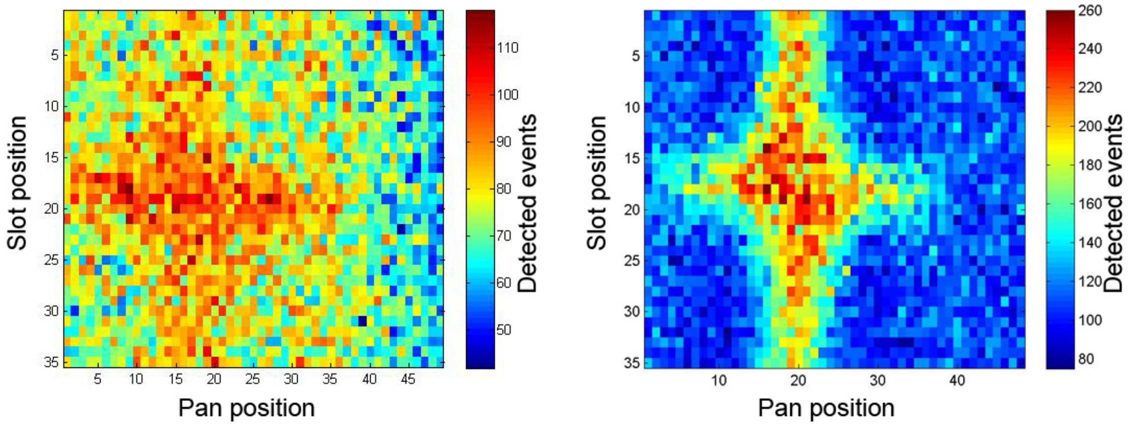

(a) Neutron image data

(b) Gamma-ray image data

Figure 5.6 Unprocessed image data obtained in experiment 2: discriminated events as a function of slot and pan position.

5.2.4 Discussion

The discrimination parameters shown in Fig. 5.5 demonstrate a clear separation of neutrons and gamma rays in the plot with some overlapping at lower energies. A modified polyline was applied in post-processing for neutron-gamma discrimination, allowing a lower GARR than in Experiment 1. This indicated better isolation of the neutron field, though a small

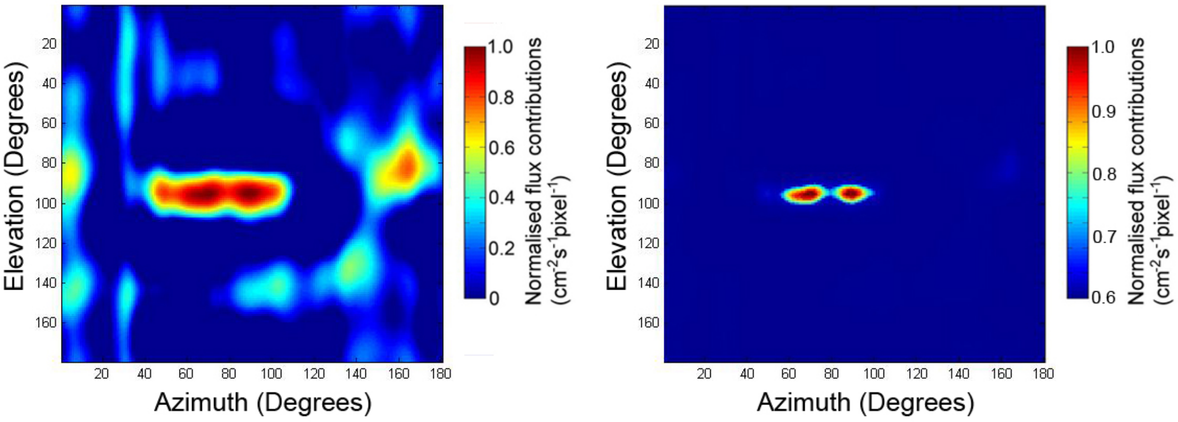

(a) Neutron image solution

(b) Neutron image solution with applied threshold

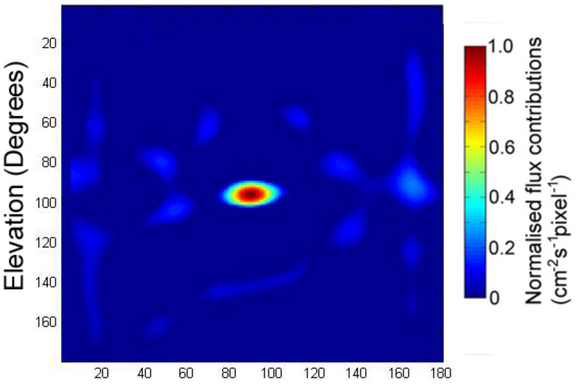

(c) Gamma-ray image solution

Figure 5.7 Radiation images produced in experiment 2 as a function of elevation and azimuth angle. Two sources are (left to right) ^{241}Am/Be and ^{252}Cf placed level with the imager at a separation of 20° in azimuth.

percentage of neutrons, estimated by GARR, will have been misclassified as gamma rays. The neutron image solution in Fig. 5.7a shows two hotspot regions, one centrally and one to the right-hand side of the plot. The central hotspot corresponds to the location of the two neutron sources which have not been individually resolved in this image solution. The hotspot to the right-hand side is an image artefact and does not correspond to the location of a neutron source; other smaller image artefacts also appear in other regions. These artefacts are a result of a mismatch between the sensitivity map and the physical collimated detector and manifest in regions where there is the least data available to define the solution, in these cases on the outsides of the image space. Applying a low-flux threshold to these images (Fig. 5.7b) removes these image artefacts and allows the two sources to be resolved. The

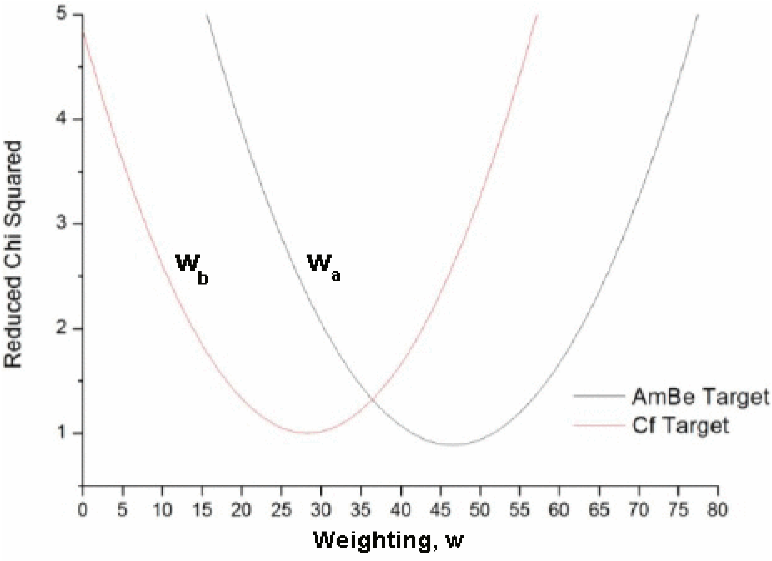

Figure 5.8 Plot of reduced chi squared values as a function of weighting, *w*, when comparing target spectra from ^{241}Am/Be (w_a) and ^{252}Cf (w_b) with hypothetical spectra comprising the fraction *w* of ^{241}Am/Be and (1-*w*) ^{252}Cf measured in isolation.

gamma-ray image in Fig. 5.7c shows a single hotspot corresponding to the location of the ^{252}Cf source. The ^{241}Am/Be source was not visible in the gamma-ray image which was thought to be due to the 1 cm lead shield reducing a significant proportion of the emitted gamma rays. These result therefore demonstrates the benefits of neutron imaging in addition to gamma-ray imaging allowing neutron sources to be identified in the presence of high-Z shielding.

The pulse-height spectrum fitting results in Fig. 5.8 show two minima at distinct weightings of *w* for each target. This demonstrates that the pulse-height spectra observed were significantly different in terms of containing unequal weightings of the ^{241}Am/Be and ^{252}Cf spectra. It can also be seen that when ^{241}Am/Be was the target, the spectrum could be identified to have a larger component of the ^{241}Am/Be spectrum when compared with the case when ^{252}Cf was the target and vice versa ($w_a > w_b$). These results indicate that a method of spectral analysis, such as this simplistic approach, performed alongside this method of radiation imaging, can be used to discern two sources of neutron radiation which emit different energy spectra.

The ability to discern each source in the image with this method demonstrates the successful application of the slot-modulated approach with ART reconstruction to combined fast-neutron and gamma-ray imaging. These images contained significant image artefacts which was a focus of further research. The limitations of this imaging approach were thought to be associated with the collimator C0 which only provided a limited spatial biasing compared with the further developments (see section 4.4), although the success of source identification was likely due in part to the preservation of the neutron energy spectra by limited energy loss in elastic scatters with tungsten. Spectral source identification with hydrogenous collimators would have to be investigated separately due to the moderating effects of such collimators. These results indicate that an integrated imaging system with combined source identification could be achievable. The ability to identify the radionuclide constituents in neutron emitters may also lead to higher accuracy in image reconstruction. This is because the collimator sensitivity map is a function of neutron energy, knowledge of the radionuclide type and emitted energy allows the sensitivity map to be calculated more accurately leading to more accurate image solutions. A possible research direction from this point was to expand upon this method by applying a more rigorous spectral analysis tool directly to image data. This was however discontinued because of the need to move to higher data collection speeds where spectral data was no longer supported by the MFAs.

5.3 Experiment 3: Survey of a ^{252}Cf neutron tank with ART

This section is adapted from a publication in a peer-reviewed journal [123].

Table 5.4 Summary of materials and methods used in experiment 3.

MFA	4 channel MFAX4.1 [section 3.2.2]
Data collection	Custom pulse counter [section 3.2.5]
Discrimination	Real-time
Detector(s)	Miniature EJ-301 4 ml and 1×10 cm cubic EJ-309 [section 3.2.1]
Collimator	Tungsten and P.E. C2 [section 3.2.3]
Imaging method	ART reconstruction [section 3.3.3]
Imaging parameters	88 slot × 91 pan (t_d in Table 5.5)
Radiation sources	^{252}Cf (75 MBq) [section 3.5.1]

5.3.1 Introduction and rationale

This experiment was performed to simulate a field deployment of the imager investigating combined neutron and gamma-ray fields and interactions with civil structures and shielding materials including concrete, steel and water. Survey points inside the laboratory were chosen quasi-randomly to simulate limited access associated with such surveys in the field. Inside the laboratory is a ^{252}Cf source stored in a water tank and surrounded by a steel shield (see section 3.5.1). The exposed neutron source was also in close proximity to the concrete floor and concrete block walls, therefore some contributions to the image were from scatter. For this reason, imaging parameters were optimised: a high number of slot and pan positions were used, i.e. many data points and the exposure time was chosen to be relatively long (t_d in Table 5.5) to ensure maximum fidelity of images in the reconstruction process.

5.3.2 Experimental set-up and apparatus

The apparatus used in this experiment is summarised in Table 5.4. This experiment was performed in the Department of Engineering, Lancaster University, UK.

The probe was assembled and moved to point C where radiation events were accumulated for 30 minutes from the exposed source to allow the discrimination parameters to be set. The layout of the lab environment and model for Monte Carlo interrogation in x-y plane, i.e. overhead view, is shown in Fig. 5.10. The ^{252}Cf source was contained within a cubic metre of water, and surrounded by 33 mm of steel shielding; the room has concrete block walls and a concrete floor. The imaging system was then moved to the required position and the imaging routine was initiated. Images were taken from points A and B with the source exposed (moved to the outside edge of the water tank) with image parameters according to Table 5.5. The cubic EJ-309 detector was placed in the proximity of the imaging probe where the background was measured in synchronization with each measurement performed by the imager.

Figure 5.9 Photograph of image data collection at position B of the ^{252}Cf neutron tank imaging survey [123].

Table 5.5 Imaging parameters associated with experiment 3.

Survey point	Height† (cm)	$r^{\ddagger}_{SI}$ (cm)	Source location	t_d (s)
A	108	237	Exposed	35
B	62	157	Exposed	20

† Height of the detector (image origin) above concrete floor
‡ Distance from the source to the image origin

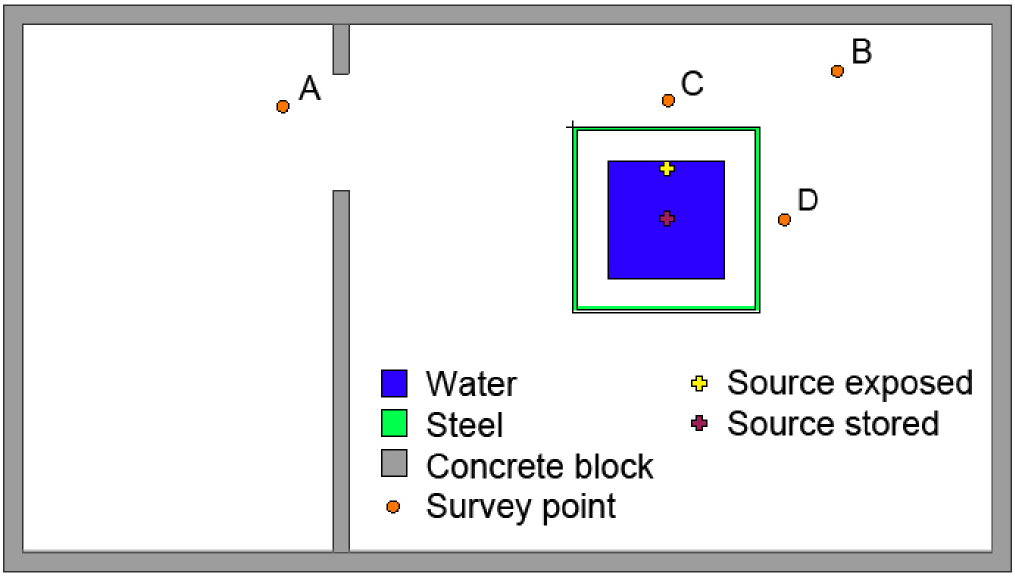

Figure 5.10 2D schematic of the radiation lab including walls, neutron tank detail and imaging survey points as for the ^{252}Cf neutron tank imaging survey [123].

5.3.3 Results

The calibration data and discrimination parameters used for this experiment are shown in Fig. 5.11. This figure shows the discrimination parameters before and after image data were collected, these parameters were checked constantly through the imaging survey and were not seen to change. The GARR value was measured before the experiment with a ^{137}Cs source was 0.0874%. The unprocessed image data and accompanying background measurements are shown for survey point A in Fig. 5.12 and survey point B in Fig. 5.13. The corresponding reconstructed radiation images obtained in this experiment are shown in Fig. 5.14.

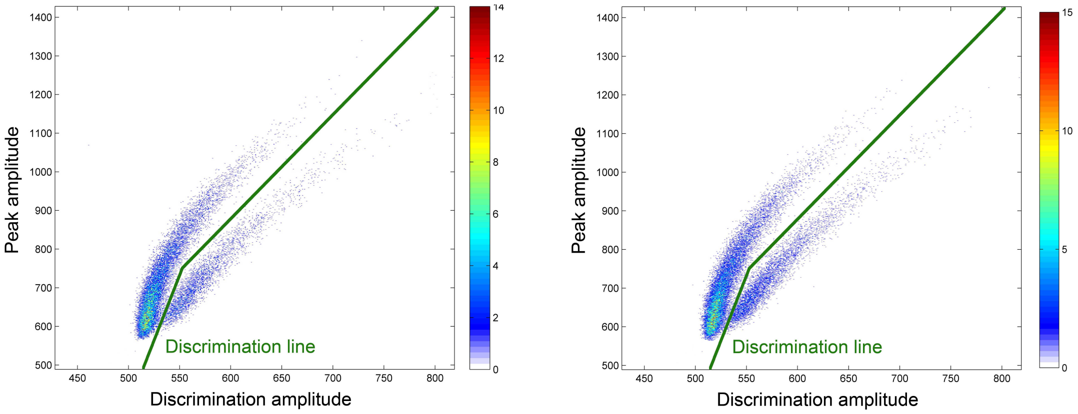

(a) Before imaging routines

(b) After imaging routines

Figure 5.11 Plot of events as a function of the discrimination parameters and discrimination line associated with experiment 3.

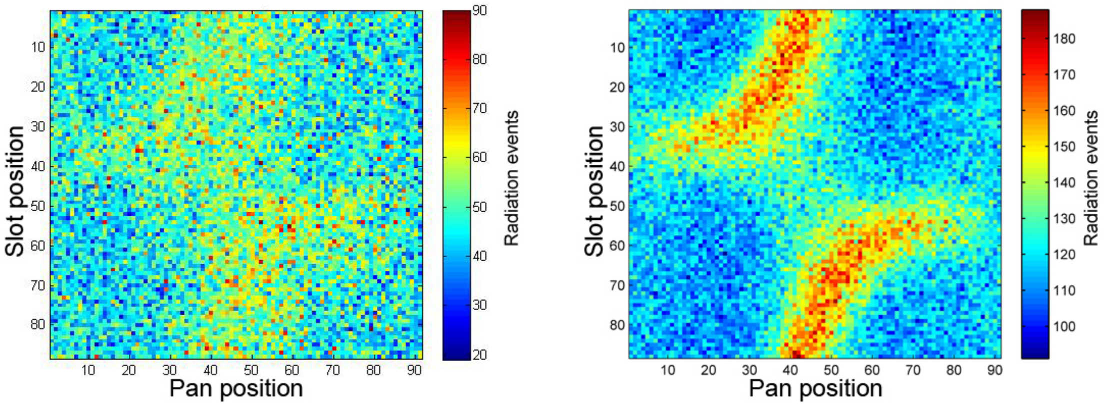

(a) Neutron image data

(b) Gamma-ray image data

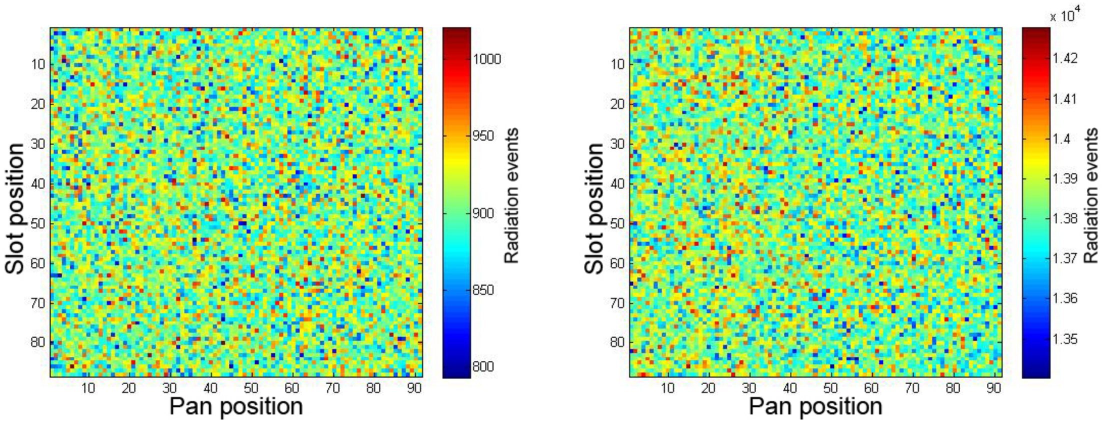

(c) Neutron background

(d) Gamma-ray background

Figure 5.12 Unprocessed image data obtained in experiment 3 from survey point A: discriminated events as a function of slot and pan position.

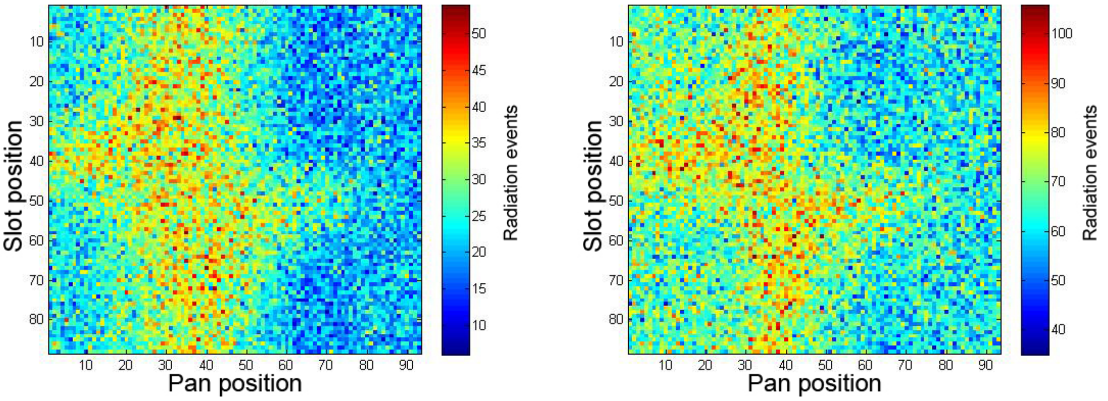

(a) Neutron image data (b) Gamma-ray image data

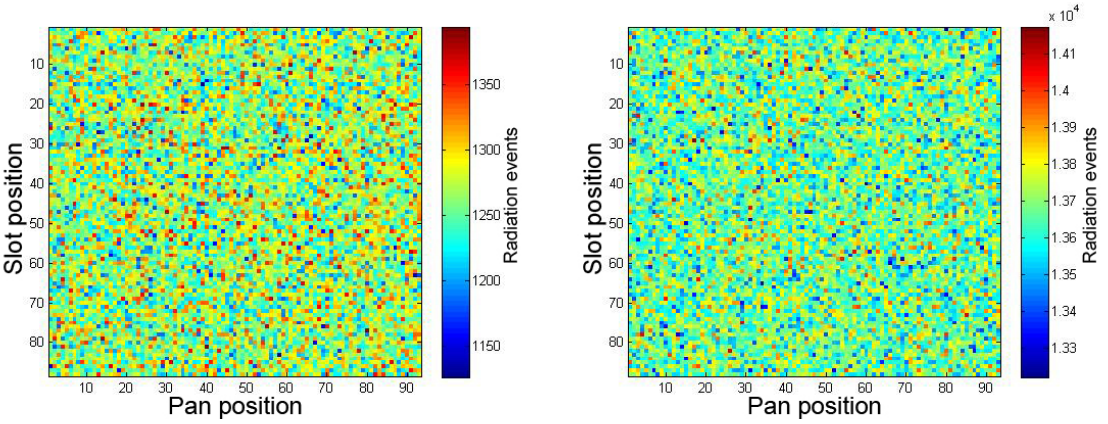

(c) Neutron background (d) Gamma-ray background

Figure 5.13 Unprocessed image data obtained in experiment 3 from survey point B: discriminated events as a function of slot and pan position.

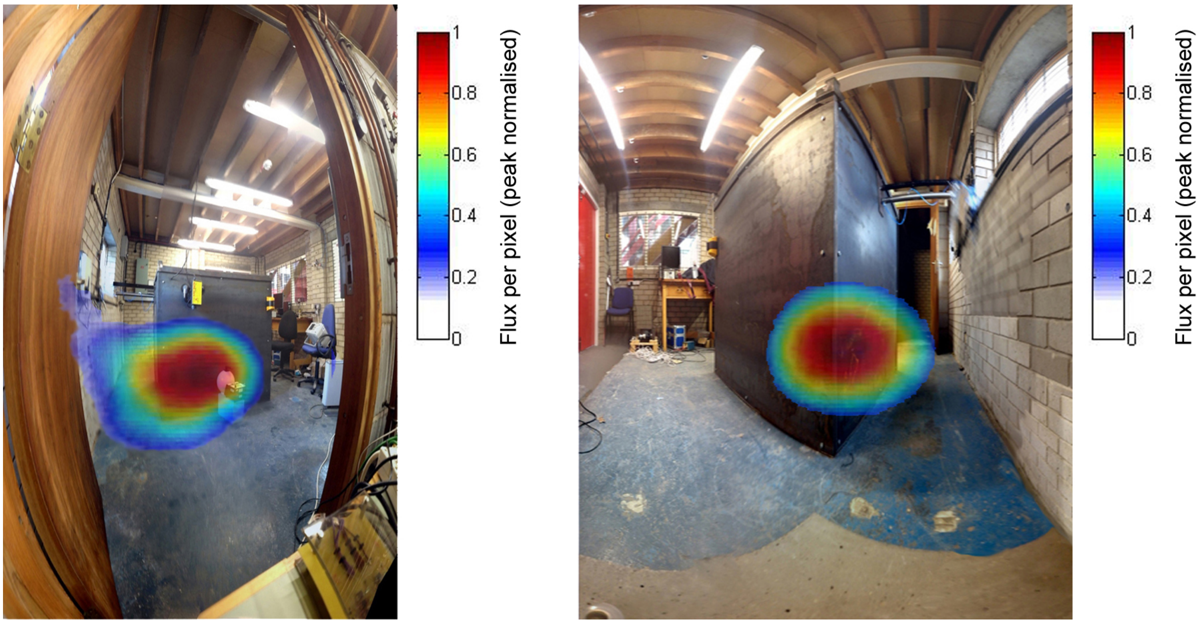

(a) Neutron image from survey point A [123]

(b) Neutron image from survey point B [123]

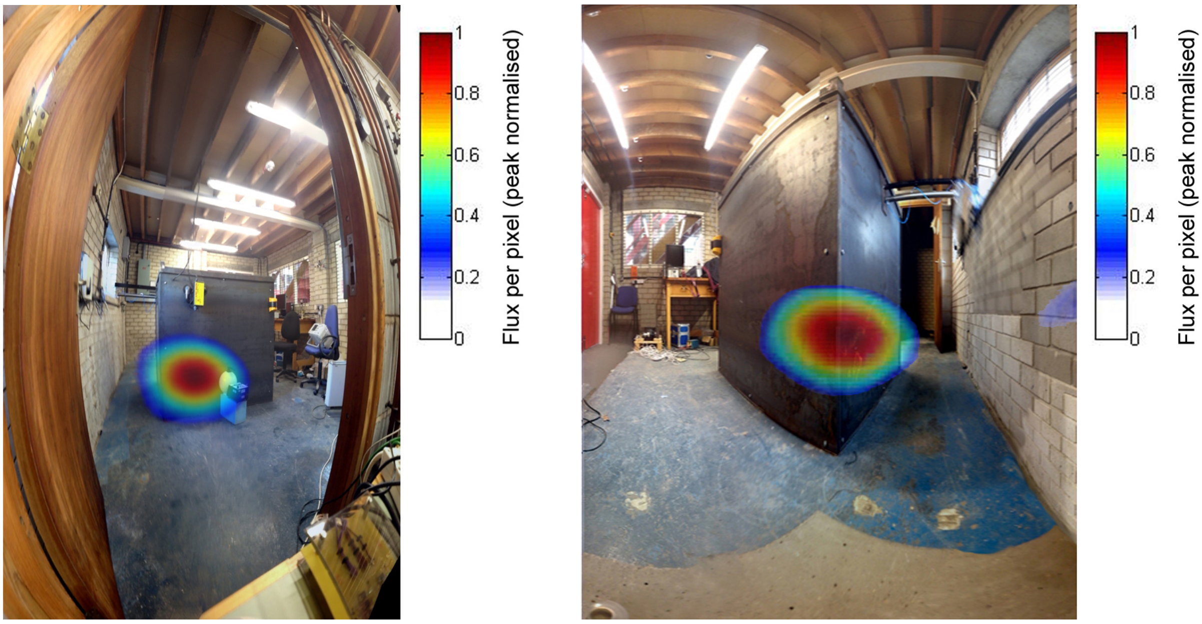

(c) Gamma-ray image from survey point A [123]

(d) Gamma-ray image from survey point B [123]

Figure 5.14 Radiation images from survey points A and B in the ^{252}Cf neutron tank imaging survey overlaid on optical images.

5.3.4 Simulation results

Simulations were performed in MCNP5 to provide more information on the imaged radiation distributions. Pin-hole images corresponding to the experimental set-ups are shown in Fig. 5.15. A Gaussian blur has been applied to these images to allow better representation of the smaller contributions (see section 3.4.4).

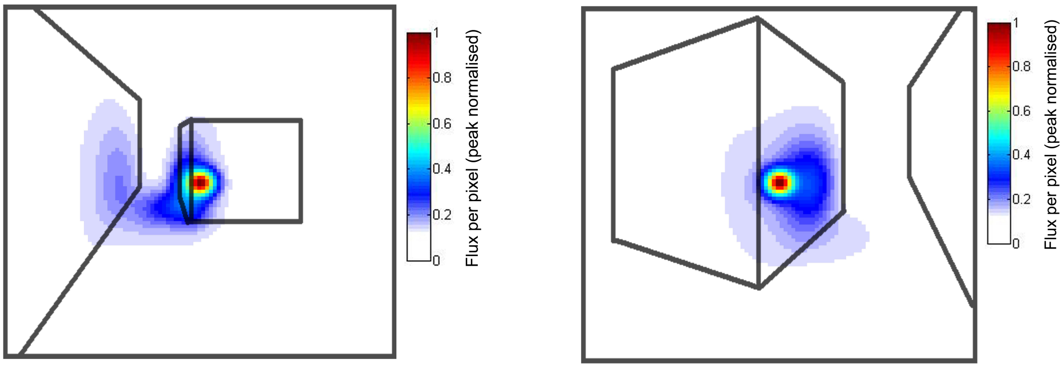

(a) Simulated neutron image from survey point A [123] (b) Simulated neutron image from survey point B [123]

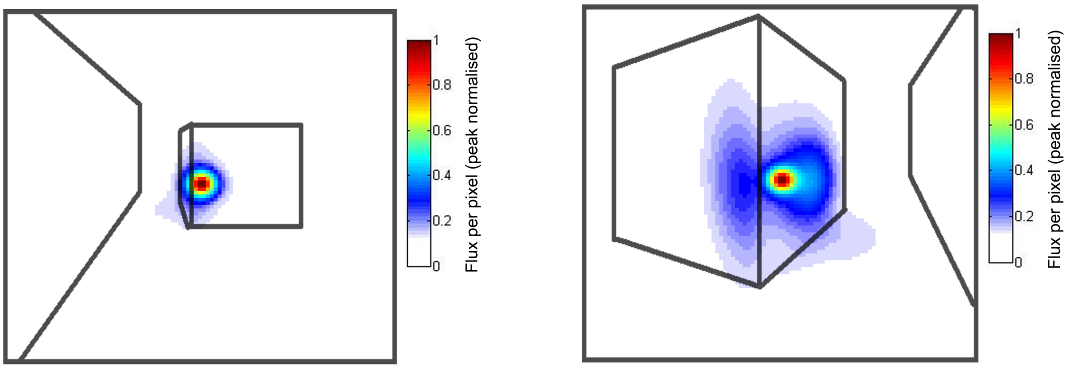

(c) Simulated gamma-ray image from survey point A [123] (d) Simulated gamma-ray image from survey point B [123]

Figure 5.15 Simulated radiation images as a function of elevation and azimuth angle from survey points A and B in experiment 3.

MCNP Visual Editor was used to plot 5000 radiation tracks emitted from the source in the horizontal plane, these are shown for neutrons and gamma rays in Fig. 5.16. Each blue point represents a site where an interaction between the radiation and the surroundings has taken place.

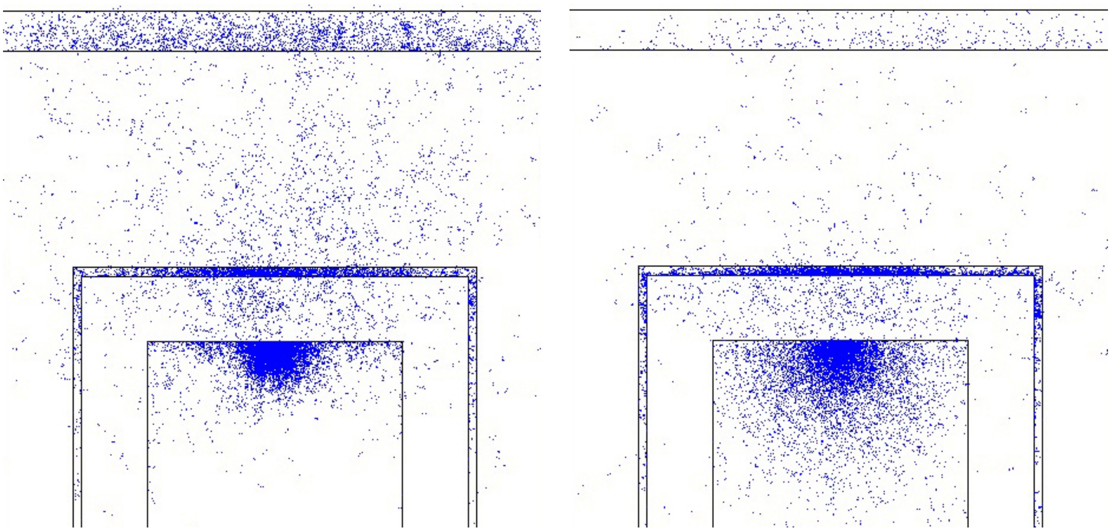

(a) Neutron interaction points [123] (b) Gamma-ray interaction points [123]

Figure 5.16 MCNP-calculated interaction points resulting from 5000 particle histories emitted from the ^{252}Cf source in the exposed position in the water storage tank.

5.3.5 Discussion

The calibration data and discrimination parameters in Fig. 5.11 demonstrate an unchanging good level of neutron-gamma discrimination throughout the survey.

The neutron image from survey point A (Fig. 5.14a) appears to show a single major hotspot of radiation correlated with the location of the ^{252}Cf source, plus some contributions and skewing to the left. The simultaneous gamma-ray image (Fig. 5.14c) appears to show the source location as a hotspot with a small amount of skewing to the left-hand side. This effect is also present in the corresponding simulated pin-hole images for neutrons (Fig. 5.15a) and gamma rays (Fig. 5.15c). This skewing was demonstrated to be associated with scatter from the steel shield in the region closest to the radiation source. The steel is 3.3 cm thick and is shown in MCNP5 simulations to interact significantly with neutrons (Fig. 5.16a) and to a lesser extent with gamma rays (Fig. 5.16b). The contribution to the skewing of the hotspot in the neutron image is from scatter and production of neutrons in (n,xn) reactions in the steel, though those due to neutron production reactions are calculated to contribute less than 1%. The major consolidated contribution of scatter in this image is calculated from the simulations to account for 25% of the imaged flux and is located 5° to the left side of the source location. This equates to 21 ± 3 cm in front of the tank, consistent with the location of the steel at 22 cm in front of the source and agreeing spatially with the neutron survey image. Additionally in the neutron image some scatter appears to come from the wall and floor which agrees with the simulated data.

The neutron (Fig. 5.14b) and gamma-ray (Fig. 5.14d) images produced at survey point B also show good agreement and similar features; a single hotspot consistent with the position of the ^{252}Cf source. The neutron image does appear to show some skewing of the hotspot to the right-hand side and the gamma-ray image appears flattened. This is consistent with the simulated images in Figs. 5.15b and 5.15d.

In these low-shielded scenarios the neutron and gamma-ray images determine the location of the hotspot within $\pm 1^\circ$ in azimuth and elevation of the location of the ^{252}Cf source. It can therefore be concluded that this method is effective at identifying the presence of a single source of neutron and/or gamma-ray radiation and locating in the local environment. The presence of radiation field components other than the major hotspot and their validation from simulations indicate that this imaging method can be used to identify smaller contributions of the radiation fields, namely scatter from the steel shield, concrete wall and floor (survey point A neutron image only) in these scenarios. With prior knowledge, e.g. that only one source is present it could be possible to use these scatter contributions to reconstruct the shape of the surrounding environment, this would however require further research.

5.4 Experiment 4: Long exposure low-dose imaging of a ^{252}Cf neutron tank with ART

This section is adapted from a publication in a peer-reviewed journal [123].

5.4.1 Introduction and rationale

This experiment investigates an application of the slot-collimated imaging method in extremely low fields, to locate sources of radiation in the local environment even when the emission rate is close to background levels. This was achieved by increasing the data acquisition time of the image. This forms a close analogy with shutter speeds in a conventional camera; by increasing exposure time, more light can be collected and dim objects can be detected.

The low field was created in this experiment using approximately one cubic metre of water to shield a central ^{252}Cf source. There are many situations in the nuclear industry where radiation fields and hydrogenous shielding materials, such as water or concrete, are in close proximity. Such as spent-fuel repositories, fuel processing and fission reactors. The capability to image shielded sources may therefore be valuable in these scenarios as well as all nuclear decommissioning projects where these shielding materials are commonplace amongst radioactive materials. Topical examples are the boiling water reactors at the Fukushima Daiichi site in Japan. For some of the reactors, access inside the primary containment vessel (PCV) is difficult and it is not known if, or to what extent, the fuel material has melted. The knowledge of this fuel distribution is a crucial step in planning the decommissioning strategy. Fuel material which has been burned inside the reactor contains ^{244}Cm, as well as other materials (see Tables 2.2 and 2.3), which emits a significant number of neutrons through spontaneous fission. The ability to image these neutrons, and therefore the fuel in a reactor environment, through all or part of the concrete PCV structure and/or water, is therefore desirable. The situation described here is clearly less challenging but similarly involves a spontaneous fission source and hydrogenous shielding.

5.4.2 Experimental set-up and apparatus

The apparatus used in this experiment are summarised in Table 5.6. This experiment was performed in the Department of Engineering, Lancaster University, UK.

The layout of the lab environment and model for Monte Carlo interrogation in x-y plane, i.e. overhead view is shown in Fig. 5.10. The ^{252}Cf source was contained within a cubic metre of water and surrounded by 33 mm of steel shielding. The room has concrete block

Table 5.6 Summary of materials and methods used in experiment 4.

MFA	4 channel MFAX4.1 [section 3.2.2]
Data collection	Custom pulse counter [section 3.2.5]
Discrimination	Real-time
Detector(s)	Miniature EJ-301 4 ml and 1×10 cm cubic EJ-309 [section 3.2.1]
Collimator	Tungsten and P.E. C2 [section 3.2.3]
Imaging method	ART reconstruction [section 3.3.3]
Imaging parameters	88 slot × 74 pan, t_d = 300s
Radiation sources	^{252}Cf (75 MBq) water shielded [section 3.5.1]

Table 5.7 Imaging parameters associated with experiment 4.

Survey point	Height† (cm)	$r_{SI}^{\ddagger}$ (cm)	Source location	t_d (s)
C	34	94	Stored	300

† Height of the detector (image origin) above concrete floor
‡ Distance from the source to the image origin

walls and a concrete floor. For this experiment the source was in the stored position, i.e. fully shielded in the centre of the water tank. The image was taken from point D, in close proximity to the steel shield due to the extremely low flux of the neutron field in this position which would diminish further with additional distance. The distance from the detector to the source was 94 cm.

Figure 5.17 Data collection at position D of the ^{252}Cf neutron tank imaging survey [123].

The discrimination parameters had to be set carefully to ensure the neutron field was fully isolated from the gamma-ray field. Here it was favourable to sacrifice some neutron counts to ensure there was very little contribution from misclassified gamma rays; this would also protect the discrimination in case of electronic drift which would in turn effectively drift the discrimination line. This method was employed given the length of data acquisition.

The probe was placed at position C and the source was moved into the exposed position; data were collected for 10 minutes followed by set-up of the neutron-gamma discrimination parameters. Once complete, the probe was moved to position D and the imaging routine was initiated again. Data were collected continuously over 30 days. Due to the length of this experiment it was possible that the number of detected neutron events could be influenced by the cosmic neutron background which can fluctuate by up to 30% in a given year, hence the monitoring of the background. The discrimination parameters were also reinvestigated at the end of the experiment using the same method. Radiation images were reconstructed using the method outlined in section 3.3.3.

5.4.3 Results

The discrimination parameters used in this experiment are illustrated in Fig. 5.18. GARR was measured with a ^{137}Cs source at 0.00531%.

The unprocessed image data and background recorded by a second detector in this experiment are illustrated in Fig. 5.19. The neutron and gamma-ray images of the ^{252}Cf source stored in the water tank are shown in Fig. 5.20.

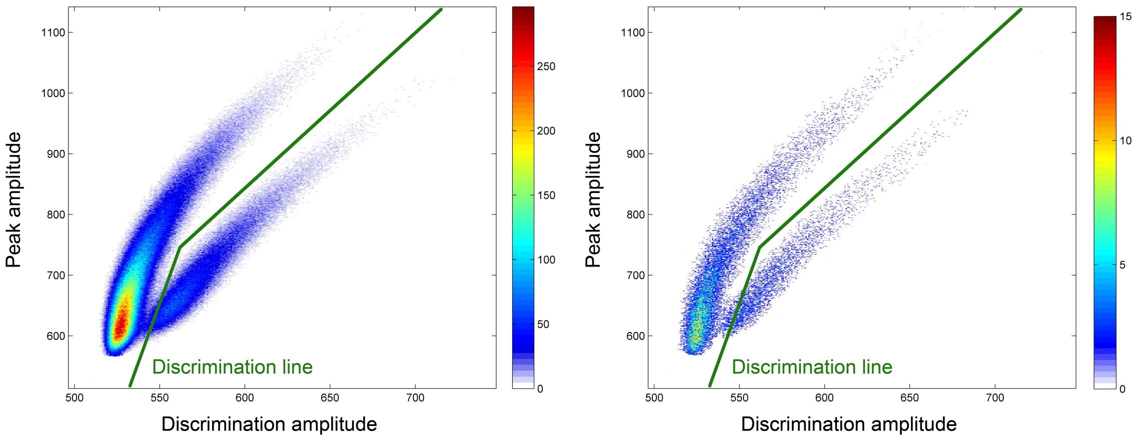

(a) Prior to experiment

(b) After experiment

Figure 5.18 Plot of events as a function of the discrimination parameters and discrimination line associated with experiment 4.

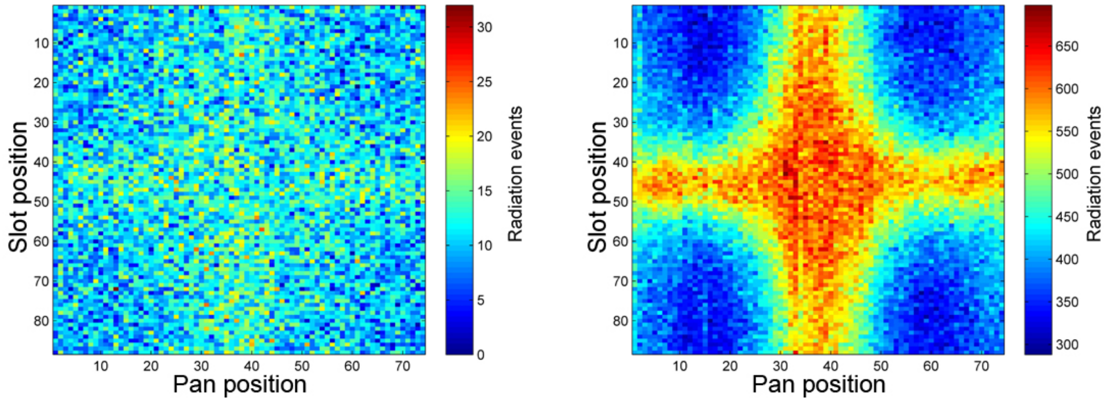

(a) Neutron

(b) Gamma ray

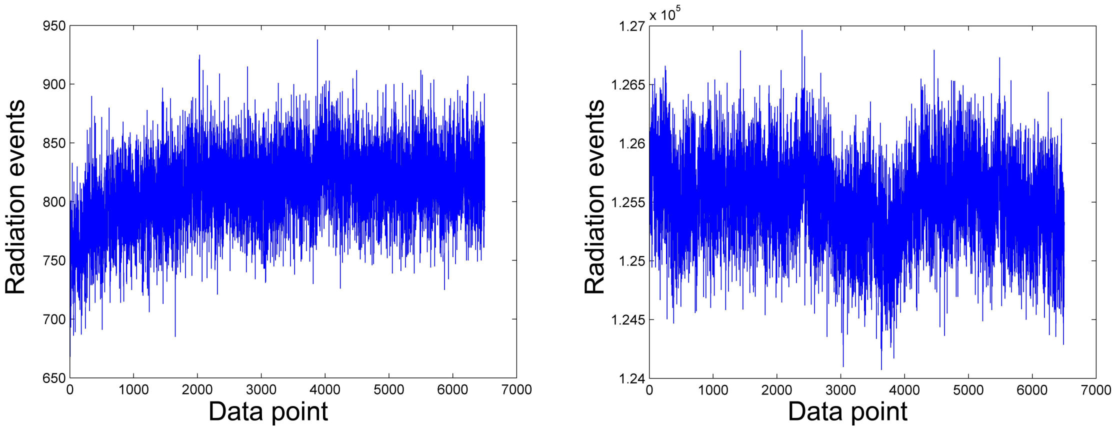

(c) Neutron background

(d) Gamma-ray background

Figure 5.19 Unprocessed image data obtained in experiment 4: discriminated events as a function of slot and pan position (a and b). Background data, discriminated events as function of data point (c and d).

5.4.4 Simulation results

The corresponding simulated pin-hole images are shown in Fig. 5.21. A Gaussian blur has been applied to these images to allow better representation of the smaller contributions (see section 3.4.4 for definition).

5.4.5 Discussion

The discrimination parameters in Fig. 5.18 and associated GARR determine that the neutron and gamma-ray fields can be considered well isolated during this experiment and that no

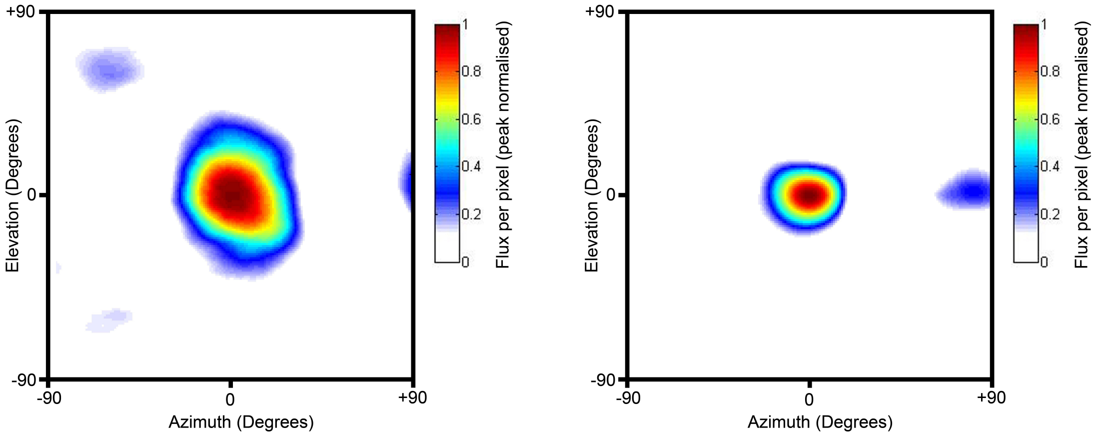

(a) Neutron image [123]

(b) Gamma-ray image [123]

Figure 5.20 Radiation images of a shielded ^{252}Cf source from survey point D in experiment 4 as function of elevation and azimuth angle.

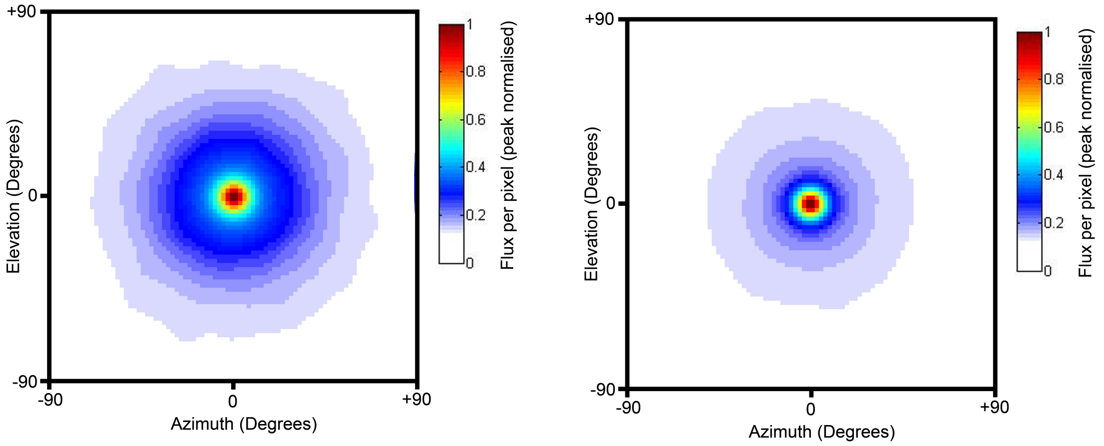

(a) Neutron image simulation [123]

(b) Gamma-ray image simulation [123]

Figure 5.21 Simulated radiation images of a shielded ^{252}Cf source from survey point D in experiment 4 as function of elevation and azimuth angle.

significant drift of these parameters was seen over the duration of the experiment. A change of around 6% was seen in the detector monitoring the neutron background in Fig. 5.19c. The collimated imaging detector was well shielded from cosmic neutrons and did not see the same effects, therefore no correction was made.

The neutron and gamma-ray images of the stored source, shown in Figs. 5.20a and 5.20b respectively, each show a single radiation hotspot at the location of the ^{252}Cf source; these clearly identify the source through 45 cm of air, 46 cm of water shielding and 3.3 cm of steel. The neutron image appears to have some skewing and both images contain some small artefacts which cannot be attributed to an accurate characterisation of the local radiation fields. These effects were related to the larger error on the measurements due to the weaker field and the lower signal-to-noise ratio (in relation to the cosmic neutron background and gamma-ray background) when compared with other images in this research. These properties also lead to a greater sensitivity to any instabilities in the system, contributing to the overall noise which exacerbated these effects.

The pin-hole simulation image corresponding to the stored source neutron image can be seen in Fig. 5.21a, showing a radially symmetric distribution of neutrons with wide dispersion. The majority of the imaged neutrons ($>$99%) have scattered at least once in the water moderator, causing this effect. The simulated image for the gamma-ray field shown in Fig. 5.21b shows similar characteristics of a single hotspot with some smaller dispersion. The experimental and simulated images show good agreement in terms of the relative size and shape of the neutron and gamma-ray fields. Differences are attributed to the unequal point spread functions in each approach.

The low-dose images of a heavily shielded ^{252}Cf source were validated with Monte Carlo simulations and used to determine the location of the source within $\pm 1^\circ$ in azimuth and elevation. It can therefore be concluded that this technique can be used to image low-dose radiation fields ($<1\mu$Sv/h) arising from a spontaneous fission source, and to determine its location when surrounded by significant amounts of hydrogenous shielding.

5.5 Experiment 5: High-intensity imaging of a TRIGA reactor core with ART

This section is adapted from a publication in a peer-reviewed journal [120].

5.5.1 Introduction and rationale

The purpose of this experiment was to test the functionality of the imager in the high-dose fields located in close proximity to operational nuclear reactors, as well as to expand upon the previous experiment in relation to imaging in the presence of significant hydrogenous shields. In this experiment high radiation tolerance and compactness of the probe and portability of the system were key to success.

Imaging the neutron field allows localised neutron-emitting material to be viewed discretely from other radiation sources, such as the gamma rays produced by fission, fission products and activation products which are commonplace in such scenarios. The neutron field is therefore related exclusively to nuclear fuel within the reactor where neutron production takes place from fission or (α,n) reactions. Imaging this field yields information on the fuel only, ignoring other radiation sources. This therefore gives advantage over gamma-ray-only imaging which would be subject to complications from any other gamma-ray sources such as fission products which can migrate outside of the fuel, particularly in the case of water-soluble Cs isotopes.

This method could be used as an alternative to in-core instrumentation, to monitor the distribution of neutrons within a reactor core. Alternatively the system could be deployed in accident scenarios to assay reactors and the distribution of core material and any continuing fission reactions post-accident.

5.5.2 Experimental set-up and apparatus

The apparatus used in this experiment is summarised in Table 5.8. The experiment was performed at the Atominstitut, Vienna University of Technology, Austria.

A schematic of the experimental set-up is shown in Fig. 5.22. More information on the reactor is included in section 3.5.2. The system was assembled and the imaging probe was lowered into position using a small service lift. Once in position the image origin, i.e. the detector location, was at a horizontal displacement of 229 cm and a vertical displacement of 25 cm above the geometric centre of the reactor core. An aperture in the heavy concrete shielding allowed the unattenuated passage of radiation from the core structure to the probe.

Table 5.8 Summary of materials and methods used in experiment 5.

MFA	Single channel MFAX1 [section 3.2.2]
Data collection	Custom pulse counter [section 3.2.5]
Discrimination	Real-time
Detector(s)	Miniature EJ-301 [section 3.2.1]
Collimator	Tungsten and P.E. C2 [section 3.2.3]
Imaging method	ART reconstruction [section 3.3.3]
Imaging parameters	88 slot × 115 pan, $t_d = 0.5$ s
Radiation sources	Low-shielded TRIGA mk II test reactor core [section 3.5.2]

The water collimator was drained to allow maximum fast-neutron flux and the cadmium shield was kept in place to prevent activation of the probe by thermal neutrons.

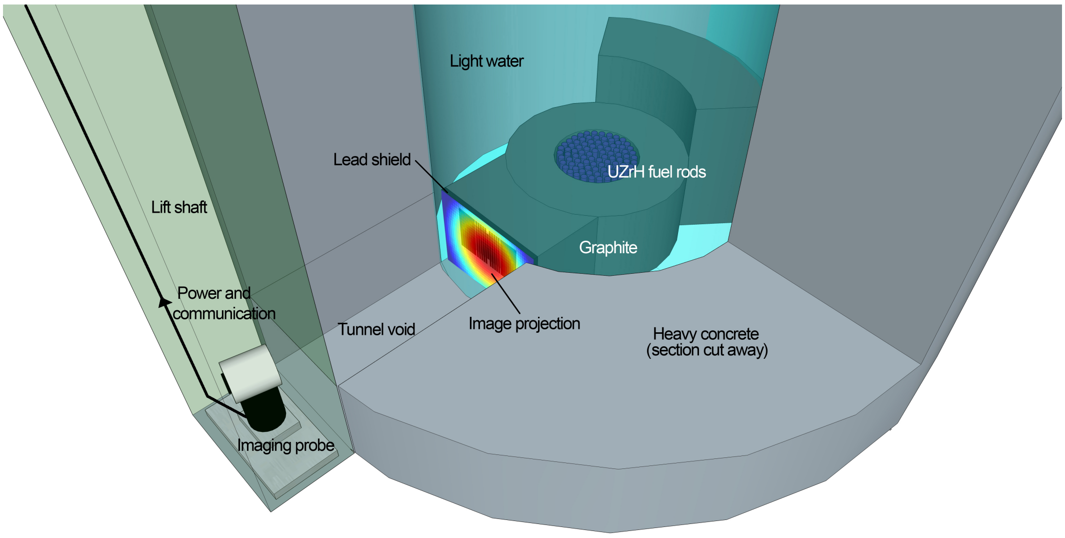

Figure 5.22 Annotated schematic of probe deployment in relation to TRIGA reactor core components and shielding in experiment 5 [120].

The probe was rotated through the pan angle such that the detector was facing the core location. The reactor was brought to a steady-state power of 10 kW and data were collected for 10 minutes to provide for the neutron-gamma discrimination calibration.

The reactor was brought to the desired steady-state power and the imaging routine was initiated. Images were conducted at 40 kW, 100 kW and 250 kW (the reactor's full power). The neutron-gamma discrimination parameters were checked before and after each image, no change was observable. Note that a temporary electronics malfunction resulted in 26% of the data missing from the final image and due to time constraints this could not be repeated.

5.5.3 Results

The calibration data and discrimination parameters used for this experiment are shown in Fig. 5.23. The unprocessed image data recorded in this experiment are shown in Fig. 5.24.

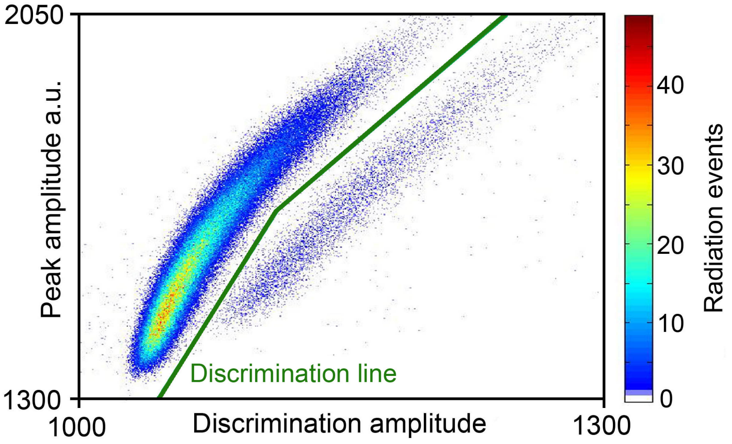

Figure 5.23 Plot of events as a function of the discrimination parameters and discrimination line associated with experiment 5 [120].

The radiation images produced from this experiment are given in Fig. 5.25. Fig. 5.25a shows the images plotted on a scale common to each radiation type and includes values for the flux in each image. Fig. 5.25b shows each image with normalisation for direct comparison of the flux distributions. Table 5.9 gives parameters associated with data collection, solved images and simulated images. Radiation events in the data describe the total number of radiation events recorded in a given image; note that the 250 kW value has been adjusted to represent a full data set including data missing due to a temporary electronics malfunction. The peak flux gives the location of the pixel in the image solution with the highest flux. The flux fractions in column four were calculated based on the 250 kW image solution.

A sequence of images depicting a linear power increase of the Vienna TRIGA reactor, produced from interpolation of the three images in Fig. 5.25a, is given in Supplementary Video 3 (appendix A.1).

5.5.4 Simulation results

Simulated images for each radiation type were produced using MCNP and are shown in Fig. 5.26. These images provide direct comparisons for the images shown in Fig. 5.25b.

Additionally, further simulated neutron images were included to demonstrate the application of this technique to monitor individual fuel rods. Figs. 5.27 and 5.27a were produced to

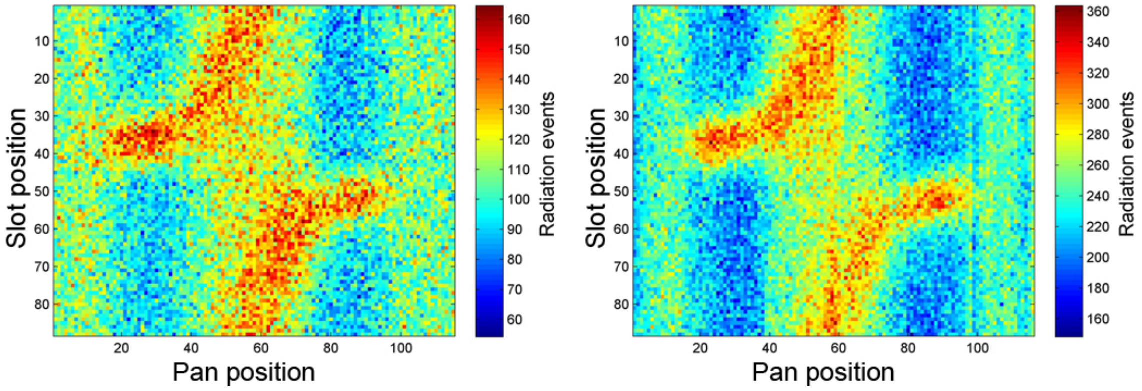

(a) 40 kW neutron data (b) 100 kW neutron data

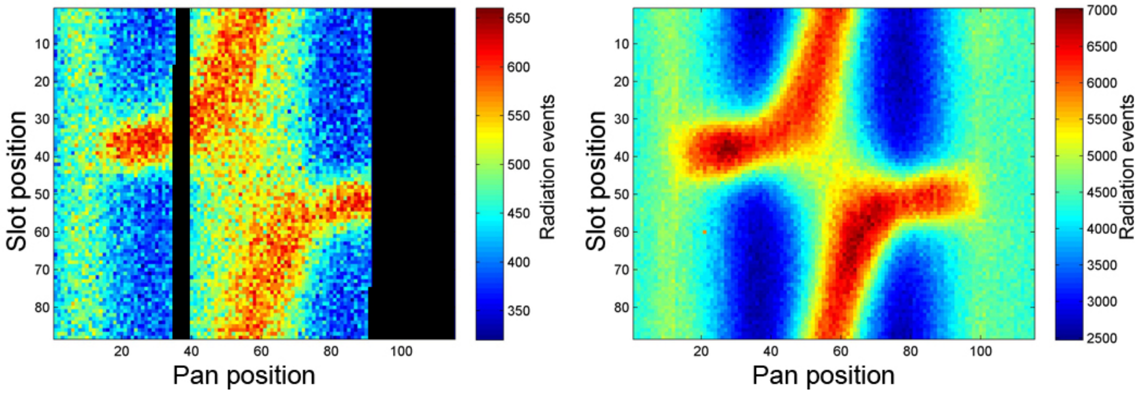

(c) 250 kW neutron data (d) 40 kW gamma-ray data

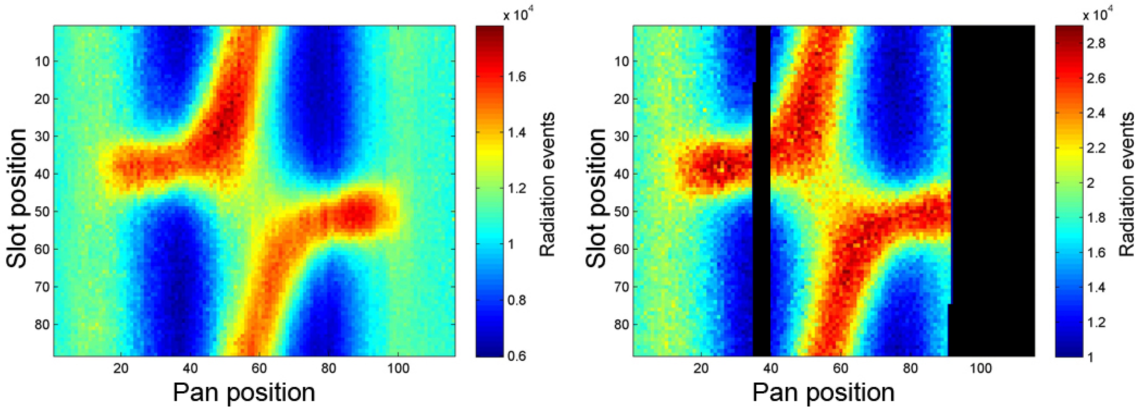

(e) 100 kW gamma-ray data (f) 250 kW gamma-ray data

Figure 5.24 Unprocessed image data obtained in experiment 5 of discriminated events as a function of slot and pan position. Black regions indicate missing data.

Table 5.9 Summary and further analysis of image data produced in experiment 5 summarising radiation events, relative detected flux and peak flux location.

	Radiation events in data ($\times 10^6$)		Flux from core (in image) as fraction of full power		
Image	Neutrons	Gamma rays	Neutrons	Gamma rays	Expected
40 kW	1.11	44.8	0.207	0.229	0.25
100 kW	2.49	111	0.470	0.556	0.5
250 kW	4.76	187	1	1	1

	Peak flux (degrees) [elevation, azimuth]	
Image	Neutrons	Gamma rays
40 kW	[-4, 0]	[0, 0]
100 kW	[-4, 0]	[0, 0]
250 kW	[-4, 0]	[0, 0]
MCNP	[-4, 0]	[0, 0]

show the neutron image resulting from a single fuel rod with uniform neutron emission. This is an unrealistic scenario and is completely hypothetical; this was included to demonstrate that information on each fuel rod is retained in the radiation field at the probe position after passing through the reactor. The image shown in Fig. 5.27b is the same image with energy gating applied to isolate neutrons between 6 and 7 MeV. This energy range has the lowest contribution from scatter and best depicts a single fuel rod. The methods used in this section are outlined in section 4.3.4.

5.5.5 Discussion

The discrimination calibration plot in Fig. 5.23 shows a good separation of neutrons and gamma rays; a higher applied threshold provides no overlap of these regions. Although the MFA provides some resistance to pile-up events due to the nature of the PSD algorithm, some of these events are evident in the right-hand side of the plot outside of the usual neutron plume. These events are most likely due to gamma-gamma pile-up, therefore giving false positives on neutron detection. These occurrences can be seen to be small in number and therefore were not expected to significantly affect the outcome of this imaging experiment. At higher dose rates, more sophisticated pile-up rejection algorithms may have to be applied to remove these false-neutron events when occurring in significant amounts.

The radiation images of the TRIGA reactor clearly show the location of the reactor core (Figs. 5.25b). The origin of the radiation in each image matches the location of the fuel rods of the reactor where the fission process is taking place, though it is noticeable that the flux extends beyond the fuel and into the moderator. This result is closely consistent with simulated images of the core (Fig. 5.26), and implies that the image also depicts the scatter distribution of the radiation in the moderator, i.e. radiation emitted from the core which has reflected from the water moderator towards the imager. Fundamental differences between neutrons and gamma rays can be observed in these images, manifesting in the region of the graphite structure where scattering is most dissimilar.

The images in Fig. 5.25a have been plotted on a scale consistent across radiation type and, when viewed together, clearly illustrate the changes in the internal conditions of the reactor. Table 5.9 shows that the peak flux in each image agrees with the simulated data and that integrating the flux in each image yields a linear response with reactor power; this suggests that further refinement of this technique might be used to quantitatively assess the power distribution and fission rate within the reactor core. An important distinction here is that the gamma-ray image depicts gamma rays from fission and other non-fission reactions alike, whereas the neutron image in this context comprises events arising from ongoing criticalities in fissile material and the interaction of alpha particles on light isotopes in the core (the latter process being a significant contributor to decay heat). The latter would normally be a minority reaction channel during reactor operation and, in any case, would not respond directly to power changes. Contributions from spontaneous fission in ^{238}U and even-numbered plutonium isotopes are extremely small by comparison. Hence, it is clear that the neutron distribution presented in this research shows the distribution of reacting nuclear fuel exclusively, and the change of this in correspondence with changes in power.

Multiple images taken from different locations would allow three-dimensional computer tomography of the neutron and gamma-ray distributions inside the core. The simulated images in Fig. 5.27 indicate that the neutron field retains localised information on a given volume of the core. This information could be used to non-destructively investigate isolated sections of fuel during reactor operation. The dose rate at the probe location due to gamma rays has been measured at 62 mSv/h at max reactor power. This provides the minimum tolerance of the imager which was able to perform an imaging survey under these conditions.

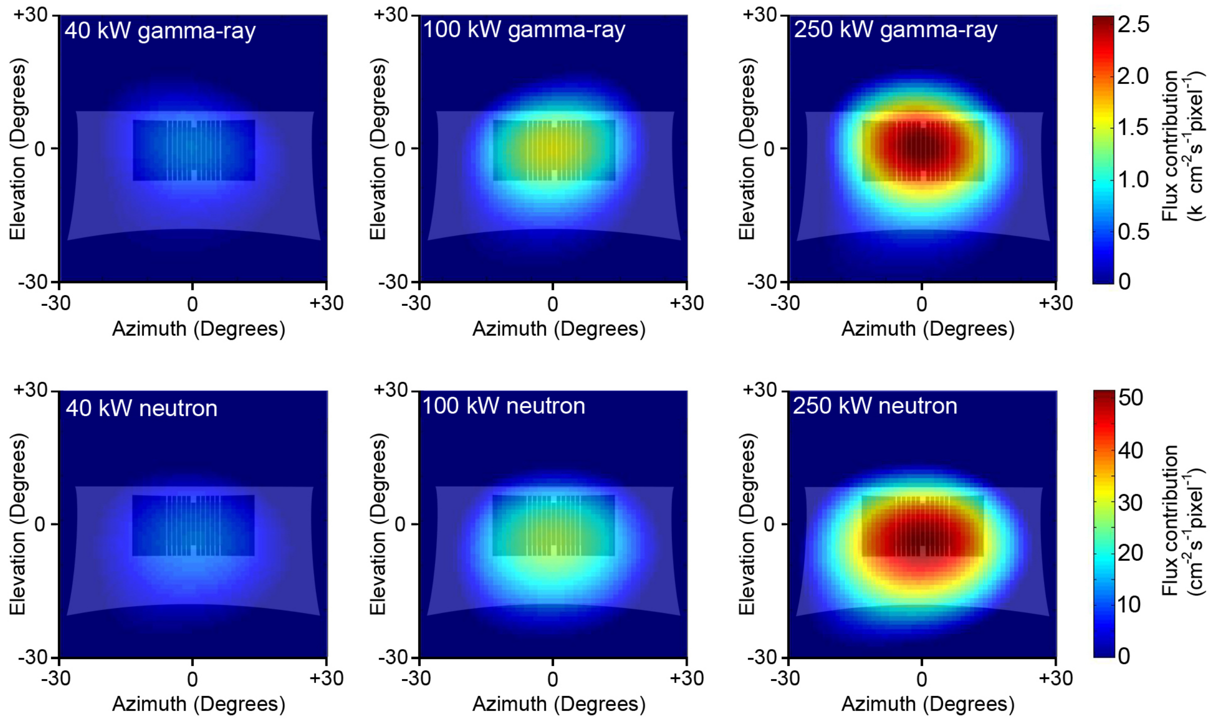

(a) Radiation flux plotted on a constant scale [120]

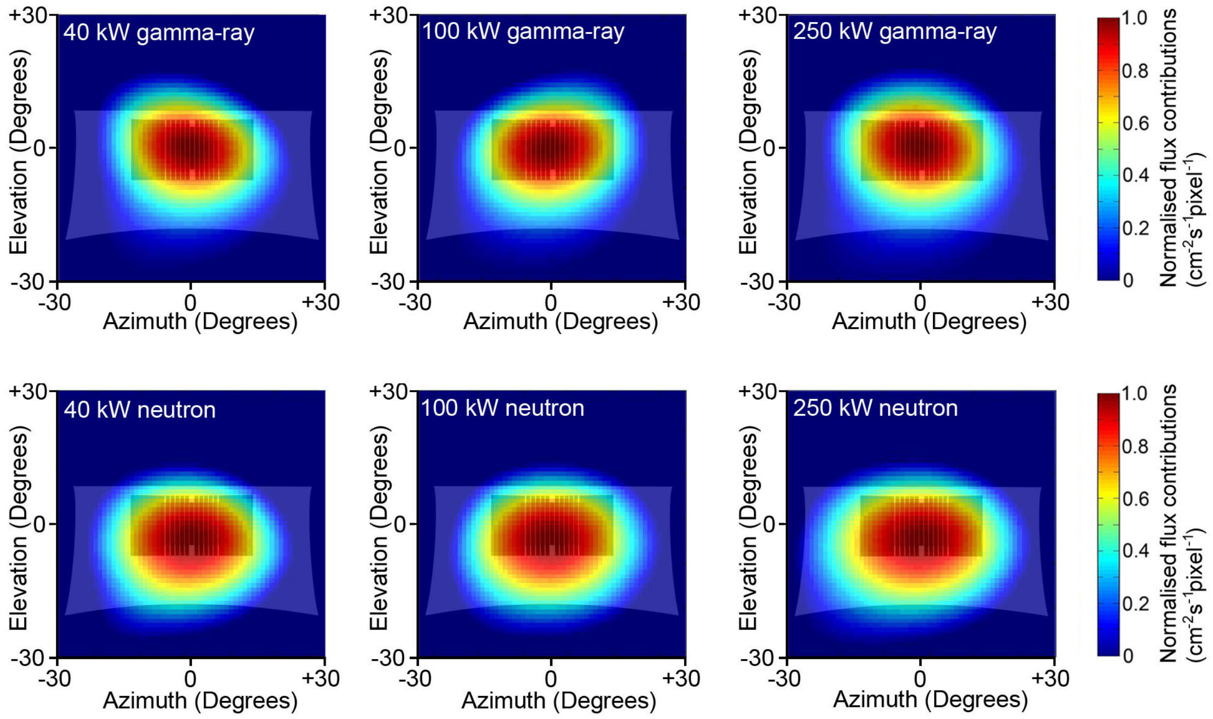

(b) Radiation flux normalised in each image [120]

Figure 5.25 Radiation images as a function of elevation and azimuth angle of a TRIGA test reactor core obtained in experiment 5. Neutron and gamma-ray images are shown for three different reactor powers 40 kW, 100 kw and 250 kW.

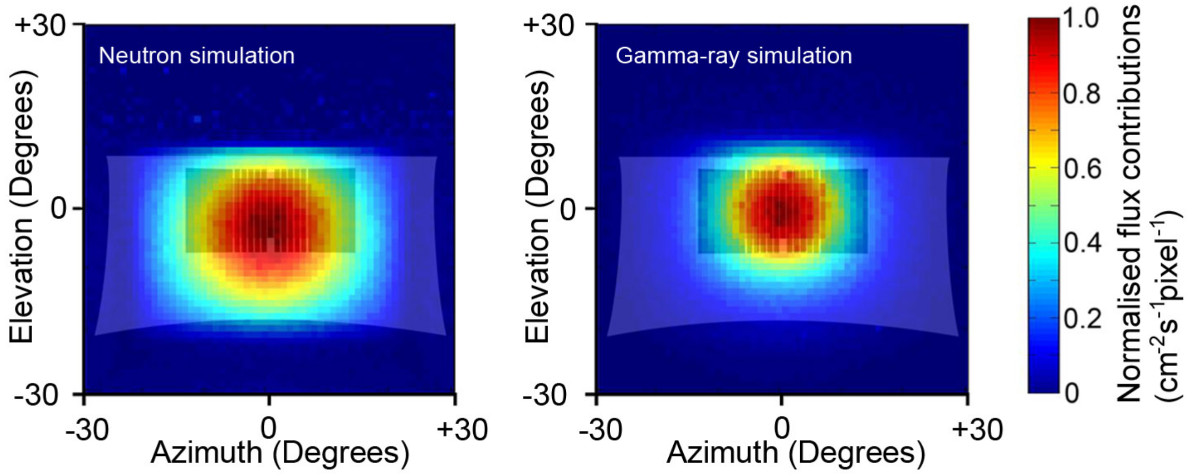

Figure 5.26 Simulated radiation images of the TRIGA test reactor core as a function of elevation and azimuth angle [120].

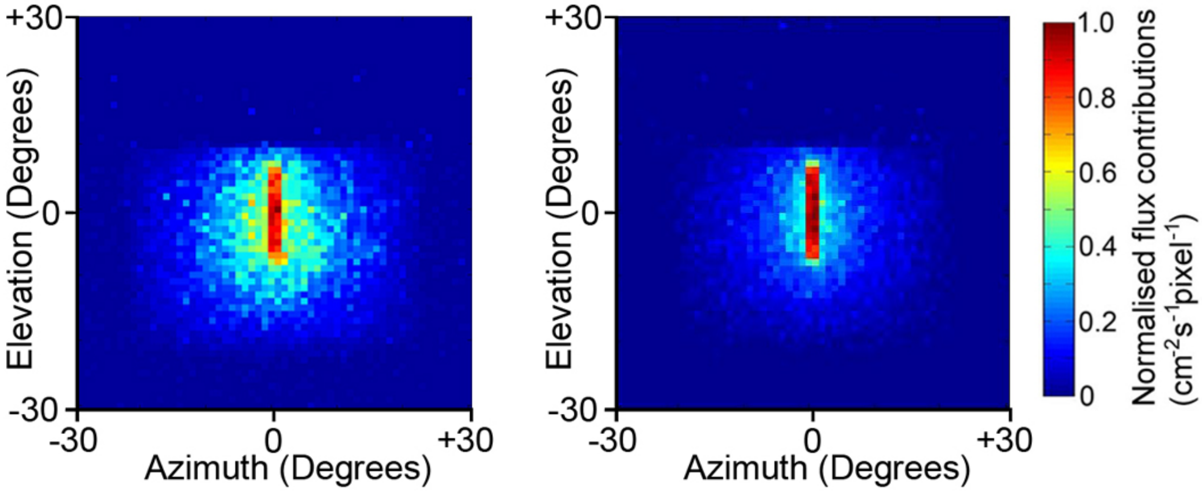

(a) Full detector response

(b) Isolating 6 to 7 MeV neutrons

Figure 5.27 Simulated (hypothetical) images of neutron emission from a single fuel rod as a function of elevation and azimuth angle demonstrating that information in the field is retained when passing through the core and moderator.

Chapter 6

Anti-collimated single-detector imaging

Chapter summary

This chapter includes information on imaging experiments performed with the anti-collimated single-detector imager configuration during the research, including the set-up, calibrations, unprocessed image data and the image solutions. Simulation results are also provided where applicable to provide comparison with recorded images or to illustrate additional information.

6.1 Experiment 6: Survey of a ^{252}Cf neutron tank with ART utilising an anti-collimated detector

6.1.1 Introduction and rationale

Due to the difficulty of shielding neutrons and maintaining a compact probe, further research was conducted into better understanding neutron and gamma-ray interactions in the collimator (sections 4.4.6 and 4.4.7). A new generation collimator was designed to improve upon the shortcomings of the C2 collimator used previously by improving the sensitivity maps, specifically the signal amplitude and contrast in the collimator response. An anti-collimator configuration was built to improve upon these issues and to further reduce the size and weight of the probe, which can be a common restriction in industry. An overall improvement in imaging capabilities in higher energy regimes and all low-mid dose applications was expected from this design; the trade off was the vulnerability to background radiation due to the majority of the detector being unshielded. These experiments were performed to test the capabilities of this imaging system.

6.1.2 Experimental set-up and apparatus

The apparatus used in this experiment is summarised in Table 6.1. This experiment was performed in the Department of Engineering at Lancaster University, UK.

The layout of the laboratory and survey points were identical as those used in Experiment 5.3, see Fig. 5.10. Two images were conducted from survey point C with the source in the exposed position, t_d = 1.5 seconds. One image included a polyethylene block of dimensions 5 cm × 50 cm × 50 cm which was placed against the front face of the steel shield between the source and the imager. A photograph of data collection in this scenario is shown in Fig. 6.1. Images were also conducted from survey points A and B with the source exposed and t_d = 10 seconds.

Table 6.1 Summary of materials and methods used in experiment 6.

MFA	4 channel MFAX4.1 [section 3.2.2]
Data collection	Custom pulse counter [section 3.2.5]
Discrimination	Real-time
Detector(s)	Miniature EJ-301 [section 3.2.1]
Collimator	Tungsten C3 [section 3.2.3]
Imaging method	ART reconstruction [section 3.3.3]
Imaging parameters	91 slot × 88 pan, t_d = 1.5 s, t_d = 10 s
Radiation sources	^{252}Cf (75 MBq) water shielded [section 3.5.1]

Table 6.2 Imaging parameters associated with experiment 6.

Survey point	Height† (cm)	$r^{\ddagger}_{SI}$ (cm)	Source location	t_d (s)
A	108	237	Exposed	1.5
B	62	157	Exposed	1.5
C	62	37	Exposed	10

† Height of the detector (image origin) above concrete floor
‡ Distance from the source to the image origin

Figure 6.1 Photograph of data collection at position C of the anti-collimator test survey.

6.1.3 Results

The calibration data and discrimination parameters used for this experiment are shown in Fig. 6.2. This figure shows the discrimination parameters before and after image data were collected; these parameters were checked constantly through the imaging survey and were not seen to change. GARR was measured with a ^{137}Cs source at 0.122%.

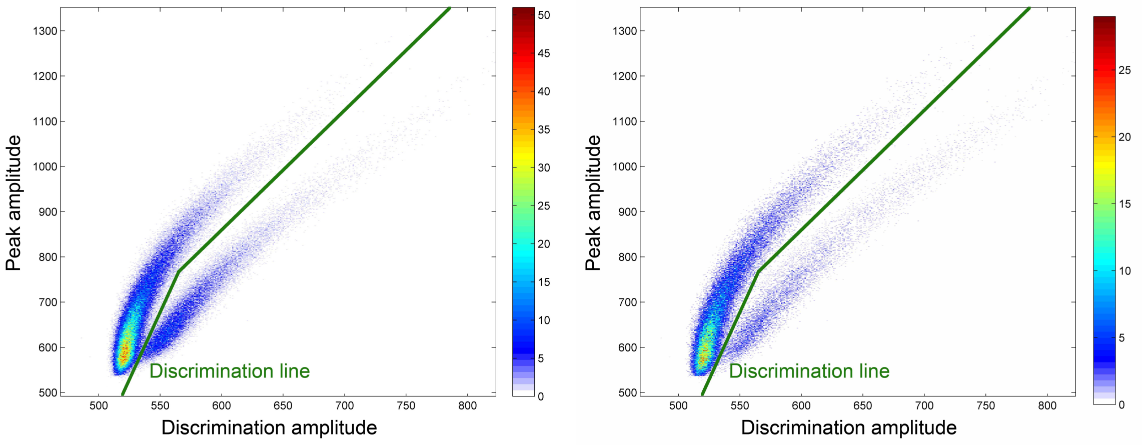

(a) Before imaging routines (b) After imaging routines

Figure 6.2 Plot of events as a function of the discrimination parameters and discrimination line associated with experiment 6.

The unprocessed image data recorded at survey points A and B are shown in Fig. 6.3. The unprocessed image data recorded at point C are shown in Fig. 6.4. The detector offset corrections for survey points B and C are shown in Fig. 6.5. The reconstructed radiation images obtained in this experiment are shown in Figs. 6.6 and 6.7.

6.1.4 Simulation results

The simulations appropriate for comparison with these results are the same as those produced for experiment 3 with the addition of an image from point C. The neutron and gamma-ray simulations from survey points A and B are shown in Fig. 5.15. The neutron and gamma-ray simulations from survey point C are shown in Fig. 6.8. A Gaussian blur has been applied to these images to allow better representation of the smaller contributions (see section 3.4.4).

6.1.5 Discussion

The discrimination plots in Fig. 6.2 show little change over the duration of the experiment. The neutron field was considered to be well isolated from the gamma-ray field. The detector offset corrections show a good fit between the data and the fitted function in all cases (Fig. 6.5), the maxima appear at the same values for neutron and gamma-ray data in the same image demonstrating consistency.

The neutron and gamma-ray images in Figs. 6.6 and 6.7 all show a single hotspot corresponding to the location of the ^{252}Cf source. All the images have several low-flux image

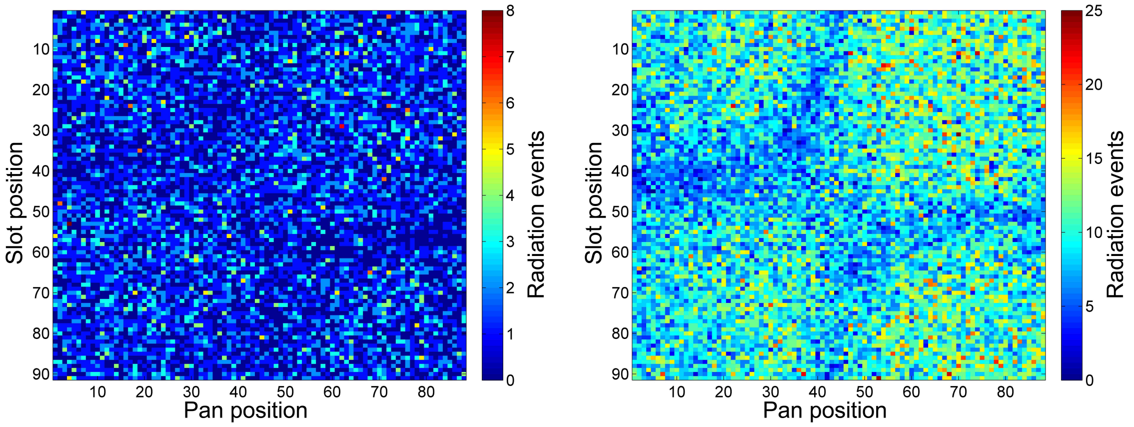

(a) Neutron data, survey point A

(b) Neutron data, survey point B

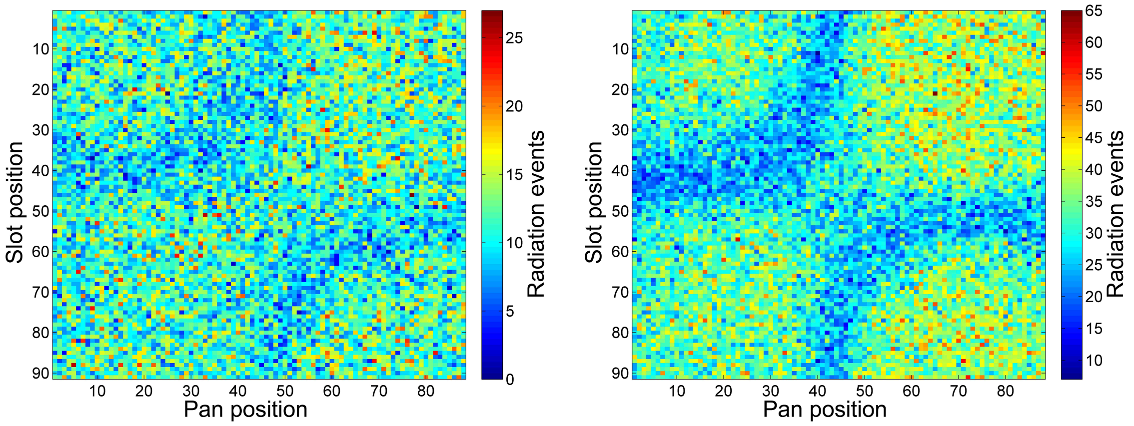

(c) Gamma-ray data, survey point A

(d) Gamma-ray data, survey point B

Figure 6.3 Unprocessed image data obtained in experiment 3 from survey points A and B: discriminated events as a function of slot and pan position.

artefacts resulting from either a greater amount of noise in the data or a mismatch between the real and modelled response functions of the collimator. The latter is a possibility as the MCNP model only accounted for the tungsten collimator and detector cell, other components of the geometry such as the aluminium jig and the mount were not included.

The neutron image from survey point A shows some skewing of the hotspot to the left-hand side. This is in part consistent with the predicted flux distribution shown in the associated pin-hole image (Fig. 5.15). The major contributions of the flux match though the smaller contributions from scatter from the wall and floor have not been produced in the image output. Similarly with the neutron image from point B, some skewing to the right-hand side appears but is not well matched. The gamma-ray images for these survey points appear

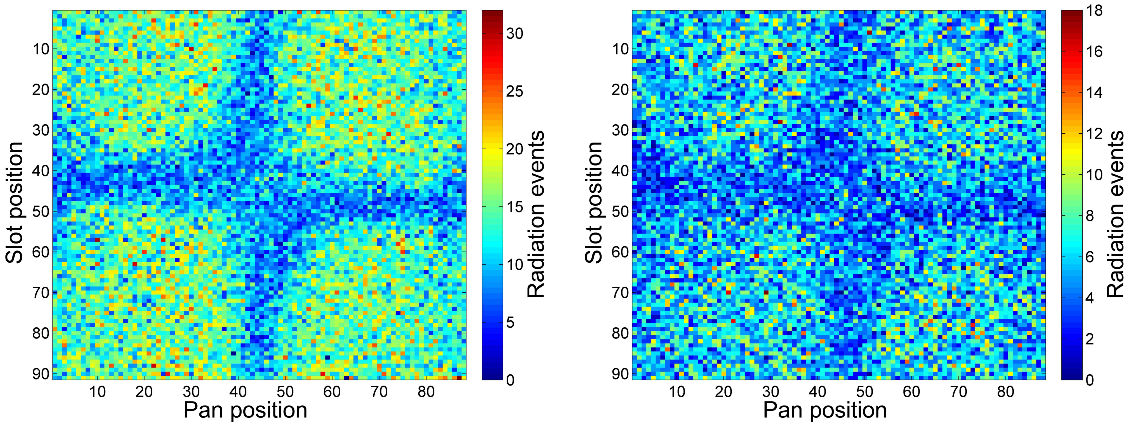

(a) Neutron data, no PE shield

(b) Neutron data, PE shield present

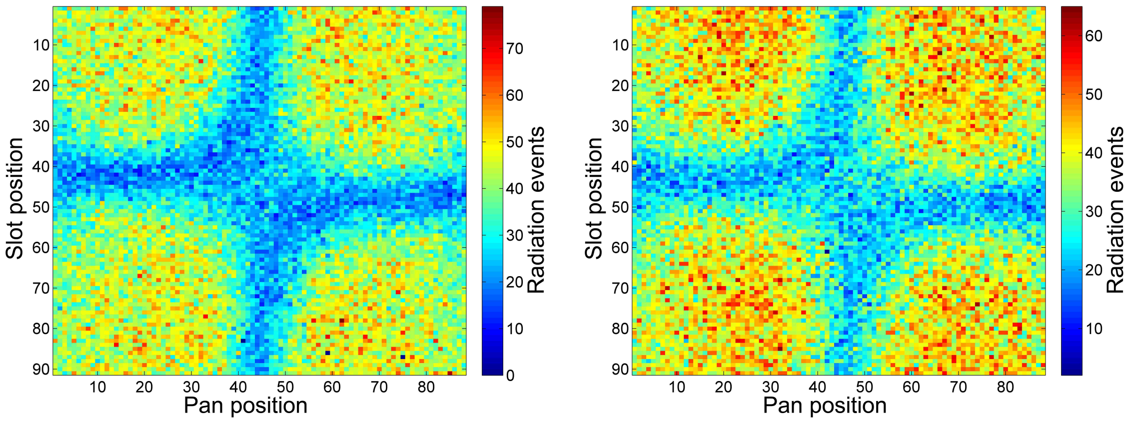

(c) Gamma-ray data, no PE shield

(d) Gamma-ray data, PE shield present

Figure 6.4 Unprocessed image data obtained in experiment 6 from survey point C: discriminated events as a function of slot and pan position.

to more closely follow the predictions from the MCNP pin-hole images though one of the features corresponding to the corner of the steel shield does not appear.

The images conducted from survey point C (Fig. 6.7) show a much more isotropic source distribution than from the other survey points. This appears consistent with the corresponding simulations (Fig. 6.8). The isotropy in these images, unlike those obtained from survey points A and B, further supports that those features are derived from real flux contributions as opposed to artefacts in the solution. The images performed using the 5 cm polyethylene shield give a substantial drop in neutron flux in the image solution (approximately a factor of 3) and a smaller drop in the gamma-ray solutions (approximately 20%) as would be expected for a significant hydrogenous shield. The images conducted with the PE shield also

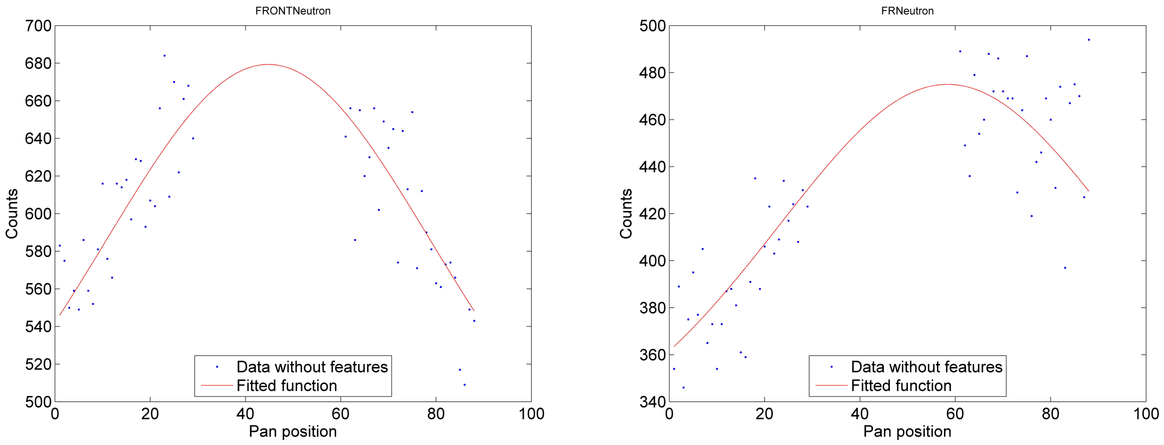

(a) Survey point C neutron fit

(b) Survey point B neutron fit

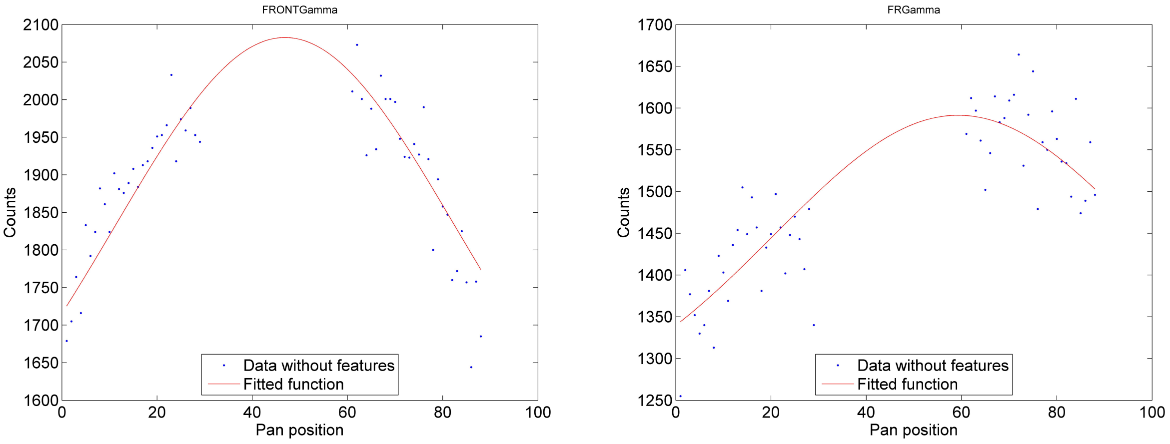

(c) Survey point C gamma-ray fit

(d) Survey point B gamma-ray fit

Figure 6.5 Discriminated events as a function of $\hat{\beta}$ with $\hat{\alpha} = 0°$ fitted with geometric correction for experiment 6. For details of the correction see section 4.4.8.

appear to have more image artefacts which are due to the poorer statistics as a result of fewer detections.

These results demonstrate that an anti-collimated slot imaging approach with ART image reconstruction can be successfully applied to imaging combined neutron and gamma-ray fields. Four of the images produced here can be directly compared with those produced by the collimated detector in Experiment 3. This comparison finds that the collimated approach appears better at identifying smaller contributions from scatter, however it should be accounted for that the anti-collimator imager was an initial prototype whereas the system in Experiment 3 had undergone several stages of development.

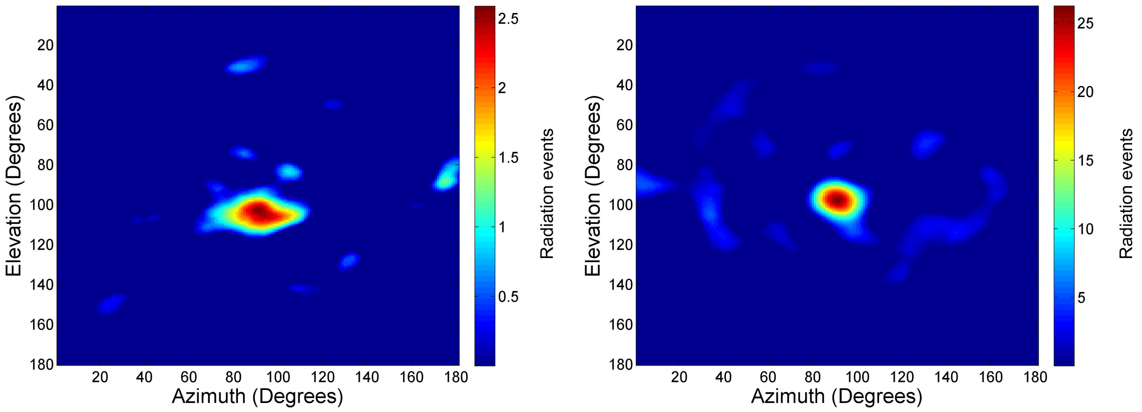

(a) Neutron image from survey point A (b) Neutron image from survey point B

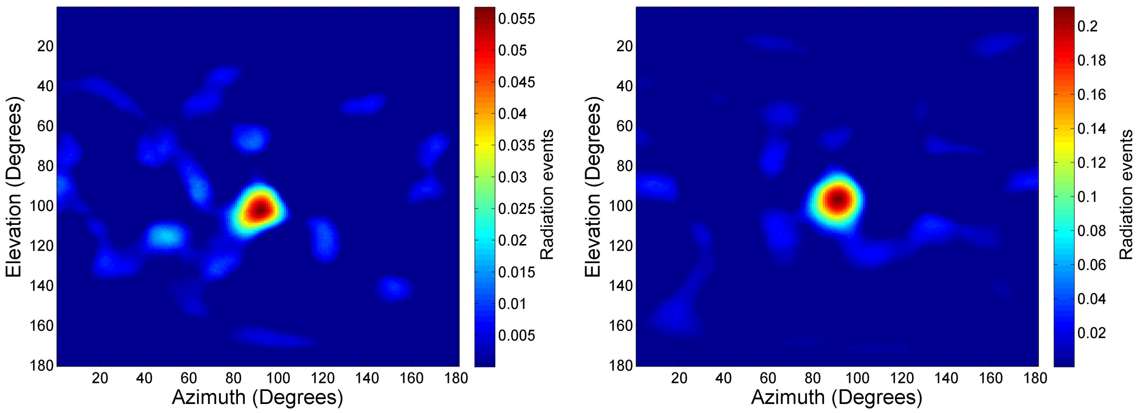

(c) Gamma-ray image from survey point A (d) Gamma-ray image from survey point B

Figure 6.6 Radiation images produced from survey points A and B in experiment 6 as a function of elevation and azimuth angle.

In practical applications of this approach the main advantages are that the mass and size of the collimator can be greatly reduced which may be critical in some cases. The drawbacks are that the detector is mostly unshielded and therefore could be easily degrade PSD in high-dose environments. Taking the pulse length (rise and decay) as 200 ns, PSD would begin to break down when spacing between events approaches the pulse length, i.e. when the event rate approaches 5 MHz.

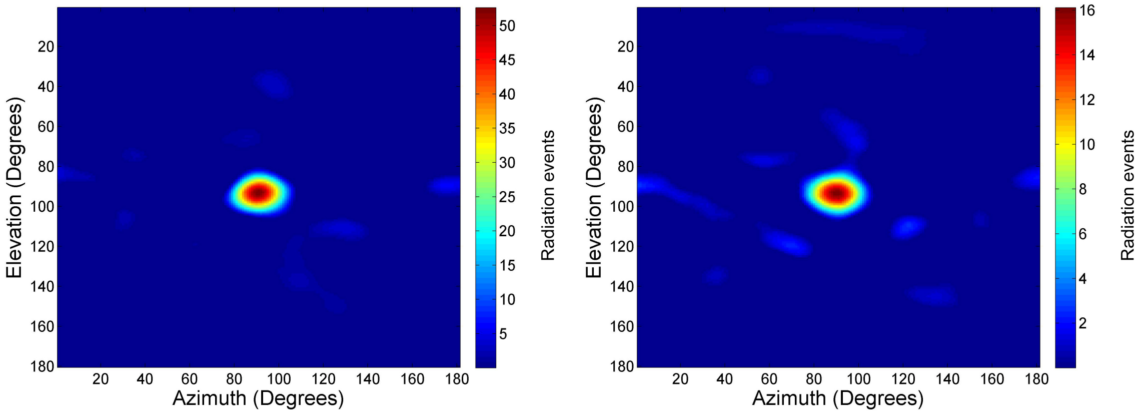

(a) Neutron image, no PE

(b) Neutron image, PE shield present

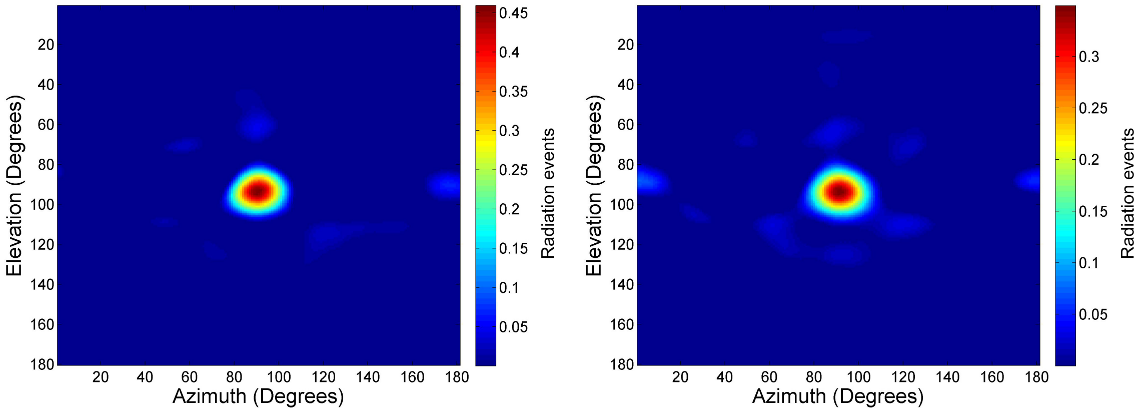

(c) Gamma-ray image, no PE

(d) Gamma-ray image, PE shield present

Figure 6.7 Radiation images produced from survey point C with and without PE shielding in experiment 6 as a function of elevation and azimuth angle.

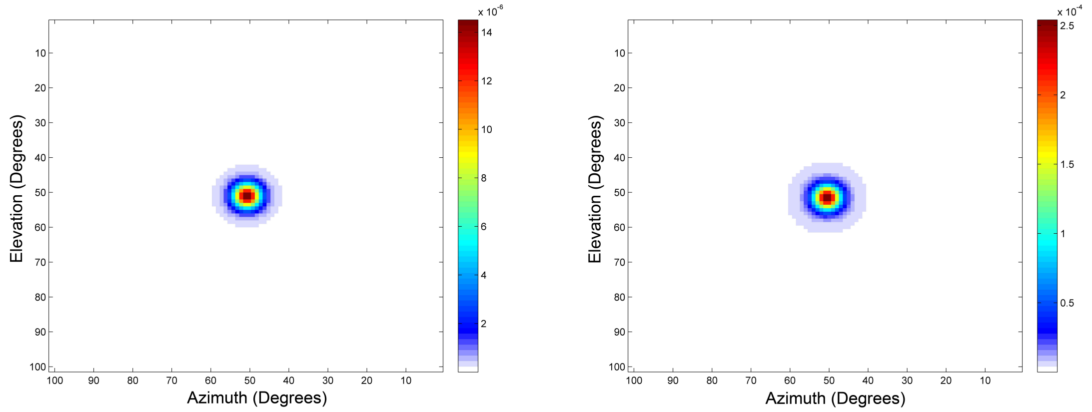

(a) Simulated neutron image from survey point C (b) Simulated gamma-ray image from survey point C

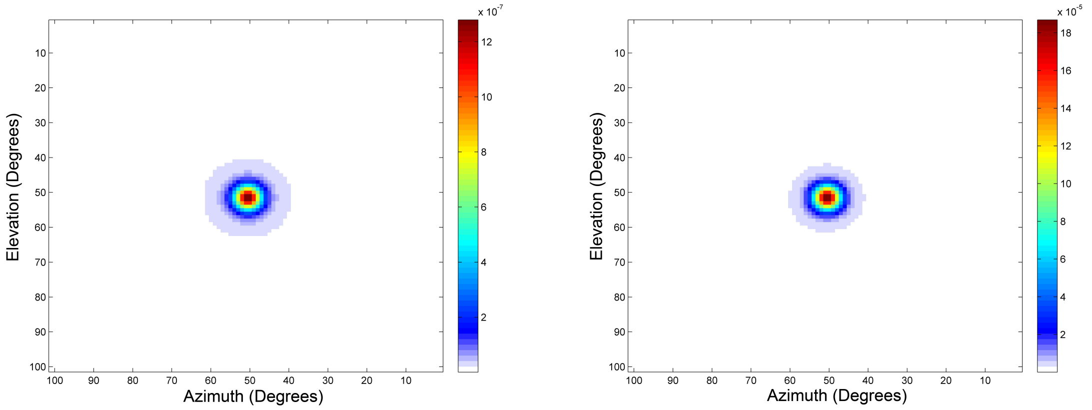

(c) Simulated neutron image from survey point C with 5 cm PE shield (d) Simulated gamma-ray image from survey point C with 5 cm PE shield

Figure 6.8 Simulated radiation images produced from survey point C with and without PE shielding in experiment 6 as a function of elevation and azimuth angle.

Chapter 7

Uncollimated multi-detector system for source locating in real-time

Chapter summary

This chapter includes information on imaging experiments performed with the uncollimated multi-detector imager configuration including the set-up, calibrations, unprocessed image data and the image solutions.

7.1 Experiment 7: Real-time radiation source tracking

7.1.1 Introduction and rationale

The work in this thesis so far has investigated the imaging of unknown radiation distributions produced by multiple sources in a local environment. However, there are also situations where a single radiation source (or a close approximation) is used and knowledge of the location in real-time is valuable. This experiment demonstrates a method for tracking a single radiation source without prior knowledge of activity or emission energy. A neutron or gamma-ray source can be tracked in real-time in three dimensions with this method, using 4 low-hazard liquid scintillation detectors. This system is compact, portable and modular and could be easily expanded to include more detectors. This method could be used to track a single source or cluster of activity in applications such as nuclear decommissioning (e.g. monitoring pipe flow of radioactive materials) or in radiotherapy to monitor the dose to a patient or nurse.

7.1.2 Experimental set-up and apparatus

The apparatus used in this experiment is summarised in Table 7.1. This experiment was performed in the Department of Engineering, Lancaster University, UK.

Table 7.1 Summary of materials and methods used in experiment 7.

MFA	4 channel MFAX4.1 [section 3.2.2]
Data collection	Custom pulse counter [section 3.2.5]
Discrimination	NA
Detector(s)	4×10 cm cubic EJ-309 [section 3.2.1]
Collimator	None
Imaging method	Detector ratio localisation [section 3.3.5]
Imaging parameters	Data read every 1s
Radiation sources	^{137}Cs (1.3 MBq)

The imaging system was assembled in the radiation lab. The z axis was taken as the vertical axis, the x and y planes were within the horizontal. Three of the detectors were placed in the same horizontal plane on the desk surface, with displacements of $l = 40$ cm (from geometric centres of the scintillation chambers) in x or y from the first. The fourth detector was placed in an elevated position 40 cm above the first detector. A photograph of the experimental set-up is shown in Fig. 7.2.

The ^{137}Cs source was placed equidistant from the detectors and the gamma-ray energy spectra were accumulated in the MFA software. The high voltage and gain of each detector were adjusted such that the Compton edge peaks in the gamma-ray spectra were located at the same channel, channel $Ch_{peak} = 238$ as shown in Fig. 7.1. The background rate at each detector was recorded for time $t_b = 100$ seconds.

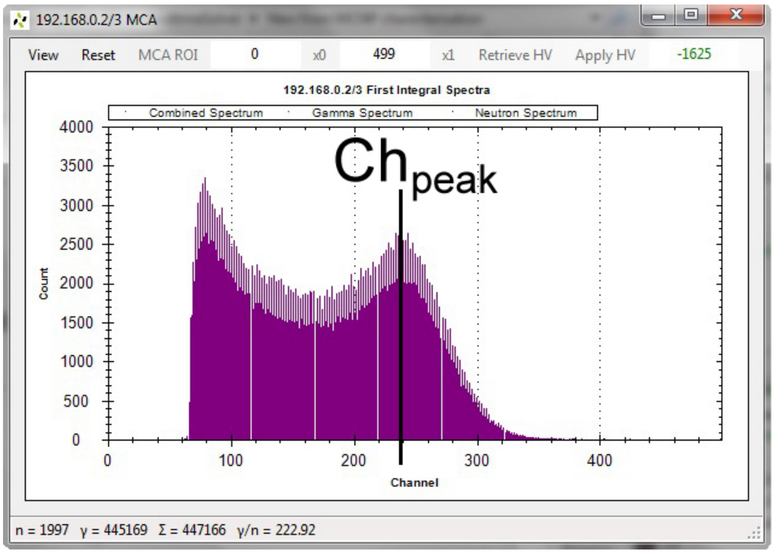

```
n = 1997   γ = 445169   Σ = 447166   γ/n = 222.92
```

Figure 7.1 Detector energy calibration in experiment 7 using the peak close to the Compton edge to set the gain of the detectors for normalisation. Detector HV was adjusted such that Ch$_{peak}$ occurred at the same channel in each case.

Following calibration, the source tracking routine was initiated and the number of radiation events at each detector were accumulated repetitively in one second intervals. This information was passed into the MATLAB environment where the position of the source was calculated using the method outlined in section 3.3.5.

7.1.3 Results

The system underwent an initial investigation to determine the mapping of the source in image space to real space. A ^{137}Cs source was placed sequentially at thirteen points in the

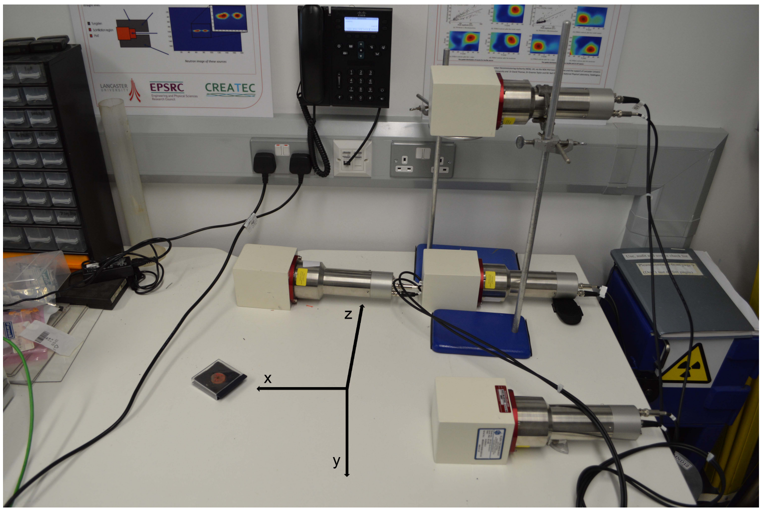

Figure 7.2 Experimental set-up for experiment 7 showing the arrangement of 4 liquid scintillation detectors in relation to the 3D coordinate system. The ^{137}Cs source is also shown.

z=20 plane. The true coordinates clockwise from the top right cluster: (16,16,20), (16,21,20), (16,31,20), (16,31,20), (16,41,20), (16,51,20), (31,51,20), (46,51,20), (46,41,20), (46,31,20), (46,21,20), (46,16,20). Centre: (31,31,20). The corresponding heat map of the position solutions is shown in Fig. 7.3.

The tracked points in each position were analysed to find the standard deviation in the x, y and z planes. $\bar{\sigma}_r$ is the sum of these values in quadrature and represents the standard deviation of the distance of the solutions in 3D. These results are shown in Table 7.2.

Table 7.2 Mean standard deviations of tracked coordinates in 1D: x, y, z and 3D: r.

Standard deviation parameter	Value (cm)
$\bar{\sigma}_x$	2.42
$\bar{\sigma}_y$	2.42
$\bar{\sigma}_z$	4.78
$\bar{\sigma}_r$	5.88

The capabilities of this system to track a radiation source in real-time were investigated. The source was moved within the z=20 plane, moved along straight lines from true positions: (19,24,20) to (45,42,20) to (45,19,20), i.e. in a “V” shape. x and y coordinates are mapped in the top left corner; the scale on the diagram is in voxels of width 2 cm. The calculated z-value is given above each diagram. The position was calculated using data collected over 1

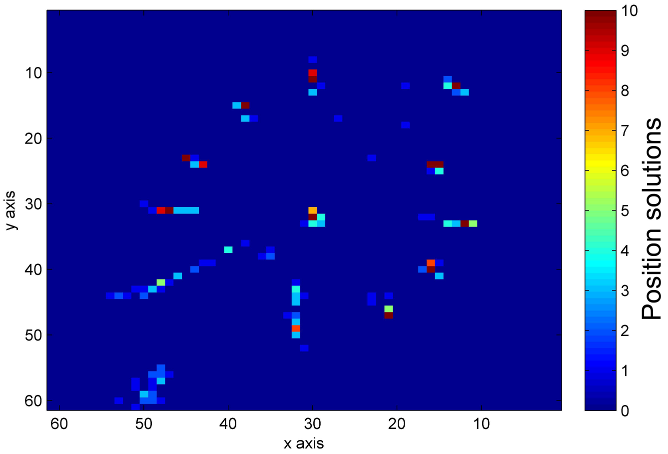

Figure 7.3 Tracking results from the sequential placement of a 1.3 MBq ^{137}Cs source at thirteen positions in a grid in the z plane. Each solution for location was binned cumulatively into the x-y plane. Some biases in the position solutions exist leading to a circular shape rather than a grid.

s intervals, including processing time gives a reading approximately every 2 seconds. These results are best viewed in the Supplementary Video 4, see appendix A.1.

7.1.4 Discussion

Discrimination parameters were not used in this experiment and the total count rates were used to determine the source location.

The two-dimensional positional response in Fig. 7.3 shows that, when static, the source position was calculated with a reasonable level of accuracy, yielding reproducible calculations. The average standard deviation of the calculated position vector from the true positions was 5.88 cm (Table 7.2) over a range of 60 cm × 60 cm × 60 cm in 2 cm × 2 cm × 2 cm voxels. This demonstrates that this method provides useful tracking information to typically within 3 × 3 × 3 = 27 voxels out of a total of 27,000, i.e. if restructuring the voxel geometry, the voxel containing the source can be determined out of 1000 voxels with single sigma confidence. It can be seen in Fig. 7.3 that the position calculation is not perfect and biases exist between measured and true values. This should be addressed firstly by improving the characterisation of the detector and environment; the used modelling approach was simplistic. The presence of PMTs, the table and walls not included in the model, will perturb the position response due to scatter contributions; including these aspects in the model would likely yield a more accurate calculation. Secondly improving the method of position calculation may allow more accurate results. Any further biases could be addressed using a geometric mapping technique

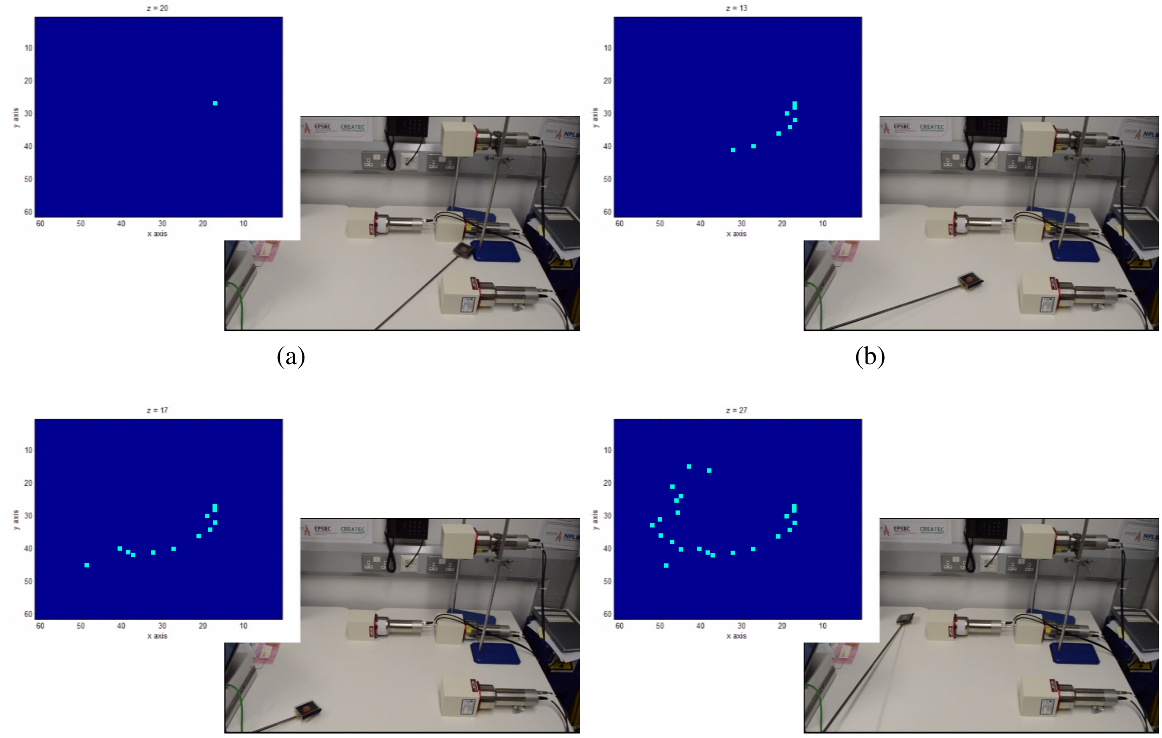

(a) (b) (c) (d)

Figure 7.4 Four stills from Supplementary Video 4 (appendix A.1) showing the real-time movement and tracking of a 1.3 MBq ^{137}Cs source through the x-y plane.

between calculated voxels and known real positions, in effect a calibration, for each such system once installed.

Supplementary Video 4 (appendix A.1) and stills (Fig. 7.4) show that this method can be applied to track a 1.3 MBq gamma-ray radiation source in a local 60 × 60 × 60 cm volume with the aforementioned accuracies. The source position was calculated and displayed approximately every two seconds based on a data collection time of one second. Whilst there are clearly many improvements to be made in processing speed and geometric calculation, these preliminary results demonstrate that this method is feasible and can yield meaningful position tracking results in near real-time.

This experiment was designed as a precursor to a combined fast-neutron and gamma-ray tracking system. If the fields could be well isolated, one neutron and one gamma-ray source could be tracked simultaneously with an identical set-up and minor adaptations. Only a second duplicate program would be required to perform neutron calculations which could run on the same processor. It is also worth noting that this imaging method is invariable with source activity. A rapidly reducing activity such as with medical sources of short half-lives would not affect the calculation other than statistically with count rate. The ability to track multiple sources with this approach is also a possibility and can be further investigated. This experiment was performed with 4 detectors, the minimum needed to locate a single source in 3 dimensions. Adding additional detectors would provide more degrees of freedom and would allow more accurate results as well as allowing a higher number of sources to be resolved.

Chapter 8

Conclusions

Chapter summary

A summary of the developed imaging techniques is provided with details on the development, capabilities and cost associated with each imaging system. These imagers are discussed and compared against alternative fast neutrons imagers in active research in the context of industrial deployment. The novel achievements of the research, the achievements in comparison with the initial research goals, suggestions for future work and implementation of the research in an industrial context are also discussed.

8.1 Imager development, capabilities and cost

8.1.1 Collimated single-detector imaging

The main aim of this research has been to engineer a compact, remotely operated probe with the capability to image combined fast-neutron and gamma-ray fields using a collimated slot-modulation approach. Four differently modified probes of this type have been investigated.

The general approach of imaging fast-neutrons with a tungsten slot-collimator was shown to be feasible through experiment 1, though at this stage with significant limitations such as prior knowledge of the bounds of the source location. The ability to correlate items in an optical image with sources of neutron radiation was shown. Experiment 2 demonstrated that the ART reconstruction algorithm could be used to overcome these limitations, extending the capabilities of the system to image radiation fields without the requirement for prior knowledge. This experiment also provided an investigation into combined neutron spectroscopy indicating that source-identification was achievable and should be further explored. This was not pursued, the reason being that to surpass the 35 cps limit imposed by the Ethernet connection, the TTL outputs of the MFAs had to be used from experiment 3 onwards. These did not support transfer of pulse-height information in their current state. Experiment 2 also demonstrated that the two-point resolution of the imager was at least 20°.

Through Experiments 1-3 the main driver for development was to improve image quality which was physically restricted by the sensitivity matrix of the system. The sensitivity matrix is essentially defined by the collimator which was a major area of development (section 4.4). The resulting collimator was a combination of a cylindrical tungsten core which provided the majority of gamma-ray shielding and some neutron shielding, and an exterior cylindrical polyethylene collimator which mostly improved the neutron shielding. This configuration was compact, balancing the trade-off between collimator size and quality, and provided a level of contrast sufficient to produce accurate images. The slot width was also found to be a reasonable compromise between resolution and statistics from radiation detection (a narrow collimator provides higher resolution but lower efficiency). Further development of the collimator is highlighted as the major focus for further research if improved image resolution, statistics or contrast is required. The ART algorithm and collimator characterisation were sufficient to provide accurate source imaging with few image artefacts. The demonstration of image quality attributed to the aforementioned developments is exhibited in Experiments 2-5, showing that the radiation images are consistent with the true field distributions, smaller contributions, e.g. from neutron scatter can be resolved and the imager could be deployed in a survey scenario to locate sources present within a room.

Experiment 4 provided an opportunity to test the feasibility of imaging a heavily shielded fission source emitting a very weak neutron field. Here, the stability of the system and immunity to background neutron radiation were key facilitators to the flexibility of the imager in terms of exposure time; these were demonstrated to be sufficient. Experiment 5 was the main driver to overcome the count rate restriction of the Ethernet, which was undertaken with a long lead time. This prompted the development of an electronics module to improve the data transfer rate from 35 events per second to the limitation of the MFA at 9 Mpps, (section 3.2.5). This experiment presented the capabilities of the system for field-deployment at a nuclear facility. As well as high-dose operation; the probe was found to operate without issue at a minimum of 62 mSv/h dose rate. Here an operational reactor core comprising special nuclear materials undergoing a critical fission reaction were imaged in a hydrogenous environment. The capabilities demonstrated in Experiments 1-5 are summarised below.

- Compact, lightweight (15 kg) imaging probe and portable system can be transported and deployed in the field by a single individual
- Images of fast-neutron and gamma-ray fields can be discretely obtained which accurately represent the true radiation fields
- Sources of neutron and gamma-ray radiation can be independently correlated with objects in an optical image
- Different sources of neutron radiation can be discriminated using spectroscopy in conjunction with radiation images
- Flexibility of exposure time at least between hours to one month
- Weak fields $< 1\mu$Sv/h from heavily shielded sources can be imaged with extended image times

- System is robust to high levels of radiation and fields of at least 62 mSv/h can be imaged successfully
- Critical fission reactions and fission sources can be imaged in hydrogenous environments

The advantages of this design are as follows. Only a single detector is required; this gives the system robustness through simplicity and minimises the cost of detectors and signal processing electronics which are costly components. A collimator is required, which is reasonably expensive, however the excess cost is easily made up by the saving on detectors and processing electronics. The system can be made compact, portable and lightweight with this approach.

The cost of the commercial off-the-shelf components and custom components for this configuration are expected to be in the range of £16-23k and are summarised in Table 8.1. The probe excludes the MFA, laptop and pulse counter therefore the cost of the probe would be around £7.5-12.5k. This is cheap enough to warrant this component being sacrificial in some cases, if required.

Table 8.1 Collimated single-detector imager approximate cost (excluding VAT) in 2016 and suppliers.

Item	Supplier	Cost
Detector and PMT	John Caunt Scientific Ltd.	£1500
Single-channel MFA	Hybrid Instruments	£7500
Tungsten collimator	M&I Materials	£3-6k
Manufactured custom pulse counter	Various suppliers	£400-500
Chassis and motors	Various suppliers	£2-3k
Radiation-tolerant optical cameras	Various suppliers	£1-2 k
Laptop PC	Various suppliers	£1-2 k
Total		£16.4 - 22.5k

8.1.2 Anti-collimated single-detector imaging

The anti-collimator imager is very much a continuation of the previously mentioned goals, addressing in particular the need for a more compact and lightweight imager. This system was shown in section 4.4.8 to have a superior image contrast in comparison with the collimated system. The system also has potential to image much higher neutron energy ranges, due to the different collimation approach. However, the survey performed in experiment 6 indicated that the imaging capabilities are not superior to the collimated imager; this could be due to the unshielded nature of the detector and the resulting contributions of background and scattered neutrons to measurement noise, subsequently decreasing the signal to noise ratio. The imager was shown to have the ability to locate neutron and gamma-ray radiation sources with some indication that smaller scatter contributions could be resolved. The following capabilities were demonstrated in experiment 6:

- Compact, lightweight (5 kg) imaging probe and portable system can be transported and deployed in the field by a single individual (improvement on the collimated single-detector imager)
- Images of fast-neutron and gamma-ray fields can be discretely obtained which accurately represent the true radiation fields

The cost of the commercial off-the-shelf components and custom components for this configuration are expected to be in the range of £14-18k are summarised in Table 8.2.

Table 8.2 Anti-collimated single-detector imager approximate cost (excluding VAT) in 2016 and suppliers.

Item	Supplier	Cost
Detector and PMT	John Caunt Scientific Ltd.	£1500
Single-channel MFA	Hybrid Instruments	£7500
Tungsten collimator	M&I Materials	£1-1.2k
Manufactured custom pulse counter	Various suppliers	£400-500
Chassis and motors	Various suppliers	£2-3k
Radiation-tolerant optical cameras	Various suppliers	£1-2k
Laptop PC	Various suppliers	£1-2 k
Total		£14.4-17.7k

8.1.3 Uncollimated multi-detector system for source locating in real-time

This configuration presented an opportunity to take advantages of the real-time pulse processing properties of the MFA to obtain spatial information in real-time. A basic trial of this system found that a single radiation source could be tracked using gamma rays to produce repeatable results which correlated with the position of the source and was updated every 2 seconds.

The following capabilities were demonstrated in experiment 7:

- Gamma-ray source can be tracked to 6 cm precision in 60 × 60 × 60 cm subject to some geometric mapping
- Spatial information is produced in real-time every 2 s

In its current state this system could be easily adapted to image a neutron source with the same capabilities, which was the intended next step of development.

The cost of the commercial off-the-shelf components and custom components for this configuration are summarised in Table 8.3.

Table 8.3 3D source tracking imager approximate cost (excluding VAT) in 2016 and suppliers.

Item	Supplier	Cost
4 × detectors and PMTs	John Caunt Scientific Ltd.	£8k
4-channel MFA	Hybrid Instruments	£10k
Manufactured custom pulse counter	Various suppliers	£500-600
Chassis	Various suppliers	£0.5-1k
Laptop PC	Various suppliers	£1-2 k
Total		£20-21.6k

8.2 Summary of fast-neutron imagers

A summary table of fast-neutron imagers including this research is provided in Table 8.4. This table has been expanded from Table 2.5 by adding the imagers in this research. Additional information on the table follows:

*Criteria in the following Tables 8.4 and 8.5 are port. (portability of whole system), compac. (compactness of front end only, i.e. detector and physically attached components, motors, collimators etc), weight (of front end only), eff. (efficiency of detectors), sens. (demonstrated sensitivity of system: good indicates ability to measure weak neutron fields such as those from large stand-off distances or in conjunction with heavy shielding), res. (position resolution of a single source), art. (good indicates that artefacts are not present in image solutions), speed (of data collection: good indicates fast), FOV (field of view), and mult. (good indicates good image quality when imaging multiple sources of the same radiation type).

Table 8.4 Summary table of alternative fast-neutron imagers*.

Imager	Port.	Compac.	Weight	Eff.	Sens.	Res.	Art.	Speed	FOV	Mult.
PINEX-2 pin-hole	poor	poor	poor	v. poor	v. v. poor	v. good	poor	v. good	poor	good
Penumbral imaging technique	poor	poor	poor	v. poor	v. poor	v. good	med	v. good	poor	no info
Brookhaven NL scatter camera	med	poor	poor	good	v. good	good	med	good	poor	no info
FNIT	med	good	poor	med	no info	med	med	med	good	no info
Sandia NL scatter camera	med	med	poor	good	good	good	med	good	poor	no info
U. Michigan scatter camera	med	med	poor	good	med	med	med	good	v. good	good
U. New Hampshire scatter	good	med	poor	med	good	med	med	med	poor	no info
ORNL, SNL, INL coded aperture	poor	poor	poor	good	med	good	good	good	poor	good
CLYC Radcam	good	good	med	poor	no info	good	poor	v. poor	v. good	no info
Sandia NL time-encoded	good	good	med	poor	no info	good	good	poor	med	good
U. Lancaster single-detector †	good	med	med	poor	no info	med	med	good	poor	no info
Time projection chamber	med	good	poor	poor	good	good	med	good	v. good	no info
Collimated single-detector	v. good	v. good	good	poor	v. good	good	good	med	v. good	good
Anti-collimated single-detector	v. good	v. good	v. good	poor	no info	good	good	med	v. good	good
Uncollimated multi-detector	v. good	good	v. good	med	no info	med	N/A	v. good	med	N/A

† This imager is not fully-automated

Table 8.5 Requirements for imager capabilities in different scenarios*, dose also included[†]. Plus ‘+’ indicates that higher capabilities would be beneficial.

Scenario	Port.	Compac.	Weight	Eff.	Sens.	Res.	Art.	Speed	FOV	Mult.	Dose[†]
D1. Contaminated equipment	med+	med+	poor+	NA	v. good	good+	good+	poor/med+	good+	good+	poor
D2. Contaminated hot cell	med+	v. good	v. good	NA	med+	good+	good+	poor+	v. good	good+	v. good
D3. Fuel debris in reactor pos 1.	poor+	v. good	v. good	NA	med+	good+	good+	poor+	v. good	good+	v. v. good
D4. Fuel debris in reactor pos 2.	poor+	v. good	v. good	NA	good+	v. good+	good+	poor+	med+	good+	v. good+
NS1: Source location	med+	poor+	med+	NA	good+	poor+	good	good	good+	poor+	NA
NS2: Source tracking	NA	NA	NA	v. good	good+	good+	good+	v. good	med+	poor+	NA
SG1: Attribute testing	v. good	v. good	v. good+	NA	good+	v. good	good	good	good+	good	NA
SG2: Source location	med+	poor+	med+	NA	good+	poor+	good	good	good+	poor+	NA
ND1: Neutron dosimetry	NA	NA	NA	med+	good+	med+	v. good	v. good	NA	NA	NA
R1: Radiotherapy	med+	med+	med+	NA	good+	good+	good	NA	good+	good	NA

[†] Dose: dose tolerance of front-end probe

8.3 Summary of novel achievements and addition to the field

The following novel achievements have been attained in this thesis and contribute to scientific knowledge.

1. Neutron imaging with a collimated slot-modulation approach
2. Neutron imaging with an anti-collimated slot-modulation approach
3. Characterisation of neutron fields with a portable, lightweight and compact probe under 50 cm outer radius
4. Characterisation of the neutron and gamma-ray fields within an operational nuclear reactor with combined gamma-ray and neutron imaging
5. High-dose neutron imaging with a portable, lightweight and compact probe
6. Imaging of heavily shielded sources of neutron radiation with resultant neutron field below 1 μSv/h
7. Real-time motion tracking of radioactive sources in three dimensions

8.4 Achievement of research goals

A summary of the research goals and achievement is given in Table 8.6.

8.5 Research applications

Applications of fast-neutron imagers to industry are considered. It is assumed that the ability to image the gamma-ray field (discretely from the neutron field) is always advantageous in such scenarios as information on gamma-ray emitting materials can also be obtained. The discussion focuses on neutron imaging aspects.

8.5.1 Nuclear decommissioning

In nuclear decommissioning, knowledge of the distribution and abundance of radiological materials is paramount for the decommissioning strategy. These materials range from residues in walls to nuclear fuel in reactors. These sources are also in the presence of high-Z shielding (e.g. structural steel, lead shields), low-A shielding (e.g. hydrogenous shielding), or both which reduce the flux and change the distribution of the emitted neutron and gamma-ray fields. Combined neutron and gamma-ray imaging is therefore advantageous

Table 8.6 Summary of research goals in this thesis and achievements.

Goal	Required	Desired	Achieved
Discretely image combined fast-neutron and gamma-ray fields	Yes		Yes
Image resolution allows individual sources to be resolved	20°	2°	<20°
Determine relative detected flux associated with each source or localised source distribution	Yes		Yes
Associate source distributions with locations in real space	Yes		Yes
No interference with plant operations during imaging process	Yes		Yes
Quickly assembled, disassembled and packaged	Yes		< 20 min
Compact probe outer diameter	50 cm	15 cm	25 cm
Lightweight probe	10 kg	5 kg	15kg / 5 kg
Fast data acquisition time	< 8 hours	2 hours	3 hours
Discern special nuclear materials from other radioactive materials	No	Yes	No
System can be transported by a single individual and vehicle	No	Yes	Yes
System fully operated remotely	Yes		Yes
Imaging probe is radiation tolerant	50 mSv/h	1 Sv/h	> 62 mSv/h

in these scenarios. Neutron detection is particularly useful at locating special fissile materials of paramount strategic importance. Three nuclear decommissioning scenarios are considered where deployment of a fast-neutron imager may add value; the requirements for these scenarios are outlined in Table 8.5.

Scenario D1: contaminated equipment. Small residues can accumulate in machinery, glove boxes or other apparatus, allowing a build-up over time of special nuclear materials or other neutron-emitting materials. If the amount and location of material is unknown, decontamination may be difficult. If disposal was required, the entire item might be classified as high-level waste and therefore would be costly. Characterising the item using fast-neutron imaging would give information on the distribution of such materials, allowing the item to be more easily decontaminated or the classification reduced for constituent parts; either option reduces the cost of disposal. These scenarios would require an imager with sufficient portability to move it to the contaminated area but compactness and weight would not be critical. A very high sensitivity, good resolution and capabilities to image multiple sources in a large field of view with minimal image artefacts would be necessary to accurately locate small amounts of residues. High radiation fields are not expected where human operators are present, hence high-dose tolerance is not required. If the facility was in use and interference was costly, deployment time might be an important factor.

For this scenario, the collimated single-detector imager would be a candidate, fulfilling all required criteria. The critical points for this problem are the capabilities of high image quality in combination with the imaging of very weak neutron fields. The demonstration of weak field imaging in experiment 4, and the ability to image weak field components (scatter) in experiment 3 demonstrate the applicability of this imager to this scenario. The best candidate from alternative imagers is the Brookhaven National Laboratory Scatter Camera due to its very high sensitivity, meeting the specification with the exception of the field of view which is much smaller. If the imager deployment interfered with the plant operations, moving a large and bulky imager around to several positions may significantly reduce the cost benefit of such a deployment.

In conclusion the collimated single-detector imager may provide a solution for this problem and would be expected to perform well in comparison with alternative imagers. An adaptation of this approach specifically to a scenario may significantly improve results. For example, if imaging a glove box, changing the scanning process to $\hat{\alpha}$ rotation and horizontal translation instead of $\hat{\alpha}$ and $\hat{\beta}$ rotation around a point would make the sensitivity more spatially uniform. This method could be approximated with the current system by imaging from several survey points and combining data into a three-dimensional point cloud, though this would increase deployment time.

Scenario D2: contaminated hot cell. The next scenario is the survey of a hot cell where the goal is to locate and characterise sources of neutrons such as special fissile materials. Critical capabilities are likely to be the restriction in terms of access; human access to an area may be impossible and often the probe may have to fit through an access port as small as 15 cm, hence compactness and weight would be key for deployment. These areas may have very high gamma-ray and thermal neutron backgrounds, contributing to the radiation dose which can easily exceed 50 mSv/h; dose tolerance a strong requirement. If the facility was in use, imaging time would be restricted to hours or days and usually a full field of view would be required if no prior knowledge of source distribution was available, given that there may only be a single access point. Good image quality in general would be required for location of such materials.

The capabilities of the collimated single-detector neutron imager are suited to these conditions. This scenario might be very similar to experiment 3, but where more intense radiation fields would be expected. This imager has been tested to a minimum of 62 mSv/h. The image quality is fit for purpose and, although in its infancy, the ability to discern different source types by their neutron emissions would be extremely useful and is recommended for further investigation if these applications are pursued. The requirement for a 15 cm outer radius probe has not yet been met and mass restrictions may also be paramount in some scenarios if access can only be provided through robotics. These scenarios may be addressed by the anti-collimated imager which improved on the compactness and weight. Here more testing would be required to determine the dose tolerance, image quality and effect of background dose on image quality. The alternative portable imagers discussed are less compact and have not been tested in high-dose fields, giving a significant advantage to the collimated single-detector neutron imager. The CLYC Radcam and Sandia National Laboratory time-encoded imagers with good compactness and medium weight would be the next best options, however the size and weight are in significant excess of the collimated and uncollimated single detector imagers. The alternatives also have some limitations to their fields of view and the impact of high backgrounds is unknown.

The two single-detector imagers in this research could therefore be potentially useful in these applications, though further development is recommended to minimise size and weight and increase image quality in high background fields.

Scenario D3 and D4: Fuel debris in reactor. Fissile materials are burned in reactors where they can be transmuted into other transuranics produced by the fission process (through neutron capture). Table 2.2 outlines passive neutron-emitting materials, and neutron emission from irradiated fuel in Fukushima Daiichi Unit 1 BWR reactor is summarised in Table 2.3. These materials create a significant fast-neutron field; the neutron emission at time of shut down for reactor Unit 1 was calculated to be 1.42×10^{10} neutrons per second one year after shut down, all emitted from nuclear fuel material. The reactor environment is heavily shielded with steel in the structure and pressure vessel (high-Z) and concrete and water (low-A) and will provide significant scattering and shielding to fuel materials. In the event of pressure vessel rupture, soluble Cs isotopes leak from the core and will contaminate large volumes of the primary containment vessel which makes nuclear fuel difficult to discriminate with gamma-ray-only imaging, or other gamma-ray measurement techniques, against very high gamma-ray backgrounds. In these situations, images of the neutron field would correspond directly to the layout of nuclear fuel materials as no other sources of neutron radiation would be present with the exception of start-up neutron sources in some reactors, which could be discriminated from fuel by the geometric shape in the image, i.e. a single point. The application of neutron imaging to these scenarios therefore seems extremely advantageous over gamma-ray imaging. Fig. 8.1 shows the shielding in a typical BWR reactor with hydrogenous concrete shielding in red (low-A), water in green and the steel reactor pressure vessel (RPV) (high-Z). A successful image obtained from position 1 inside the primary containment vessel (PCV) would inform on the distribution of neutron radiation and subsequently the fuel, e.g. in the RPV, at the base of the PCV. A single image would also give a lot of information about the radial distribution. This would be extremely useful information for the decommissioning program of such a reactor. An image from position 1 would be significantly challenged by the extremely high-dose environment which may blind the detector, or make PSD extremely difficult due to pile-up and detector saturation; this could cause problems with the mechatronics and PMT. To avoid such high doses it may be possible to obtain an image from outside the PCV in position 2. At this location the neutron field would be significantly weaker, though the gamma field may still be high in such cases if the PCV had ruptured. Due to the different image origin, the regions of interest would occupy a smaller field of view and a higher neutron sensitivity and resolution would be required given the large stand-off distances.

The collimated single-detector imager has been demonstrated to some degree as a possible imager for these applications. The imager has been shown to operate at a dose of 62 mSv/h (the highest dose tested in this research) and could potentially extend far beyond this range. The ability to image a reactor core and heavily shielded fission sources are direct contributions to the foundations of this application and have been demonstrated uniquely with this imager (experiment 5). These attributes, coupled with the compactness, portability and image quality of the system, make this approach feasible. High sensitivity was demonstrated in experiment 4. The stability and flexibility of the imager to perform a scan over weeks or months might allow the fuel material to be located. In position 1, no other imagers would be capable of deployment, given the requirement for compactness and weight, and none have been tested to significant radiation hardness. In position 2 the requirements for compactness and portability would also exclude the alternative imagers. After passing through reactor shielding, the neutron flux distribution is hardened and therefore may benefit from an anti-collimated approach which has the potential to provide much higher contrast at these hardened energies. The deployment would depend heavily on the background radiation, which may or may not rule out the anti-collimated imager.

In position 1 the conditions would be extremely challenging but the demonstration of the TRIGA reactor core imaging has made significant steps towards this possibility making it the first choice over the alternatives. Further testing would be required to determine if such an imager or a subsequent development could cope with such conditions. In position 2 the anti-collimated single-detector imager might be considered if radiation fields are low, otherwise the collimated single-detector imager could be deployed.

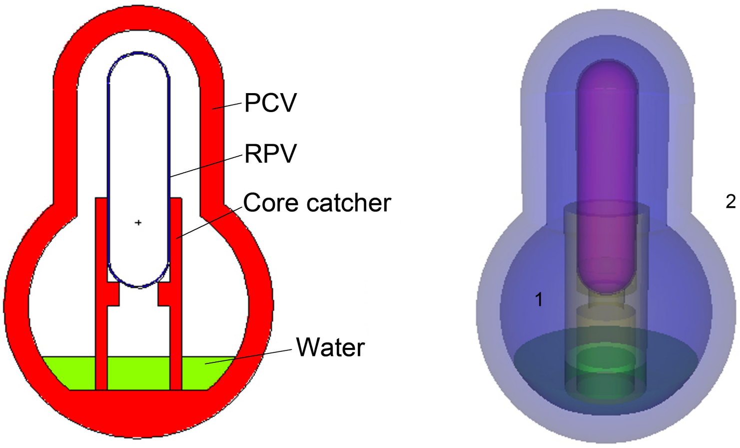

Figure 8.1 Schematic of major components and shielding in a BWR reactor.

8.5.2 Nuclear security

The goal of nuclear security is to prevent, detect and respond to the theft, sabotage, unauthorised access or illegal movement of radioactive substances [124]. The most critical of these are special fissile materials which refers to ^{239}Pu and uranium enriched in ^{233}U or ^{235}U. These substances emit gamma rays and often emit neutrons (as outlined in Table 2.2). Gamma-ray and neutron detection are therefore important components of nuclear security. Illicit movement of these materials would likely involve high-Z and hydrogenous shielding to mask their presence. These scenarios have largely been addressed by portal monitors, highly sensitive detectors which operate through non-imaging detection in scenarios where spatial confinement is already applied, e.g. in vehicles or shipping containers. There are however some nuclear security scenarios where fast-neutron and gamma-ray imaging may be applied, when the objective is to rapidly find radiological material including special fissile materials on a person, in vehicles or in buildings. These scenarios are suited for an imaging system which can detect such objects through shielding, with very low detection thresholds and as quickly as possible, with an image being formed in minutes or ideally in seconds. The quality of an image is not likely to be important; a simple hotspot locator would usually be sufficient. Two nuclear security scenarios are considered where deployment of a fast-neutron imager may add value, the requirements for these scenarios are outlined in Table 8.5.

Scenario NS1: Source location. This scenario considers the need to rapidly locate an illicit radiation source in a civil structure environment such as an apartment block or a shipyard. The ability to image neutron and gamma ray radiation fields increases the probability that these materials can be located and is therefore greatly advantageous. Such a system would be to have some level of portability to allow the system to be moved to such areas during a search; compactness and weight are not important beyond portability. It is very likely that only a single source would be present and therefore image quality is not beneficial, other than to locate the position accurately and to not provide false artefacts. The most critical capabilities would be high sensitivity and speed.

The collimated single-detector imager is the closest match to these circumstances, fulfilling the criteria for portability, image quality and sensitivity. The speed is however not up to requirement, as a measurement takes hours. The alternatives offer better matches for these scenarios, in particular the Brookhaven National Laboratory scatter camera, the Sandia National Laboratory scatter camera and the time projection chamber, therefore these systems would therefore be advantageous.

In its current form the collimated single-detector imager is not suited for these scenarios and could not compete with the alternatives. In order to compete, significant further development would be required. There is a trade-off between image time and quality which would allow significantly shorter scan time if high quality was not required. The reduced size and weight of this imager would allow multiple deployments on several individuals and could allow competition with speed.

NS2: Source tracking. Another nuclear security scenario would be to monitor a flow of objects, such as pedestrians or traffic, in which may be hidden an illicit radiation source. For this circumstance it is assumed that prior knowledge of the location is known, e.g. within the bounds of a corridor or road. Such scenarios are addressed currently with portal monitors, but rely on the passage of a single object at a time through a portal. This method removes such a restriction, allows larger areas to be monitored and assumes that an illicit source could be tracked to a person or vehicle without the restriction of flow. This scenario is only concerned with having a high sensitivity, resolution, efficiency and speed with no false positives (artefacts).

The uncollimated multi-detector system could be applied to this scenario meeting all requirements with the exception of sensitivity, which is currently unknown. The ability to track a single source in 3D, with real-time results (and with minimal data collection time), makes this system ideal for such a problem assuming that the sensitivity and detection probability would be sufficient. The Brookhaven National Laboratory scatter camera has demonstrated such a high sensitivity and efficiency and ranks as first choice amongst the alternatives for this scenario. The high speed however has not been demonstrated to the level of the uncollimated multi-detector system and therefore may make this unsuitable.

The uncollimated multi-detector system appears to show promise for this application and further research and development is recommended. The system should be developed to image neutron and gamma ray fields simultaneously, adapting the system for higher detection probability, such as by adding more detectors with higher efficiency.

8.5.3 Nuclear safeguards

There are many situations in nuclear safeguards where the characterisation of neutron-emitting materials is required. Bias and partial defect testing, where quantities of special fissile materials are measured, are beyond the scope of radiation imaging, however attribute testing (measuring the presence of characteristic radiation) may be within scope of an imager for gross defect testing (determining if an item is present or not). During physical inventory verification, inspectors perform a set of tests to measure special fissile materials and to ascertain if the measurements agree with the declared material balance. Different tests have varying measurement accuracy, measurement time and detection probability and are structured together to give a set detection probability against all methods of diversion. Improving the speed of any test is advantageous to measurement success on restricted time-scales and may allow improvements to overall detection probabilities. Attribute testing is often required for a given number of randomly selected items. This might be fuel assemblies, fuel rods, drums containing special fissile materials etc. The ability to survey all materials simultaneously with an attribute test, e.g. for neutron emission, would allow gross defect testing to be performed quicker and for a larger sample, particularly if the system was fully autonomous and required minimal contact time from an inspector. Two nuclear safeguards scenarios are considered where deployment of a fast-neutron imager may add value, the requirements for these scenarios are outlined in Table 8.5.

SG1: Attribute testing. This scenario considers testing a single hard to access item (reducing time or complexity required for the test), or an array of items (multiple simultaneous tests reduce total time or increase sample strata) for characteristic neutron emission. Assuming that the system would be transported by personnel the necessary requirements would be very good portability, compactness and weight. Depending of the type of items under scrutiny and the presence of shielding, at least a good level of sensitivity would be needed. Good image quality in terms of resolution, artefacts and ability to image multiple sources would be important along with a good field of view. Speed is also a strong consideration.

The anti-collimated single-detector imager offers the only reasonable option for such applications, given the very high portability, compactness and weight. Further research is recommended to better optimise such an imager design for this purpose in terms of further improving the portability, compactness and weight, and demonstrating the ability to image multiple sources of weak neutron fields within a time-scale of 1-2 hours. The ability to discern Pu from Cf or other neutron-emitting materials would be greatly advantageous in such scenarios.

SG2: Source location. Inspections performed under complimentary access, where a site may be visited for the first time, would benefit from the deployment of an imager to search for any neutron-emitting materials within a civil structure to prompt further investigations. The requirements and conclusions for this scenario can be considered to be the same as with NS1: Source location.

8.5.4 Dosimetry

Modern neutron dosimetry is performed with electronic personal dosimeters or film badges which have the fundamental drawback of having a fixed position on the body. The dose is only measured at a single position and therefore limits the accuracy of this technique. The error on measurement for neutron dosimeters is also extremely large, typically ±50%, providing significant room for improvement [125]. The use of a system such as the real-time radiation source tracker, with further improvements, could be used to accurately track the position of the source in 3D space. This information and prior information of the source's gamma-ray and neutron dose could be combined with body-tracking machine vision to provide considerably higher precision and accuracy than a personal dosimeter. Doses to individuals could be better monitored, providing more accurate feedback on any exposure; this would allow procedures to be better planned to ensure dose is as low as reasonably achievable (ALARA). This would also allow more exposure time within given dose limits as the worst-case scenario dose could be reduced with the error on measurement. The requirements for this scenario are outlined in Table 8.5.

ND1: Neutron dosimetry. The requirements for such a system would be to have very good position resolution and speed, producing few artefacts or incorrect readings. The sensitivity would vary with application. One specific application, for a gamma-ray field, would be to accurately track a single source used in brachytherapy treatments. Here, absorbed dose could be more accurately calculated and could be used to fine-tune the procedure to ensure the dose is as low as reasonably practical. This provides benefit to both the patient and staff, reducing stochastic radiation effects. More accurate dosimetry for medical professionals would allow more procedures to be performed within their individual dose limits.

The uncollimated multi-detector system, if used to track a neutron source, could be applied to such scenarios and most closely matches the requirements. Other fast neutron imagers would not be suitable for this task given the lack of speed. Further development would be required, in particular addressing the mapping and position resolution which would be critical for these circumstances and subsequent integration with machine vision for position tracking of a human body.

8.5.5 Radiotherapy

The ability to characterise neutron fields may be useful to many disciplines where neutron fields are involved, for example radiotherapy. Accelerator and reactor driven fast-neutron fields have been trialled as a method of radiotherapy [126] [127] and are also produced as secondary fields in other methods of radiotherapy. Photon radiotherapy can produce a significant fast-neutron dose to the patient via the photoneutron reaction in the tungsten collimator used to shape the beam [128].

R1: Radiotherapy. Fast-neutron imaging could be applied to the characterisation of these secondary fields, including the effects of scatter within the room which would be unique to each facility. Depending on the scenario, these fields could range between very high-dose to very low-dose. The required capabilities would be a reasonable level of portability, compactness and weight. Good sensitivity would be needed and images of multiple sources would be formed with good resolution and without artefacts. The requirements for this scenario are outlined in Table 8.5.

The collimated single-detector imager in this research could be used to characterise fields over this dose range, meeting the requirements. The ability of the system to resolve scatter contributions, as demonstrated in experiment 3, may also be beneficial to dose investigations, the end result of which could lead to changes in the surroundings, i.e. removing or reducing scattering materials which might reduce the secondary neutron dose. Compactness and weight may not usually be severe restrictions in these scenarios, this gives little advantage to the imager over other portable imagers available. When considering neutron dose thermal neutrons should also be considered, which would give some advantages to the CLYC Radcam discussed in section 2.5.3. However the dose in these scenarios is found to be mostly due to the fast neutrons [128] which undermines the benefits of a combined thermal and fast neutron imager. Additionally the CLYC Radcam was seen to have some significant image artefacts in the solution which may not make this imager suitable for these scenarios. The Sandia National Laboratory time encoded imager complies with all the requirements for this scenario with the exception of field of view. Assuming that sensitivity and field of view could be improved this imager may be an option for this scenario.

The collimated single-detector imager in this research is considered to be a potential candidate for these applications but is not the only option available. A boron loaded EJ-309 liquid scintillator is commercially available which could expand capabilities to image thermal neutrons if required.

8.6 Future work

From study of Table 8.6 it can be seen that the majority of the research aims have been achieved; the following aspects have been left outstanding. The diameter and weight of the later stage collimated prototype was 25 cm and 15 kg. Although this complied with the required research goal, a lighter and more compact probe would provide many more options for deployment, particularly in nuclear decommissioning. A next-generation collimator could be geometrically optimised to improve the sensitivity matrix and therefore give better imaging capabilities within a smaller, more compact configuration. The mechatronics related to the rotation of the collimator could also be better integrated and miniaturised. The same applies to the anti-collimated imager.

There is significant scope to reduce the deployment time, particularly in high-dose conditions where the data acquisition time can be significantly reduced in addition to the mechatronic positioning time, e.g. faster rotation. The probe was tested to 62 mSv/h radiation dose rates which could be further extended to find the maximum operating range for the device. As with geometry and weight, this would be a limiting factor in nuclear decommissioning applications. The ability to discern materials according to their emitted neutron energy spectra was demonstrated as feasible between some radiation sources, however this was yet to be extended to nuclear materials.

Further research would therefore focus on: further miniaturisation of the probe geometry in terms of geometry and mass, fast motor positioning to reduce data collection times, high radiation-dose tolerance and a development of spectroscopic identification in nuclear materials.

8.7 Implementation in industry

This research has provided a thorough investigation with proof-of-concept in fast-neutron imaging with slot-modulation techniques (and one other technique), considering various system designs, collimator materials and applications of these approaches. The next steps for industry implementation would be to target a fast-neutron imager to a specific application, such as those discussed in section 8.5, and to develop a next-generation imaging system optimised for these conditions. The range of applications which may be economically viable are reasonably diverse and are dissimilar enough to warrant different paths for development, however an end product would include the following considerations: geometric refinement (compact, lightweight and effective design of the collimator and the mechanical modulation), additional sensors (optical cameras, laser range-finder and others), deployment considerations (facilitating mechatronics external to probe, sacrificial casings to prevent contamination), integrated user software and full integration of the entire imaging system.

Bibliography

[1] Geneviève Leuba and Rudolf Kraftsik. Changes in volume, surface estimate, three-dimensional shape and total number of neurons of the human primary visual cortex from midgestation until old age. *Anatomy and embryology*, 190(4):351–366, 1994.

[2] Guillaume A Rousselet, Simon J Thorpe, and Michele Fabre-Thorpe. How parallel is visual processing in the ventral pathway? *Trends in cognitive sciences*, 8(8):363–370, 2004.

[3] Karlk Guthe Jansky. Radio waves from outside the solar system. *Nature*, 132(3323): 66–66, 1933.

[4] Mohamed ElBaradei. Treaty on the non-proliferation of nuclear weapons. In *Statement to the 2005 Review Conference of the Treaty on the Non-Proliferation of Nuclear Weapons*, volume 2, 2005.

[5] world nuclear.org. Nuclear power in the world today, July 2016. URL http://www.world-nuclear.org/information-library/current-and-future-generation/nuclear-power-in-the-world-today.aspx.

[6] world nuclear.org. Nuclear power in france, July 2016. URL http://www.world-nuclear.org/information-library/country-profiles/countries-a-f/france.aspx.

[7] Kyoto Protocol. United nations framework convention on climate change. *Kyoto Protocol, Kyoto*, 19, 1997.

[8] world nuclear.org. Decommissioning nuclear facilities, January 2016. URL http://www.world-nuclear.org/information-library/nuclear-fuel-cycle/nuclear-wastes/decommissioning-nuclear-facilities.aspx.

[9] Nuclear Decommissioning Authority. Annual report and accounts 2015 - 2016, July 2016. URL https://www.gov.uk/government/uploads/system/uploads/attachment_data/file/537397/NDA_Annual_Report_and_Accounts_2015_to_2016.pdf.

[10] Nuclear Decommissioning Authority. About us, July 2016. URL https://www.gov.uk/government/organisations/nuclear-decommissioning-authority/about.

[11] Createc Ltd. Createc ltd. website, 2016. URL https://www.createc.co.uk/.

[12] Matthew Paul Mellor. Radiation imaging apparatus, November 17 2015. US Patent 2014/0029731 A1.

[13] Createc Ltd. N-visage™ gamma imager, October 2016. URL https://www.createc.co.uk/case_study/n-visage-gamma-imager/.

[14] ICRP. International commission on radioogical protection website, 2016. URL http://www.icrp.org/.

[15] Antoine Henri Becquerel. Sur les radiations invisibles émises par les corps phosphorescents. *CR Acad. Sci. Paris*, 122:501, 1896.

[16] MM Villard. Sur la réflexion et la réfraction des rayons cathodiques et des rayons déviables du radium. *CR Acad. Sci. Paris*, 130:1010, 1900.

[17] Ernest Rutherford. Xv. the magnetic and electric deviation of the easily absorbed rays from radium. *The London, Edinburgh, and Dublin Philosophical Magazine and Journal of Science*, 5(26):177–187, 1903.

[18] Kenneth S Krane. Introductory nuclear physics. 1987.

[19] Albert Einstein. Uber einen die erzeugung und verwandlung des lichtes betreffenden heurischen gesichtpunkt. *Ann. Phys.*, 17:132–148, 1905.

[20] Arthur H. Compton. A quantum theory of the scattering of x-rays by light elements. *Phys. Rev.*, 21:483–502, May 1923. doi: 10.1103/PhysRev.21.483. URL http://link.aps.org/doi/10.1103/PhysRev.21.483.

[21] Glenn F Knoll. *Radiation detection and measurement.* John Wiley & Sons, 2010.

[22] Patrick MS Blackett and Giuseppe PS Occhialini. Some photographs of the tracks of penetrating radiation. *Proceedings of the Royal Society of London. Series A, Containing Papers of a Mathematical and Physical Character*, 139(839):699–726, 1933.

[23] Robley Dunglison Evans and Atome Noyau. *The atomic nucleus*, volume 582. McGraw-Hill New York, 1955.

[24] James Chadwick. Possible existence of a neutron. *Nature*, 129(3252):312, 1932.

[25] Enrico Fermi. Possible production of elements of atomic number higher than 92. *Nature*, 133:898–899, 1934.

[26] Otto Hahn and Fritz Straßmann. Über den nachweis und das verhalten der bei der bestrahlung des urans mittels neutronen entstehenden erdalkalimetalle. *Naturwissenschaften*, 27(1):11–15, 1939.

[27] Lise Meitner and Otto Robert Frisch. Products of the fission of the uranium nucleus. *Nature*, 143(239):1939, 1939.

[28] Brian R Martin and Graham Shaw. *Particle physics.* John Wiley & Sons, 2013.

[29] R Bodu, H Bouzigues, N Morin, and JP Pfiffelmann. Sur l'existence d'anomalies isotopiques rencontrées dans l'uranium du gabon. *CR Acad. Sci. Paris*, 275(D):1731, 1972.

[30] Richard T. Kouzes, James H. Ely, Allen Seifert, Edward R. Siciliano, Dennis R. Weier, Lindsay K. Windsor, Mitchell L. Woodring, James Borgardt, Elise Buckley, Eric Flumerfelt, Anna Oliveri, and Matt Salvitti. Cosmic-ray-induced ship-effect neutron measurements and implications for cargo scanning at borders. *Nuclear Instruments and Methods in Physics Research Section A: Accelerators, Spectrometers, Detectors and Associated Equipment*, 587(1):89 – 100, 2008. ISSN 0168-9002. doi: http://dx.doi.org/10.1016/j.nima.2007.12.031. URL http://www.sciencedirect.com/science/article/pii/S0168900207025090.

[31] MS Gordon, P Goldhagen, KP Rodbell, TH Zabel, HHK Tang, JM Clem, and P Bailey. Measurement of the flux and energy spectrum of cosmic-ray induced neutrons on the ground. *Nuclear Science, IEEE Transactions on*, 51(6):3427–3434, 2004.

[32] C Vega, D Hernandez, M Rivera, A Sanchez, et al. Characterization of a 239 pube isotopic neutron source. 2012.

[33] A. Zimbal. Measurement of the spectral fluence rate of reference neutron sources with a liquid scintillation detector. *Radiation Protection Dosimetry*, 126(1-4):413–417, 2007. doi: 10.1093/rpd/ncm085. URL http://rpd.oxfordjournals.org/content/126/1-4/413.abstract.

[34] N Soppera, M Bossant, and E Dupont. Janis 4: An improved version of the nea java-based nuclear data information system. *Nuclear Data Sheets*, 120:294–296, 2014.

[35] TR England and BF Rider. Evaluation and compilation of fission product yields. *ENDF-349, LA-UR-94-3106, Los Alamos National Laboratory*, 1994.

[36] JP Lestone. Watt parameters for the los alamos model: Subroutine getab. *arXiv preprint arXiv:1410.1769*, 2014.

[37] Marco Cecconello, M Turnyanskiy, S Conroy, G Ericsson, Emanuel Ronchi, S Sangaroon, R Akers, I Fitzgerald, A Cullen, and Matthias Weiszflog. A neutron camera system for masta). *Review of Scientific Instruments*, 81(10):10D315, 2010.

[38] RK Fisher, RB Stephens, L Disdier, JL Bourgade, A Rouyer, PA Jaanimagi, TC Sangster, RA Lerche, and N Izumi. High-resolution neutron imaging of laser fusion targets using bubble detectors. *Physics of Plasmas (1994-present)*, 9(5):2182–2185, 2002.

[39] L Petrizzi, R Barnsley, L Bertalot, B Esposito, H Haskell, E Mainardi, D Marocco, S Podda, C Walker, and S Villari. Neutronic design of the iter radial neutron camera. *Fusion Engineering and Design*, 82(5):1308–1314, 2007.

[40] PW Lisowski, CD Bowman, GJ Russell, and SA Wender. The los alamos national laboratory spallation neutron sources. *Nuclear Science and Engineering*, 106(2): 208–218, 1990.

[41] Doug Reilly, Norbert Ensslin, Hastings Smith Jr, and Sarah Kreiner. Passive nondestructive assay of nuclear materials. Technical report, Nuclear Regulatory Commission, Washington, DC (United States). Office of Nuclear Regulatory Research; Los Alamos National Lab., NM (United States), 1991.

[42] Kenji Nishihara, Hiroki Iwamoto, and Kenya Suyama. Estimation of fuel compositions in fukushima-daiichi nuclear power plant. Technical report, Japan Atomic Energy Agency, 2012.

[43] J Kenneth Shultis and Richard E Faw. *Fundamentals of Nuclear Science and Engineering Second Edition*. CRC press, 2007.

[44] Gerhard Lutz et al. *Semiconductor radiation detectors*, volume 10. Springer, 1999.

[45] RA Nobles, RB Day, RL Henkel, GA Jarvis, RP Kutarnia, JL McKibben, JE Perry Jr, and RK Smith. Response of the long counter. *Review of Scientific Instruments*, 25(4): 334–335, 1954.

[46] DJ Thomas and AV Alevra. Bonner sphere spectrometers—a critical review. *Nuclear Instruments and Methods in Physics Research Section A: Accelerators, Spectrometers, Detectors and Associated Equipment*, 476(1):12–20, 2002.

[47] RB Murray. Use of li6i (eu) as a scintillation detector and spectrometer for fast neutrons. *Nuclear Instruments*, 2(3):237–248, 1958.

[48] CD Bass, EJ Beise, H Breuer, CR Heimbach, TJ Langford, and JS Nico. Characterization of a 6 li-loaded liquid organic scintillator for fast neutron spectrometry and thermal neutron detection. *Applied Radiation and Isotopes*, 77:130–138, 2013.

[49] JM Neill, D Huffman, CA Preskitt, and JC Young. Calibration and use of a 5-inch diameter lithium glass detector. *Nuclear Instruments and Methods*, 82:162–172, 1970.

[50] Garry B Spector, Tom McCollum, and Alexander R Spowart. Advances in lithium-loaded glass scintillator fiber development. *Nuclear Instruments and Methods in Physics Research Section A: Accelerators, Spectrometers, Detectors and Associated Equipment*, 313(3):373–376, 1992.

[51] M Mayer, J Nattress, V Kukharev, A Foster, A Meddeb, C Trivelpiece, Z Ounaies, and I Jovanovic. Development and characterization of a neutron detector based on a lithium glass–polymer composite. *Nuclear Instruments and Methods in Physics Research Section A: Accelerators, Spectrometers, Detectors and Associated Equipment*, 785: 117–122, 2015.

[52] K. Becker. *Some advances in solid-state fast neutron dosimetry*. Apr 1975. doi: 10.2172/4276799. URL http://www.osti.gov/scitech/servlets/purl/4276799.

[53] EF Bennett. Fast neutron spectroscopy by proton-recoil proportional counting. *Nuclear Science and Engineering*, 27(1):16–27, 1967.

[54] M Birk, G Goldring, and P Hillman. Fast neutron spectroscopy with solid state detectors. *Nuclear Instruments and Methods*, 21:197–201, 1963.

[55] LJ Perkins and Malcolm C Scott. The application of pulse shape discrimination in ne 213 to neutron spectrometry. *Nuclear Instruments and Methods*, 166(3):451–464, 1979.

[56] Jonathan Rose, Abbas El Gamal, and Alberto Sangiovanni-Vincentelli. Architecture of field-programmable gate arrays. *Proceedings of the IEEE*, 81(7):1013–1029, 1993.

[57] Sara A Pozzi, James A Mullens, and John T Mihalczo. Analysis of neutron and photon detection position for the calibration of plastic (bc-420) and liquid (bc-501) scintillators. *Nuclear Instruments and Methods in Physics Research Section A: Accelerators, Spectrometers, Detectors and Associated Equipment*, 524(1):92–101, 2004.

[58] Marvin L Roush, MA Wilson, and William F Hornyak. Pulse shape discrimination. *Nuclear Instruments and Methods*, 31(1):112–124, 1964.

[59] Alice Tomanin, Paolo Peerani, Hamid Tagziria, Greet Maenhout, Peter Schillebeeckx, Jan Paepen, Antony Lavietes, Romano Plenteda, Nick Mascarenhas, and L Marie Cronholm. Design of a liquid scintillator-based prototype neutron coincidence counter for nuclear safeguards. *ESARDA BULLETIN*, 49:28–36, 2013.

[60] M Moszynski, G Bizard, GJ Costa, D Durand, Y El Masri, G Guillaume, F Hanappe, B Heusch, A Huck, J Peter, et al. Study of n-γ discrimination by digital charge comparison method for a large volume liquid scintillator. *Nuclear Instruments and Methods in Physics Research Section A: Accelerators, Spectrometers, Detectors and Associated Equipment*, 317(1-2):262–272, 1992.

[61] B D'Mellow, MD Aspinall, RO Mackin, MJ Joyce, and AJ Peyton. Digital discrimination of neutrons and γ-rays in liquid scintillators using pulse gradient analysis. *Nuclear Instruments and Methods in Physics Research Section A: Accelerators, Spectrometers, Detectors and Associated Equipment*, 578(1):191–197, 2007.

[62] Ryan P Kelley, Andreas Enqvist, and Kelly A Jordan. Pulse shape discrimination in helium-4 scintillation detectors. *Nuclear Instruments and Methods in Physics Research Section A: Accelerators, Spectrometers, Detectors and Associated Equipment*, 830: 44–52, 2016.

[63] CC Sartain. Pinex: The pinhole neutron experiment. Technical report, Lawrence Livermore National Lab., CA (United States), 1958.

[64] Alex H. Lumpkin and Daniel S. Pappas. Neutron-imaging technique for monitoring high-temperature plasma dynamics. *Journal of Fusion Energy*, 8(1):69–74, 1989. ISSN 1572-9591. doi: 10.1007/BF01050779. URL http://dx.doi.org/10.1007/BF01050779.

[65] D Ress, RA Lerche, RJ Ellis, SM Lane, and KA Nugent. Neutron imaging of laser fusion targets. *Science*, 241(4868):956, 1988.

[66] D Ress, RA Lerche, RJ Ellis, SM Lane, and KA Nugent. Neutron imaging of inertial confinement fusion targets at nova. *Review of Scientific Instruments*, 59(8):1694–1696, 1988.

[67] Peter E Vanier, Leon Forman, Cynthia Salwen, and Istvan Dioszegi. Design of a large-area fast neutron directional detector. In *2006 IEEE Nuclear Science Symposium Conference Record*, volume 1, pages 93–97. IEEE, 2006.

[68] Peter E Vanier, Istvan Dioszegi, Cynthia Salwen, Vinita Ghosh, and Leon Forman. Stand-off detection of special nuclear materials using neutron imaging methods. In *2008 IEEE Nuclear Science Symposium Conference Record*, pages 681–685. IEEE, 2008.

[69] Peter E Vanier, Istvan Dioszegi, Cynthia Salwen, and Leon Forman. Directional stand-off detection of fast neutrons and gammas using angular scattering distributions. In *Nuclear Science Symposium Conference Record (NSS/MIC), 2009 IEEE*, pages 931–935. IEEE, 2009.

[70] John R Macri, Ulisse Bravar, Jason S Legere, Procheta Malik, Benoit Pirard, James M Ryan, and Richard S Woolf. The fast neutron imaging telescope (fnit)-hardware development and prototype testing. In *2007 IEEE Nuclear Science Symposium Conference Record*, volume 1, pages 173–178. IEEE, 2007.

[71] Ulisse Bravar, Richard S Woolf, Paul J Bruillard, Erwin O Fluckiger, Jason S Legere, Alec L MacKinnon, John R Macri, Procheta C Mallik, Mark L McConnell, Benoit Pirard, et al. Calibration of the fast neutron imaging telescope (fnit) prototype detector. *IEEE Transactions on Nuclear Science*, 56(5):2947–2954, 2009.

[72] B Pirard, RS Woolf, U Bravar, PJ Bruillard, EO Flückiger, JS Legere, AL MacKinnon, JR Macri, PCV Mallik, MR Moser, et al. Test and simulation of a fast neutron imaging telescope. *Nuclear Instruments and Methods in Physics Research Section A: Accelerators, Spectrometers, Detectors and Associated Equipment*, 603(3):406–414, 2009.

[73] Ulisse Bravar, Paul J Bruillard, EO Fluckiger, John R Macri, Alec L MacKinnon, Mark L McConnell, Michael R Moser, James M Ryan, and Richard S Woolf. Development of the fast neutron imaging telescope. In *IEEE Nuclear Science Symposium Conference Record, 2005*, volume 1, pages 107–111. IEEE, 2005.

[74] Peter Marleau, James Brennan, Kevin Krenz, Nicholas Mascarenhas, and Stanley Mrowka. Advances in imaging fission neutrons with a neutron scatter camera. In *2007 IEEE Nuclear Science Symposium Conference Record*, volume 1, pages 170–172. IEEE, 2007.

[75] Nicholas Mascarenhas, James Brennan, Kevin Krenz, Peter Marleau, and Stanley Mrowka. Results with the neutron scatter camera. *Nuclear Science, IEEE Transactions on*, 56(3):1269–1273, 2009.

[76] James Brennan, Robert Cooper, Mark Gerling, Peter Marleau, Nick Mascarenhas, and Stanley Mrowka. Applying the neutron scatter camera to treaty verification and warhead monitoring. In *IEEE Nuclear Science Symposuim & Medical Imaging Conference*, 2010.

[77] Nick Mascarenhas, Jim Brennan, Kevin Krenz, Jim Lund, Peter Marleau, Julia Rasmussen, Jim Ryan, and John Macri. Development of a neutron scatter camera for fission neutrons. In *2006 IEEE Nuclear Science Symposium Conference Record*, volume 1, pages 185–188. IEEE, 2006.

[78] Nicholas Mascarenhas, James Brennan, Charles H Greenberg, Peter Marleau, and Stan Mrowka. Field-portable fast-neutron imager for snm detection. In *2009 IEEE Nuclear Science Symposium Conference Record (NSS/MIC)*, pages 944–946. IEEE, 2009.

[79] James Brennan, Erik Brubaker, Robert Cooper, Mark Gerling, Charles Greenberg, Peter Marleau, Nicholas Mascarenhas, and Stanley Mrowka. Measurement of the fast neutron energy spectrum of an source using a neutron scatter camera. *IEEE Transactions on Nuclear Science*, 58(5):2426–2430, 2011.

[80] Nicholas C Mascarenhas, James S Brennan, and Charles H Greenberg. Neutron scatter camera for improved neutron detection, August 7 2012. US Patent 8,237,130.

[81] Nicholas Mascarenhas, Peter Marleau, James S Brennan, and Kevin D Krenz. Neutron scatter camera, June 22 2010. US Patent 7,741,613.

[82] K Ide, MF Becchetti, M Flaska, A Poitrasson-Riviere, MC Hamel, JK Polack, CC Lawrence, SD Clarke, and SA Pozzi. Analysis of a measured neutron background below 6mev for fast-neutron imaging systems. *Nuclear Instruments and Methods in Physics Research Section A: Accelerators, Spectrometers, Detectors and Associated Equipment*, 694:24–31, 2012.

[83] Alexis Poitrasson-Rivière, J Kyle Polack, Michael C Hamel, Dietrich D Klemm, Kai Ito, Alexander T McSpaden, Marek Flaska, Shaun D Clarke, Sara A Pozzi, Alice Tomanin, et al. Angular-resolution and material-characterization measurements for a dual-particle imaging system with mixed-oxide fuel. *Nuclear Instruments and Methods in Physics Research Section A: Accelerators, Spectrometers, Detectors and Associated Equipment*, 797:278–284, 2015.

[84] A Poitrasson-Rivière, M Flaska, MC Hamel, JK Polack, MF Becchetti, BM Wieger, A Enqvist, SD Clarke, and SA Pozzi. Digital data acquisition and processing for a neutron-gamma-ray imaging system. In *Nuclear Science Symposium and Medical Imaging Conference (NSS/MIC), 2012 IEEE*, pages 1597–1599. IEEE, 2012.

[85] J Kyle Polack, Alexis Poitrasson-Rivière, Michael C Hamel, Kiyotaka Ide, Kyle L McMillan, Shaun D Clarke, Marek Flaska, and Sara A Pozzi. Dual-particle imager for standoff detection of special nuclear material. In *Nuclear Science Symposium and Medical Imaging Conference (NSS/MIC), 2011 IEEE*, pages 1494–1500. IEEE, 2011.

[86] J Kyle Polack, Alexis Poitrasson-Rivière, Michael C Hamel, Marc F Becchetti, Kiyotaka Ide, Shaun D Clarke, Marek Flaska, and Sara A Pozzi. Image reconstruction using a three-plane, dual-particle imager for standoff detection of special nuclear material. In *Nuclear Science Symposium and Medical Imaging Conference (NSS/MIC), 2012 IEEE*, pages 118–121. IEEE, 2012.

[87] MC Hamel, JK Polack, A Poitrasson-Rivière, M Flaska, SD Clarke, SA Pozzi, A Tomanin, and P Peerani. Stochastic image reconstruction for a dual-particle imaging system. *Nuclear Instruments and Methods in Physics Research Section A: Accelerators, Spectrometers, Detectors and Associated Equipment*, 810:120–131, 2016.

[88] Michael C Hamel, J Kyle Polack, Alexis Poitrasson-Rivi, Dietrich D Klemm, Marek Flaska, Shaun D Clarke, Sara A Pozzi, Alice Tomanin, Paolo Peerani, et al. Time-of-flight neutron spectrum unfolding for mixed-oxide nuclear fuel and plutonium metal using a dual-particle imager. In *2014 IEEE Nuclear Science Symposium and Medical Imaging Conference (NSS/MIC)*, pages 1–5. IEEE, 2014.

[89] Alexis Poitrasson-Rivière, Michael C Hamel, J Kyle Polack, Marek Flaska, Shaun D Clarke, and Sara A Pozzi. Dual-particle imaging system based on simultaneous detection of photon and neutron collision events. *Nuclear Instruments and Methods in Physics Research Section A: Accelerators, Spectrometers, Detectors and Associated Equipment*, 760:40–45, 2014.

[90] Amanda C Madden, Peter F Bloser, Dominique Fourguette, Liane Larocque, Jason S Legere, Matt Lewis, Mark L McConnell, Marissa Rousseau, and James M Ryan. An imaging neutron/gamma-ray spectrometer. In *SPIE Defense, Security, and Sensing*, pages 87101L–87101L. International Society for Optics and Photonics, 2013.

[91] James M Ryan, Christopher Bancroft, Peter Bloser, Dominique Fourguette, Liane Larocque, Jason Legere, Amanda Madden, Mark L McConnell, Jane Pavlich, Greg Ritter, et al. An imaging neutron/gamma-ray spectrometer. In *SPIE Optical Engineering+ Applications*, pages 850905–850905. International Society for Optics and Photonics, 2012.

[92] Paul Hausladen, Matthew A Blackston, E Brubaker, David Chichester, P Marleau, and Robert Jason Newby. Fast neutron coded-aperture imaging of special nuclear material configurations. Technical report, Oak Ridge National Laboratory (ORNL), 2012.

[93] Matthew A Blackston, Braden L Brown, E Brubaker, Paul Hausladen, P Marleau, and Robert Jason Newby. Fast-neutron coded-aperture imaging for warhead counting. Technical report, Oak Ridge National Laboratory (ORNL), 2011.

[94] Chad M Whitney, Lakshmi Soundara-Pandian, Erik B Johnson, Sam Vogel, Bob Vinci, Michael Squillante, Jarek Glodo, and James F Christian. Gamma–neutron imaging system utilizing pulse shape discrimination with clyc. *Nuclear Instruments and Methods in Physics Research Section A: Accelerators, Spectrometers, Detectors and Associated Equipment*, 784:346–351, 2015.

[95] L Soundara-Pandian, C Whitney, J Christian, J Glodo, A Gueorgiev, R Hawrami, MR Squillante, and KS Shah. Clyc in gamma-neutron imaging system. In *Nuclear Science Symposium and Medical Imaging Conference (NSS/MIC), 2012 IEEE*, pages 101–105. IEEE, 2012.

[96] J Brennan, E Brubaker, M Gerling, P Marleau, K McMillan, A Nowack, N Renard-Le Galloudec, and M Sweany. Demonstration of two-dimensional time-encoded imaging of fast neutrons. *Nuclear Instruments and Methods in Physics Research Section A: Accelerators, Spectrometers, Detectors and Associated Equipment*, 802: 76–81, 2015.

[97] KAA Gamage, MJ Joyce, and JC Adams. Combined digital imaging of mixed-field radioactivity with a single detector. *Nuclear Instruments and Methods in Physics Research Section A: Accelerators, Spectrometers, Detectors and Associated Equipment*, 635(1):74–77, 2011.

[98] KAA Gamage, MJ Joyce, and GC Taylor. A digital approach to neutron–γ imaging with a narrow tungsten collimator aperture and a fast organic liquid scintillator detector. *Applied Radiation and Isotopes*, 70(7):1223–1227, 2012.

[99] K.A.A. Gamage, M.J. Joyce, and G.C. Taylor. Investigation of three-dimensional localisation of radioactive sources using a fast organic liquid scintillator detector. *Nuclear Instruments and Methods in Physics Research Section A: Accelerators, Spectrometers, Detectors and Associated Equipment*, 707:123 – 126, 2013. ISSN 0168-9002. doi: http://dx.doi.org/10.1016/j.nima.2012.12.119. URL http://www.sciencedirect.com/science/article/pii/S0168900212017007.

[100] KAA Gamage and GC Taylor. Neutron gamma fraction imaging: Detection, location and identification of neutron sources. *Nuclear Instruments and Methods in Physics Research Section A: Accelerators, Spectrometers, Detectors and Associated Equipment*, 788:9–12, 2015.

[101] AO Gasparyan, VM Kukarev, EP Markaryan, GG Mkrtchyan, and RN Pikhtelev. Amplitude-time analysis for recoil nuclei in projection chamber. *Nuclear Instruments and Methods*, 133(3):485–488, 1976.

[102] NS Bowden, M Heffner, G Carosi, D Carter, P OMalley, J Mintz, M Foxe, and I Jovanovic. Directional fast neutron detection using a time projection chamber. *Nuclear Instruments and Methods in Physics Research Section A: Accelerators, Spectrometers, Detectors and Associated Equipment*, 624(1):153–161, 2010.

[103] Seunghee Son, Georgia A De Nolfo, MP Dion, Stanley D Hunter, and Noel A Guardala. Neutron imaging camera. In *Nuclear Science Symposium Conference Record (NSS/MIC), 2010 IEEE*, pages 298–301. IEEE, 2010.

[104] F. Pino, L. Stevanato, D Cester, G. Nebbia, L. Sajo-Bohus, and G. Viesti. The light output and the detection efficiency of the liquid scintillator ej-309. *Applied Radiation and Isotopes*, 89:79 – 84, 2014. ISSN 0969-8043. doi: http://dx.doi.org/10.1016/j.apradiso.2014.02.016. URL http://www.sciencedirect.com/science/article/pii/S0969804314000682.

[105] D.E. GonzÃ¡lez Trotter, F. Salinas Meneses, W. Tornow, A.S. Crowell, C.R. Howell, D. Schmidt, and R.L. Walter. Neutron detection efficiency determinations for the tunl neutron-neutron and neutron-proton scattering-length measurements. *Nucl. Instr. Meth. Phys. Res. A.*, 599(2-3):234 – 242, 2009. ISSN 0168-9002. doi: http://dx.doi.org/10.1016/j.nima.2008.10.036. URL http://www.sciencedirect.com/science/article/pii/S0168900208015878.

[106] L. Stevanato, D. Cester, G. Nebbia, and G. Viesti. Neutron detection in a high gamma-ray background with ej-301 and ej-309 liquid scintillators. *Nucl. Instr. Meth. Phys. Res. A.*, 690(0):96 – 101, 2012. ISSN 0168-9002. doi: http://dx.doi.org/10.1016/j.nima.2012.06.047. URL http://www.sciencedirect.com/science/article/pii/S0168900212007139.

[107] Eljen Technology. Material safety data sheet ej-301 liquid scintillator, . URL http://www.eljentechnology.com/images/stories/Data_Sheets/MSDS/301MSD.pdf.

[108] Eljen Technology. Material safety data sheet ej-309 liquid scintillator, . URL http://www.eljentechnology.com/images/stories/Data_Sheets/MSDS/309MSD.pdf.

[109] Malcolm Joyce. Personal communication 2014-11-14.

[110] *Assembly diagram for radiation detector 19 A 15/0,75-E1-LS-X-Neg VS-0653-2*. Scionix Holland BV, May 2009.

[111] *Assembly diagram for radiation detector V94 A 94/3 M - EJ309 - E1 - X - Neg VS-1105-21*. Scionix Holland BV, February 2012.

[112] Michael Aspinall and Malcolm Joyce. Apparatus and method for radiation analysis, August 5 2014. US Patent 8,796,632.

[113] M.J. Joyce, M.D. Aspinall, F.D. Cave, and A. Lavietes. A 16-channel real-time digital processor for pulse-shape discrimination in multiplicity assay. *IEEE Trans. Nuc. Sci*, 61(4):2222–2227, 2014. ISSN 0018-9499. doi: 10.1109/TNS.2014.2322574.

[114] K. A. A. Gamage, M. J. Joyce, and N. P. Hawkes. A comparison of four different digital algorithms for pulse-shape discrimination in fast scintillators. *Nucl. Instr. Meth. Phys. Res. A.*, 642(1):78–83, 2011. ISSN 0168-9002. doi: {10.1016/j.nima.2011.03.065}.

[115] Matthew P Mellor, B Alan Shippen, and Malcolm J Joyce. Efficient single-detector gamma imaging for civil nuclear inspection. In *Nuclear Science Symposium and Medical Imaging Conference (NSS/MIC), 2012 IEEE*, pages 433–438. IEEE, 2012.

[116] R. Gordon. A tutorial on art (algebraic reconstruction techniques). *IEEE Trans. Nuc. Sci*, 21(3):78–93, 1974. ISSN 0018-9499. doi: 10.1109/TNS.1974.6499238.

[117] MCNP. A general monte carlo n-particle (mcnp) transport code url: https://mcnp.lanl.gov/. 2015.

[118] Luka Snoj, Gašper Žerovnik, and Andrej Trkov. Computational analysis of irradiation facilities at the jsi triga reactor. *Applied Radiation and Isotopes*, 70(3):483–488, 2012.

[119] H. Böck and M. Villa. Practical course on reactor physicsand reactor kinetics. *NTEC course material AIAU 27309*, 2008.

[120] Jonathan S. Beaumont, Matthew P. Mellor, Mario Villa, and Malcolm J. Joyce. High-intensity power-resolved radiation imaging of an operational nuclear reactor. *Nat Commun*, 6:–, October 2015. URL http://dx.doi.org/10.1038/ncomms9592.

[121] V. V. Verbinski, Hans Weber, and R. E. Sund. Prompt gamma rays from $^{235}\mathrm{U}(n,f)$, $^{239}\mathrm{Pu}(n,f)$, and spontaneous fission of $^{252}\mathrm{Cf}$. *Phys. Rev. C*, 7:1173–1185, Mar 1973. doi: 10.1103/PhysRevC.7.1173. URL http://link.aps.org/doi/10.1103/PhysRevC.7.1173.

[122] Jonathan Beaumont, Matthew P. Mellor, and Malcolm J. Joyce. The analysis of complex mixed-radiation fields using near real-time imaging. *Radiat. Prot. Dosimetr.*, 161(1-4):331–334, 2014. doi: 10.1093/rpd/ncu044. URL http://rpd.oxfordjournals.org/content/161/1-4/331.abstract.

[123] Jonathan S. Beaumont, B. Alan Shippen, Matthew P. Mellor, and Malcolm J. Joyce. Imaging of fast neutrons and gamma rays from 252cf in a heavily shielded environment. *Nuclear Instruments and Methods in Physics Research Section A: Accelerators, Spectrometers, Detectors and Associated Equipment*, pages –, 2016. ISSN 0168-9002. doi: http://dx.doi.org/10.1016/j.nima.2016.11.043. URL http://www.sciencedirect.com/science/article/pii/S0168900216311962.

[124] International Atomic Energy Agency. *IAEA safety glossary: terminology used in nuclear safety and radiation protection; including the IAEA Safety fundamentals*. Internat. Atomic Energy Agency, 2008.

[125] David J Thomas. The system of radiation protection for neutrons: does it fit the purpose? *Radiation protection dosimetry*, 161(1-4):3–10, 2014.

[126] George E Laramore, JM Krall, FJ Thomas, Kenneth J Russell, MH Maor, FR Hendrickson, KL Martz, TW Griffin, and LW Davis. Fast neutron radiotherapy for locally advanced prostate cancer: Final report of a radiation therapy oncology group randomized clinical trial. *American journal of clinical oncology*, 16(2):164–167, 1993.

[127] B Jones, TSA Underwood, A Carabe-Fernandez, C Timlin, and RG Dale. Fast neutron relative biological effects and implications for charged particle therapy. *The British journal of radiology*, 2014.

[128] Jao-Perng Lin, Wei-Chung Liu, and Chun-Chih Lin. Investigation of photoneutron dose equivalent from high-energy photons in radiotherapy. *Applied radiation and isotopes*, 65(5):599–604, 2007.

Appendix A

Supplementary information

A.1 Videos

The following supplementary videos are provided at the following link:
https://drive.google.com/drive/folders/0B604mDPudVfsQ2RYc3JZSFoxTnc?usp=sharing

Supplementary Video 1: Sensitivity matrix transformation. This video depicts the changing sensitivity maps (fast-neutron and gamma-ray) through 2-dimensional angular space due to the rotation of the collimator. The image shows a cut down version of a full 4π spatial interrogation, the pan and slot positions are indicated. Parts of this sequence were used in experiments 2-5 during data acquisition. This media is available supplementary to a peer-reviewed publication [120].

Supplementary Video 2: Energy dependent sensitivity matrices for the C2 collimator. A sequence of sensitivity matrices dependent on incoming radiation where the interrogation flux was uniformly distributed in 0.5 MeV energy bands between 1 and 10 MeV.

Supplementary Video 3: TRIGA linear power increase. A sequence of neutron and gamma-ray images depicting a linear power increase of the Vienna TRIGA reactor. These images are produced from interpolation of the 3 images produced in experiment 5 and demonstrate the appearance of multiple experimental images. This media is available supplementary to a peer-reviewed publication [120].

Supplementary Video 4: Real-time radiation source tracking. This video shows the tracked positions of a ^{137}Cs source in motion in synchronisation with an optical recording.

These results were produced in experiment 7.

A.2 Code

A.2.1 Monte Carlo models

Imager with C2 collimator

```
Imager with C2 collimator. Created by J. Beaumont
c
c ############## Define cells #########################
c
10 1 -0.874 -101 202 -203        imp:n 1 $detectorc
c
21 2 -18.1 102 -103 201 -203     imp:n 1 $coll part 1
22 2 -18.1 -103 203 -204
#(-103 203 -204 301 -302)  imp:n 1 $coll part 2 - void
c
30 0 -103 203 -210 301 -302      imp:n 1 $slot void
c
41 3 -7.9 -104 103 206 -205      imp:n 1 $steel sleeve
c
42 5 -2.7 207 -201 -103 102      imp:n 1 $aluminium sleeve
c
c extra shield
52 4 -1.1 205 -208 103 -104
#(203 103 -104 303 304)    $not V
#(203 103 -104 -303 -304)  $not V2
imp:n 1 $inner
53 4 -1.1 104 -105 -208 207
#(203 104 -105 303 304)   $not V
#(203 104 -105 -303 -304) $not V2
imp:n 1 $outer
c
c
98 0 999                         imp:n 0 $outside world
```

```
99 0 -999
#(-101 202 -203) #(-103 102 201 -204)
#(-102 203 -204) #(-104 103 206 -205)
#52 #53   #30 #42   imp:n 1 $inside world

c ############## Define surfaces #####################
c
c x-cylinders
101 cx 0.95          $scint cylinder
102 cx 1.7           $pmt void
103 cx 3.4           $outside of coll
104 cx 4.5           $steel exterior
105 cx 7.25          $outside shield
c
c x-planes
201 px -0.2         $rear of coll
202 px 2.1          $rear of detector
203 px 3.9          $detector/coll interface
204 px 6.4          $front of coll
205 px 3.1          $front of steel
206 px -8           $back of steel
207 px -7           $back of PE
208 px 7.4          $front of PE
210 px 7
c
c y-planes
301 py -0.3          $slot void
302 py 0.3           $slot void
c
c other planes
303 p 0 -3.4 0.8 0   $V void
304 p 0 3.4 0.8 0    $V void
c
c
999 so 200           $define world 2m sphere
c
```

```
c ########## Define materials #############################
c scintillator rho=0.874 gpcc
m1 6000.60c 1 1001.60c 1.212
c
c tungsten alloy rho=18.1 gpcc
m2 74000.55c -0.97 28000.50c -0.021 26000.50c -0.009
c
c iron rho=18.1 gpcc
m3 26000.55m 1   $iron .55m
m4 6000.60c 1 1001.60c 2 $polyethylene
c aluminium alloy 6082 density 2.70
m5 13027.50m 1
c
c ########## Define source ###############################
c 1.5 to 2 MeV plane source
SDEF POS=63.90193 70.97028 38.58448
AXS=-63.90193 -70.97028 -38.58448  EXT=0 RAD=d2
ERG=d1 VEC= -63.90193 -70.97028 -38.58448  DIR=1
SI2 0 7 $sampling radius
SP2 -21 1 1 $weighting r^1
SI1 h 0 1.5 2
SP1 d 0 0 1
```

Imager with anti-collimator

```
Imager with anti-collimator. Created by J. Beaumont
c
c ########## Define cells ############################
c
44 9  -0.874 -301 302 -303 imp:p 1   $detector
c
55 7 -18.1 201 -202 101 501 -401 #44  imp:p 1  $inverse col
c
98     0          999  imp:p 0 $outside world
99     0         -999 #44 #55 imp:p 1 $inside world
```

```
c ########### Define surfaces #######################
c
101        px 0  $ plane x = 0
c
c thickness of fan
201 py -0.9
202 py 0.9
c
c outer radius of fan
401 cy 10 $outer radius
c
c inner radius of fan
501 cy 5
c
c detector cylinder
301 cx 0.9  $ inner radius of shield
302 px -0.9 $back of detector
303 px 0.9  $detector front and back
c
999        so 200  $define world 2m sphere

c ########## Define source #########################
c
SDEF POS=100 0 0
AXS=-100 0 0  EXT=0 RAD=d2
ERG=d1 VEC= -100 0 0  DIR=1
c default watt fission spectrum
sP1 -3
SI2 0 10 $sampling radius
SP2 -21 1 1 $weighting r^1
c
c
c ########## Define materials ######################
c
m1 1001.60C 2 8016.60C 1 $light water rho = 1
c
```

```
c tungsten alloy rho = 18.1
m7 74000.55C -0.95 28000.50C -0.025 26000.50C -0.025
c
m9 6000.60C 1 1001.60C 1.212 $scintillator rho = 0.874
```

^{252}Cf tank and laboratory environment

```
252Cf tank and laboratory environment. Created by J. Beaumont
c
c ########## Define Cells ########################
c
c tank structure
1 1 -1 -201 #3 #6 imp:n 1 $water box
2 2 -7.847 302 -301 #3 imp:n 1 $steel
3 3 -2.25 102 -101 -999 imp:n 1 $floor
c
c walls
4 3 -2 401 -402 101 -103 imp:n 1 $ext walls
5 3 -2 -401 412 -411 #(422 -421) -103 imp:n 1 $int w
c
c steel cradle
6 2 -7.847 -399 -201 imp:n 1
c
c world
98 0 -999  #1 #2 #3 #4 #5 #6 imp:n 1
99 0 999 imp:n 0

c ########## Define Surfaces ####################
c
c z-planes
101 pz 0
102 pz -15
103 pz 200
c
c water box
201  rpp 27.5 120.5 -120.5 -27.5 1 91
c
```

```
c steel shield
301 rpp 0 148 -148 0 0 132 $out
302 rpp 3.3 144.7 -144.7 -3.3 0.1 128.7 $in
c
c steel cradle surrounding source
399 s 74 -74 35 1.5
c
c walls
401 rpp -437 333 -338 81 0 250  $inner
402 rpp -452 348 -353 96 0 251   $outer
411 px -178
412 px -190
421 py 41
422 py -51
c
c define world
999 so 1000        $world sphere

c ########## Define Source ######################
c
c 252Cf point source
sdef pos= 74 -74 35 erg=d1
sp1 -3 1.18 1.03419
c
c ########## Define Materials ###################
c light water rho = 1 gpcc
m1 1001.60c 2 8016.60C 1
c
c iron rho = 7.847 gpcc
m2 26000.50c 1
c
c concrete rho = 2.00-2.25 gpcc
m3 1001.60c 8.47636E-02 8016.60c 6.040868-01 11023.60c 9.47250E-03
12000.60c 2.99826E-03 13027.60c 2.48344E-02
14000.60c 2.41860E-01 19000.60c 6.85513E-03
20000.60c 2.04808E-02 26054.60c 2.74322E-04
```

```
26056.60c 4.26455E-03 26057.60c 9.76401E-05
26058.60c 1.30187E-05
```

TRIGA mk 2 test reactor Vienna Atominstitut

```
TRIGA mk 2 test reactor Vienna Atominstitut. Created by J. Beaumont
c
c ########## Define Cells ######################
c
1 1 -2.69 -10 12 -11 imp:n 1 $fuel active volume
c
c graphite moderator around core
2 2 -2.15 -21 22 -23 #1 imp:n 1
c
c graphite column 1 - small
3 2 -2.15 21 22 -23 -31 32 -33 34 #1    imp:n 1
c
c lead shield
4 4 -11.34 22 -23 31 32 -33 -51  #1  imp:n 1
c
c water pool
5 3 -1 41 -42 -43 #1 #2 #3 #4 #6 imp:n 1
c
c tunnel void part 1
6 0 22 -23 32 -33 51 -43 #1  imp:n 1
c
c tunnel void part 2
7 0 22 -23 32 -33 43 -71 51 #1 imp:n 1
c
c concrete wall
8 5 -2.25 41 -42 43 -71 #7 imp:n 1
c
c world
98 0 -999  #1 #2 #3 #4 #5 #6 #7 #8 imp:n 1
99 0 999 imp:n 0

c ########## Define Surfaces ####################
```

```
c
10 cz 24
c core active volume
13 cz 24
11 pz 19.05
12 pz -19.05
c
c graphite cylinder around core
21 cz 54.5
22 pz -28.45
23 pz 25.65
c
c graphite column 1 - small
31 px 79.0
32 py -38.1
33 py 38.1
34 px 24.01
c confined in z as above
c
c water in tank
41 pz -100
42 pz 100
43 cz 107 $inner concrete wall boundary
c
c lead shield
51 px 84.08 $outside face
c
c concrete shielding
71 cz 214 $outside edge concrete
c
c define world
999 so 1000        $world sphere

c ############ Define Source ########################
c
c homogenous core cell source at origin
```

```
sdef pos=0 0 0  cel=1 rad=d2 erg=d1
c default watt fission spectrum
sp1 -3
si2 0 50
sp2 -21 2
c
c ############ Define Materials #####################
c
c homogenous core approximation //assumed density 2.69
c UZrH fuel at 20% enrichment
m1 92235.50c 1.242 92238.50c 4.97 40090.66c 37.38
40091.66c 8.13 40092.66c 12.48 40094.66c 12.63
8016.50c 16.07 6000.50c 16.07 1001.50c 2.78
c
c graphite shielding around core //assumed density 2.15
m2 6000.50c 1
m3 1001.50c 2 8016.50C 1 $light water //density 1.0
c
c lead //density 11.34
m4 82000.50c 1
c concrete // assumed density 2.25
m5 1001.50c 8.47636E-02 8016.50c 6.040868-01 11023.50c 9.47250E-03
12000.50c 2.99826E-03 13027.50c 2.48344E-02
14000.50c 2.41860E-01 19000.50c 6.85513E-03
20000.50c 2.04808E-02 26054.60c 2.74322E-04
26056.60c 4.26455E-03 26057.60c 9.76401E-05
26058.60c 1.30187E-05
```

A.2.2 Control code

Custom pulse counter microcontroller control code

```
//READ 12 CHANNEL COUNTER BOARD
//Created by J. Beaumont

//VARIABLES
//TIMER
```

```
const unsigned long readPeriod = 1000;  //ms
//NOTE THAT THE READ TIME OF THIS ROUTINE IS 24 ms
const int readDelay = 5;  //5ms usual

char address = 0x22;
//  1  2    3  4    5  6    7  8    9  10    11  12
//  0x22    0x23    0x24    0x25     0x26     0x27

//IO EXPANDER
#include "Wire.h"
byte input1w=0;
byte input1x=0;
byte input1y=0;
byte input1z=0;
byte input2w=0;
byte input2x=0;
byte input2y=0;
byte input2z=0;

//channel index
int channel = 0;

//SET PINS
//AL - BU
const int BU = 12;
const int BL = 11;
const int AU = 10;
const int AL = 9;
//CCLR
const int CCLR = 8;
//RCLK
const int RCLK = 13;


//COUNT SERIAL
int serialcount = 0;
```

```
void setup() {

//initialise I2C
Wire.begin();

//initialize ouputs
pinMode(AL, OUTPUT);
pinMode(AU, OUTPUT);
pinMode(BL, OUTPUT);
pinMode(BU, OUTPUT);

pinMode(CCLR, OUTPUT);
pinMode(RCLK, OUTPUT);

//serial comms
Serial.begin(9600);
//Serial.println("Serial test");
}

void loop(){
readcounters();//read counters
}


//readcounters
void readcounters(){
//CCLR
digitalWrite(CCLR, HIGH); //CCLR HIGH to count
//counting time
delay(readPeriod);
//counts number
//Serial.print("Reading number: ");
//Serial.println(serialcount);
serialcount = serialcount +1;
//activate RCLK to update counter
```

```
digitalWrite(RCLK, HIGH);
digitalWrite(RCLK, LOW);

for (int COUNTERNUMBER = 34; COUNTERNUMBER <40; COUNTERNUMBER++){

channel = (COUNTERNUMBER -34)*2+1;
address = COUNTERNUMBER;
////////////////////////READ1
//read A lower on counter 1, B upper counter 2
digitalWrite(AL, LOW);  //GAL   A lower
digitalWrite(AU, HIGH); //GAU    A upper      low to read
digitalWrite(BL, HIGH); //GBL     B lower     otherwise high
digitalWrite(BU, HIGH); //GBU     B upper
delay(readDelay);//wait 5ms
//Read bytes
Wire.beginTransmission(address);
Wire.write(0x13); //send pointer to GPIO A   (0x12:A   0x13:B)
Wire.endTransmission();
Wire.requestFrom(address,1);//request one byte
input1w=Wire.read();
Wire.beginTransmission(address);
Wire.write(0x12); //send pointer to GPIO B   (0x12:A   0x13:B)
Wire.endTransmission();
Wire.requestFrom(address,1);//request one byte
input2z=Wire.read();
///////////////////////READ1
////////////////////////READ2
//read A UPPER on counter 1, B LOWER counter 2
digitalWrite(AL, HIGH);  //GAL   A lower
digitalWrite(AU, LOW); //GAU    A upper       low to read
digitalWrite(BL, HIGH); //GBL     B lower     otherwise high
digitalWrite(BU, HIGH); //GBU     B upper
delay(readDelay);//wait 5ms
//Read bytes
Wire.beginTransmission(address);
Wire.write(0x13); //send pointer to GPIO A   (0x12:A   0x13:B)
```

```
Wire.endTransmission();
Wire.requestFrom(address,1);//request one byte
input1x=Wire.read();
Wire.beginTransmission(address);
Wire.write(0x12); //send pointer to GPIO B   (0x12:A   0x13:B)
Wire.endTransmission();
Wire.requestFrom(address,1);//request one byte
input2y=Wire.read();
///////////////////////READ2
////////////////////////READ3
//read B lower on counter 1, A upper counter 2
digitalWrite(AL,HIGH);  //GAL   A lower
digitalWrite(AU, HIGH); //GAU    A upper     low to read
digitalWrite(BL, LOW); //GBL     B lower     otherwise high
digitalWrite(BU, HIGH); //GBU     B upper
delay(readDelay);//wait 5ms
//Read bytes
Wire.beginTransmission(address);
Wire.write(0x13); //send pointer to GPIO A   (0x12:A   0x13:B)
Wire.endTransmission();
Wire.requestFrom(address,1);//request one byte
input1y=Wire.read();
Wire.beginTransmission(address);
Wire.write(0x12); //send pointer to GPIO B   (0x12:A   0x13:B)
Wire.endTransmission();
Wire.requestFrom(address,1);//request one byte
input2x=Wire.read();
///////////////////////READ3
////////////////////////READ4
//read A lower on counter 1, B upper counter 2
digitalWrite(AL, HIGH);  //GAL   A lower
digitalWrite(AU, HIGH); //GAU    A upper      low to read
digitalWrite(BL, HIGH); //GBL     B lower     otherwise high
digitalWrite(BU, LOW); //GBU     B upper
delay(readDelay);//wait 5ms
//Read bytes
```

```
Wire.beginTransmission(address);
Wire.write(0x13); //send pointer to GPIO A   (0x12:A   0x13:B)
Wire.endTransmission();
Wire.requestFrom(address,1);//request one byte
input1z=Wire.read();
Wire.beginTransmission(address);
Wire.write(0x12); //send pointer to GPIO B   (0x12:A   0x13:B)
Wire.endTransmission();
Wire.requestFrom(address,1);//request one byte
input2w=Wire.read();
//////////////////////READ4

//print data to serial
Serial.print(input1z);
Serial.print(' ');
Serial.print(input1y);
Serial.print(' ');
Serial.print(input1x);
Serial.print(' ');
Serial.print(input1w);
Serial.print(' ');
Serial.println(channel);

channel = channel + 1;
Serial.print(input2w);
Serial.print(' ');
Serial.print(input2x);
Serial.print(' ');
Serial.print(input2y);
Serial.print(' ');
Serial.print(input2z);
Serial.print(' ');
Serial.println(channel);
}

//CCLR
```

```
digitalWrite(CCLR, LOW); //CCLR LOW TO RESET
}// end of readcounters
```

A.2.3 Analysis code

ART algorithm

```
function sources = ART(systemMatrix, im, pos_list, sources, iterations, lambda)
% iterative ART algorithm to find most likely distribution of source term
% "sources". Written by Createc Ltd. Edited by Jonathan Beaumont.

[ncol,npan] = size(im);
ncol,
npan,

pos_length = length(pos_list);

%calculate the systemMatrix magnitudes
mags = zeros(ncol,npan);
for n=1:ncol,
for m=1:npan,
mags(n,m) = sum(systemMatrix{n,m}(:).^2);
end;
end;

%calculate source term
for it = 1:iterations,
for p=1:length(pos_list),

n = pos_list(p,1);
m = pos_list(p,2);

sources = sources + lambda*(im(n,m)-sum(sum(systemMatrix{n,m}.*sources)))
.*systemMatrix{n,m}./mags(n,m);
sources = max(sources,0);
end;
```

```
%show iterations
it,
end;
```

A.3 PCB design

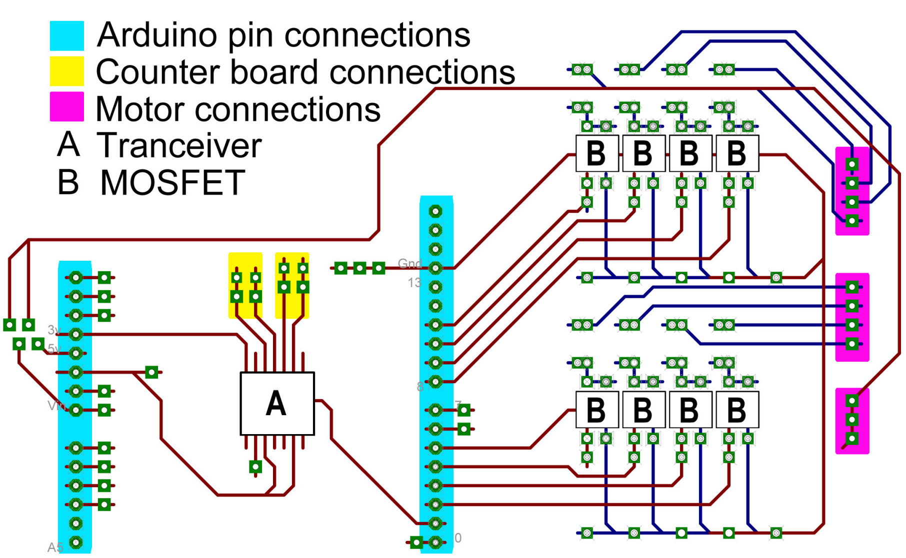

Figure A.1 Custom motor control board interfaced with an Arduino Microcontroller.

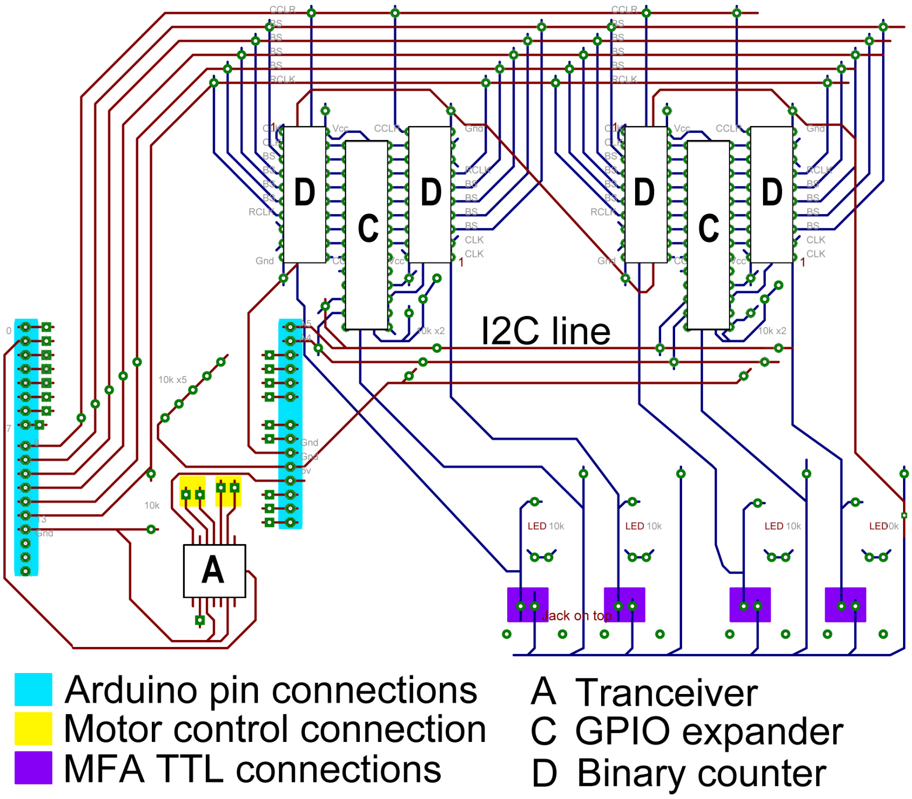

Figure A.2 Custom four channel pulse counter board interfaced with an Arduino microcontroller.

Appendix B

Associated external documentation

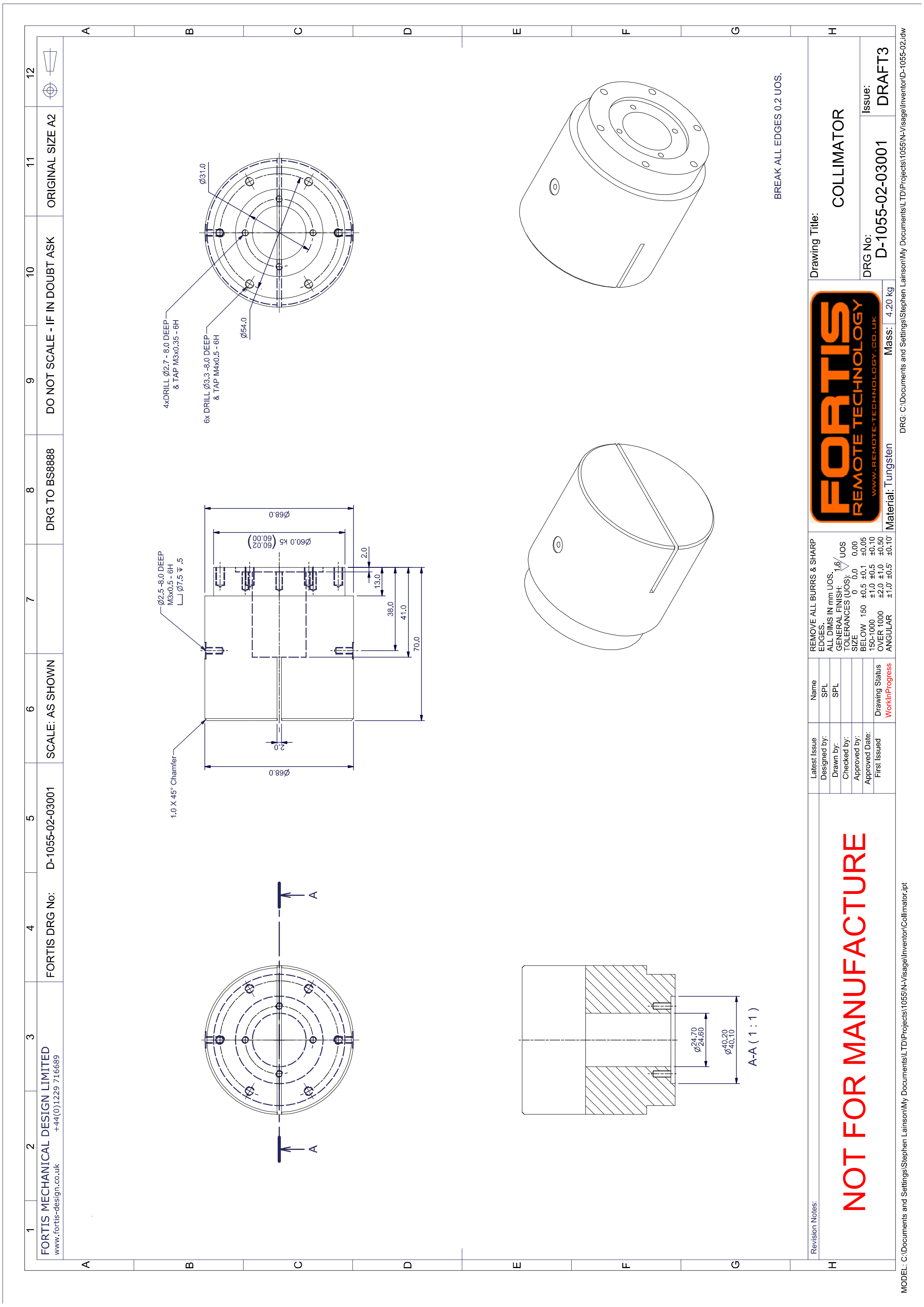

Figure B.1 C0 tungsten collimator design drawings

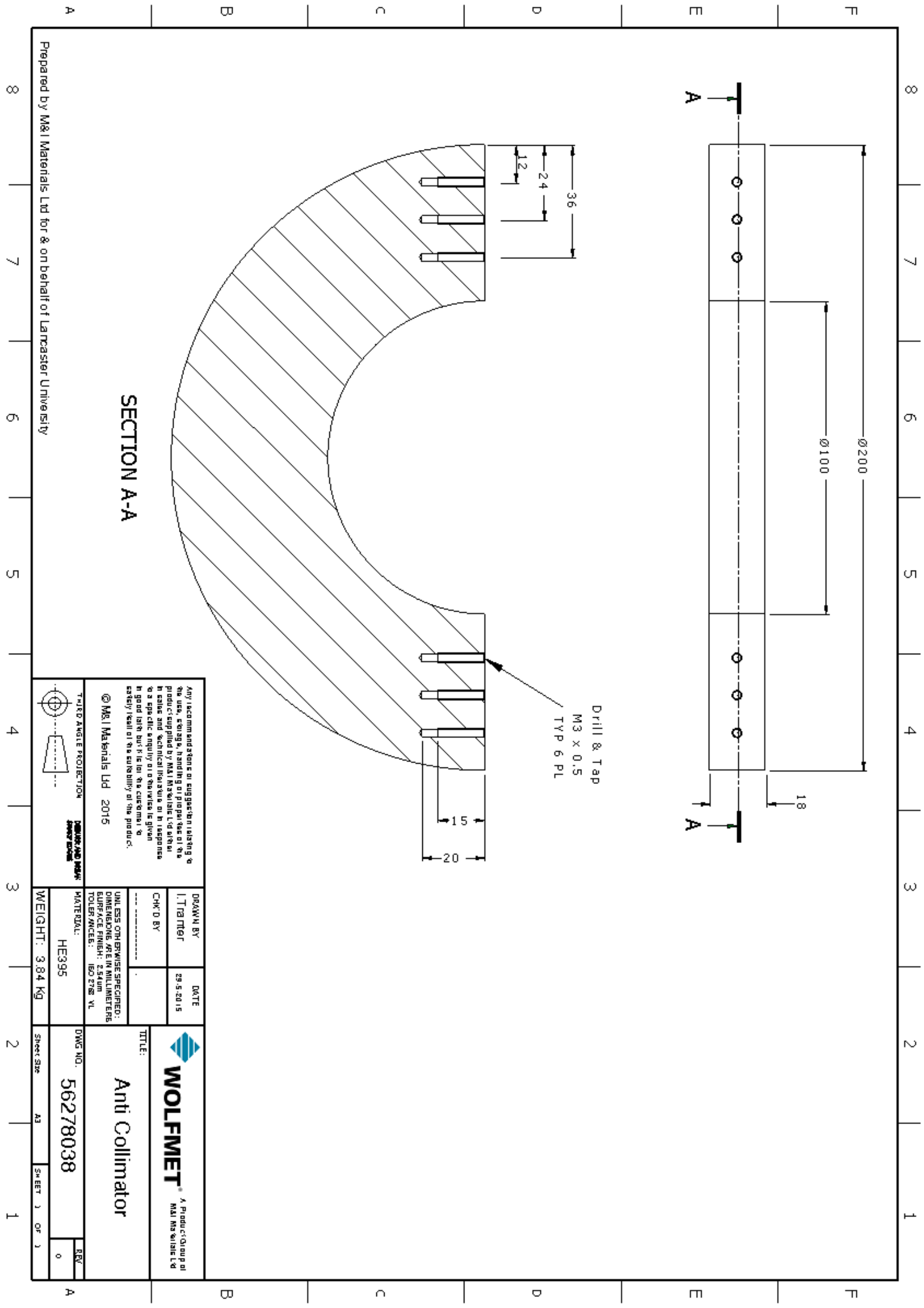

Figure B.2 Anti-collimator design drawings

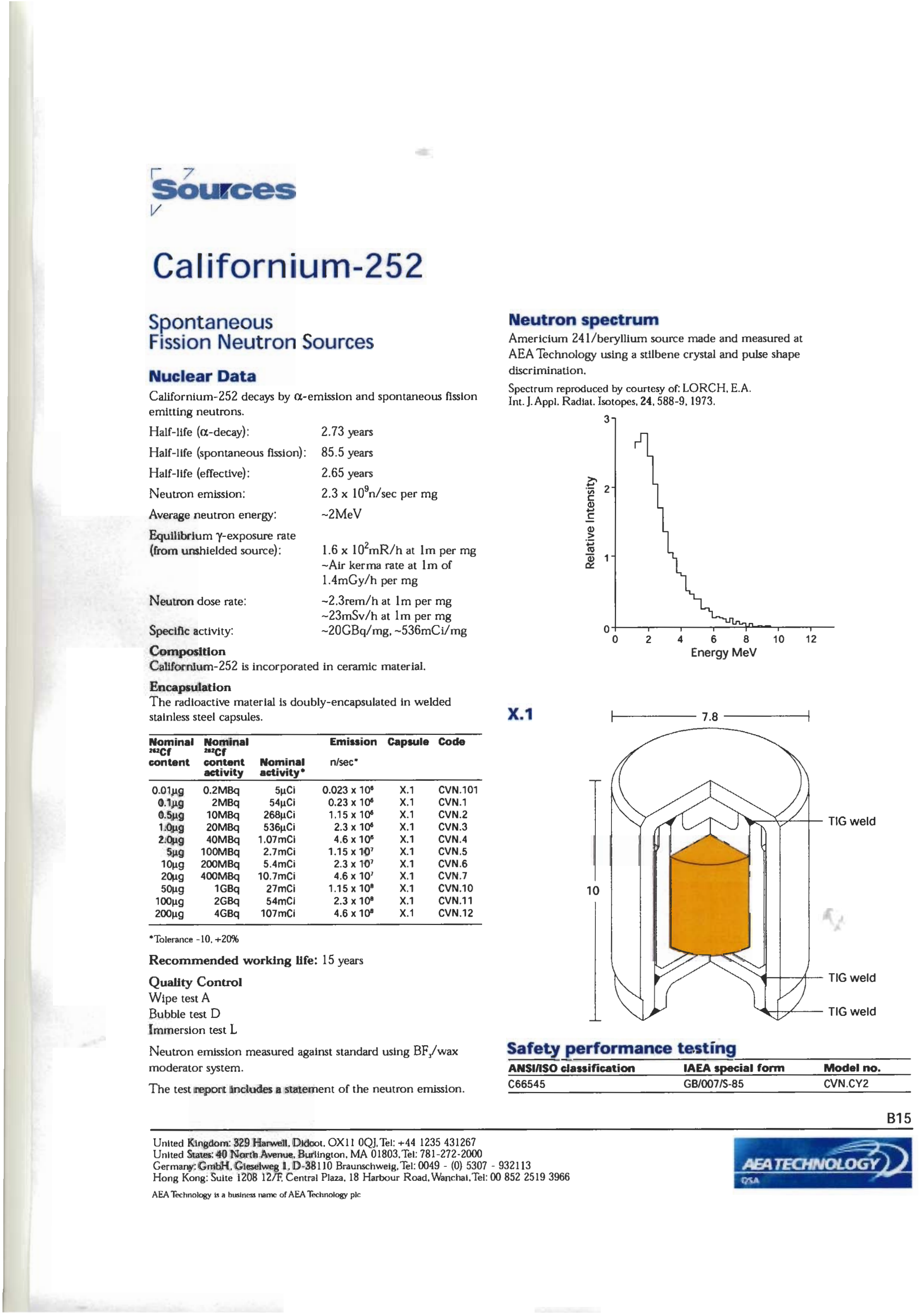

Sources

Californium-252

Spontaneous Fission Neutron Sources

Nuclear Data

Californium-252 decays by α-emission and spontaneous fission emitting neutrons.

Half-life (α-decay):	2.73 years
Half-life (spontaneous fission):	85.5 years
Half-life (effective):	2.65 years
Neutron emission:	2.3 x 10^9n/sec per mg
Average neutron energy:	~2MeV
Equilibrium γ-exposure rate (from unshielded source):	1.6 x 10^2mR/h at 1m per mg ~Air kerma rate at 1m of 1.4mGy/h per mg
Neutron dose rate:	~2.3rem/h at 1m per mg ~23mSv/h at 1m per mg
Specific activity:	~20GBq/mg, ~536mCi/mg

Composition
Californium-252 is incorporated in ceramic material.

Encapsulation
The radioactive material is doubly-encapsulated in welded stainless steel capsules.

Nominal ^{252}Cf content	Nominal ^{252}Cf content activity	Nominal activity*	Emission n/sec*	Capsule	Code
0.01μg	0.2MBq	5μCi	0.023 x 10^6	X.1	CVN.101
0.1μg	2MBq	54μCi	0.23 x 10^6	X.1	CVN.1
0.5μg	10MBq	268μCi	1.15 x 10^6	X.1	CVN.2
1.0μg	20MBq	536μCi	2.3 x 10^6	X.1	CVN.3
2.0μg	40MBq	1.07mCi	4.6 x 10^6	X.1	CVN.4
5μg	100MBq	2.7mCi	1.15 x 10^7	X.1	CVN.5
10μg	200MBq	5.4mCi	2.3 x 10^7	X.1	CVN.6
20μg	400MBq	10.7mCi	4.6 x 10^7	X.1	CVN.7
50μg	1GBq	27mCi	1.15 x 10^8	X.1	CVN.10
100μg	2GBq	54mCi	2.3 x 10^8	X.1	CVN.11
200μg	4GBq	107mCi	4.6 x 10^8	X.1	CVN.12

*Tolerance -10, +20%

Recommended working life: 15 years

Quality Control
Wipe test A
Bubble test D
Immersion test L

Neutron emission measured against standard using BF_3/wax moderator system.

The test report includes a statement of the neutron emission.

Neutron spectrum

Americium 241/beryllium source made and measured at AEA Technology using a stilbene crystal and pulse shape discrimination.

Spectrum reproduced by courtesy of: LORCH, E.A.
Int. J. Appl. Radiat. Isotopes, **24**, 588-9, 1973.

X.1

Safety performance testing

ANSI/ISO classification	IAEA special form	Model no.
C66545	GB/007/S-85	CVN.CY2

B15

United Kingdom: 329 Harwell, Didcot, OX11 0QJ, Tel: +44 1235 431267
United States: 40 North Avenue, Burlington, MA 01803, Tel: 781-272-2000
Germany: GmbH, Gieselweg 1, D-38110 Braunschweig, Tel: 0049 - (0) 5307 - 932113
Hong Kong: Suite 1208 12/F, Central Plaza, 18 Harbour Road, Wanchai, Tel: 00 852 2519 3966

AEA Technology is a business name of AEA Technology plc

Figure B.3 ^{252}Cf source information

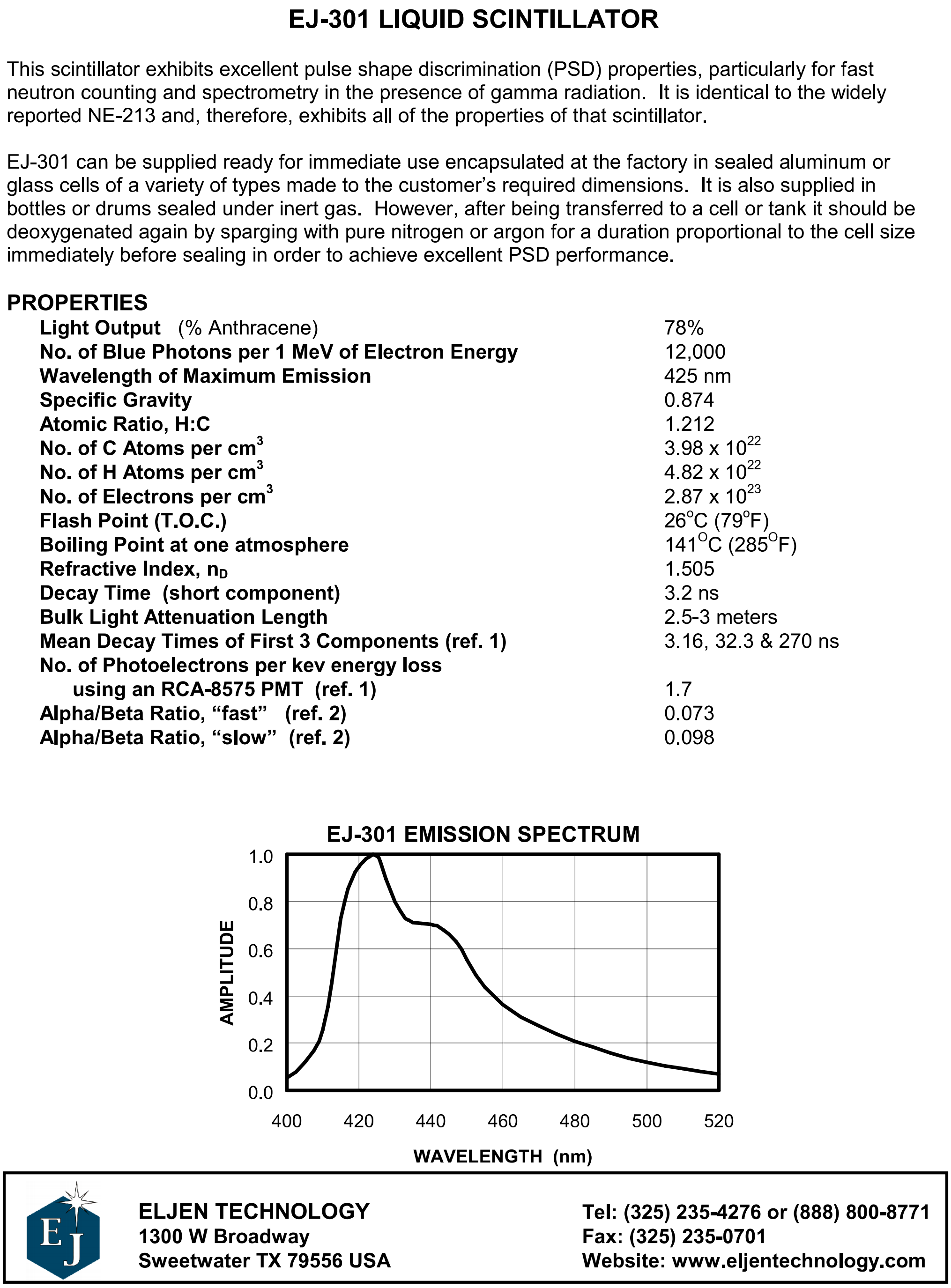

EJ-301 LIQUID SCINTILLATOR

This scintillator exhibits excellent pulse shape discrimination (PSD) properties, particularly for fast neutron counting and spectrometry in the presence of gamma radiation. It is identical to the widely reported NE-213 and, therefore, exhibits all of the properties of that scintillator.

EJ-301 can be supplied ready for immediate use encapsulated at the factory in sealed aluminum or glass cells of a variety of types made to the customer's required dimensions. It is also supplied in bottles or drums sealed under inert gas. However, after being transferred to a cell or tank it should be deoxygenated again by sparging with pure nitrogen or argon for a duration proportional to the cell size immediately before sealing in order to achieve excellent PSD performance.

PROPERTIES

Light Output (% Anthracene)	78%
No. of Blue Photons per 1 MeV of Electron Energy	12,000
Wavelength of Maximum Emission	425 nm
Specific Gravity	0.874
Atomic Ratio, H:C	1.212
No. of C Atoms per cm^3	3.98×10^{22}
No. of H Atoms per cm^3	4.82×10^{22}
No. of Electrons per cm^3	2.87×10^{23}
Flash Point (T.O.C.)	26°C (79°F)
Boiling Point at one atmosphere	141°C (285°F)
Refractive Index, n_D	1.505
Decay Time (short component)	3.2 ns
Bulk Light Attenuation Length	2.5-3 meters
Mean Decay Times of First 3 Components (ref. 1)	3.16, 32.3 & 270 ns
No. of Photoelectrons per kev energy loss using an RCA-8575 PMT (ref. 1)	1.7
Alpha/Beta Ratio, "fast" (ref. 2)	0.073
Alpha/Beta Ratio, "slow" (ref. 2)	0.098

EJ-301 EMISSION SPECTRUM

ELJEN TECHNOLOGY
1300 W Broadway
Sweetwater TX 79556 USA

Tel: (325) 235-4276 or (888) 800-8771
Fax: (325) 235-0701
Website: www.eljentechnology.com

Figure B.4 EJ-301 data sheet I

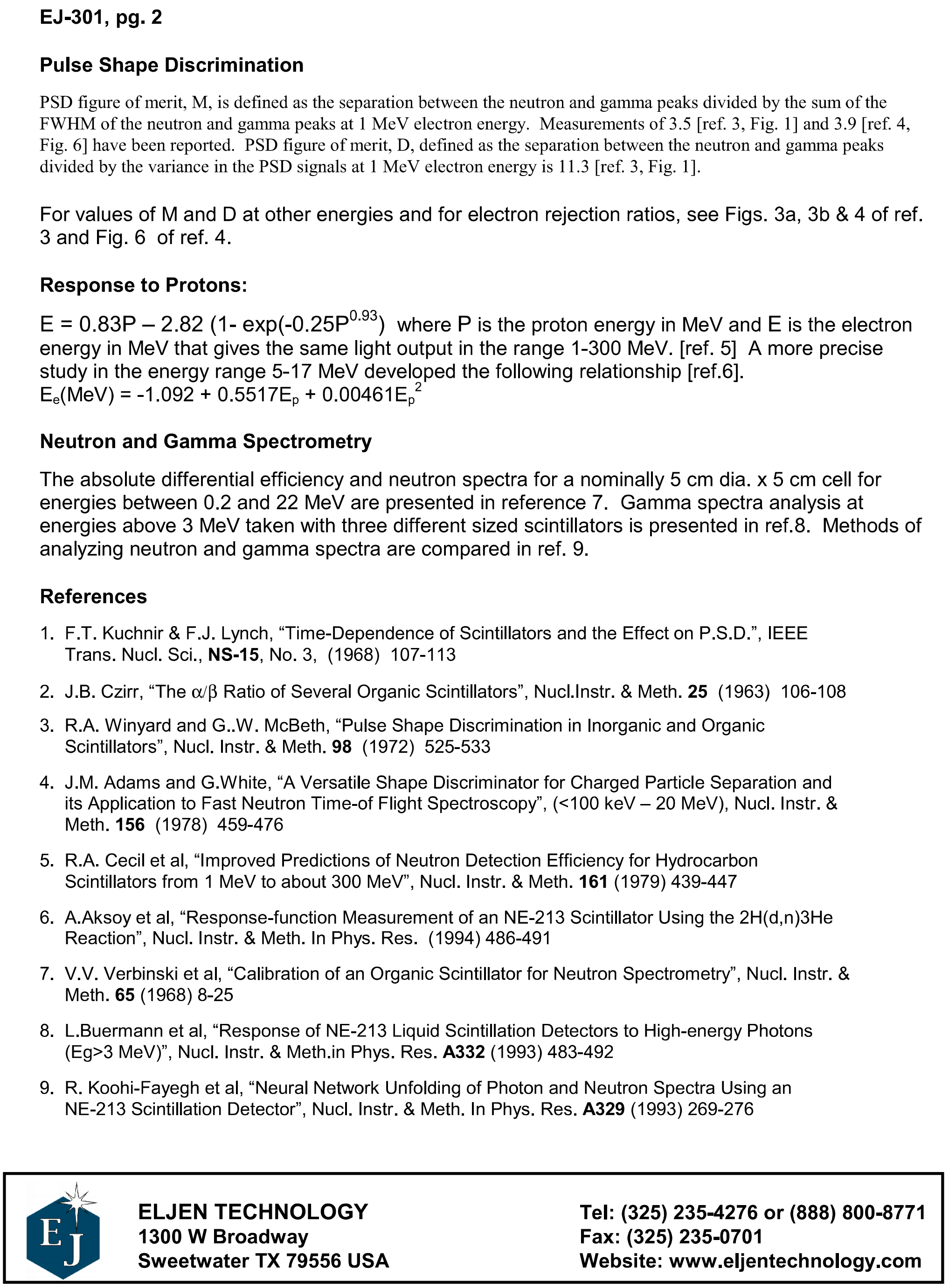

EJ-301, pg. 2

Pulse Shape Discrimination

PSD figure of merit, M, is defined as the separation between the neutron and gamma peaks divided by the sum of the FWHM of the neutron and gamma peaks at 1 MeV electron energy. Measurements of 3.5 [ref. 3, Fig. 1] and 3.9 [ref. 4, Fig. 6] have been reported. PSD figure of merit, D, defined as the separation between the neutron and gamma peaks divided by the variance in the PSD signals at 1 MeV electron energy is 11.3 [ref. 3, Fig. 1].

For values of M and D at other energies and for electron rejection ratios, see Figs. 3a, 3b & 4 of ref. 3 and Fig. 6 of ref. 4.

Response to Protons:

$E = 0.83P - 2.82 (1- \exp(-0.25P^{0.93})$ where P is the proton energy in MeV and E is the electron energy in MeV that gives the same light output in the range 1-300 MeV. [ref. 5] A more precise study in the energy range 5-17 MeV developed the following relationship [ref.6].
$E_e(\mathrm{MeV}) = -1.092 + 0.5517E_p + 0.00461E_p^2$

Neutron and Gamma Spectrometry

The absolute differential efficiency and neutron spectra for a nominally 5 cm dia. x 5 cm cell for energies between 0.2 and 22 MeV are presented in reference 7. Gamma spectra analysis at energies above 3 MeV taken with three different sized scintillators is presented in ref.8. Methods of analyzing neutron and gamma spectra are compared in ref. 9.

References

1. F.T. Kuchnir & F.J. Lynch, “Time-Dependence of Scintillators and the Effect on P.S.D.”, IEEE Trans. Nucl. Sci., **NS-15**, No. 3, (1968) 107-113
2. J.B. Czirr, “The α/β Ratio of Several Organic Scintillators”, Nucl.Instr. & Meth. **25** (1963) 106-108
3. R.A. Winyard and G..W. McBeth, “Pulse Shape Discrimination in Inorganic and Organic Scintillators”, Nucl. Instr. & Meth. **98** (1972) 525-533
4. J.M. Adams and G.White, “A Versatile Shape Discriminator for Charged Particle Separation and its Application to Fast Neutron Time-of Flight Spectroscopy”, (<100 keV – 20 MeV), Nucl. Instr. & Meth. **156** (1978) 459-476
5. R.A. Cecil et al, “Improved Predictions of Neutron Detection Efficiency for Hydrocarbon Scintillators from 1 MeV to about 300 MeV”, Nucl. Instr. & Meth. **161** (1979) 439-447
6. A.Aksoy et al, “Response-function Measurement of an NE-213 Scintillator Using the 2H(d,n)3He Reaction”, Nucl. Instr. & Meth. In Phys. Res. (1994) 486-491
7. V.V. Verbinski et al, “Calibration of an Organic Scintillator for Neutron Spectrometry”, Nucl. Instr. & Meth. **65** (1968) 8-25
8. L.Buermann et al, “Response of NE-213 Liquid Scintillation Detectors to High-energy Photons (Eg>3 MeV)”, Nucl. Instr. & Meth.in Phys. Res. **A332** (1993) 483-492
9. R. Koohi-Fayegh et al, “Neural Network Unfolding of Photon and Neutron Spectra Using an NE-213 Scintillation Detector”, Nucl. Instr. & Meth. In Phys. Res. **A329** (1993) 269-276

ELJEN TECHNOLOGY
1300 W Broadway
Sweetwater TX 79556 USA

Tel: (325) 235-4276 or (888) 800-8771
Fax: (325) 235-0701
Website: www.eljentechnology.com

Figure B.5 EJ-301 data sheet II

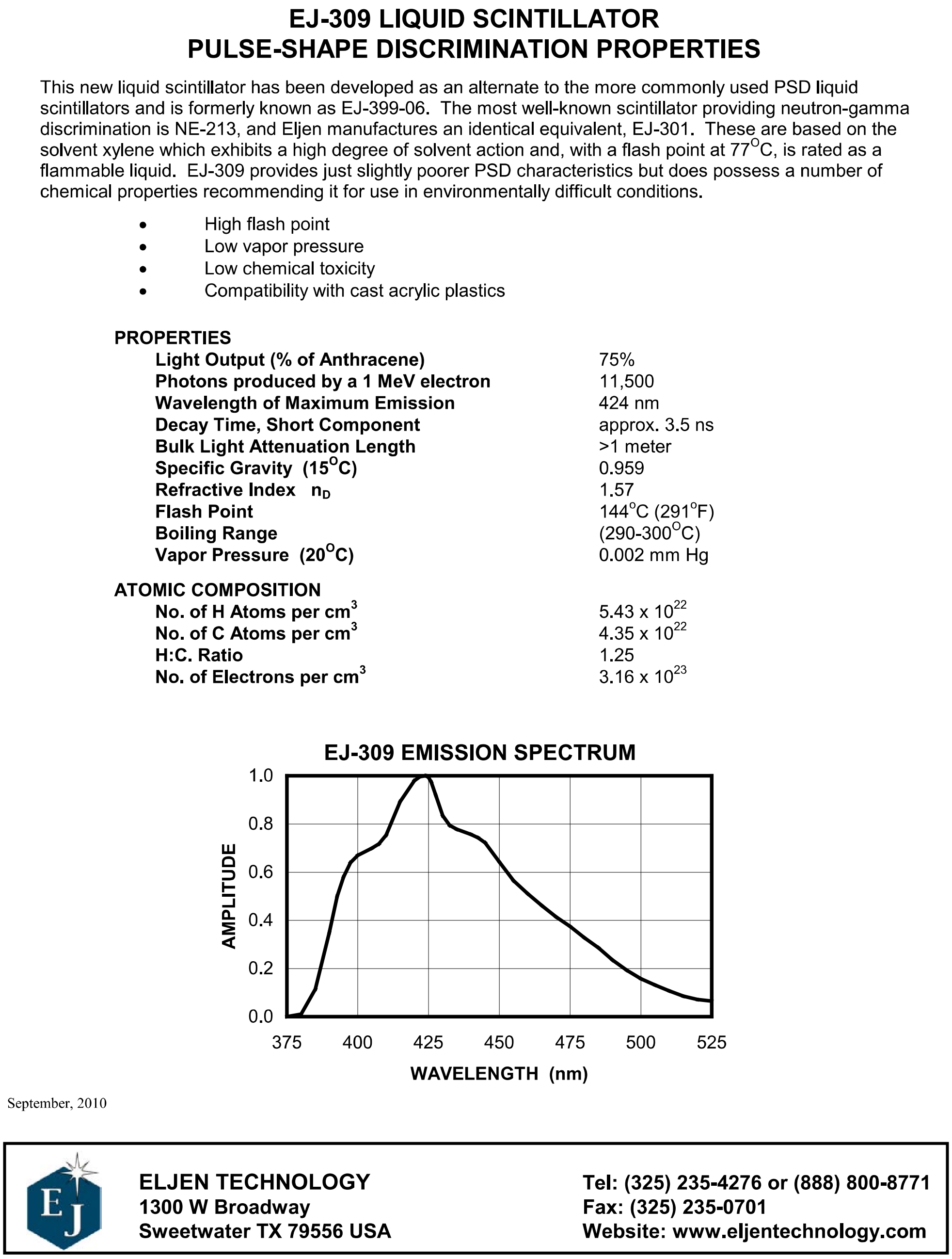

EJ-309 LIQUID SCINTILLATOR PULSE-SHAPE DISCRIMINATION PROPERTIES

This new liquid scintillator has been developed as an alternate to the more commonly used PSD liquid scintillators and is formerly known as EJ-399-06. The most well-known scintillator providing neutron-gamma discrimination is NE-213, and Eljen manufactures an identical equivalent, EJ-301. These are based on the solvent xylene which exhibits a high degree of solvent action and, with a flash point at 77^{O}C, is rated as a flammable liquid. EJ-309 provides just slightly poorer PSD characteristics but does possess a number of chemical properties recommending it for use in environmentally difficult conditions.

- High flash point
- Low vapor pressure
- Low chemical toxicity
- Compatibility with cast acrylic plastics

PROPERTIES

Light Output (% of Anthracene)	75%
Photons produced by a 1 MeV electron	11,500
Wavelength of Maximum Emission	424 nm
Decay Time, Short Component	approx. 3.5 ns
Bulk Light Attenuation Length	>1 meter
Specific Gravity (15^{O}C)	0.959
Refractive Index n_D	1.57
Flash Point	144°C (291°F)
Boiling Range	(290-300^{O}C)
Vapor Pressure (20^{O}C)	0.002 mm Hg

ATOMIC COMPOSITION

No. of H Atoms per cm^3	5.43×10^{22}
No. of C Atoms per cm^3	4.35×10^{22}
H:C. Ratio	1.25
No. of Electrons per cm^3	3.16×10^{23}

EJ-309 EMISSION SPECTRUM

September, 2010

ELJEN TECHNOLOGY
1300 W Broadway
Sweetwater TX 79556 USA

Tel: (325) 235-4276 or (888) 800-8771
Fax: (325) 235-0701
Website: www.eljentechnology.com

Figure B.6 EJ-309 data sheet

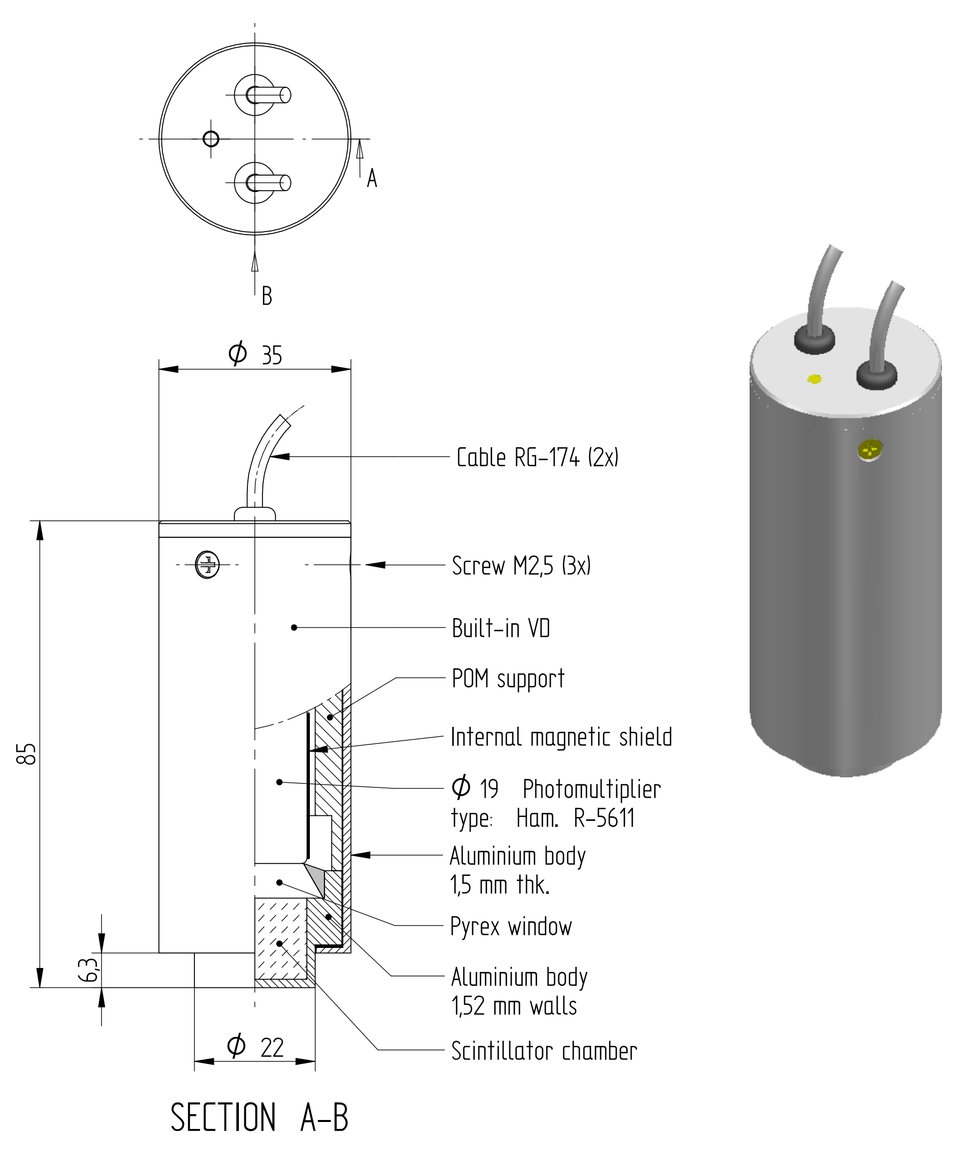

SCIONIX

SCIONIX HOLLAND BV
Radiation Detectors & Crystals

P.O. Box 143
3980 CC Bunnik
The Netherlands
Tel. 31 (0)30 657 0312
Fax. 31 (0)30 656 7563

schaal 1 : 1
datum 14-05-2009
get. C.V.
akk.
type: 19 A 15/0,75 – E1 – LS – X – Neg

wijzigingen

datum	lett.	opm.

onderdeel: ASSEMBLY
tek.nr: VS-0653-2
A4

Figure B.7 Assembly data for miniature EJ-301 detector [110]

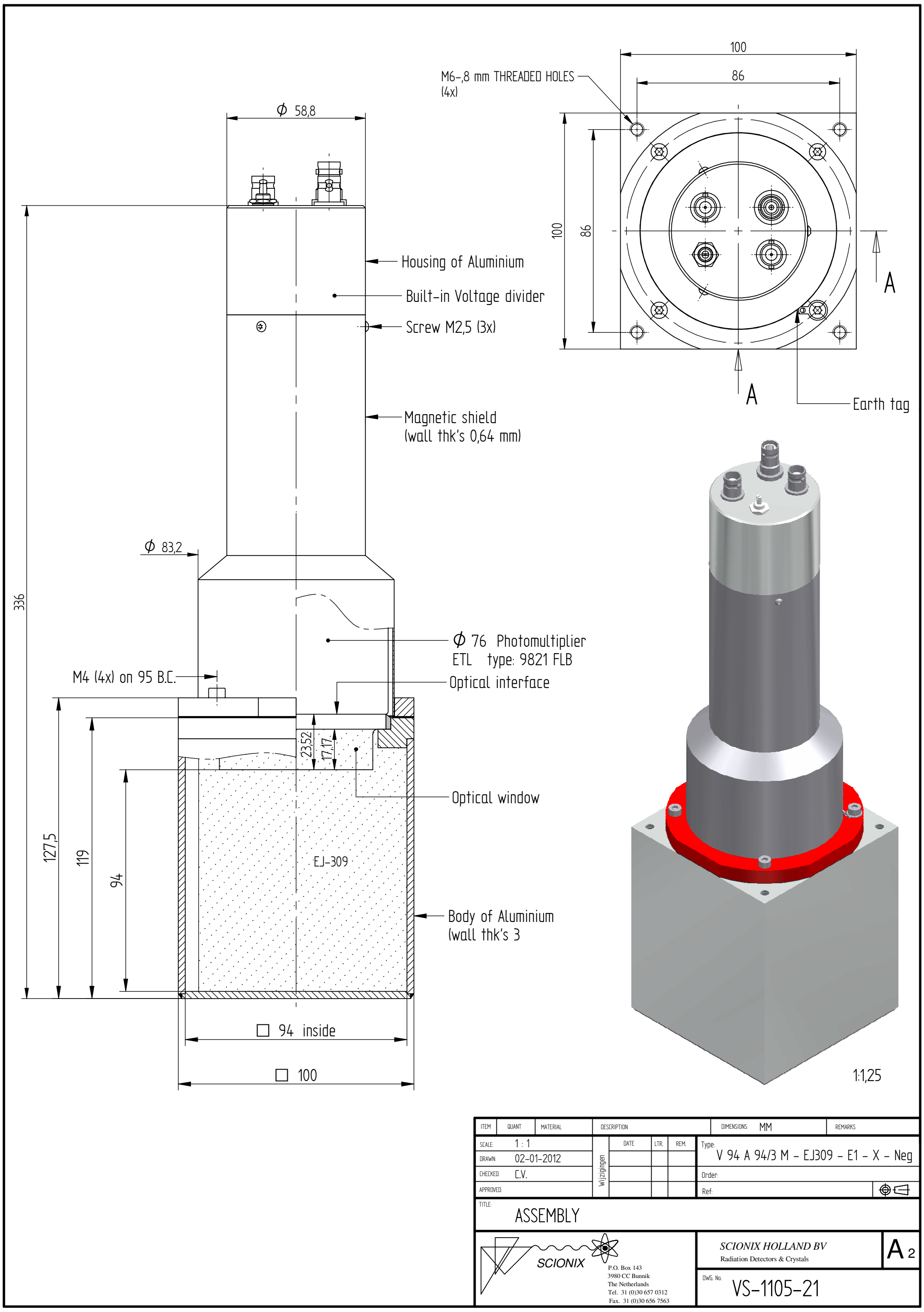

Figure B.8 Assembly data for 10 cm cubic EJ-309 detector data sheet [111]

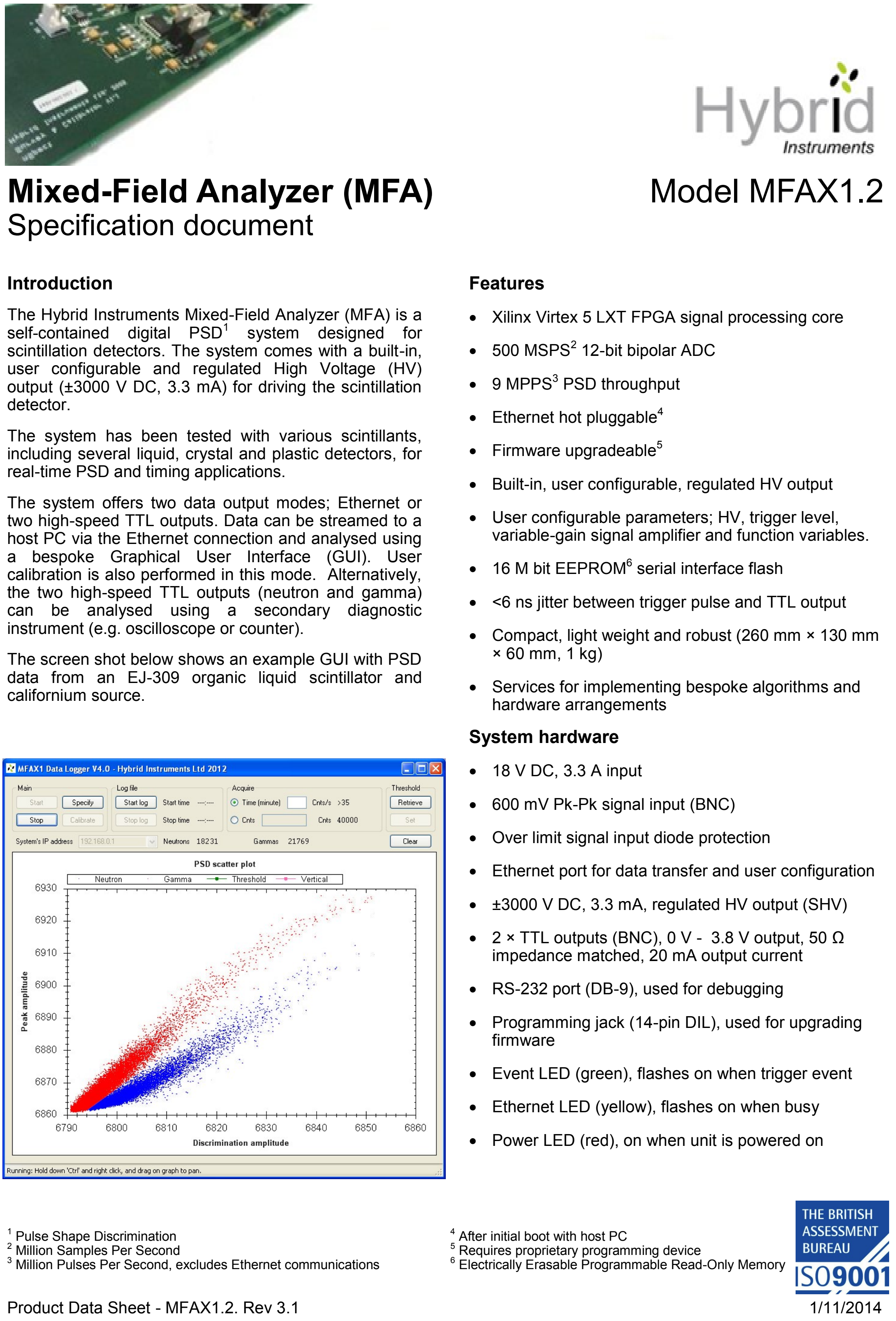

Hybrid Instruments

Mixed-Field Analyzer (MFA)

Specification document

Model MFAX1.2

Introduction

The Hybrid Instruments Mixed-Field Analyzer (MFA) is a self-contained digital PSD[1] system designed for scintillation detectors. The system comes with a built-in, user configurable and regulated High Voltage (HV) output (±3000 V DC, 3.3 mA) for driving the scintillation detector.

The system has been tested with various scintillants, including several liquid, crystal and plastic detectors, for real-time PSD and timing applications.

The system offers two data output modes; Ethernet or two high-speed TTL outputs. Data can be streamed to a host PC via the Ethernet connection and analysed using a bespoke Graphical User Interface (GUI). User calibration is also performed in this mode. Alternatively, the two high-speed TTL outputs (neutron and gamma) can be analysed using a secondary diagnostic instrument (e.g. oscilloscope or counter).

The screen shot below shows an example GUI with PSD data from an EJ-309 organic liquid scintillator and californium source.

MFAX1 Data Logger V4.0 - Hybrid Instruments Ltd 2012

Start time ----:----

Stop time ----:----

● Time (minute)

○ Cnts

Cnts/s >35

Cnts 40000

System's IP address 192.168.0.1

Neutrons 18231

Gammas 21769

Running: Hold down 'Ctrl' and right click, and drag on graph to pan.

Features

- Xilinx Virtex 5 LXT FPGA signal processing core
- 500 MSPS[2] 12-bit bipolar ADC
- 9 MPPS[3] PSD throughput
- Ethernet hot pluggable[4]
- Firmware upgradeable[5]
- Built-in, user configurable, regulated HV output
- User configurable parameters; HV, trigger level, variable-gain signal amplifier and function variables.
- 16 M bit EEPROM[6] serial interface flash
- <6 ns jitter between trigger pulse and TTL output
- Compact, light weight and robust (260 mm × 130 mm × 60 mm, 1 kg)
- Services for implementing bespoke algorithms and hardware arrangements

System hardware

- 18 V DC, 3.3 A input
- 600 mV Pk-Pk signal input (BNC)
- Over limit signal input diode protection
- Ethernet port for data transfer and user configuration
- ±3000 V DC, 3.3 mA, regulated HV output (SHV)
- 2 × TTL outputs (BNC), 0 V - 3.8 V output, 50 Ω impedance matched, 20 mA output current
- RS-232 port (DB-9), used for debugging
- Programming jack (14-pin DIL), used for upgrading firmware
- Event LED (green), flashes on when trigger event
- Ethernet LED (yellow), flashes on when busy
- Power LED (red), on when unit is powered on

---

[1] Pulse Shape Discrimination
[2] Million Samples Per Second
[3] Million Pulses Per Second, excludes Ethernet communications
[4] After initial boot with host PC
[5] Requires proprietary programming device
[6] Electrically Erasable Programmable Read-Only Memory

THE BRITISH ASSESSMENT BUREAU ISO9001

Product Data Sheet - MFAX1.2. Rev 3.1

1/11/2014

Figure B.9 Mixed-field analyser data sheet